Vapour-based growth of inorganic compounds for next-generation, stable photovoltaics

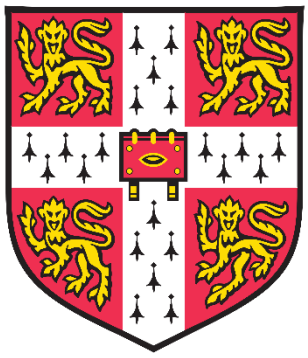

Lana Catherine Lee

Robinson College

University of Cambridge

A dissertation submitted for the degree of

Doctor of Philosophy

in the

Department of Materials Science and Metallurgy

University of Cambridge

June 2019

Dedicated to Essie Sheehan

Acknowledgements

First, I'd like to thank my supervisors for their support over the past few years. Prof Judith MacManus-Driscoll for finding funding for my work and providing useful feedback, and Dr Robert Hoye for giving up time to help me learn to become a researcher, for guidance and discussions on my work and training me on equipment. I'd also like to thank Prof Ken Durose and Prof Alison Walker for setting up the Centre for Doctoral Training in New and Sustainable Photovoltaics who funded my work.

From the Device Materials Group, I'd like to thank Dr Nadia Stelmashenko and Dr Ahmed Kursumovic for training me on equipment and being willing to share their knowledge and expertise. Ravi Raninga and Dr Tom Higgs for their moral support, crosswords, quizzes, pub trips and every other distraction to keep my mind off work (apart from mocking the north). Tahmida Huq, for being the most kind and selfless person ever. Claire Armstrong for all her help and guidance with the AP-SALD and other equipment when I joined the group. Jane Dukes, for keeping me in check with my admin and always being around for a friendly chat. Dr Weiwei Li and Dr Kelvin Zhang for helping with XPS measurements, and Rob Jagt for the useful discussions. And the rest of the Device Materials Group for their help and support and trips to the Alma. I'd also like to thank Mary Vickers, for training and help with X-Ray equipment, and my collaborators in optoelectronics: Dr Dawei Di; Dr Baodan Zhao; Dr Le Yang and Dr Mojtaba Abdi-Jalebi, as well as Lissa Eyre. Also, my friends in the CDT-PV; for helping me survive first year and being the best group of people to explore the country testing out free wine with.

Finally, and most importantly, I'd like to thank my family and friends who have helped me get to this point. My mum and dad, who have supported and encouraged me without ever questioning what I choose to do, and who have shown me the meaning of hard work. My sister Carrie-Anne, who I've looked up to as long as I can remember (maybe since she found my bottler), for inspiring me to do my best. Grandma Essie, who believed in us all so much, accompanied by prayers to St Theresa and drenchings in Holy water, for teaching me maths and how to spell. Nicola and Chris, for always looking out for me and being the best biggest big sister and big brother, and Rob, Kim, Millie, Daniel and Dexter. Auntie Geraldine for being Geraldine; Siobhan for checking up on me when I drop off radar, and John, Chris, Phil and Sam, for always being welcoming. To all the rest of my family: my grandparents, Uncle Joe, the Sheehans and Lees. I'd also like to thank my friends. Sam Kofler, for being the best friend I could ever ask for and an all-round great human, for helping me make the best 'one time me and Sam…' stories. Sarah Waterman, for reminding me that I like science on my bad days. The Bradford lot for making home feel like home, and to all my friends from Imperial. Finally, my partner India

Jordan; for putting up with me through the hundreds of breakdowns and making sure I didn’t quit when I wanted to, for being reassuring and helping to put things into perspective, for their general love and support and for being right that it would all turn out alright in the end.

Declaration of Originality

I declare that the work presented in this thesis is the outcome of research carried out at the Department of Materials Science and Metallurgy between September 2014 and June 2019, under the supervision of Professor Judith MacManus-Driscoll and Dr Robert Hoye. The contents of this thesis are the result of my own original work and none of the work is a result of collaboration unless acknowledged within the text. Chapters 2, 4 and 10 include small parts of work which were included in the submission for the Certificate of Postgraduate Study in the Department of Materials Science and Metallurgy, University of Cambridge. Aside from this, no contents have been submitted for any other degree, diploma or other qualification at the University of Cambridge or any other institution. Parts of chapters 3, 6 and 10 have contributed to publications in references [1–4]. Additionally, parts of chapter 8 are being prepared for a further first author publication. Other than this, none of the work contained within this thesis has been submitted to any other publications.

Including all tables, figures, appendices and references, this dissertation does not exceed the word limit set out by the Faculty of Physics and Chemistry (60,000 words).

Abstract

This thesis investigates the growth of stable inorganic compounds for photovoltaic applications using vapour-based fabrication techniques. In the literature section, chemical vapour deposition is identified as a versatile family of growth techniques through which a wide range of materials can be grown, and morphologies accessed. Of these, furnace based chemical vapour deposition holds the advantages of ease of set up and simplicity of equipment. Meanwhile, owing to the removal of lengthy vacuum and gas purging steps relative to temporal atomic layer deposition and the possibility of continuous substrate feeds, atmospheric pressure spatial atomic layer deposition reactors are identified as promising tools for high-throughput fabrication of metal oxide films, offering up to two orders of magnitude improvements to deposition rates over vacuum-based growth. For these reasons, both techniques are utilised for work in this thesis. Following this, a review of recent studies into low-toxicity bismuth containing photovoltaic absorber materials is presented. Most of these are predicted to form defect states close to the band edges such that carriers trapped in these states can be readily thermally de-trapped rather than undergoing Shockley-Read-Hall recombination across the bandgap. BiOI is identified as a promising photovoltaic material amongst compounds such as methylammonium bismuth iodide and bismuth-based double perovskite structured compounds due to its relatively favourable bandgap (1.9 eV), small predicted electron and hole effective masses and large dielectric constant.

Part A of the results and discussion section focuses on the growth, materials properties and application of BiOI in solar cells. Despite its predicted tolerance to defects, BiOI solar cells have traditionally performed poorly due to sub-optimal film morphology. In this thesis, compact BiOI thin films consisting of large crystallites are grown by chemical vapour deposition at atmospheric pressure in a tube furnace. Incorporation into photovoltaic devices almost doubles the efficiency of literature reports, achieving a record efficiency of 1.8 %, as well as the highest external quantum efficiency for any bismuth-based photovoltaic material of 80 % (at $\lambda = 460$ nm). Additionally, device performance is stable after 3 days storage in ambient conditions under laboratory illumination. Growth at higher temperature is then explored to assess whether the structural properties of BiOI can be improved. A decrease in Urbach energy from 70 to 40 meV occurs when the deposition temperature is raised from 360 ºC to 500 ºC, proposed to enable higher device open-circuit voltage. However, micron-sized particles form on the film surface due to unwanted gas phase reactions at temperatures $\geq$ 400 ºC, limiting their potential application. Finally, films are annealed under vacuum to deliberately introduce iodine deficiency. Phase purity is maintained despite up to 40 % iodine loss at the film surface, whilst, over the same measurement area in photoelectron spectroscopy measurements, the Fermi level of BiOI remains constant after

48 hours of vacuum annealing at 100 ºC, indicating that iodine loss does not induce a doping effect and suggesting BiOI shows tolerance to iodine deficiency.

Part B of the results and discussion section focuses on high throughput fabrication of NiO_x thin films for application as a hole transport layer in perovskite solar cells. This aims to overcome the throughput limitations of solution and vacuum based batch processing routes towards NiO_x which have been used in *p-i-n* perovskite devices. Deposition conditions for NiO_x film growth using the Vertical Cambridge University Close Proximity reactor are established. Using growth curves, growth is determined to occur *via* a decomposition mechanism, typical of chemical vapour deposition reactions. Additionally, growth rates over 30 times faster than vacuum-based temporal atomic layer deposition are achieved. Incorporation into *p-i-n* organolead halide perovskite devices gives a champion efficiency of 16.6 %, which is comparable to the best devices using solution- and vacuum- based NiO_x processing techniques. An annealing strategy to reduce the defect concentration in NiO_x films is identified, whilst preliminary experiment exploring alternative solar cell device architecture which result in improved device currents are discussed.

List of Publications

1. L. C. Lee, T. N. Huq, J. L. MacManus-Driscoll and R. L. Z. Hoye, Research Update: Bismuth-Based Perovskite-Inspired Photovoltaic Materials, *APL Mater.*, 2018, **6**, 084502.

2. R. L. Z. Hoye, L. C. Lee, R. C. Kurchin *et al.*, Strongly Enhanced Photovoltaic Performance and Defect Physics of Air-Stable Bismuth Oxyiodide (BiOI), *Adv. Mater.*, 2017, **29**, 1702176.

3. B. Zhao, L. C. Lee, L. Yang *et al.*, In Situ Atmospheric Deposition of Ultrasmooth Nickel Oxide for Efficient Perovskite Solar Cells, *ACS Appl. Mater. Interfaces*, 2018, **10**, 41849–41854.

4. R. E. Brandt, J. R. Poindexter, P. Gorai *et al.*, Searching for 'Defect-Tolerant' Photovoltaic Materials: Combined Theoretical and Experimental Screening, *Chem. Mater.*, 2017, **29**, 4667–4674.

5. L. C. Lee *et al.*, An Experimental Study of Defect Tolerance in Bismuth Oxyiodide, (*in preparation*)

Table of Contents

List of Figures

List of Tables

1 Introduction

The greatest threat to global life is human-caused climate change. Continuously increasing CO_2 emissions from burning fossils fuels are causing the planet to heat, resulting in rising sea levels and unpredictable weather patterns with devastating outcomes. These events almost exclusively affect those in the poorest areas of the world, whilst those who contribute to and benefit the most from fossil fuel usage live in the most developed areas. On top of this, a growing population and improvements to quality of life worldwide mean that global energy consumption is anticipated to rise from 167,500 TWh in 2018 to 208,100 TWh by 2040.[5] A complete overhaul of human behaviour and the way energy is consumed is essential to minimise the impact of this on the planet. The need for greater investment in renewable energy sources is obvious.

Renewable energy sources contributed towards 10 % of the global electricity market in 2018.[6] This figure is predicted to rise by 260 % in 2040, with the total contribution of renewables anticipated to replace coal as the primary electricity source by then.[6] Yet the Intergovernmental Panel on Climate Change (IPCC) predicts that renewables must contribute > 60 % to the electricity market by 2050 to limit global warming to 1.5 ºC above pre-industrial levels.[7] Thus, further utilisation of renewable energy sources is needed. Of the renewable resources, the sun has the greatest capacity to supply the human population. The earth is irradiated with 3.9×10^{24} J of energy by the sun every year, 1 % of which is in a suitable location to be harnessed by photovoltaic or photothermal technologies.[8] This is 100 times the current global energy consumption.

At present, silicon modules dominate the photovoltaics field; the latest Fraunhofer ISE Photovoltaics Report states that crystalline silicon contributes to 95 % of the global photovoltaics market.[9] Whilst this technology has been historically limited by high costs, prices continue to fall due to the demand for silicon wafers for electronics.[10,11] However, wafers are produced by energy intensive means, for example the Czochralski method uses temperatures in excess of 1400 °C to grow single crystal ingots from molten silicon.[12] Clearly there exists a need to investigate alternative technologies which require less energy intensive processing methods, whilst developing scalable processing routes is important to aid high volume manufacturing.

Work in this thesis focuses on vapour-phase fabrication of inorganic materials at temperatures below 500 ºC for emerging photovoltaic technologies. The first half explores the potential of a bismuth-based light absorber, BiOI, in photovoltaic applications, whilst the second half investigates the growth of NiO_x by a potentially scalable method, using an atmospheric pressure spatial atomic layer deposition reactor.

2 An introduction to photovoltaics: working principles and devices

2.1 The photovoltaic effect

A solar cell converts light energy into electrical energy *via* a phenomenon known as the photovoltaic effect. A semiconductor absorbs a photon of energy equal to or greater than its bandgap (E_g), promoting an electron into an excited state. The electron can either relax back to its ground state or, as in the case of the photovoltaic effect, can be swept away due to the presence of an electric field. This field is provided by putting the semiconductor in contact with another semiconductor or a metal. The electron is pulled into an external circuit where it can do work due to the energy gained from photoexcitation, the photovoltage.[13]

2.2 *p-n* junctions

In many photovoltaic devices, the electric field arises across a *p-n* junction. Here a *p*-type and an *n*-type semiconductor are brought into contact with one another. They may be the same semiconductor doped *p*- and *n*- type as for crystalline silicon[14] and GaAs[13] solar cells, or two different semiconductors, e.g. in CdTe-CdS[15] and Cu_2O-ZnO[16] heterojunction solar cells. Upon contact, there is a redistribution of charge at the interface caused by the higher concentration of electrons in the n-type region than the p-type region. As a result, diffusion of charges down the concentration gradient occurs (*i.e.* diffusion of electrons from the *n*- to *p*- type region and diffusion of hole from the *p*- to *n*- type region), named the diffusion current. The diffusion of charges creates a region made up of oppositely charged ion cores called the depletion region, across which an electric field is present, and band bending at the interface (Figure 2.1).[13,17] A drift current which opposes the diffusion current occurs as a result of the electric field. At equilibrium the drift and diffusion currents are balanced and the Fermi levels of the *p*- and *n*- sides of the junction are aligned. A built-in potential, V_{bi}, remains, which is the energy difference between the Fermi levels of the isolated *p*- and *n*- type semiconductors.[13]

In a *p-n* junction photovoltaic device, absorption of a photon of energy equal to or greater than the bandgap, excites electrons across the bandgap from the valence band (VB) to the conduction band (CB, Figure 2.2).[18] For inorganic materials, which typically have large dielectric constants, the electron and hole pair formed are not attracted to one another and can be considered free carriers due to charge screening effects.[19] The photo-generated electrons at the *p*-type side and holes at the *n*-type side of the junction are the minority carriers. These diffuse towards the

depletion region and are swept across the junction by the electric field,[20] beyond which they become majority carriers. They are collected at the electrodes to join the external circuit.

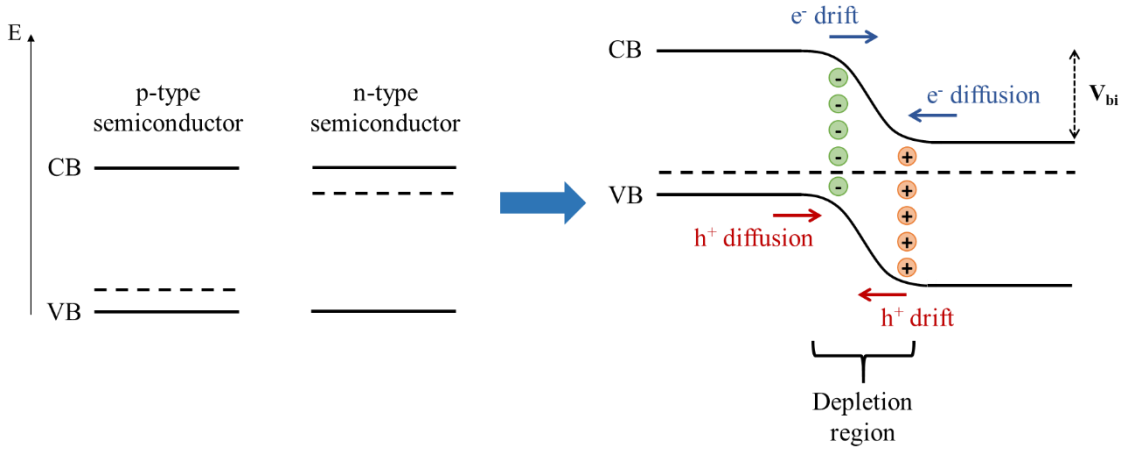

Figure 2.1 The formation of a p-n junction due to redistribution of carriers when a p-doped and an n-doped semiconductor are brought into contact.[18] CB and VB are the conduction band and valence band, V_{bi} is the built-in voltage across the junction.

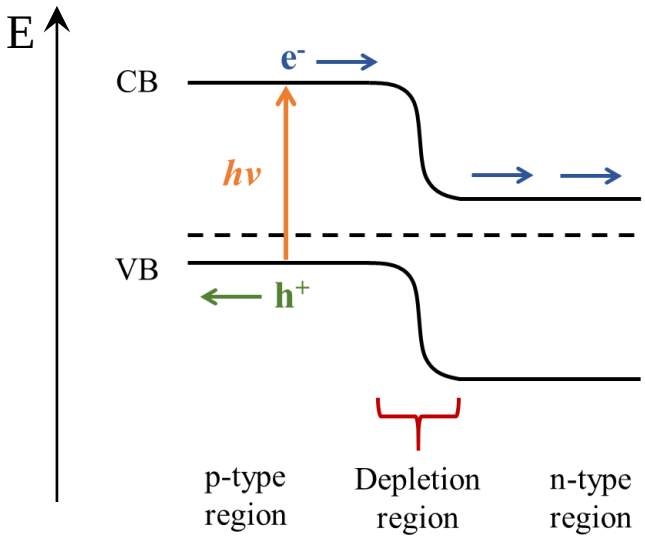

Figure 2.2 Absorption of photons at a *p-n* junction results in the formation of minority carriers (electrons in the *n*-type and holes in the *p*-type region). The minority carriers diffuse to the depletion region and are swept across by the electric field, towards the external circuit to do useful work.[13]

2.3 Measurement of device performance

1.1.1 JV measurements

Solar cells are defined by their power conversion efficiency (PCE, %),[13]

$$PCE = \frac{P_{max}}{P_{in}} \times 100\% \quad \textbf{(2.1)}$$

where P_{max} is the maximum power output of the device and P_{in} is the power of incident light (which in practice are defined as power densities, $mWcm^{-2}$). P_{max} is determined by measuring the current output of a device under illumination when a direct voltage sweep is applied (Figure 2.3). The current output of a solar cell depends on the incident spectrum (the wavelengths and intensity of incident light), therefore conditions are standardised to the air mass 1.5 global spectrum (AM 1.5 G) with a power density of 100 mW/cm^{-2}. The AM 1.5 G spectrum represents solar radiation after it has passed through the equivalent of 1.5 atmospheres, typical conditions that a solar panel in a mid-latitude location would experience.[21] Note that the current density, J (mA/cm^{-2}), is measured rather than the current.

From the product of the current density and voltage a power curve can be established, from which the P_{max} is determined (Figure 2.3). The current density and voltage at the maximum power point are defined as J_{mpp} ($mAcm^{-2}$) and V_{mpp} (V) respectively. Thus,

$$PCE = \frac{J_{mpp}V_{mpp}}{P_{in}} \quad \textbf{(2.2)}$$

Other parameters which define solar cell performance are the short-circuit current density, J_{SC} ($mAcm^{-2}$), and the open-circuit voltage, V_{OC} (V). The J_{SC} is the maximum current that can be achieved for a device and corresponds to when the device is at short-circuit conditions (*i.e.* the two terminals are contacted and there is no load across them). In the case where a load is present between the terminals, the current decreases from J_{SC}. The load forms an opposing electric field across the device which generates an opposing current to the photocurrent, known as the dark current.[13] This can be thought of as a decrease in the drift current across the depletion region due to the reduced electric field (or an increase in the diffusion current due to the excess carriers) under forward bias (Figure 2.4).[13] Thus, the dark current is equivalent to the response of a diode under forward bias and is described by the diode equation:

$$J_{dark}(V) = J_0(e^{\frac{qV}{mk_bT}} - 1) \quad \textbf{(2.3)}$$

where J_{dark} is the dark current density (mA cm^{-2}) , J_0 is the recombination parameter (mA cm^{-2}),[22] k_b is Boltzmann's constant (J K^{-1}), V is the voltage (V), T is the temperature (K) and q is the elementary charge (C). An ideality factor, m, is included to model non-ideal diode behaviour,[23] the relevance of which will be discussed in section 2.5.2.

The current density under illumination (or photocurrent, J_{ph} (mA cm^{-2})) when bias is applied is therefore approximated as the dark current subtracted from the short-circuit current density:

$$J_{ph} = J_{SC} - J_0(e^{\frac{qV}{mk_bT}} - 1) \quad \textbf{(2.4)}$$

The V_{OC} is the maximum voltage achieved by a device and occurs when the device is at flat band conditions such that no current flows.[13] At this point J_{dark} is equal to J_{sc}, and rearrangement of equation **2.4** gives:[23]

$$V_{OC} = \frac{mk_bT}{q} ln(\frac{J_{SC}}{J_0} + 1) \quad \textbf{(2.5)}$$

The fill factor, FF, is a unitless shape factor between 0 and 1 which describes resistive losses within the device. It can be pictured as a ratio of the blue and orange boxes in Figure 2.3, or expressed mathematically as:

$$FF = \frac{J_{mpp}V_{mpp}}{J_{SC}V_{OC}} \quad \textbf{(2.6)}$$

Thus,

$$PCE = \frac{J_{SC}V_{OC}FF}{P_{in}} \quad \textbf{(2.7)}$$

A fill factor closer to 1 will maximise device efficiency.

The two resistances in the device which act to reduce FF are the series resistance, R_S, and the shunt resistance, R_{SH}. These can be approximated as the inverse of the slope of the JV curve near the V_{OC} and J_{SC} respectively.[24–26] The series resistance arises from resistance at the contacts

and within the materials[13] whilst the shunt resistance stems from current leakage pathways in the device,[26] for example recombination of a hole in the *p*-type region with an electron at the opposite contact. Current leakage arises due to morphology issues such as pinholes.[1] The shunt resistance is a parallel resistance, meaning that devices are improved by maximising R_{SH}, whilst the series resistance should be minimised.[13]

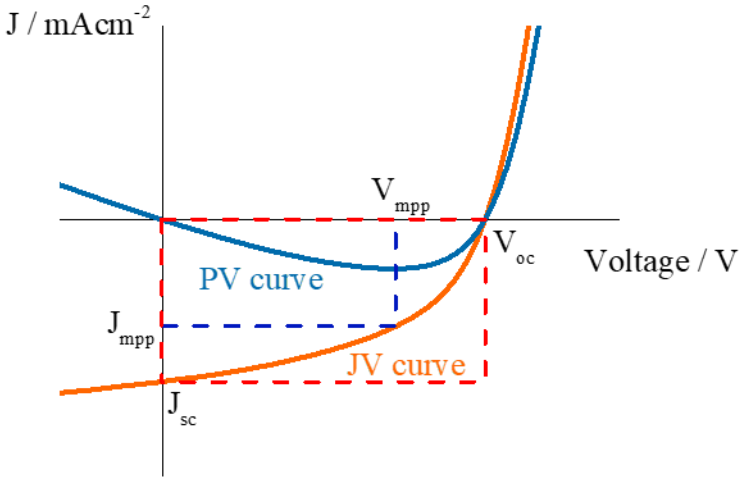

Figure 2.3 A typical current-voltage (JV) curve for a solar cell measured under illumination (orange trace) and the power-voltage curve (PV) for the same device (blue trace). J_{mpp} and V_{mpp} mark the current density and voltage at the maximum power point, J_{sc} indicates the short-circuit current density and V_{oc} indicates the open-circuit voltage. The fill factor (FF) is the ratio of the blue and orange dashed rectangles.

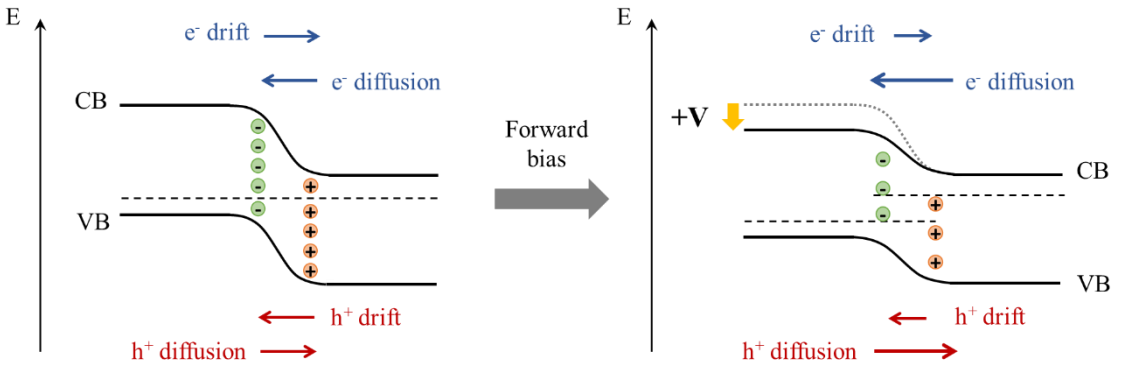

Figure 2.4 Forward bias at a *p-n* junction. Application of a positive potential at the p-doped region pushes the Fermi level down in energy. This results in an increase in diffusion current to redistribute charge carriers and a decrease in drift current as a result of reduced band-bending at the interface.

2.3.1 External quantum efficiency

The external quantum efficiency (EQE) is a measure of the ability of a device to turn a photon into current at wavelength λ. It depends on the light harvesting ability of the semiconductor and the efficiency of charge separation and collection. The EQE is related to the J_{SC} by:[13]

$$J_{SC} = q \int b_s(\lambda) EQE(\lambda) d(\lambda) \qquad \textbf{(2.8)}$$

where q is the electronic charge (C) and $b_s(\lambda)$ is the incident photon flux at λ (cm^{-2} s^{-1}), *i.e.* the EQE is integrated over the incident spectrum. EQE is 0 at wavelengths where the semiconductor does not absorb.

The AM 1.5 G solar spectrum is shown in Figure 2.5. According to equations **2.7** and **2.8**, maximising the PCE can be achieved by maximising the EQE, namely by improving light absorption over the solar spectrum. Thus, using materials with smaller bandgaps gives higher J_{SC}s. However, reducing the bandgap means that the maximum photovoltage which a charge carrier possesses (and hence the device V_{OC}) is reduced.[27] As such, an optimum bandgap which achieves a balance between the J_{SC} and V_{OC} exists.[28,29] This was calculated by Shockley and Queisser, who calculated the theoretical maximum efficiency as a function of bandgap for the AM 1.5 G spectrum, known as the Shockley-Queisser limit,[29] as will be discussed in section 2.4.3.1.

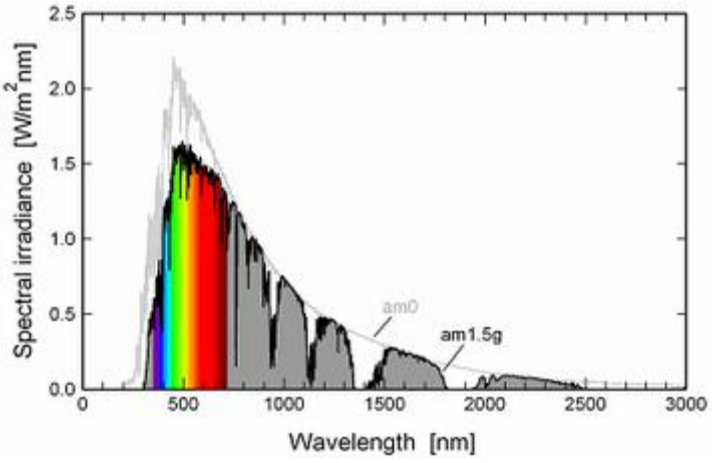

Figure 2.5 The AM 1.5 G spectrum, the standard spectrum used for measuring photovoltaic devices at a power density 100 $mWcm^{-2}$. Reproduced from reference [30]

2.4 Device losses

Many sources of performance loss occur within devices, some of which are intrinsic and uphold thermodynamic principles, whilst others are avoidable with careful consideration of device materials and processing conditions.

2.4.1 The Shockley-Queisser limit

The Shockley-Queisser (SQ) limit as a function of bandgap for the AM 1.5 G solar spectrum is shown in Figure 2.6.[29,31] A bandgap of ~1.3 eV has been determined as optimum for a solar cell, where the maximum theoretical efficiency for a single junction solar cell is ~34%.[29,31,32] Calculation of the limit considers several intrinsic losses in a device, processes **1** – **5** in Figure **2.7**b.[33] Photons of energy smaller than the bandgap are not absorbed (**1**) and so do not generate minority carriers.[33,34] Minority carriers generated by photons of energy greater than the bandgap thermalise to the band-edges within picoseconds, releasing heat (**2**).[35] Minority carries which drift across the depletion region lose energy due to the potential difference across the *p-n* junction (**3**).[13] Additionally, photo-generation of carriers must be a reversible process to maintain thermodynamic equilibrium, therefore radiative recombination losses (the emission of a photon due to recombination of photo-generated electrons and holes across the bandgap) occur (**4**).[13,29,31,33] Finally, other losses occur due to reflection.[29]

Ways to overcome the SQ limit, such as multiple exciton generation and hot carrier extraction,[28] are under investigation but remain outside the scope of this thesis. However, tandem devices have relevance. These multi-junction devices contain two or more semiconductors which absorb in different regions to simultaneously maximise J_{SC} and V_{OC}, and to minimise spectral losses.[27,32] These give the potential to build upon existing infrastructure of silicon modules, which dominate the market,[9] with potentially significant efficiency improvements. For example, considering a two-junction tandem with a silicon bottom cell, Todorov *et al.* calculate a maximum achievable efficiency of ~ 45% for a top cell with bandgap 1.7 – 1.9 eV.[32] Multi-junction devices to date with 3 – 5 junctions have already exceeded 37% efficiency[36] but these have used expensive fabrication methods, limiting them to niche markets.

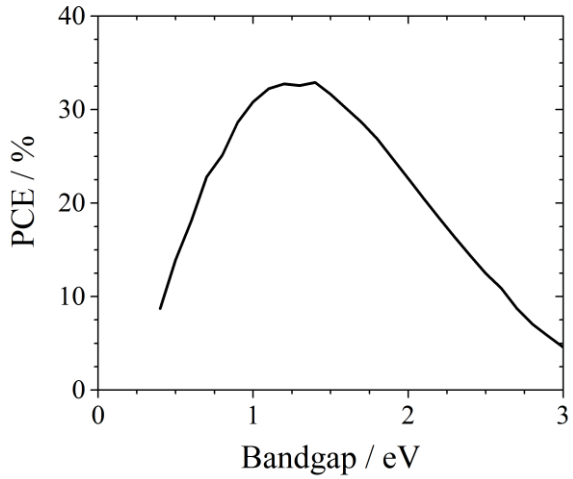

Figure 2.6 The Shockley-Queisser limit for a single junction solar cell as a function of bandgap energy. Graph produced using data with permission from reference [31].

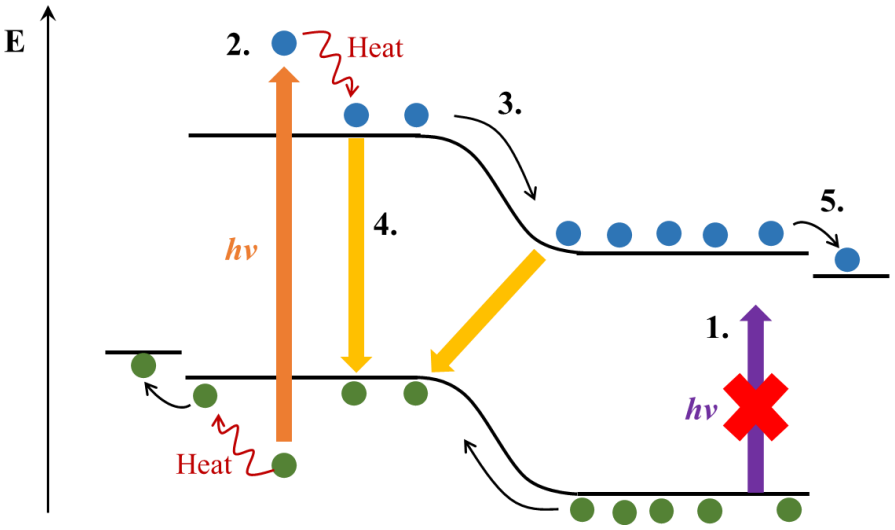

Figure 2.7 The sources of energy loss in a single-junction solar cell: **1.** Photon of energy smaller than the bandgap is unable to promote an electron into the conduction band, **2.** Electrons and holes generated by photon of energy greater than the bandgap thermalise to the band edges, **3**. Voltage loss due to the potential difference across the *p-n* junction, **4.** Recombination of carriers across the bandgap and **5.** Energy loss on carrier injection into the contacts. Image adapted with permission from reference [33].

2.4.2 Voltage loss at interfaces

Device losses due to non-optimised device materials will be discussed in more detail throughout the text. However, briefly, materials with poor energy matching, *e.g.* at the contacts, result in voltage losses at the charge transfer interfaces (see Figure **2.7** process **5**).[1,33]

2.4.3 Recombination

The photoexcitation of a semiconductor generates excess carriers, removing the material from its equilibrium state.[37] There is a thermodynamic drive for the semiconductor to return to its equilibrium state *via* relaxation of the excited carriers, known as recombination (Figure 2.7 process **4**).[33] This recombination of an electron and hole is accompanied by the release of energy as a photon (radiative) or heat (non-radiative). All recombination processes reduce V_{OC}.[38]

Radiative recombination (Figure 2.8a) is the opposite process to photo-absorption, as described in section 2.4.1. It is dominant in direct semiconductors but less so in indirect semiconductors,[38] as a change in momentum of the electron is required for an indirect transition. Two types of non-radiative recombination are Auger and Shockley-Read-Hall recombination. In Auger recombination, the energy released on the recombination of an electron and hole promotes a third electron or hole into a higher energy state, followed by thermalisation (Figure 2.8c).[13,39,40] Auger recombination is dominant in materials with high doping levels due to high dependency on carrier concentration.[13,41] Shockley-Read-Hall (SRH) recombination is the main recombination process in indirect semiconductors and occurs through trap states situated within the bandgap (Figure 2.8c).[42] This is also described as trap-assisted recombination. These states are introduced by defects such as vacancies, interstitials and dislocations which occur at interfaces or within the bulk material (*e.g.* at grain boundaries).[39,42] Carriers become trapped in these states and can either be thermally re-emitted or recombine with a carrier of opposite charge at the band edge, releasing the excess energy as heat (although the recombination process may also be radiative). SRH recombination can occur within the bulk material or across the junction and is more likely to occur from deep traps closer to mid-gap,[28] where thermal energy (k_bT) is insufficient to de-trap the carriers.

For all recombination processes, the recombination current opposes the flow of the photocurrent.[43] Therefore, all recombination processes reduce the V_{OC} *via* an increase in J_{dark} (see equation **2.4**).

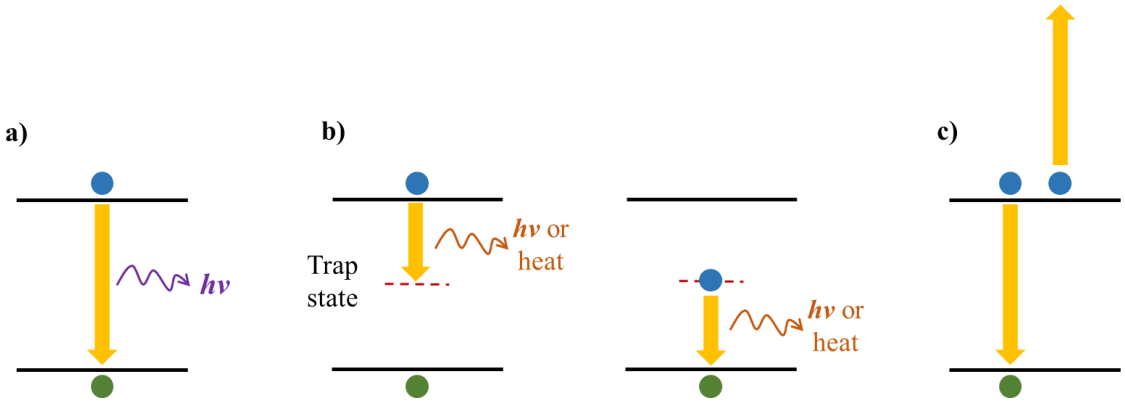

Figure 2.8 a) radiative recombination between an electron in the conduction band and a hole in the valence band resulting in the emission of a photon equal in energy to the band gap, b) trap-assisted SRH recombination, where a hole recombines with an electron trapped within a trap state; energy is lost as either heat or light, and c) Auger recombination, where the energy released on recombination of carriers across the bandgap promotes a third carrier into a higher energy state.

2.4.3.1 Measurement of recombination processes

An indication of the type of recombination is the ideality factor (*m*) introduced in equation **2.3**. This models the behaviour of a non-ideal diode under bias due to trap-assisted recombination across its depletion region[23,39]. *m* tends towards 2 when SRH recombination dominates in a solar cell,[23,44,45] with values closer to 2 for deeper trap states.[45,46] Auger recombination is also calculated to influence the ideality factor, resulting in values below 1.[44]

m is calculated in one of two ways. Firstly, considering equation **2.3** the dark current of a solar cell has an exponential dependence on 1/*m*. Thus, *m* can be determined from the gradient of a semi-logarithmic plot of ln[J_{dark}] *vs* voltage, where the current response of the device is measured under forward bias in the dark.[23] The second method is argued to be more representative of a working diode under illumination.[23] Equation **2.8** indicated that a greater spectral flux (*i.e.* light intensity) causes an increase in J_{SC}, therefore the J_{sc} can be considered proportional to light intensity, ϕ.[13] Equation **2.5** becomes:[24,46]

$$V_{OC} = \frac{mk_bT}{q} ln(\phi) + c \qquad \textbf{(2.9)}$$

where *c* is a constant. Hence, *m* can be extracted from the gradient when V_{OC} is plotted against *ln*(light intensity).

Photoluminescence spectroscopy can also be used to probe recombination processes. A semiconductor is excited by a photon with energy greater than its bandgap, and the wavelength and intensity of emitted light is measured. Where non-radiative recombination is dominant, little to no photons are emitted. For band-to-band radiative recombination, the emitted photon has energy equal to the bandgap. Otherwise emission may occur *via* defect states, where the emitted photon is red-shifted relative to the bandgap.[47] These trap states will act as centres for trap-assisted recombination.

2.4.3.2 Minority carrier lifetime and diffusion length

Recombination processes have severe consequences on device performance. Trap-assisted recombination influences the transport properties of a material, which in turn influences current collection. The minority carrier lifetime is a measure of the time taken for a minority carrier to recombine with an oppositely charged carrier.[48] Radiative, Auger and SRH recombination contribute to the overall (bulk) lifetime:[48,49]

$$\frac{1}{\tau_{bulk}} = \frac{1}{\tau_{rad}} + \frac{1}{\tau_{Auger}} + \frac{1}{\tau_{SRH}} \qquad \textbf{(2.10)}$$

where τ_{bulk} is the bulk lifetime (s), τ_{rad} is the lifetime for radiative recombination (s), τ_{Auger} is the lifetime for Auger recombination (s) and τ_{SRH} is the lifetime for SRH recombination (s). Maximising the lifetime means more time is available for the minority carrier to be extracted, which has been correlated with device efficiency.[1,4,50] Whilst radiative recombination is an intrinsic process, SRH recombination can be controlled by limiting the defect density of the semiconductor. This is achieved by careful materials processing, for example by growing a material at a higher fraction of its melting point or through slow crystallisation.[1,4,51,52] This will be discussed in more detail in chapter 4.

There are many methods to measure minority carrier lifetime, which involve creating an excess of minority carriers and measuring their decay.[48] The method of interest for this work is an optical method; time-resolved photoluminescence (TRPL) spectroscopy. The semiconductor is excited by a laser pulse and the light emitted due to recombination is measured over time. For an exponential decay, the change in intensity over time is given by:

$$\frac{I(t)}{I(0)} = Ae^{-t/\tau} \qquad \textbf{(2.11)}$$

Where I(0) is the intensity at 0 s, I(t) is the intensity at time t, A is the amplitude and τ is the minority carrier lifetime (s). The lifetime can be approximated as the time when the intensity drops to 1/*e*.

The minority diffusion length, L_D (cm), is the distance that minority carriers can diffuse before recombining with an oppositely charged carrier. It is directly related to τ by:[53]

$$L_D = \sqrt{D\tau} \quad \textbf{(2.12)}$$

Where D is the diffusivity of the minority carrier (cm^2s^{-1}). L_D has an important implication on devices; if a minority carrier is generated at a distance $x > L_D$ from the depletion region, it will recombine before reaching the junction and will not contribute to the photocurrent. Device thickness needs to reach a balance between L_D and the absorption length;[19,20] the distance at which the intensity of light of wavelength λ decreases by 1/*e*. The absorption depth, δ (cm), is determined from:

$$\delta(\lambda) = \frac{1}{\alpha(\lambda)} \quad \textbf{(2.13)}$$

Where α is the absorption coefficient (cm^{-1}). Thus, to minimise δ, photovoltaic materials should have high absorption coefficients.[19] Hence ideally, to absorb most of the incident light, the thickness of the device, *w*, should be $\sim \delta e$ (*i.e.* ~ 3 times the absorption length),[28] whilst for optimum charge collection requires $L_D \approx w$.[19]

As such, two strategies have been taken in the search for efficient photovoltaic devices:

(i) Using relatively thick absorber materials with energy intensive fabrication routes to maximise minority carrier diffusion lengths[20,54]

(ii) Using strongly absorbing semiconductors ($\alpha \sim 10^4 – 10^5$ cm^{-1}), allowing the use of thinner absorber layers placing less constraints on the material quality (can have shorter diffusion lengths).[54,55]

The emergence of different photovoltaic technologies based on these principles will be discussed in the following chapter.

2.5 Types of devices

2.5.1 Silicon solar cells

The most established photovoltaic technology which dominates the PV market uses silicon (doped by boron and phosphorous) to form a *p*-*n* junction. As an indirect semiconductor, Si is a poor light absorber, possessing an absorption length of ~ 100 μm just above its bandgap, meaning several hundred-micron thick wafers must be used to absorb enough incident light.[17,38,54] Therefore, the silicon must be defect free to maximise L_D (as discussed for strategy (i) in section 2.4.3.2), requiring energy intensive fabrication, and is often cut from single crystal ingots or multi-crystalline silicon blocks. Growth temperatures of 1500 – 1900 ºC are used, whilst diffusion doping occurs at temperatures in excess of 850 ºC.[12,20,38,56] Through a combination of improved growth methods, defect passivation and the development of anti-reflective coatings and new device architectures,[38] PCEs as high as 26.7% for single crystal and 24.4% for modules have been achieved (Table 2.1).[36,57]

2.5.2 Thin film solar cells

Despite the progress in crystalline silicon photovoltaics, elimination of the energy intensive processing steps and material usage could reduce module fabrication costs by up to 20%.[38] As such, a drive towards alternative semiconductors with high absorption coefficients, such as CdTe, $CuIn_xGa_{1-x}Se_2$ (CIGS) and $Cu_2ZnSnS_ySe_{4-y}$ (CZTS(Se)), based on the principles of enabling shorter diffusion lengths (strategy (ii) above) has occurred.[54] These compounds possess absorption coefficients of $10^4 – 10^5$ cm^{-1} over the visible range, an order of magnitude larger than silicon, meaning that only a few microns of material are required in devices (Table 2.1).[54,58] They form a class of PV devices named thin film solar cells (or 2nd generation solar cells). CdTe and CIGS cells have both reached > 20% efficiency (Table 2.1)[36] and their modules are on the market.[59,60] However, concerns remain over their use of low-abundant metals (Te 1 ppb, In 160 ppb in earth's crust) as well as toxic Cd.[61,62] Conversely, CZTS(Se) contains all earth-abundant elements, however efficiencies remain limited to ~ 11%.[36,63] Fabrication of phase pure CZTS is difficult, due to thermodynamically stable competing phases such as CuS, ZnS, Cu_2SnS_3 and SnS.[64] Additionally, low formation energy defects such as Cu_{Zn} (formation energy 0.01 eV) and Zn_{Cu} anti-sites introduce trap states within the bandgap which limit the V_{OC}.[65,66] As a result, even the V_{OC} of the best CZTS device is < 50% of the bandgap energy (V_{OC} 0.71 eV *c.f.* E_g 1.5 eV).[63]

The only single-junction technology which out-performs Si to date uses GaAs; a direct bandgap semiconductor resulting from substitution of group IV Si with group III and group V elements. Whilst PCEs have reached as high as 29.1% (Table 2.1),[36] raw materials costs are high

such that they are almost exclusively used in space applications.[67] They also act as the bottom cell of a range of multi-junction devices which have reached > 37%.[36,68]

Whilst strategies (i) and (ii) have facilitated the development of marketed photovoltaic technologies, a third research strategy which offers the possibilities of solution processing and high-throughput 'printing' processes has been investigated extensively over the past few decades, forming part of a class of devices called 3rd generation solar cells. This involves:

(iii) Separating the roles of light absorption and transport within the device, placing less constraints on the materials quality of the light absorbing material.

Such devices are based on *p*-*i*-*n* junctions rather than *p*-*n* junctions, as will be discussed in the next section.

2.5.3 *p*-*i*-*n* junction devices

At a *p*-*i*-*n* junction, an intrinsic semiconductor (*i*, which in practice is slightly doped),[37] is placed between a *p*-type and an *n*-type semiconductor (Figure 2.9). As a result, an electric field extends across the whole devices, and photo-generated electrons and holes within the *i*-type region drift towards the *n*- and *p*-type regions respectively. The low doping levels in the 'intrinsic' region results in low levels of minority carrier recombination, facilitating potentially long lifetimes.[37] This places fewer constraints on the material quality, allowing low temperature and solution processing methods.[1,54] However, structural defects (*e.g.* at grain boundaries) still act as recombination sites and need to be controlled.

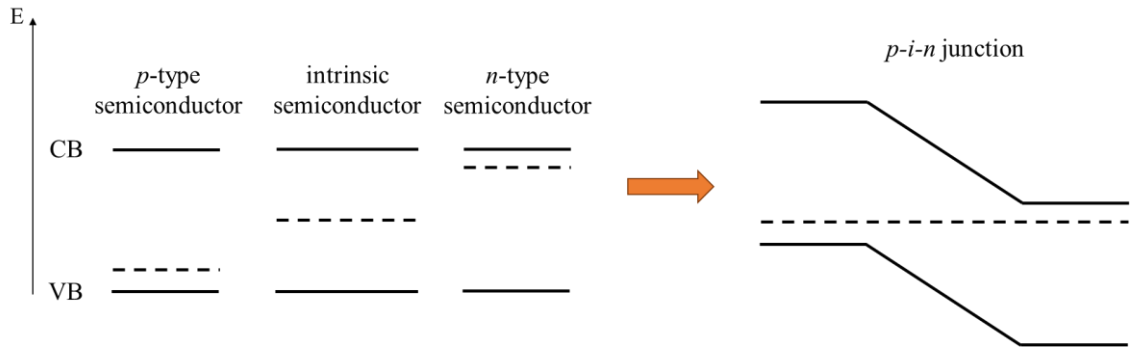

Figure 2.9 Formation of a *p*-*i*-*n* junction when an intrinsic semiconductor is sandwiched between *p*- and *n*- type semiconductors

The *p*-type layer is often referred to as the hole transport material or layer (HTM or HTL) and the *n*-type layer as the electron transport material or layer (ETM or ETL). These can be referred to collectively as the charge transport materials (CTMs). For efficient charge collection, the CTMs must be charge selective (*i.e.* electron or hole blocking), therefore often possessing large bandgaps,[69] and must be conductive enough to carry charges to the contacts. Furthermore, good alignment of the valence band of the HTM with that of the light absorber (*i*) and the conduction band of the ETM with the conduction band of *i* is necessary to reduce voltage loss at the charge transfer interfaces (*p*|*i* and *i*|*n*)[69] and maximise V_{OC}.

The *p*-*i*-*n* device configuration has been used to bypass the energy intensive production of crystalline silicon, allowing the use of amorphous silicon in devices. However, efficiencies have been limited to ~10%.[36] Dye-sensitised solar cells (DSSCs) represent another *p*-*i*-*n* technology (where the more common configuration is *n*-*i*-*p*). The intrinsic layer is a strongly absorbing dye, a metal complexes with conjugated aromatic ligands or metal-free organic compounds, which binds to a mesoporous TiO_2 ETM and, traditionally, a redox active electrolyte as HTM.[70,71] Due to stability issues and to reduce voltage loss at charge transfer interfaces, liquid electrolytes have been substituted with cobalt-based solid-state electrolytes.[72] Their more common device configuration is *n*-*i*-*p*, where devices are illuminated from the *n*- side. An important feature of DSSCs is that all layers can be processed from solution, facilitating large area printing of devices (*e.g.* using screen printing methods).[73] However, their record device efficiency remains < 50% that of crystalline silicon,[36] and many companies who began their commercialisation have since ceased production or turned their attention to a more promising emerging technology; the lead halide perovskites,[74] which will be discussed in more detail in the following chapter. However, the DSSCs have inspired solar cells using a range of sensitizers in place of dyes, such as Sb_2S_3,[75] $AgBiS_2$[76] and a range of quantum dots,[77] where organic semiconductors usually act as the HTM. Additionally, advances in spectroscopy, probing the dynamics of charge transfer processes, and materials understanding have been made investigating these systems.[67]

Table 2.1 The record power conversion efficiency for different types of photovoltaic device.[36] Cell area is defined as ≥ 1 cm^2, module area is ≥ 800 cm^2 and sub-module is ≥ 200 cm^2.[36]

Type of device	Best cell PCE / %	Best module PCE / %	Absorber layer thickness / μm	α / cm^{-1}
Single crystal Si	26.7 [57]	24.4 [57]	> 100 [38,54]	$10^3 – 10^4$ [58]
Multi-crystalline Si	22.3 [78]	19.9 [36]	> 100 [38]	$10^3 – 10^4$ [58]
GaAs (thin film)	29.1 [79]	25.1 [80]		$10^4 – 10^5$ [58]
CdTe	22.1 [81]	18.6 [36]	1 – 2 [54]	$10^4 – 10^5$ [58]
CIGS	22.9 [36]	19.2 [59]	1 – 2 [54]	$10^4 – 10^5$ [58]
CZTSSe	11.3 [36]	-	1 – 2 [54]	10^4 [82]
DSSC	13.0 [70],a	8.8 (sub-module) [83]	Monolayer (order of Å) [84]	$10^4 – 10^5$ [$M^{-1}cm^{-1}$] [71]
Perovskite	23.2 [85],b	11.6 [36]	0.1 – 1 [86]	$10^4 – 10^5$ [58]
Organic	11.2 [87]	8.7 [87]	0.01 – 0.1 [69]	10^5 [88]

[a] Uncertified device efficiency, [b] unpublished record efficiency of 25.2 % has been reported for a perovskite solar cell[89]

2.5.4 Perovskite solar cells

2.5.4.1 The properties of organolead halide perovskites and their defect tolerance

Perovskite solar cells are a 3rd generation photovoltaic technology which have emerged over the past decade, gaining an unprecedented rise in device efficiency from 3.8%[90] to > 24%[85,89] during this time. They use a class of materials which crystallise into the classic calcium titanate perovskite structure as the light absorbing layer. However, the family of compounds are based on organolead trihalides. These form the ABX_3 crystal structure (Figure 2.10), where A^+ is a cation such as methylammonium (MA), formamidinium (FA) or Cs^+, B^{2+} is Pb^{2+} and X^- is a halide ion.[91,92] Halogen sharing Pb-X octahedra occupy the corners of a cube, whilst A^+ in the centre of the cube (*i.e.* the ½,½,½ position).[93] Distortion from cubic symmetry can occur with different sized ions.[91,92]

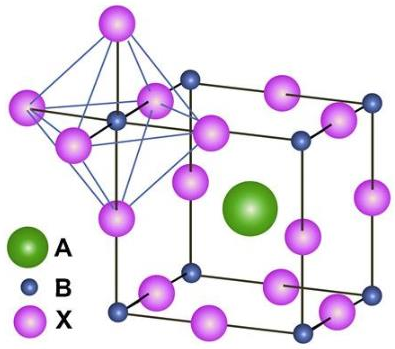

Figure 2.10 The perovskite crystal structure. B represents the Pb^{2+} ion, X represents the halide ion and A is an organic (*e.g.* methylammonium) or inorganic (*e.g.* Cs^+) cation. Image reproduced from reference [93] ((DOI: 10.1016/j.mattod.2014.07.007, reproduced with permission under the Creative Commons Attribution-Non Commercial-No Derivatives License (CC BY NC ND))

The lead halide perovskites possess large absorption coefficients (> 10^4 cm^{-1} at 550 nm for $MAPbI_3$)[94]. Additionally, an exciton binding energy of 5 meV has been measured for $MAPbI_3$,[95] meaning that free carriers are readily generated on photoexcitation, whilst predicted dielectric constants are large (20.1), thus effective screening of carriers from oppositely charged carriers or defects is expected.[19] Whilst these factors are all characteristic of good photovoltaic materials, their remarkable transport properties are the main contributor towards greater efficiencies over other technologies.[93] For $MAPbI_3$, electron and hole diffusion lengths > 100 nm have been measured, whilst for $MAPbI_{3-x}Cl_x$ values have exceeded 1 μm, despite deposition from solution and annealing temperatures of ~ 100ºC.[1,96] These diffusion lengths are 1 – 2 orders of magnitude greater than other solution processed photovoltaic materials,[97] and allow the use of simple planar

heterojunction (PHJ) devices, where a several hundred nanometre thick compact perovskite layer is sandwiched between compact CTMs. As the penetration lengths tend to be shorter than the carrier diffusion lengths,[94,98] EQEs close to 100% over the absorption region are common.[99]

One of the proposed theories behind the excellent carrier diffusion lengths (and subsequently lifetime and mobility) of the perovskites is their proposed 'defect tolerance', which is related to their band structure.[1,4,19,100] When two atomic orbitals come together, they form two new orbitals; a bonding orbital and an anti-bonding orbital. For a defect-intolerant semiconductor (Figure 2.11a), the bonding orbital, 1σ, is occupied by electrons whilst the antibonding orbital, 1σ*, is empty.[100] The resultant bandgap is the energy between the bonding and antibonding orbital.[1,19] Defects such as dangling bonds (*e.g.* at grain boundary or vacancy) will result in electron density on an atomic orbital, in energy states close to the original position of the atomic orbital. Material dependent, these states can be shallow or deep (*e.g.* for an elemental semiconductor such as Si).[100] Deeper states result in greater likelihood of SRH recombination and are detrimental to semiconductor properties.[28,42] Conversely, in an ideal defect-tolerant material, an antibonding orbital is occupied by electrons, forming the valence band maximum, and a bonding orbital forms the conduction band minimum (1σ* and 2σ respectively in Figure 2.11b). Defects are again proposed to form in the gap between the molecular orbital pairs (*i.e.* between 1σ and 1σ* or 2σ and 2σ*), however neither region now forms the bandgap.[4,19] As a result, the defect states form at energies within the bands, such that trap-assisted/SRH recombination is minimised. Note that rather than discrete orbitals, the conduction and valence bands are better described as energy bands.

DFT calculations have predicted a more complex electronic structure for the lead halide perovskites (Figure 2.11c)[19], of which a simplified diagram showing the bonding interactions between Pb and I is shown in Figure 2.11d. Owing to the 6*s* valence of Pb^{2+}, molecular orbitals are occupied up to the first antibonding orbital (1σ* in Figure 2.11c). As a result, both the valence band maximum (VBM) and conduction band minimum (CBM) are made from antibonding orbitals, which have large I(5*p*) and Pb(6*p*) behaviour respectively.[4,19,100] Lead vacancies are therefore more likely to form defect states within the valence band. Defects resulting in an increase in electron density on Pb (*e.g.* iodine vacancies) form close to the conduction band.[4,19,100] Whilst these may initially be considered to form within the bandgap, the lead halide perovskites benefit from spin orbit coupling effects due to Pb^{2+} ion, which is of large mass.[1,100] This widens the conduction band, effectively bringing its energy down so that iodine vacancies are resonant with the conduction band.[19] It should be noted that other defects, such as interstitials and anti-site

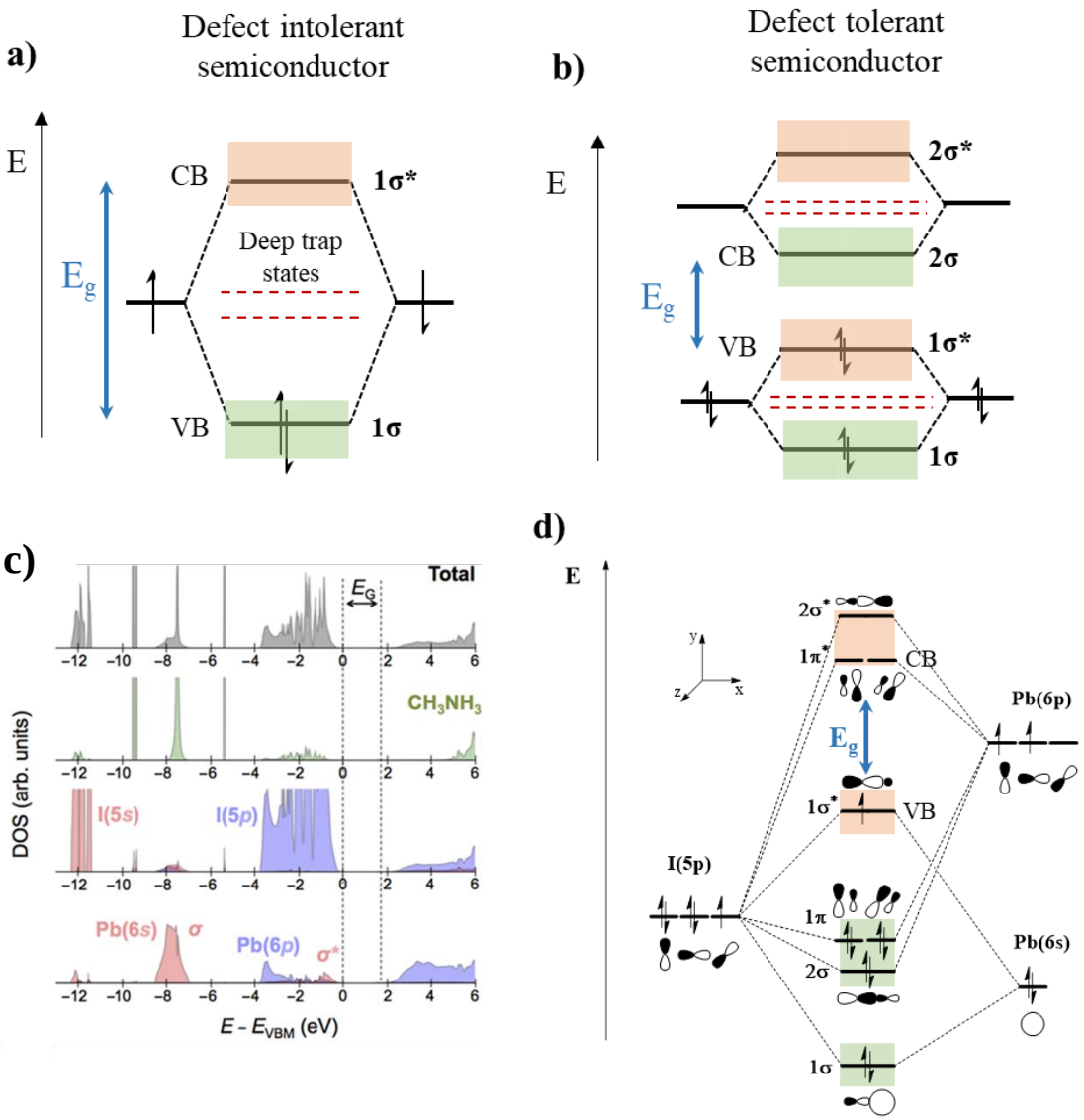

Figure 2.11 Schematics of the electronic structure of a) a defect intolerant and b) a defect tolerant semiconductor, c) shows the calculated density of states of methylammonium lead ioide and d) shows depicts a molecular orbital diagram as a simplified representation of the band structure of methylammonium lead iodide. The green bands in a), b) and d) represent bonding orbitals and the orange bands represent antibonding orbitals. Figures a) and b) are adapated from references[4,100], figure c) is reproduced from reference [19] with permission and figure d) is adapted from references [4,19,100].

defects, are predicted to sit deep within the bandgap, however they have large predicted defect formation energies meaning that they are present in small concentrations.[100] The result of the relatively clean bandgap is long carrier lifetimes, which, coupled with the small predicted electron and hole effective masses ($m_e < 0.3$, $m_h \leq 0.4$),[1] results in the micron-scale carrier diffusion lengths[96,97]. It should be noted that defects which form states within the bands may still act as scattering centres which reduce mobility;[53] this may account for the relatively low mobility of the

perovskites ($MAPbI_3$ < 70 $cm^2V^{-1}s^{-1}$)[98] relative to other high performing PV materials (CdTe, Si and GaAs > 1000 $cm^2V^{-1}s^{-1}$)[53,98].

The importance of the 6*s* valency in the search for new defect tolerant light absorbers will be discussed in more detail in section 3.

2.5.4.2 Performance of perovskite devices

In the previous section, the properties of the lead halide perovskites which have facilitated their excellent performance were discussed. In this sub-section, a brief overview on the progress in device performance will be given. Whilst an array of lead halide perovskite compounds has been since investigated, early research was based on the methylammonium lead halides ($CH_3NH_3PbX_3$ or $MAPbX_3$ where X = Cl, Br, I). Here, bandgap narrowing occurs down the series due to the contribution of the halide *p* orbital to the VBM,[101–103] such that $MAPbI_3$ has the smallest bandgap at 1.5 eV.[101] Initial device structures were inspired by DSSCs,[90,104] using a mesoporous TiO_2 scaffold loaded with $MAPbI_3$ and a solid-state organic hole transport material to facilitate good stability (Figure 2.12a). The first of these mesoporous super-structured solar cells (MSSCs) which displayed the real potential of the lead halide perovskites employed the organic molecule *spiro*-OMeTAD (2,2′,7,7′-tetrakis-(N,N-di-4-methoxyphenylamino)-9,9′-spirobifluorene) as HTM, mesoporous TiO_2 as the ETM and $MAPbI_3$.[105,106] Devices achieved > 9 % efficiency.[106] However, it was soon realised that simplified *n-i-p* devices, known as planar heterojunction (PHJ) devices, using compact thin films instead of mesoporous scaffolds could give comparable performance (Figure 2.12b and c).[107] Early planar $TiO_2|MAPbI_{3-x}Cl_x|$*spiro*-OMeTAD devices achieved champion efficiencies of 8.6% for solution processed perovskite, and up to 15.4% using a thermally evaporated perovskite film.[107] Improvements through improving the alignment of charge transport materials or to the perovskite morphology by controlling the atmosphere or processing conditions have since resulted in champion PCEs > 19% for methylammonium lead halides.[99]v The high performance of PHJ devices has been attributed to the long carrier diffusion lengths (> 1 μm) of $MAPbX_3$.[96,97] This, along with their excellent absorption properties, means that even with a several hundred nm layer of the perovskite, photogenerated carriers can diffuse to their respective contacts for collection.

Despite these advances, the hygroscopic methylammonium ion[108] has rendered $MAPbX_3$ devices instable towards air and moisture, resulting in degradation to PbX_2 within minutes of atmospheric exposure.[2,52,91] Alloying the methylammonium cation with Cs^+, Rb^+ or the organic formamidinium (FA) cation has helped to stabilise the perovskite compounds, and devices have maintained performance after 1000 hours operation (2 – 3 orders of magnitude improvement over

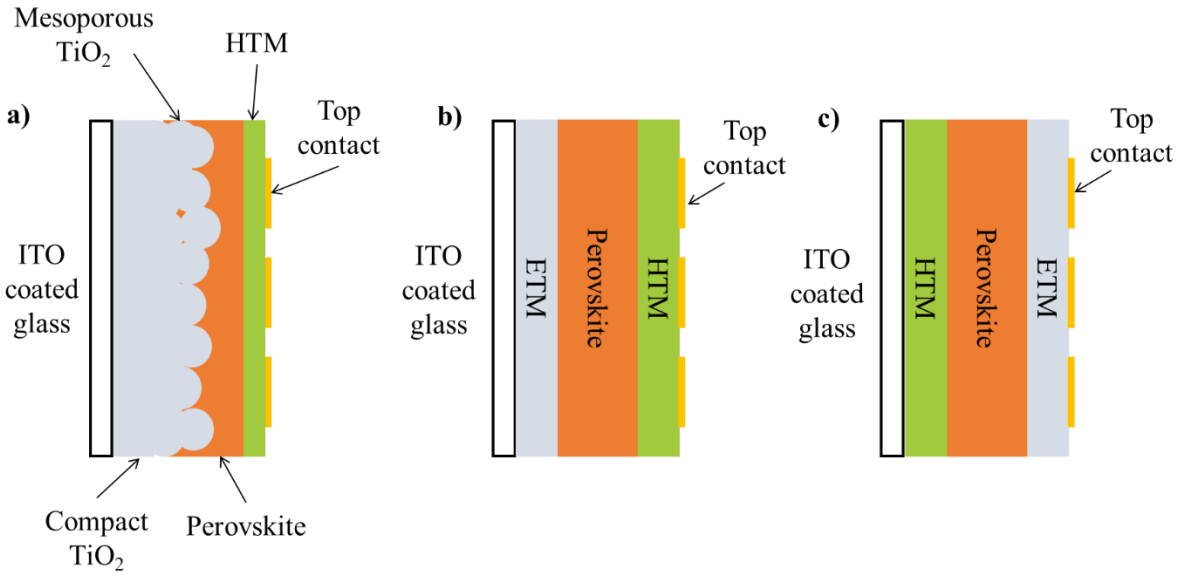

Figure 2.12 Schematics of a) a mesoporous super-structured solar cell b) an *n-i-p* planar heterojunction perovskite solar cell and c) an inverted *p-i-n* perovskite solar cell.

$MAPbI_3$).[1,109,110] It should be noted that due to the non-ideal cation sizes, the fully substituted $FAPbX_3$ and $CsPbX_3$ undergo a phase change after several weeks.[100] Despite this, the best efficiency for a perovskite device of area ~1 cm^2 was achieved using $FAPbI_3$, which has a bandgap 1.47 eV *cf.* 1.55 eV for $MAPbI_3$, at 20.9%.[111] The mixed cation compounds have also demonstrated improvements in efficiency over the $MAPbX_3$ devices, with $(FAPbI_3)_{1-x}(MAPbBr_3)_x$ achieving 25.2 % efficiency.[85] Since this, a record efficiency for a perovskite device of 24.2 % has been reported.[89] These improvements in efficiency were also facilitated by optimisation at the contacts, with un-doped and doped SnO_2, ZnO and TiO_2 often employed to achieve optimum energetic matching at the electron transfer interface,[1] whilst post-deposition treatments of CTMs are also shown to improve charge extraction.[112] Similarly, doping and functional group substitution has allowed tuning of the highest occupied molecular orbital and lowest unoccupied molecular orbital of organic compounds used as ETMs or HTMs.[85] However, inorganic compounds tend to be more stable than organic materials, offering the potential for improved long-term stability, and will be discussed in the following section.[113]

2.5.4.3 Inorganic hole transport materials for perovskite solar cells

As well as offering enhanced stability improvements, inorganic semiconductors are cheaper[114] and typically display greater hole mobility than organic semiconductors.[115] As such, CuSCN and CuI have proved as suitable HTMs in *n-i-p* devices.[114–116] For example, TiO_2|$CsFAMAPbI_{3-x}Br_x$|CuSCN|reduced graphene oxide|Au devices achieved a champion efficiency of 20.4%.[115] Additionally, the CuSCN layer inhibited diffusion of the gold electrode into the perovskite layer, discovered as a failure mechanism for control devices using *spiro*-OMeTAD as HTM.[117] *p*-type metal oxides such as NiO_x, Cu_2O, SnO and delafossite materials offer further stability to oxidation. They also often have wide bandgaps, enabling electron blocking properties (as their conduction band energy is much higher than that of common light absorbers making electron injection energetically unfavourable). Many *p*-type oxides commonly display poor hole mobility as a result of large hole effective masses stemming from their electronic structure; their valence band maxima are dominated by filled O 2*p* orbitals which are strongly localised.[118,119] Nickel(II) oxide overcomes this due to its partially filled 3 *d* valence orbital (of 3 d^8 electron configuration) which overlaps with the O 2*p* orbital, increasing delocalisation of the valence band (Figure 2.13).[119] This, and other benefits which will be discussed in the following section, have encouraged researchers to explore nickel oxide as HTM in perovskite solar cells.

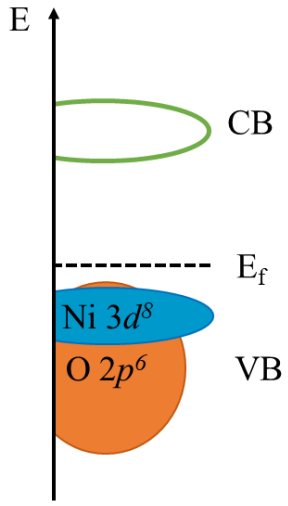

Figure 2.13 Schematic of the electronic structure of nickel oxide, where Ni 3*d* orbitals hybridise with O 2*p* orbitals at the edge of the valence band.

2.5.5 Properties of nickel oxide

As well as having a relatively disperse valence band, nickel oxide benefits from a high work-function reported in the range of 5.0 to 5.6 eV.[118] This matches well with that of $MAPbI_3$ (~ 5.4 eV)[120] and can be readily tuned using surface treatments such as controlled oxygen plasma exposure.[118] Meanwhile, its bandgap of > 3.5 eV results in electron blocking properties.[119] Nickel oxide crystallises into a highly phase stable cubic rock-salt phase (Figure 2.14b, space group *Fm3m*, lattice parameter 4.177 Å)[121] with nickel possessing its most stable oxidation state of +2. Whilst cubic NiO is insulating, nickel vacancies have a low formation energy (0.25 eV).[122] These nickel vacancies cause hole doping; charge neutrality is maintained by the presence of two holes in the lattice (which stabilise as Ni^{3+}).[123] As such, nickel oxide is sub-stoichiometric and is commonly written as NiO_x, and conductive *p*-type NiO_x suitable for applications as HTM can be readily fabricated in oxygen rich or nickel poor conditions.[122] Furthermore, hole effective masses between 0.6 – 1 have been calculated.[124,125] However, device-quality NiO_x films usually require annealing temperatures ≥ 250ºC.[123,126] At such temperatures the lead halide perovskites are thermally unstable. Whilst examples of *n-i-p* perovskite devices using low temperature processed NiO_x do exist,[127] inverting the devices to the *p-i-n* structure has proved a more effective strategy towards all-inorganic devices.

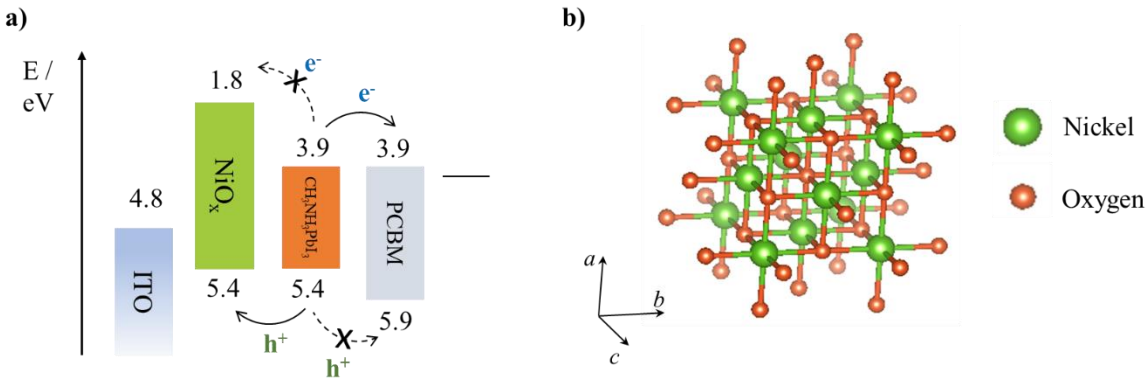

Figure 2.14 a) energy diagram of a perovskite solar cell using NiO_x as the hole transport layer and b) the crystal structure of cubic rock-salt NiO, where the orange circles are Ni and the blue circles are O atoms. Figure a) was adapted with permission from reference [112] and figure b) was made with VESTA software using crystallographic data for NiO from reference [128] (DOI 10.17188/1193796).

2.5.5.1 P-i-n perovskite devices using NiO_x as the hole transport material

Jeng *et al.* were the first to report NiO_x-based *p-i-n* perovskite devices, incorporating sol-gel NiO_x as the HTM, $MAPbI_3$ as the absorber and the fullerene derivative PCBM ([6,6]-phenyl C_{61}-butyric acid methyl ester) as the ETM.[94] They used UV-ozone treatment to improve the wetting of the perovskite on NiO_x, however the optimised perovskite coverage was ~93%, resulting in a poor maximum PCE of 7.8%. You *et al.* were able to improve the perovskite morphology on sol-gel NiO_x using two-step solution processing of the perovskite *via* a PbI_2 intermediate.[113] NiO_x films were compact and pin-hole free, with ~50 nm particle size, on top of which dense perovskite films with micron-sized particles grew. Using the same device materials as Jeng, an average PCE of ~14% was reported. By replacing PCBM with solution processed ZnO such that the device was all-inorganic, the average efficiency increased to 14.6% (champion device 16.1%). Furthermore, 90% of the efficiency of the all-inorganic device was maintained after 1440 hours storage in air, an order of magnitude improvement over devices using PCBM.[113] Despite these early advances, devices using un-doped sol-gel NiO_x as HTM have since been limited to average efficiencies 13 – 14% (champion PCEs ~16%).[129] Furthermore, NiO_x post-annealing temperatures > 300 ºC were used, putting constraints on the choice of substrate.

Several groups have overcome this by preparing NiO_x nanoparticles at high temperatures (to infer good crystallinity) before depositing from solution at < 150 ºC. ITO|NiO_x|$MAPbI_3$|PCBM|Ag devices using spin-cast solution-synthesised NiO_x nanoparticles roughly 10 nm in size achieved an average PCE of 15.0% (champion device 16.5%) on glass substrates.[126] Additionally, a champion efficiency of 13.4% was achieved on a flexible PEN (polyethylene naphthalate) substrate. Similarly, spin-cast NiO_x nanoparticles synthesised by spray-pyrolysis in $MAPbI_{3-x}Cl_x$ achieved an average efficiency ~16.5% and a champion device PCE of 17.5%, the highest for a perovskite device using NiO_x as HTM.[130] This was attributed to an optimised NiO_x|perovskite interface, resulting in minimal non-radiative losses and a V_{OC} of 1.11 V.

It should be noted that spin coating of NiO_x films, more typically from a sol but also from a solution of nanoparticles, is the most common method of preparing NiO_x thin films for solar cells. This is because it is a relatively easy, cheap and fast process; a film can be typically cast in roughly 1 minute.[131,132] However, the process has poor compatibility with large and heavy substrates,[132] whilst solvent compatibility must be met when depositing multi-layer structures to avoid damage of lower layers.[133] Furthermore, over 95 % of material is typically lost during the spinning process,[132] which is wasteful and becomes even more problematic when using expensive materials.

Alternative methods to NiO_x fabrication have used vacuum processing routes. Using atomic layer deposition (ALD) NiO_x, Seo *et al.* achieved a PCE 11.8 ± 0.3%.[112] Benefitting from the excellent thickness control achievable by ALD, they incorporated 5 nm NiO_x films in devices, achieving a balance between NiO_x coverage and electrical properties. Furthermore, annealing NiO_x at 300 ºC in air increased the work-function and hole density, resulting in a champion device efficiency 16.4%. Park *et al.* utilised the ability to control the atmosphere in pulsed laser deposition (PLD).[134] By controlling the oxygen partial pressure in the vacuum chamber, they were able to control the morphology of nanostructured, [111]-oriented NiO_x films. The optimum NiO_x porosity gave a champion device efficiency of 17.3% for an ITO|NiO_x|$MAPbI_3$|PCBM|LiF/Al device stack.

Table 2.2 The average and champion power conversion efficiencies for the best NiO_x-based *p-i-n* perovskite devices in the literature, separated by NiO_x fabrication method.

NiO_x fabrication route	Average efficiency / %	Champion device efficiency / %	Ref
Sol-gel	14.6 ± 1.5	16.1	[113]
Spin casting of NiO_x nanoparticles synthesised by spray pyrolysis	16.5 ± 1.0	17.5	[130]
Atomic layer deposition (no anneal)	11.8 ± 0.3	12.2	[112]
Atomic layer deposition (300 ºC anneal)	-	16.4	[112]
Pulsed laser deposition	-	17.3	[134]

2.5.5.2 Problems to be addressed for perovskite solar cells

Whilst much progress has been made in NiO_x-based *p-i-n* perovskite solar cells, each reported example is linked by one major flaw; all the NiO_x processing routes are batch processes. ALD and PLD are further restricted as they are vacuum methods, requiring long vacuum stages in fabrication,[135] whilst problems with spin casting were already highlighted. For perovskite solar cells to be a serious contender in the search for low cost photovoltaics, high throughput manufacturing routes (*e.g.* on continuous production lines) are vital. Whilst progress in high throughput manufacture of the perovskite layer is being made,[136,137] attention must also be paid to charge transport materials. As such, the latter half of this thesis is dedicated to developing a high throughput synthesis route towards device-quality NiO_x thin films, with device performance comparable to the best in the literature.

The second major problem with the lead halide perovskites is their lead content. Lead is a neurotoxin which is heavily regulated by the EU (on the Restriction of Hazardous Substances

Directive 2002/95/EC, (RoHS 1));[138] whilst photovoltaics are currently exempt from this restriction, the toxicity is still cause for concern. This problem is worsened by the poor stability of the lead halide perovskites, which could as a result leach into water supplies.[91] Based on predictions of defect tolerance, the former half of this thesis is dedicated to investigating the viability of BiOI as a lead-free, low-toxicity alternative to the lead halide perovskites. This compound will be introduced further in chapter 3.

It should be noted that while NiO_x acts as an efficient hole extractor in perovskite devices, it is also suitable for many other existing and emerging technologies (such as BiOI solar cells, quantum dot and hybrid inorganic-organic solar cells),[2,118,123] such that the development of large area NiO_x thin films is still relevant.

3 Bismuth-based compounds for photovoltaic applications

Section 2.5.4 introduced the lead halide perovskites and concluded that one of the major concerns for this class of materials is their toxicity. In this chapter, non-toxic alternatives to the lead halide perovskites based on bismuth compounds will be discussed. Recent experimental progress in compounds predicted to show similar 'defect tolerance' to the perovskites will be highlighted. Of these, BiOI will be discussed in more detail, forming a background for the experimental work in this thesis.

3.1 Bismuth-based non-toxic alternatives to lead halide perovskites

The remarkable increase in efficiency of the lead halide perovskites currently makes them the most promising 3rd generation solar cell as a future competitor to silicon. However, lead is on the *Restriction of Hazardous Substances Directive 2002/95/EC (RoHS 1),* which restricts its use in manufacturing in the EU.[138] This has prompted investigations into alternative lead-free compounds which may replicate the properties of the perovskites. Early attempts to replace lead involved direct substitution with group 14 ions Sn^{2+} and Ge^{2+}, in efforts to replicate the perovskite crystal structure.[1,139] However, a weakened inert pair effect up the group resulted in poor stability to oxidation of these compounds and the ready formation of Sn^{4+} and Ge^{4+}.[67] Substitution of Pb^{2+} with isoelectronic (but not isovalent) cations adjacent to Pb^{2+} in the periodic table with ns^2 valency (Bi^{3+}, Sb^{3+}, In^{+} and Tl^{+} (Figure 3.1)) has been suggested as an alternative route.[67] Of these, Bi^{3+} has been identified as the most promising substitute; Tl and Sb are both toxic whilst In is scarce and expensive.[1,62] Contrary to this, Bi has low toxicity, with applications in medicine and cosmetics, whilst being relatively inexpensive.[140] It also commonly forms Bi^{3+} compounds, due to a strong inert pair effect,[1,19] inferring a $6s^2$ valency. Being from the same period as lead, compounds should also benefit from the same spin orbit coupling effects which have been proposed to widen the conduction band of the lead halide perovskites,[1,19,53,67] enabling the formation of shallow defects whilst also narrowing the band-gap.[53]

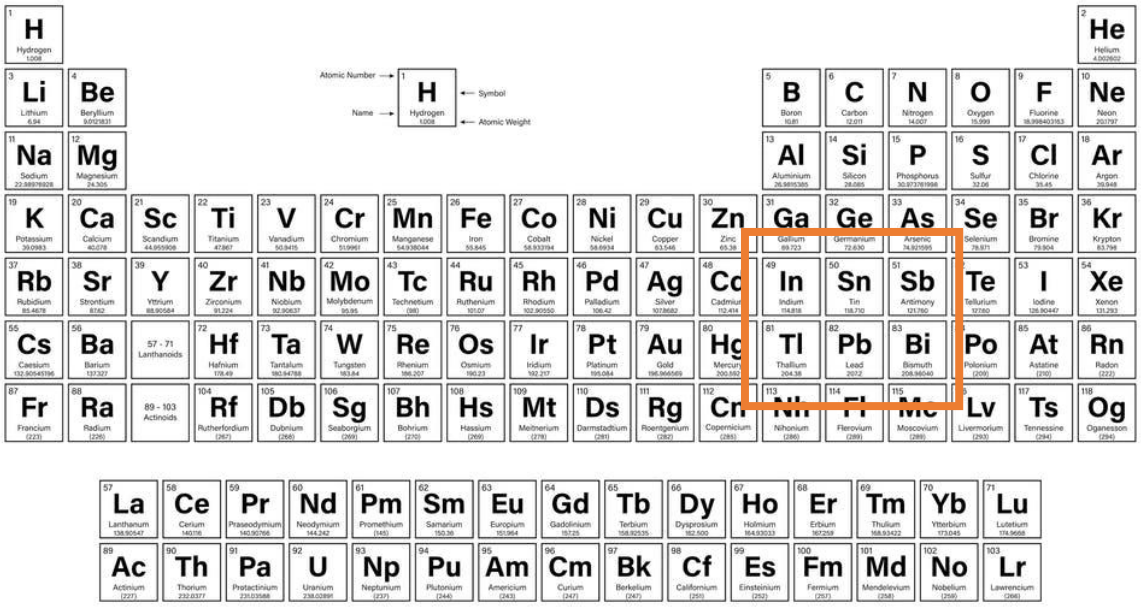

Figure 3.1 The periodic table of elements. The orange box highlights the position of lead and its neighbours, which have been considered as replacements to lead in less toxic alternatives to the lead halide perovskites. Image reproduced from reference [141].

3.2 Using theory to aid experimental design

Computational calculations can be used to predict the properties of semiconductors, such as their density of states, band structure, transport properties (m_e and m_h), defect formation energies and dielectric constants. As these are all important parameters for photovoltaic semiconductors, computations can be used to aid choices of materials and experimental design when searching for new photovoltaic materials.[1,19] The proposed defect tolerance of the lead halide perovskites was introduced in section 2.5.4. Through prediction of defect formation energies, it can be determined whether a semiconductor is likely to replicate the same tolerance to defects. A brief background into defect energy diagrams and their calculation will be given in the following sub-section.

3.2.1 Defect formation energy diagrams

Defect formation energy calculations are used to predict the formation energy of a defect (E^f) and the position of the defect charge transition level within a materials bandgap. Here, the charge transition levels represent the energy level of defect states, which act as sites for SRH recombination, relative to the valence band position.[2] These will be discussed in more detail later in this section.

It should be noted that defect formation energies are not calculated by the author of this thesis. However, calculations by the author's collaborators, reported in reference [2], form an important basis for the hypotheses of results chapters 6, 7 and 8. Therefore, a brief overview of the calculations will be given in this section, whilst the simulated defect formation energy diagrams calculated at the National Renewable Energy Laboratory (NREL) will be discussed in section 3.4.1.

3.2.1.1 Calculation of defect formation energy

Defect formation energies are calculated using density functional theory calculations which calculate the energy of a representative group of atoms in a lattice (*i.e.* a collection of unit cells) called a 'supercell'.[142,143] The supercell is usually several hundred or thousand atoms in size.[144,145] The ground state energy of the perfect supercell is first calculated; E_T^{perf} (AB) for a perfect crystal of AB. Atoms can then be removed from (forming vacancies), added to (forming interstitials) or substituted (forming antisites) within the supercell to represent defects, for which an energy can be computed.[143,144] For example, an A vacancy in a defective supercell of AB would give an energy $E_T(V_A^q)$, where q is the charge. Note that under periodic boundary conditions, the supercell in fact consists of a periodic repetition of a group of atoms within which the defect is contained.[146] Whilst the difference between the perfect and defective supercell gives an energy difference for the formation of V_A^q, defect formation energy depends on the environment; for example, oxides grown in an oxygen rich environment are less likely to contain oxygen vacancies than those grown in oxygen poor environments.[143] Thus, the chemical potential, μ_A, of the component (A) must be considered. The Fermi level must also be considered for charged defects (as electrons are removed from or donated to the 'electron reservoir', which is more difficult at low and high Fermi level energy respectively).[143,144]

Overall, the defect formation energy is calculated from:[144]

$$\Delta E^f = E_T^{def,q} - E_T^{perf} - \sum_i \Delta n_i \mu_i + q\mu_e + E_{corr} \qquad \textbf{(3.14)}$$

Where ΔE^f is the defect formation energy (eV), $E_T^{def,q}$ is the total energy of the defect supercell (eV), E_T^{perf} is the total energy of the perfect supercell (eV), Δn_i is the number of atoms of *i* added (positive) or removed (negative) from the perfect cell to form the defect supercell, μ_i is the chemical potential of atom *i* (eV), q is the charge of the defect and μ_e is the electron chemical potential ($E_{VBM} + E_F$ where E_{VBM} is the energy of the valence band maximum and E_F is the Fermi energy, eV). It should be noted that q is positive when electrons are removed from the lattice and negative when electrons are added when the defect is created.[144] E_{corr} is a correction term which

corrects for several factors (eV). The first is electrostatic interactions between charged defects and repetitions of themselves in neighbouring groups of atoms.[147] A second electrostatic correction factor is included, which accounts for the difference in the potential of a supercell with and without charge, as well as a third band-gap correction factor.[148,149] The defect formation energy is often plotted as a function of the Fermi level to form a defect diagram (for example, Figure 3.3).[145] A positive gradient is obtained for a donor defect (electron donor) whilst a negative gradient is obtained for an acceptor defect (electron acceptor/hole donor), and the intercept of the lowest energy donor and acceptor is the Fermi level under equilibrium.[2] Points where the gradient changes are the defect charge transition levels, where the charge of the defect changes(*e.g.* from an uncharged to a negatively charged vacancy).[2,143] Both charge states of the defect have the same defect formation energy at this Fermi energy.[143] The defect is an electron acceptor or donor at this Fermi-level, which allows them to act as a trap states, attracting electrons (holes) in the conduction (valence) band to initiate SRH recombination.[145] The more negative charge state of the defect is stable at higher Fermi energies than the defect transition level (and *vice versa*).[143] The defect transition levels can be probed experimentally using deep level transient spectroscopy (DLTS).

Both the defect formation energy and the position of the transition level within the bandgap are important to consider.[66,143,150] As a transition level is placed closer to mid-gap, SRH recombination rates increase (thereby reducing τ).[19] Therefore, it is desirable to have shallow transition levels which are close to the band edges (~k_bT from the band edges).[4] However, a defects concentration, c (cm^{-3}), decreases exponentially with increasing formation energy:

$$c = N_{sites}\, exp\left(-\frac{E^f}{k_bT}\right) \qquad \textbf{(3.15)}$$

Where N_{sites} is the number of sites where the defect can form (cm^{-3}).[143,150] This assumes that the defects do not interact with one another.[143] Clearly, c has a strong dependence on both E^f and the fabrication (or annealing) temperature, T. Therefore, processing temperature dependent, if a mid-gap ('deep') transition level has a large E^f its presence may be negligible.[143] Trapped charges within 'shallow' defects are readily de-trapped by thermal energy, therefore their presence is less detrimental to devices (a low E^f is acceptable), as SRH recombination will occur at low rates.[1,19,42] For reference, Figure 3.2 shows the influence of defect formation energy E^f on the defect

concentration at different processing temperatures (where N_{sites} is 10^{22} cm^{-3}, which is roughly representative of the number of Ni sites in rock-salt nickel oxide).[4]

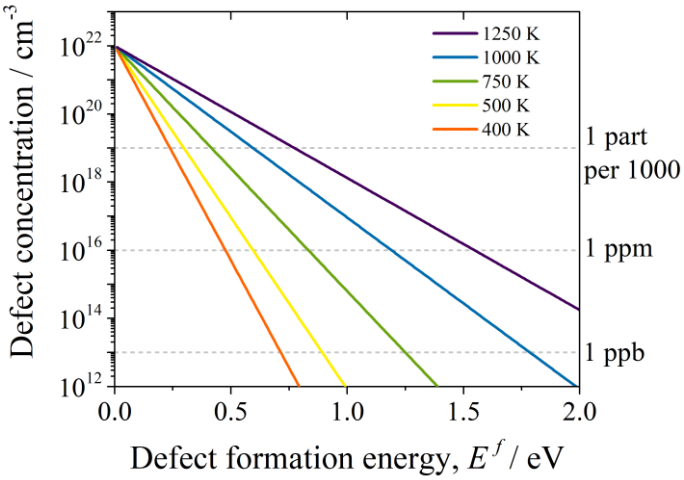

Figure 3.2 The influence of defect formation energy on defect concentration, considering processing temperatures of 400 – 1250 K and assuming $N_{sites} \sim 1 \times 10^{22}$ cm^{-3}. Figure adapted with permission from Brandt *et al.*, reference [4].

3.2.1.2 Methylammonium lead iodide defect formation energy diagram

The micron-scale minority carrier diffusion lengths of the lead halide perovskites are thought to result in part from the formation of only shallow defects in their band-gap, and hence their defect tolerance.[1,96,97,100,145,151] Yin *et al.* reported the defect formation energy diagram for $MAPbI_3$, shown in Figure 3.3, where a), b) and c) represent I- rich (from methylammonium iodide), intermediate and Pb- rich conditions respectively.[145] In all cases, the defect transition levels with low formation energy (< 1 eV) form close to the band-edges, and hence carriers which become trapped in these states can be thermally de-trapped.[145] This means that trap-assisted recombination rates will be low, resulting in excellent carrier diffusion properties.[1] Note that considering Figure 3.2 at a processing temperature of 400 K, the typical annealing temperature for $MAPbI_3$, a defect with $E^f \geq 0.5$ eV will be present at concentrations ≤ 1 ppm.[1,4] However, it should also be noted that MAPI is inherently unstable, therefore the validity of the defect formation diagrams, which require a material to be phase stable for defect formation energy calculations, remains unclear.

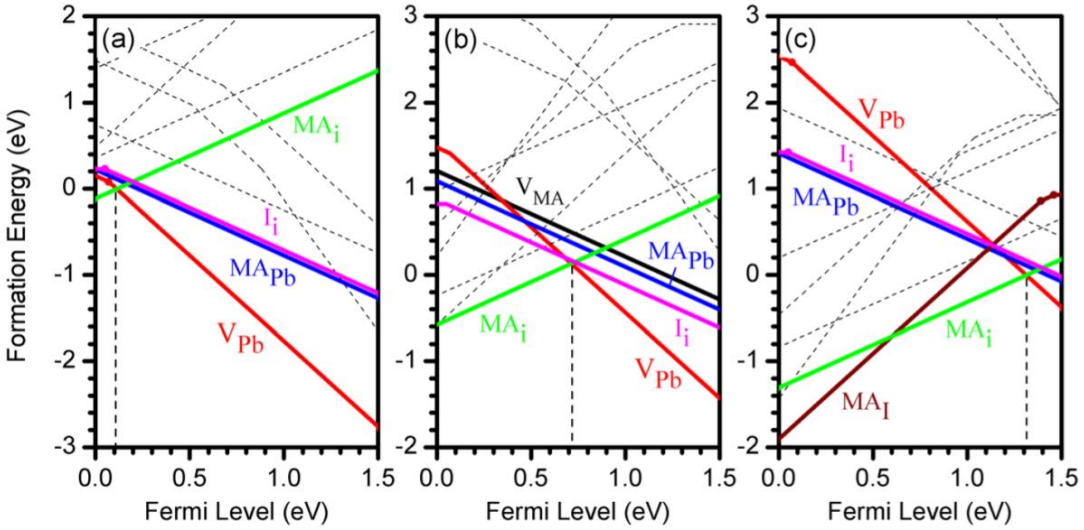

Figure 3.3 Defect formation energy diagrams calculated by Yin *et al* of methylammonium lead iodide. Figure a) was calculated under iodine rich-, b) under intermediate- and c) under lead rich-conditions. Images were reproduced with permission from reference [145].

The 6*s* lone pair on lead, and the subsequent *s* orbital contribution to the valence band, were shown as an important feature of the 'defect tolerant' band structure of the lead halide perovskites in section 2.5.4.1.[19,67,100] Several researchers have suggested that this may extend to other compounds containing metals cations with a stable ns^2 valency.[4,19,67] As such, Brandt *et al.* have highlighted families of compounds which show *s* contribution to the valence band edge in their density of states.[4,19,152] Experimental (and some theoretical) work on some bismuth-based compounds, many of which Brandt *et al.* identified, will be discussed in more detail in the following section.

3.3 Recent progress using bismuth-based materials for photovoltaics

Figure 3.4 draws together the ideal fundamental properties and the considerations for materials synthesis and device development which have been highlighted as important for good device performance in previous sections.[1] Finding new materials with each property and optimising all the processing parameters is not simple. As a result, to date, the best performing bismuth-based device is ~30% of the efficiency of the best perovskite device.[76,89,153] However, many advances in materials and device processing of bismuth-based materials have been made in recent years, providing an optimistic outlook for this group of compounds. The recent experimental advances of the most promising bismuth compounds, most of which have *s* contribution in their valence band, will be discussed in the following sections.

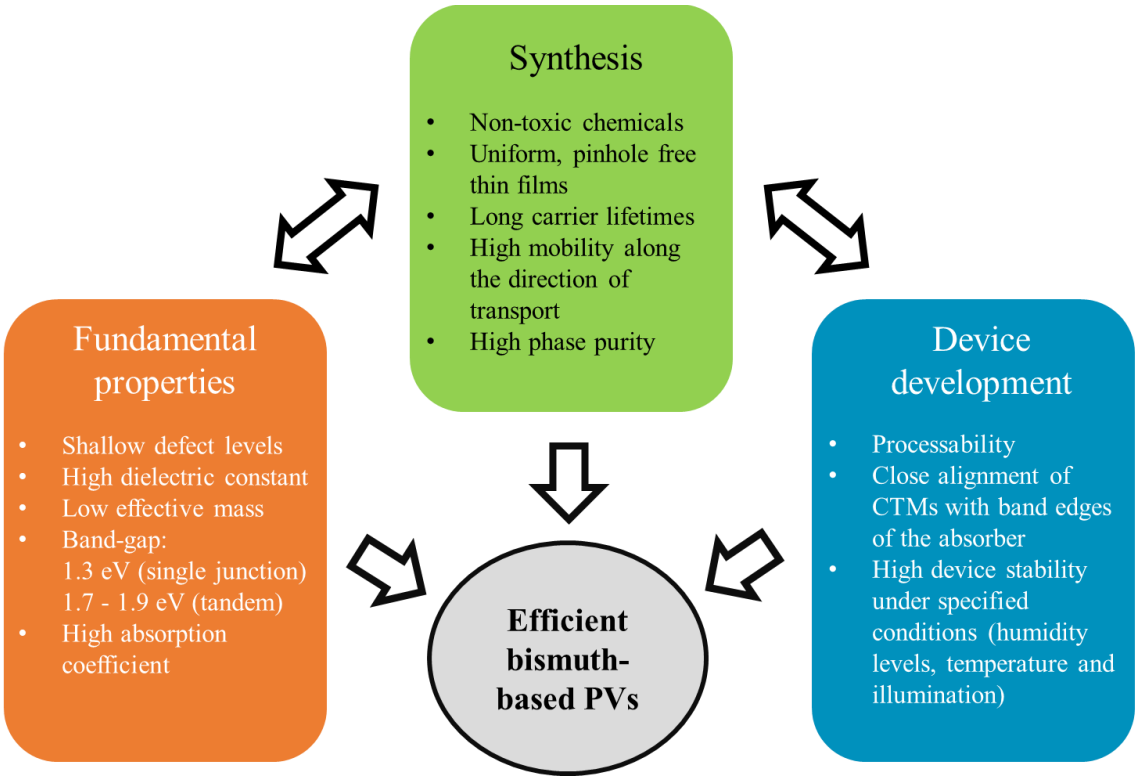

Figure 3.4 The fundamental properties, synthesis and device development considerations which need to be optimum for an efficient photovoltaic device. Figure adapted from reference [1] (with permission under Creative Commons Attribution CC BY license).

3.3.1 Methylammonium bismuth iodide and the double perovskites

The first compounds discussed are based around replication of the perovskite crystal structure. Initial approaches towards this involved direct substitution of Pb^{2+} with Bi^{3+}. However, the difference in valence of the metal ions resulted in the formation of the strongly excitonic, one-dimensional $(CH_3NH_3)_3Bi_2I_9$, for which an exciton binding energy of 300 meV was measured.[95,154,155] These factors would likely limit carrier transport and lifetime properties. Regarding processing, compact morphologies were initially only achieved using two-step processes *via* a BiI_3 intermediate, involving at least one vacuum processing step.[52,156,157] This is due to the poor solubility of bismuth salts in organic solvents causing fast crystallisation,[1,158] making direct deposition of $(CH_3NH_3)_3Bi_2I_9$ from solution challenging.[159,160] Using a two-step vacuum process the best efficiency to date for $(CH_3NH_3)_3Bi_2I_9$ was achieved, at 1.64%,[157] as a result of compact films with grain hundreds of nanometres in size, whilst Brandt *et al.* have recorded an 8.1 ns minority carrier lifetime.[4] Despite these efforts, device J_{SC} and V_{OC}s remain severely limited,[157] likely due to the large exciton binding energy.[1] However, it should be noted that Shin *et al.* have recently used a solvent engineering approach to overcome solubility problems in a one-step synthesis route, using additives to form BiI_3-Lewis acid adducts in solution resulting in slower crystallisation.[158] This could be explored and adapted for other bismuth compounds.[1]

The second family of bismuth compounds inspired by the perovskite structure is the double perovskites. Here Pb^{2+} is substituted with M^+ and M^{3+}, *e.g.* Ag^+ and Bi^{3+}, creating a three-dimensional network of alternating metal halide octahedra.[1,161,162] This overcomes the problems associated with the one-dimensionality of $(CH_3NH_3)_3Bi_2I_9$, resulting in good dispersion of the conduction and valence bands and hole effective masses down to 0.14 (for $Cs_2AgBiBr_6$ *cf.* 0.18 – 0.4 for $MAPbI_3$).[1,162–164] Other examples synthesised include $Cs_2AgBiCl_6$, $(CH_3NH_3)_2AgBiBr_6$ and $(CH_3NH_3)_2KBiCl_6$.[161,162,165] For a $Cs_2AgBiBr_6$ single crystal, Slavney *et al.* reported a photoluminescence lifetime of 667 ns, which approaches the microsecond lifetimes measured for the lead halide perovskites.[166,167] Hoye *et al.* have since proposed that the PL emission occurs *via* a defect state due to a red-shift in emission wavelength relative to the bandgap, and, using transient absorption spectroscopy, reported a lifetime > 1 μs.[47] Despite these excellent carrier properties, the double perovskites mentioned all have band-gaps ≥ 2 eV,[1] even wider than the optimum for tandem devices on silicon,[32] whilst the metal reactants suffer from the same solubility problems as bismuth salts.[168] As a result, few reports of a double perovskite thin films exist.[1,47,168] Of these, a champion device efficiency of 2.4% was reported for a ($Cs_2AgBiBr_6$) device fabricated by Greul *et al.*, using TiO_2 and *spiro*-OMeTAD as the CTMs.[168] Regarding the bandgap, thallium alloying successfully reduced the band-gap of $Cs_2AgBiBr_6$ from ~ 2.2 eV to 1.4 eV, but the toxicity of thallium limits commercial potential.[169,170]

Whilst the double perovskites have carrier lifetime properties comparable to the lead halide perovskites they are fundamentally limited by their band-gap energies (Table 3.1) and processing issues.[1] Therefore, doping and solvent engineering routes need investigating. Aside from compounds inspired by the perovskite structure, advances have also been made in bismuth compounds of differing structure but, as discussed, with *s* orbital contribution to the valence band.

Table 3.1 The bandgap energy, best device efficiency and device architecture of the best devices of methylammonium lead iodide, methylammonium bismuth iodide and a range of double perovskite compounds.

Material	Bandgap / eV	Best PCE / %	Device architecture
$MAPbI_3$	1.55[111]	21.6 [153]	FTO|La-$BaSnO_3$| $MAPbI_3$|PTAA|Au
$(CH_3NH_3)_3Bi_2I_9$	2.9 [a,163]	1.64 [157]	FTO|c-TiO_2|m-TiO_2|$(CH_3NH_3)_3Bi_2I_9$| *spiro*-OMeTAD|Ag
$Cs_2AgBiBr_6$	2.19 [162]	2.43 [168]	FTO|c-TiO_2|m-TiO_2|$Cs_2AgBiBr_6$| *spiro*-OMeTAD|Au
$Cs_2AgBiCl_6$	2.77 [162]	-	-
$(CH_3NH_3)_2AgBiBr_6$	2.02 [165]	-	-
$(CH_3NH_3)_2KBiCl_6$	3.04 [161]	-	-

FTO = fluorine-doped tin oxide, PTAA = Poly[bis(4-phenyl)(2,4,6trimethylphenyl)amine, c-TiO_2 = compact TiO_2, m-TiO_2 = mesoporous TiO_2, *spiro*-OMeTAD = 2,2',7,7'-Tetrakis[N,N-di(4-methoxy phenyl)amino]-9,9'-spirobifluorene. [a] Bandgap measured taking into account the excitonic peak for $(CH_3NH_3)_3Bi_2I_9$.

3.3.2 Other bismuth compounds based on replicating the defect tolerance of methylammonium lead iodide

BiI_3, an intermediate in $(CH_3NH_3)_3Bi_2I_9$ synthesis, possesses the optimum bandgap for a tandem device with a Si bottom cell at 1.7 eV. A photoluminescence lifetime of 7.3 ns has been measured for a film deposited by physical vapour transport at 77% of its melting point.[51] However, bismuth vacancies are predicted to have deep defect transition level ~ 0.7 eV from the conduction band edge with a formation energy of ~ 0.75 eV under iodine rich conditions.[4] Therefore, despite *s* orbital contribution to the valence band, resulting in antibonding character at the band-edge,[51] it does not display the same tolerance to defects as the lead halide perovskites.[1] Additionally, device performance has been limited due to poor film morphology which introduces shunt pathways into devices.[1,51] As a result, the champion device (using TiO_2 as ETM and V_2O_5 as HTM) reached only 1%,[171] and the best open-circuit voltage values have reached only ~ 25% of the bandgap energy.[172]

A family of materials with a more suitable bandgap for a single junction solar cell are the ternary alkali ternary alkali chalcogenides ($MBiCh_2$ where M = Li, Na, K etc and Ch = S, Se). Whilst there are few experimental reports on these materials, Rosales *et al.* recently reported the synthesis of rock-salt $NaBiS_2$ and $NaBiSe_2$ nanocrystals from solution.[173] Band-gap energies of 1.01 – 1.24 eV and 1.1 eV were measured respectively, as well as α values of $10^4 – 10^6$ cm^{-1} over the solar spectrum. Further characterisation and processing into devices are needed to evaluate the potential of these materials for PV applications. However, substituting the alkali metal with group 11 Ag yields $AgBiS_2$, which has achieved the highest efficiency for a solar cells using a bismuth compound (champion device efficiency of 6.3%, Table 3.2).[76] In this case, nanocrystals synthesised by the hot-injection method were spin cast and treated with tetramethylammonium iodide to replace insulating capping ligands. Whilst nanocrystals were only ~ 10 nm in size, they formed a compact layer.[76] Devices also benefitted from the good spectral overlap of $AgBiS_2$ (E_g = 1.3 eV), yield J_{SC} values ~18 $mAcm^{-2}$. However open-circuit voltage values only reached 500 meV regardless of the HTM valence band energy, indicating the presence of deep trap states limiting the voltage due to high levels of SRH recombination.[76] Defect formation energy calculations would be useful to confirm this, and determine processing temperatures at which deep trap states could be avoided.

The last group of materials which will be discussed are the bismuth chalcoiodides, BiChI (where Ch = S, Se, or O), of which BiOI will be investigated in this thesis and will be discussed in section 3.4. BiSI and BiSeI crystallise into 1-dimensional ribbon-like structures, proposed to be beneficial for carrier transport between electrodes in devices if the 1-dimensional back bone is situated perpendicular to the charge transport materials.[174,175] However, BiSI forms needle-like structures which have been difficult to fabricate into compact films with controlled growth

direction.[1,176,177] For example, devices incorporating spray pyrolysed BiSI with CuSCN as the HTM were only 0.01% efficient, likely due to large pin-holes visible in the SEM. Devices also suffered from poor matching of the valence band of CuSCN (-5.3 eV)[116] with the deep lying valence band of BiSI (-6.4 eV).[174] It should be noted that this is a major cause of voltage loss with many of the bismuth-based absorbers, which tend to have valence band maxima at ~ -5.9 to -6.3 eV, whilst common HTMs have their valence band/highest occupied molecular orbital at -5.2 to -5.4 eV.[1] An improvement in PCE to 0.25% was made using a liquid electrolyte (NaI + I_2 in acetonitrile), however this introduced stability issues.[176] BiSeI is yet to be made into devices, however its bandgap has an improved overlap with the solar spectrum (<1.37 eV for BiSeI *vs.* 1.59 eV for BiSI).[177] The third of the series, BiOI, has shown the best performance in photovoltaic devices,[178] forming motivation for this thesis, and will be discussed in more depth in the following chapters.

Table 3.2 Bandgap energy, best device efficiency and the device architecture of the best performing device for the bismuth containing compounds discussed in section 3.3.2.

Compound	Bandgap / eV	Highest device efficiency / %	Device architecture	Ref
BiI_3	1.8	1.0	FTO|TiO_2|BiI_3|ZnO|Al	[171]
$NaBiS_2$	1.0 – 1.2	-	-	[173]
$NaBiSe_2$	1.1	-	-	[173]
$AgBiS_2$	0.9	6.3	ITO|ZnO|$AgBiS_2$|PTB7|MoO_3|Ag	[76]
BiOI	1.9	1.0	FTO|TiO_2|BiOI| I_2/I_3^-| Pt	[178]
BiSI	1.59	0.25	FTO|BiSI|NaI/I_2 in acetonitrile|Pt	[176]
BiSeI	< 1.37	-	-	[177]

3.4 Bismuth oxyiodide – a promising candidate for photovoltaics

BiOI crystallises into the anisotropic tetragonal Matlockite crystal structure (Figure 3.5), belonging to the *P4/nmm* space group with *a* = 3.994 Å and c = 9.149 Å.[179] Here [I-Bi-O-Bi-I] layers are stacked along the *c*-axis, resulting from alternating $[I_m]^{m-}$ and $[Bi_2O_2]^{2+}$ sheets. The alternating positive and negative sheets induce a static electric field along the *c*- axis, which is thought to allow efficient separation of photogenerated electrons and holes.[180] Weak I···I van der Waals forces hold the [I-Bi-O-Bi-I] layers together along the *c*-axis, whilst covalent bonding exists within the layers (extending along the *a*- and *b*- axes). Consequently, band structure calculations show less dispersion in the 001 direction (along the *c*- axis) than in the 100 (*a*- axis) and 010 (*b*- axis) directions, resulting in smaller calculated effective masses along the *a*- and *b*- axes.[1,181,182] This means that preferential growth of *a*- or *b*- axis oriented films should give the highest mobility pathway between electrodes in devices.[1]

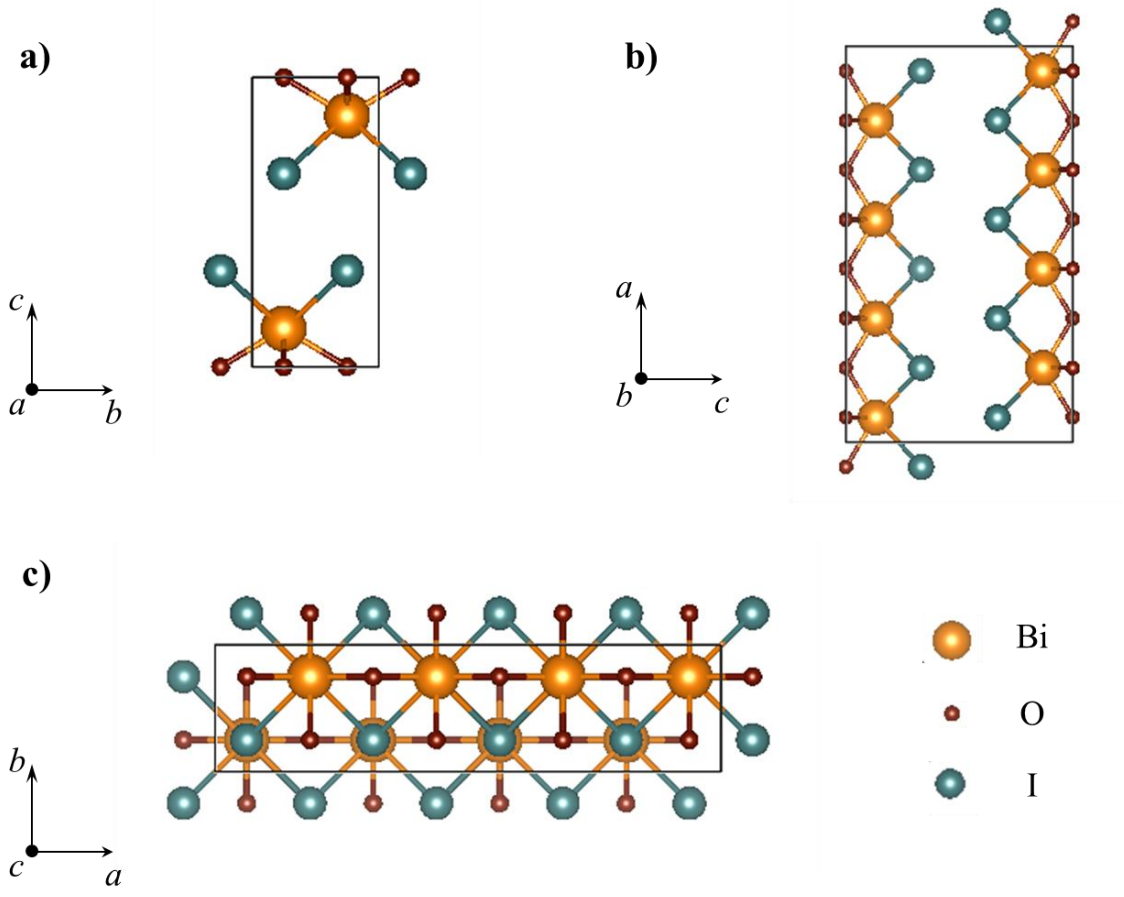

Figure 3.5 a) shows the unit cell of BiOI, which crystallises into the Matlockite structure, as viewed down the *a*-axis, b) shows a 4x1x1 supercell of BiOI, viewed down the *b*-axis and c) shows the view down the *c*-axis of a 4x1x1 supercell of BiOI. Bismuth atoms are coloured yellow, oxygen atoms are in red and iodine atoms are shown in green. The unit cell was generated with VESTA software using a crystallographic information file for BiOI from reference [183].

Whilst BiOI has demonstrated promising activity in photocatalysis and water splitting applications,[180,184] many calculated and experimentally measured properties of BiOI make it worth exploring as a photovoltaic material. It has an indirect bandgap of 1.8 – 1.9 eV,[185,186] close to the optimum for a four-terminal tandem device with a crystalline silicon bottom-cell.[32] Additionally, it has a calculated electron effective mass of 0.37,[19] close to that of $MAPbI_3$ (0.2 – 0.3)[1,164] and amongst the lowest for the bismuth compounds discussed.[1] Note that a wide range of hole effective masses are reported (1.9 – 3.75)[181,182], likely due to the transport anisotropy induced by the crystal structure.[1,180] It should also have effective charge screening properties, with a predicted dielectric constants several times larger than other traditional photovoltaic materials (BiOI 37 – 46,[2,19,181] Si 11.7,[187] CdTe 10.3,[188] GaAs 13.8[189]). As well as these properties, BiOI is predicted to tolerate defects. Density of states calculations predict that like the lead halide perovskites, antibonding orbitals (6σ*) contribute to the valence band of BiOI.[2,19] Additionally, from defect formation calculations by collaborators only shallow defects are predicted to form, as will be discussed in more detail in the following section.

3.4.1 Defect formation energy calculations for bismuth oxyiodide

Defect formation energy calculations for BiOI which were carried out by collaborators are reported in reference.[2] The phase diagram for the Bi-O-I system is shown in Figure 3.6a. This is used to find the chemical potentials of Bi, O and I (μ_{Bi}, μ_O and μ_I) at which BiOI is thermodynamically stable. It shows that BiOI is only stable in a relatively small region of chemical potentials.[2] The extrema of μ_{Bi}, μ_O and μ_I were used to calculate the formation energy of defects under different conditions. Figure 3.6b shows the defect formation energy diagrams under different conditions labelled on Figure 3.6a: point A is iodine- rich, oxygen- rich; point B is iodine- rich, oxygen- poor; point C is bismuth- rich, oxygen- poor and point D is bismuth- rich, oxygen- rich.

The Fermi-level sits roughly mid-gap under all conditions. For conditions B, C and D, the iodine vacancy (V_I) and oxygen on iodine antisite (O_I) pin the Fermi-level, whilst for condition A the bismuth vacancy (V_{Bi}) and V_I pin E_F. As these three defects have the lowest formation energy, these are of the highest concentration in the intrinsic material (according to equation **3.15**).[143] Under all conditions, V_I and O_I do not have transition levels within the band-gap; the transition levels are therefore situated within the bands and form shallow states.[2,4,143] On the other hand, V_{Bi} has a transition level close to the valence band-edge, but this is of high formation energy under all conditions (E^f is 2 – 5 eV). Whilst other defects have transition levels situated deeper in the bandgap (such as the oxygen vacancy (V_O), iodine on bismuth antisite (I_{Bi}) and bismuth on iodine antisite (Bi_I)), their formation energy is large (> 1.5 eV) in all cases. Therefore, these defects are proposed to be present in only small concentrations (< 1 ppb at processing temperature

up to ~ 850 K, see Figure 3.2).[1,2,4] Therefore, BiOI is proposed to be tolerant to V_I, O_I and V_{Bi} defects, as these form defect states close to or within the bands, whilst for all other defects computed, the formation energies are too large for them to significantly impact SRH recombination rates.[4]

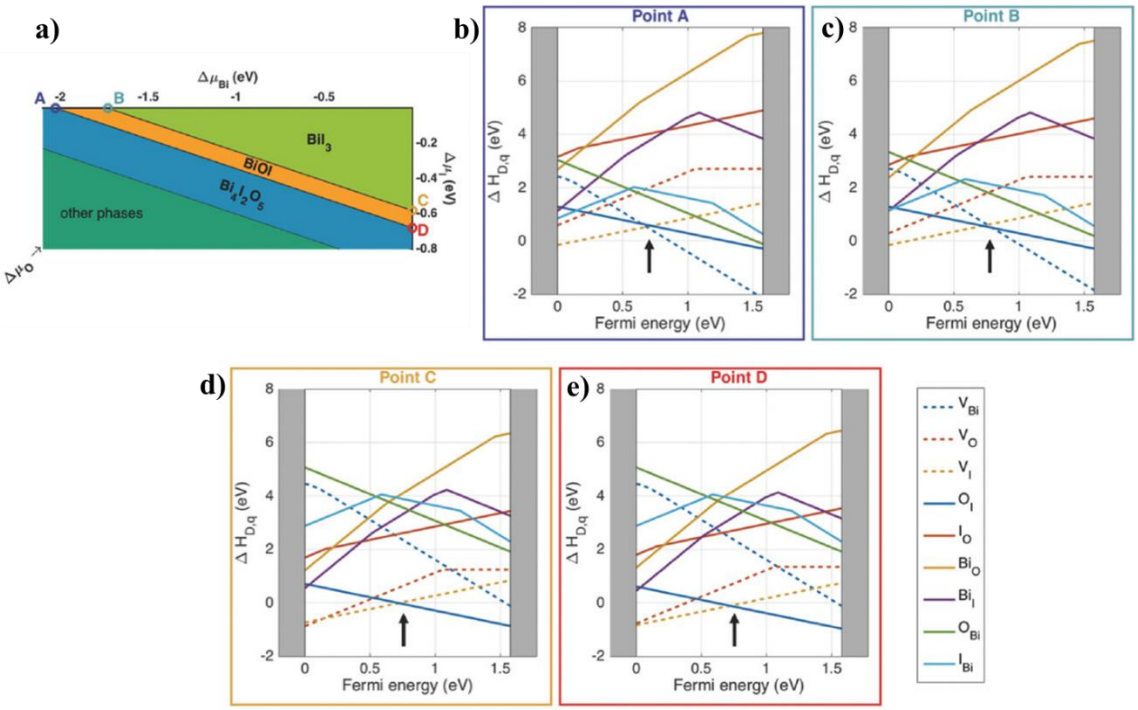

Figure 3.6 a) Theoretical phase diagram for the Bi-O-I system and defect energy formation diagrams for BiOI under different growth conditions, where figures b) and c) correspond to iodine rich growth conditions and figures d) and e) correspond to bismuth rich growth conditions. These four points are marked in figure a) as A, B, C and D. Images reproduced with permission from reference [2].

3.4.2 Performance of bismuth oxyiodide solar cells to date

Despite the promising properties of BiOI, device performance to date has been poor (Table 3.3), mainly due to non-compact BiOI morphology and poor choice of device materials. For example, in photoelectrochemical cells, Zhao *et al.* incorporated solvothermal-BiOI into a chitosan matrix (an insulating polysaccharide) deposited onto ITO and used an iodine/iodide redox couple as the hole conducting electrolyte.[190] The poor conductivity of the chitosan coupled with the lack of hole blocking layer between ITO and BiOI caused poor J_{SC} and V_{OC} values of 20 μA/cm^2 and 461 mV. Improvements were made by Sfaelou *et al.* who deposited BiOI by successive ionic layer adsorption and reaction (SILAR), resulting in large micron sized platelets.[178] Devices still used an I_2/I_3^- electrolyte, but also employed TiO_2 as the hole blocking/electron transport layer. A two

orders of magnitude improvement to the J_{SC} (3.75 mA/cm^2) resulted in 1% efficient devices. However, devices suffered from poor packing between BiOI platelets, introducing a leakage pathway between TiO_2 and the electrolyte and highlighting the need for denser BiOI films. Additionally, the need for replacement of the liquid electrolyte with a solid HTM was highlighted by Bhachu *et al.*[180] In investigations as a photocatalyst for water splitting BiOI degraded after only 100 seconds of measurement in an aqueous electrolyte. However, the first solid state BiOI solar cells,[191] which used CuI as the HTM, only achieved 0.1% efficiency. This was due to poor morphology of the BiOI layer, which was deposited by doctor blading BiOI synthesised by the hydrothermal method. Here, as was the case for Zhao *et al*,[190] BiOI forms nanoclusters consisting of BiOI particles tens of nanometres in size, which had high surface area for interfacial recombination and did not pack efficiently to form a compact film, with visible pin-holes between clusters.

Thus, the main problem encountered in the BiOI devices to date is poor morphology of the BiOI layer, highlighted by FF values < 50% in all cases (Table 3.3). A route to large BiOI platelets with good packing (and ideally *a*- or *b*- axis orientation) is desirable to minimise recombination and leakage pathways in devices. The second major problem with BiOI devices to date is non-optimal energy matching at the charge transfer interfaces, as well as stability issues associated with liquid electrolytes. Much knowledge on charge transport materials has been gained in recent years as the lead halide perovskite field has advanced, which may be transferred to the development of solid state BiOI devices.

Table 3.3 Device architecture, BiOI fabrication method and performance parameters of BiOI solar cells in the literature to date.

Device structure	BiOI fabrication method	J_{SC} / mAcm^{-2}	V_{OC} / V	FF / %	PCE / %	Ref
ITO|Chitosan-BiOI| I_2/I_3^-| Pt	Solvothermal method	0.02	0.46	46	4.0×10^{-5}	[190]
FTO|TiO_2|BiOI| I_2/I_3^-| Pt	SILAR	3.80	0.61	45	1.0	[178]
FTO|TiO_2|Chitosan-BiOI|CuI|Pt	Solvothermal method	0.96	0.34	37	0.1	[191]

3.4.3 Aims for chapters 6, 7 and 8:

1. Develop the deposition parameters for CVD growth of BiOI thin films and measure the structural and physical properties to determine their photovoltaic potential
2. Incorporate thermal CVD BiOI into a working, stable solar cell with solid charge transport materials
3. Investigate the influence of homologous growth temperature on the structural and physical properties of CVD BiOI
4. Experimentally determine whether BiOI is defect tolerant by studying the effect of induced defects (*via* compositional changes) on the optoelectronic properties of BiOI

4 Principles of thin film growth and vapour-phase growth techniques

The following chapter gives a brief overview into the theory of thin film growth, and the impact on growth temperature on the structural and defect characteristics of a material. Following this, a background into the main techniques used for thin film growth in this thesis, atmospheric pressure spatial atomic layer deposition and thermal chemical vapour deposition, will be introduced.

4.1 A short introduction to thin film growth theory

From chapter 2, requirements essential for an efficient photovoltaic device can be deduced. Films must be compact to minimise shunt pathways in devices. Additionally, a low defect density is desirable to limit non-radiative recombination. These defects may occur at grain boundaries (*e.g.* due to dangling bonds, dislocations) or throughout the bulk of the material (*e.g.* vacancies, anti-site defects).[192] Therefore, control of grain structure is an important consideration in thin film growth.

Thin film growth occurs by three main processes as reactants are delivered to a substrate surface. In the first step nucleation occurs, where small particles (or nuclei) form on the substrate surface. As more reactant arrives, the nuclei grow until they meet and coalesce.[193] A grain boundary is formed, driven by the reduction in energy from two free surfaces on the independent nuclei to a single interface between them.[193] After this, film growth occurs normal to the substrate. At this point temperature has a great influence on the grain structure. Atoms can move across grain boundaries,[194] causing one grain to grow whilst the other shrinks (which can eventually cause two grains to merge into one, known as coarsening).[193] The mobility of the grain boundaries has an exponential dependence on temperature,[193,194] such that high temperature growth or annealing results in large grained films due to mobile grain boundaries. Conversely, at low temperatures grains are immobile, resulting in small grained films. For photovoltaics, large grained films with a low grain boundary density are ideal.

Regarding the definition of ‘high’ and ‘low’ temperatures, structure-zone models exist which describe the typical characteristics of films grown at temperatures expressed as the fraction of their melting point. This is known as the homologous temperature:[192,195]

$$T_h = \frac{T_s}{T_m} \qquad \textbf{(4.16)}$$

Where T_h is the homologous growth temperature (K), T_s is the substrate temperature during deposition or annealing (K) and T_m is the melting point of the material (K). Whilst advanced

models which take low pressure and ion energy (for plasma activated reactions) into account exist,[192,195] film fabrication in this thesis is carried out at atmospheric pressure with heat activation. As such, a simplified model which only considers T_h is discussed.[196] An initial model made by Movchan and Demchishin considered three T_h zones with relatively distinct grain characteristics.[196,197] However, this was further adapted by Thornton,[195] Barna and Adamik[198] to include an intermediate fourth zone (zone T, Figure 4.1).[196] In zone I (typically at $T_h < 0.2$), both grain boundaries and arriving surface species have low mobility. As a result, the grain structure at the bottom of the film (*i.e.* at coalescence) is maintained during thickening.[193,198] In zone T, V-shaped grains are formed, as a result of 'competitive texturing'.[193,198] This typically occurs at $T_h = 0.2 – 0.4$, where grain boundary mobility is low but surface species have sufficient energy for diffusion. As thickening occurs, some crystal orientations become more favourable than others, resulting in surface texturing, whilst grains remain small and randomly oriented at the bottom of the film. In zone II, grain mobility is large and grain growth occurs throughout the coalescence and film thickening process. Through the film thickness large column-like grains occur,[196] as a result of 're-structural growth texturing'.[198] This means that the grain size and orientation change during the growth process to minimise the free energy of the surface and the substrate-film interface. This regime occurs at $T_h > 0.4$.[196,198] At higher temperatures still (dependent on the system, can be as a low as $T_h > 0.5$),[196] mass diffusion occurs and grains have large grain size but are no longer columnar, zone III.[197] It should be noted that the position of the temperature zones varies between materials,[193,196] whilst the need to consider the kinetic energy of the species arriving at the film surface has also been identified.[192] However, the main important implication of structure-zone theory is that controlling T_h may provide a route to improved device performance (*via* a reduction in the density of structural defects and thereby improvement in carrier minority carrier lifetimes).

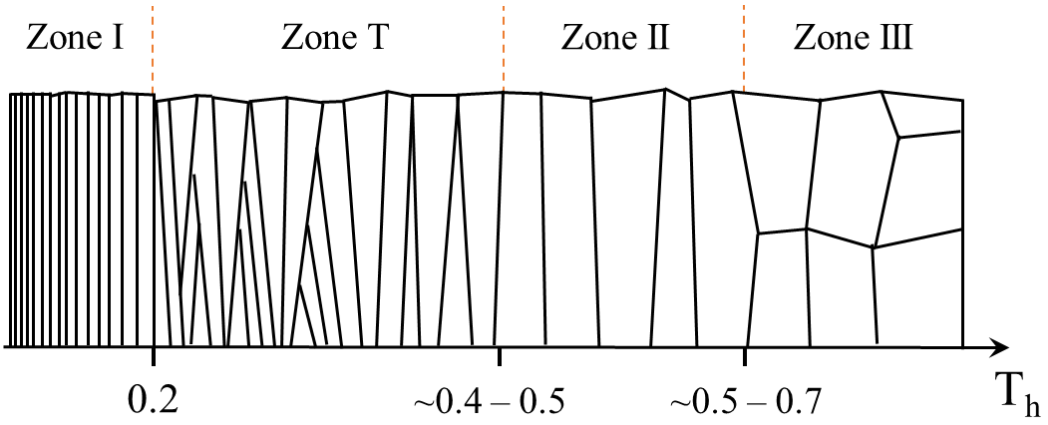

Figure 4.1 Schematic of the structure-zone model for expected grain structure characteristics of a thin film as a function of homologous growth temperature, T_h, combining the models of Movchan and Demchishin with that of Thornton, Barna and Adamik. Figure adapted with permission from reference [198].

For example, in investigations of BiI_3 for X-ray detection applications, Cuña *et al* reported a two order of magnitude reduction in dark current (indicating a reduction in defect density) by increasing the growth temperature of physical vapour deposition grown BiI_3 from 0.62 T_m to 0.64 T_m.[199] Similarly, Brandt *et al* measured a 30-fold increase in minority carrier lifetime in BiI_3 for physical vapour transport grown films at 0.77 T_m *vs* 0.63 T_m.[1,4,51]

In chapter 7, the influence of homologous growth temperature on the structural and physical properties of a low toxicity alternative to the lead halide perovskites, BiOI, will be discussed. For work in this thesis, BiOI films were grown by thermal chemical vapour deposition, a technique which will be discussed in more detail in the following section.

4.2 An introduction to chemical vapour deposition

In chemical vapour deposition (CVD), activated gaseous precursors react or decompose to form a thin film or powder.[200] Typically, precursor vapours are flowed into a chamber and over a heated substrate with which they react. The reactants may react in the gas phase or within the area close to or on the substrate surface, named the boundary layer.[200,201] Reactions on the substrate (heterogeneous reactions occurring between gas phase species and the solid substrate) form dense thin films. Alternatively, when reactions occur in the gas phase, particle formation occurs.[200] If this occurs during thin film growth, the particles can be incorporated into the film resulting in poor properties; as such, homogeneous reactions are unwanted.[202]

Precursors can be activated by different energy sources. Thermal CVD relies on heat to initiate the reaction processes, plasma-enhanced CVD (PE-CVD) uses a plasma, while photo-assisted CVD uses UV light.[200] However, the reaction mechanism can be generalised for all types of activation (Figure 4.2).[201,203] In step **1**, Gaseous precursors are first generated and transported into the reaction chamber using a carrier gas. Activated by an energy source, intermediate species which act as the reactants form in the gas phase (step **2**). These are transported towards the substrate and diffuse across the boundary layer. This is called *mass transport* (step **3**).[201,203] The reactants then adsorb onto the heated substrate (step **4**) and diffuse to surface sites where nucleation occurs (step **5**). This is followed by thin film growth as more reactant arrives (**6**). Finally, in step **7**, desorption and diffusion of by-products back across the boundary layer occurs. These are transported out of the chamber into a waste stream by the carrier gas.[202] It should be noted that the homogeneous reactions (*i.e.* between reactants in the gas phase) which result in particulate formation occur when the temperature of the gas is higher than the decomposition temperature of the intermediate species/reactants.[200]

The range of activation sources, operating conditions (*e.g.* pressure, temperature), precursors and materials which can be deposited make CVD a highly versatile deposition technique. It has found industrial applications such as wear- and corrosion- resistant coatings, optical coatings, diffusion barriers for electronics and synthetic diamonds.[204] It can also coat large areas,[179] conformally coat complex shapes and can achieve high deposition rates using relatively simple equipment.[200,201,204] Additionally, a wide range of morphologies and film densities can be achieved by controlling the deposition parameters.[200] Aside from this, it is possible to control film crystallinity by manipulating surface diffusion and growth rates of growing films through temperature and pressure control. Higher temperatures promote higher surface diffusion of adatoms on the substrate surface, which results in the growth of large crystallites or grains (*i.e.* polycrystalline or epitaxial films). Conversely, low surface diffusion at low temperatures results in amorphous films, particularly at fast growth rates.[201]

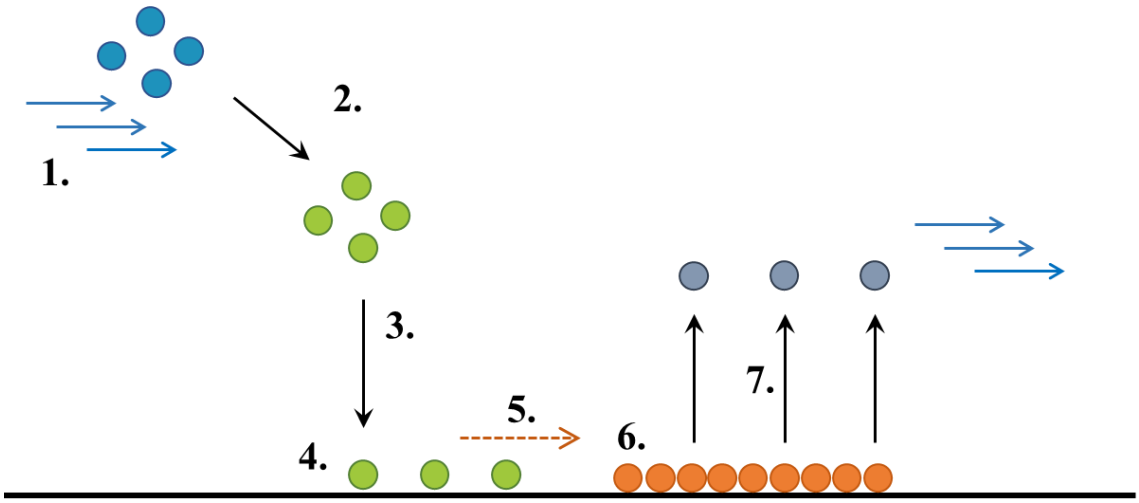

Figure 4.2 Schematic of the typical steps of a chemical vapour deposition process. **1.** Precursors enter the CVD chamber where they are activated to form reactants (**2**). The reactants are transported to the substrate surface (**3**) where the adsorb (**4**). Surface diffusion occurs (**5**), followed by nucleation and growth of a thin film (**6**). Gaseous byproducts desorb from the substrate and are carried out of the chamber (**7**). Figure adapted from reference [201].

At different deposition temperatures, the rate limiting step of the CVD process changes (Figure 4.3). Low temperature depositions are under '*kinetic control',* where the growth rate depends strongly on the energy provided for reaction.[201] At intermediate temperatures, the '*mass transport'* region, transport of reacting species across the boundary layer limits rates, whilst at higher temperatures still precursors begin to desorb from the substrate surface, known as the '*precursor depletion'* region.[201,203] As growth rates in the *mass transport* region are almost independent of temperature, this region is ideal for growth of high uniformity films, as temperature fluctuations across the substrate will have little effect on film thickness.[200] Meanwhile, the slow growth rates in the *precursor depletion* region are favourable for well controlled epitaxial film growth.[200–203,205]

For work in this thesis, heat was used as the energy source for precursor activation (thermal-CVD). An overview of the common features, advantages and disadvantages of thermal CVD, and a schematic of the reactor used for BiOI deposition, will be given in the following paragraphs.

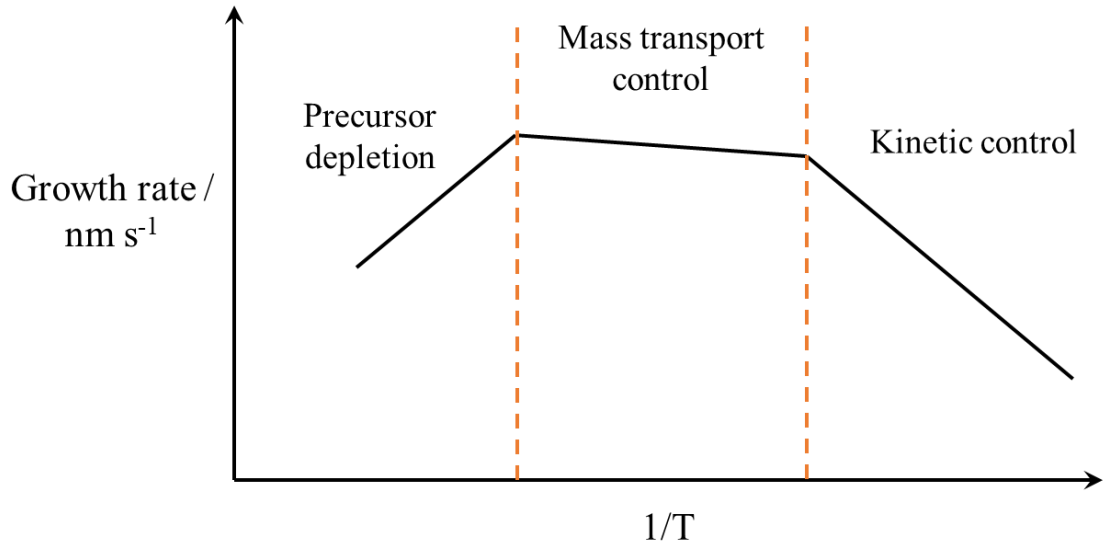

Figure 4.3 The growth control regimes at different temperatures for a chemical vapour deposition process.

4.2.1 Thermal chemical vapour deposition

Thermal CVD uses heat energy to activate precursors. It can be carried out in basic equipment such as a tube furnace and is therefore easy to set up. Additionally, depositions can be carried out at atmospheric pressure (requiring only a feed from a gas source). However, temperatures as high as > 1000 ºC can be required for reactions, making it unsuitable for heat sensitive substrates.[202] While this means that flexible plastic substrates attractive for roll-to-roll processed photovoltaics would not be suitable for thermal CVD, flexible metal foils with higher temperature stability may still be useable.

BiOI depositions for work in this thesis were carried out in a tube furnace. As well as meaning that depositions occur on both the walls of the furnace tube and the substrates, this can encourage unwanted homogeneous gas phase reactions at high temperatures.[200,203] Cold-wall reactors, where reactions are localised by only heating the substrate, can be used to overcome this.[200,204] However, the hot wall reactor was deemed appropriate for initial studies on the deposition of BiOI due to the ease of set up and inexpensive equipment.

4.2.2 Growth of bismuth oxyiodide by chemical vapour deposition

Growth of BiOI has previously been reported in studies of the BiI_3-O_2 system for bismuth oxide fabrication, using thermal CVD at low pressure.[179] BiOI was grown epitaxially onto MgO (at 490 ºC, 10 Torr), for which micron-sized square platelets were imaged using atomic force microscopy. During the timescale of this work, Qian *et al.* grew BiOI by thermal CVD at atmospheric pressure for conversion into $BiVO_4$ photoanodes for photoelectrochemical water splitting.[206] However, the films were orange in colour, which is characteristic of a film containing more oxidised phases. Additionally, films were not fully characterised as they were an intermediate to $BiVO_4$. Recently, Bhachu *et al.* reported fabrication of BiOI by aerosol assisted CVD (AACVD), using a piezoelectric to generate a fine aerosol of BiI_3 dissolved in *N*,*N*-dimethylformamide.[180] Films were reasonably compact, however small amounts of metallic Bi^0 were present in the X-ray photoelectron spectroscopy (XPS) Bi 4*f* spectrum. Despite this, these examples show that CVD is a promising route towards large grained, compact BiOI films, thereby providing motivation to use thermal CVD to deposit BiOI for solar cells for the first time. Note that alternative routes to BiOI which were mainly solution based gave small grained films with poor morphology, as was mentioned in section 3.4.2.

4.3 An introduction to atmospheric pressure spatial atomic layer deposition

In section 2.5.4, the importance of establishing a high-throughput fabrication route to NiO_x was discussed. Part of the chemical vapour deposition family of techniques, atmospheric pressure spatial atomic layer deposition is a deposition tool able to deposit metal oxides at rates several orders of magnitude higher than conventional vacuum techniques. The origin of and theory behind this deposition technique will be discussed in the following sections.

4.3.1 Atomic layer deposition

Atomic layer deposition (ALD) is a sub-category of CVD, where thin film deposition occurs *via* self-limiting reactions on the substrate.[202,207,208] This can be explained by considering a typical reaction cycle, outlined in Figure 4.4. A first precursor (precursor **A**) is pulsed into a vacuum chamber, where it chemisorbs to the substrate. This is the first half -reaction. The reaction is self-limiting, meaning only a monolayer of chemisorbed material can form, so long as the precursor pulse is long enough for the substrate to become saturated. A purge step is then used to remove any reaction by-products and unreacted precursor, before the second precursor (precursor **B**) is pulsed into the chamber. Precursor **B** reacts with the chemisorbed layer of precursor **A** in a second half-reaction, forming the first layer of a thin film. Again, this reaction is self-limiting, as it is limited by the reaction sites of activated precursor **A** available.[207] Another purge step removes by-products and excess precursor **B**, and the cycle is repeated until the desired film thickness is achieved.[202] Whilst formation of binary films is most common, ternary and elemental films can be deposited using two precursors or a plasma in place of precursor **B** respectively.[209–211]

ALD is typically used for the growth of metal oxides, sulphides and nitrides, thus one precursor is usually a metal source, such as an organometallic or metal halide, and the other is a non-metal source (e.g. H_2O, O_3, NH_3, H_2S). Due to the ligands of the metal precursor, growth rates in practice are limited to less than one monolayer per cycle as a result of steric effects.[201,202] Despite this, the film thickness *vs.* number of cycles (Figure 4.5)[212] remains linear for ALD processes resulting in sub-nanometre control of thickness, with typical growth per cycle (GPC) values of < 0.1 nm/cycle.[207] This lends to applications requiring very thin films such as optical coatings.[208,213] Additionally, due to the slow reaction times and reliance on self-limiting reactions, conformal coverage of high aspect ratio substrates is achieved,[207,214] important for applications such as trench capacitors in memory applications[208,214] and barrier materials for integrated circuit components.[214] This is otherwise unachievable with physical vapour deposition methods such as evaporation and sputtering,[207] and whilst CVD can conformally coat rough surfaces it struggles with such high aspect ratio substrates due to the fast reaction times.[207] Finally, the separation of precursors by purge steps prevents unwanted gas phase reactions which can occur in CVD.

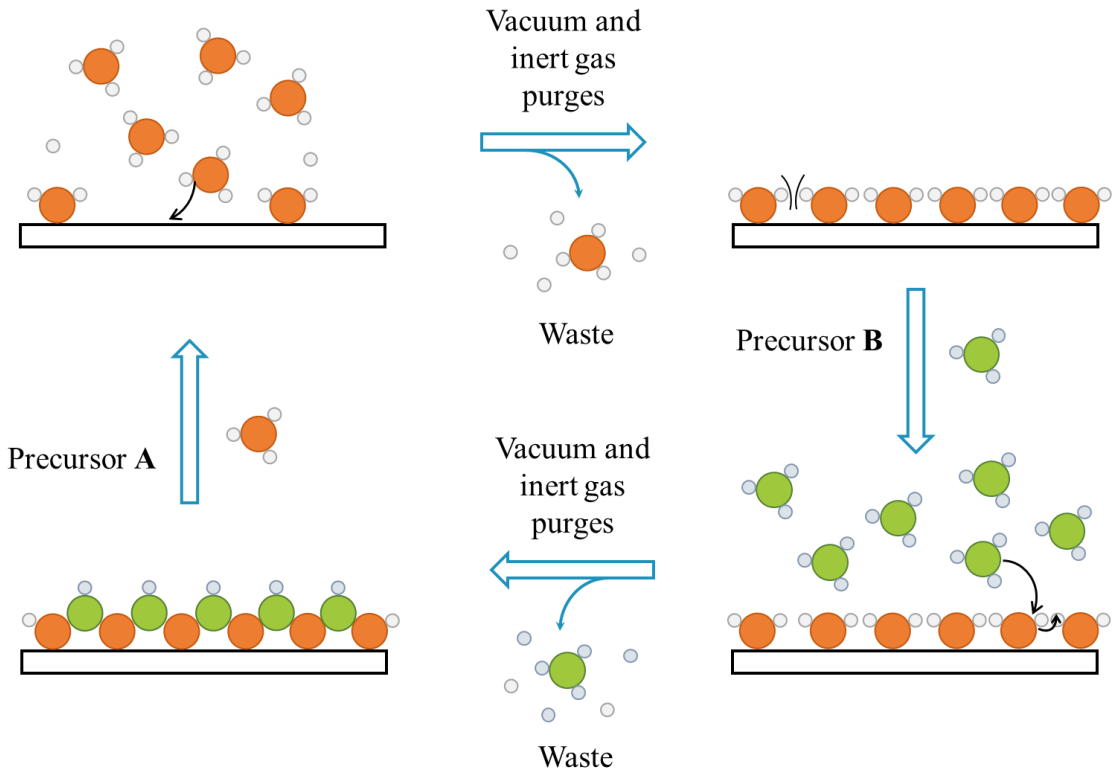

Figure 4.4 Schematic of an ALD cycle. Precursor **A** is introduced into a reaction vessel where it reacts with the substrate to form a monolayer. Vacuum and inert gas purge steps are used to remove excess precursor and by-products before precursor **B** is introduced into the chamber. Precursor **B** reacts with precursor **A** to form a monolayer. This gives a single layer of the desired compound **AB**. Further vacuum and inert gas purges to remove waste follow. The cycle is repeated to deposit films of the desired thickness.

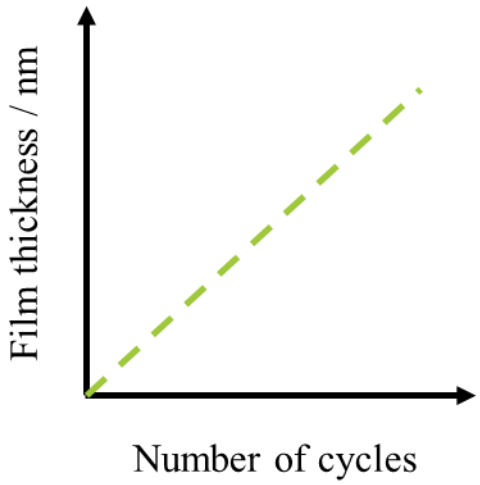

Figure 4.5 Schematic of a typical growth curve for an ALD reaction. Thickness *vs* number of cycles is linear due to the self-limiting nature of ALD reactions.

It should be noted that a temperature regime exists at which the GPC is independent of temperature and reactions are fully self-limiting. This is termed the 'ALD window' (Figure 4.6). Within this window any fluctuations in temperature will not affect surface uniformity; an advantage over CVD, particularly when working in the '*kinetic regime'* (Figure 4.3). At either end of this window the GPC can drop, due to desorption of reactants or insufficient energy for reactions to go to completion, at higher and lower temperatures respectively. Otherwise condensation at temperatures below the ALD window or decomposition processes at higher temperatures result in an increased GPC. In the decomposition case reactions are described as CVD-like. To limit condensation, precursors with high vapour pressures, such as diethyl zinc (2.7 kPa at 25 ºC), are used.[215] Precursors must also have high stability to decomposition to extend the ALD window to as high temperature as possible,[216] whilst being sufficiently reactive to deposit films at reasonable rates below the decomposition temperature (ALD processes usually occur below 350 ºC). As a result, they tend to be pyrophoric and must be handled under inert environments.

However, despite the use of highly reactive precursors, the long purge steps and multi-step nature of ALD renders very slow growth rates. These are typically 0.03 – 0.08 nm/s (100 – 300 nm/hour).[207,216] As metal oxide films in photovoltaic devices are on the order of tens of nanometres, deposition rates are too slow to be viable for high-throughput manufacture.[212] Over the last few decades spatial atomic layer deposition reactors, which maintain the advantages of ALD whilst demonstrating improved reaction times, have been researched. The theory and operation of these will be discussed in the following section.

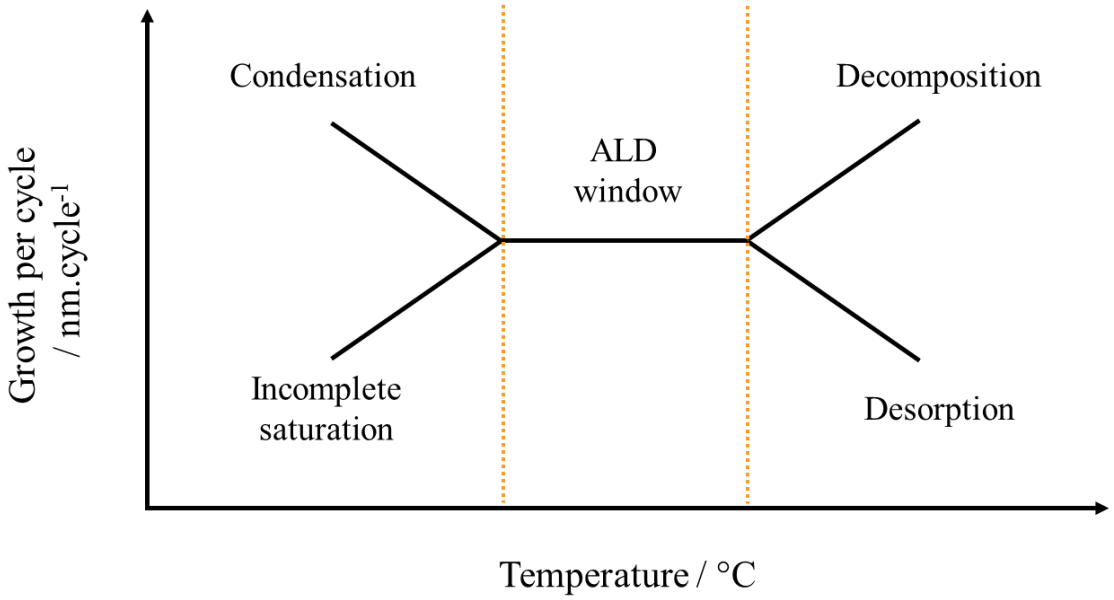

Figure 4.6 Typical temperature profile of an ALD process. At temperatures within the ALD window, reactions are fully self-limiting as the substrate becomes fully saturated with precursor. Outside of this temperature window, growth per cycle may be governed by condensation of precursor, incomplete surface saturation, desorption or decomposition of precursors.

4.3.2 Spatial atomic layer deposition

Spatial atomic layer deposition is a variant of ALD which overcomes the problematic slow deposition rates. The reactors use gas manifolds designed so that precursors are separated in space through adjacent gas channels, rather than in time by gas purge steps.[135] The substrate is sequentially exposed to precursors by moving between the gas channels which deliver the precursors continuously (Figure 4.7).[217] The purge time is now the time to move the substrate between the channels rather than the time between precursor pulses in temporal ALD.[217] By placing inert gas lines between the precursor gas channels, intermixing of precursors is prevented so that reactions occur exclusively on the substrate.[135,217,218] The inert gas also carries away unreacted precursor and by-products to the exhaust. The rate limiting step in ALD is the purge time, which through spatially separating the reaction zones is reduced to ~10 – 100s ms, relative to ~10 s for a purge step in conventional ALD. Hence growth rates can be 2-3 orders of magnitude faster for spatial ALD.[219,220] Meanwhile, similar GPC are achieved if the substrate spends enough time under the channel for reaction to go to completion, which is typically a few milliseconds.[217]

As precursors are directed towards the substrate much less precursor is wasted than in temporal ALD, where deposition on the chamber walls also occurs.

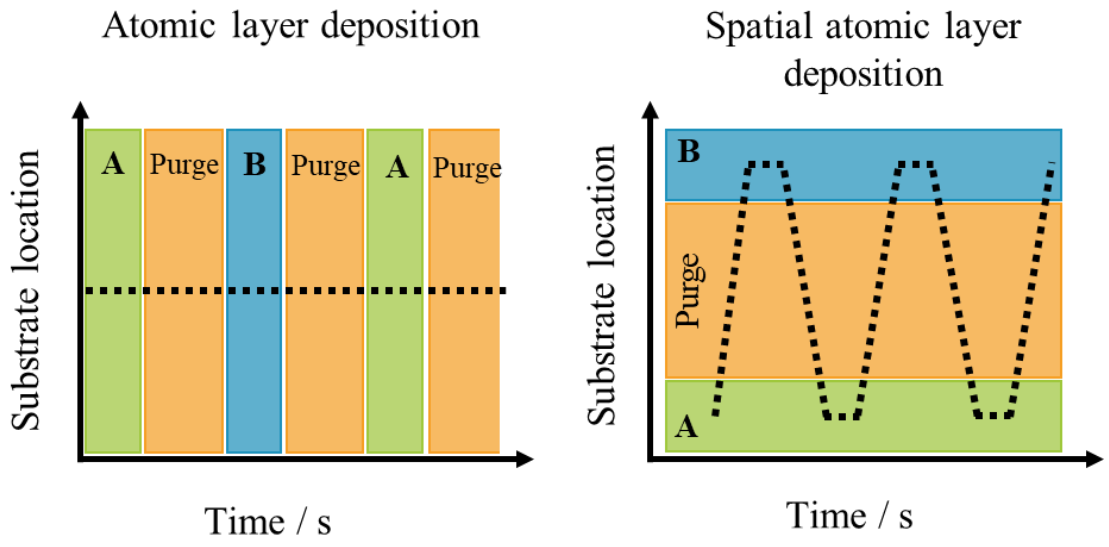

Figure 4.7 The position of the substrate as a function of time for a) conventional ALD and b) Spatial atomic layer deposition. In conventional ALD, the substrate remains stationary in a vacuum chamber as precursors **A** and **B** are introduced sequentially, separated by a purge step. In spatial atomic layer deposition, the substrate is mechanically moved between zones where precursors **A** and **B** are delivered, *via* an intermediate inert gas purge zone. Figure adapted with permission from reference [217].

The precursor pulse in a temporal ALD process must be long enough for the substrate to become fully saturated for a true ALD process. Likewise, a point on the substrate must be exposed to precursor for enough time to become fully saturated in spatial ALD (otherwise incomplete saturation occurs, Figure 4.6). The mechanical movement of the substrate is either provided by rotation or translational movement of a substrate, therefore the exposure time of a point on the substrate depends on the rotational speed (rpm) or translational speed (m/s) of the substrate holder. At fast speeds, short exposure times result in incomplete reaction and GPC is smaller than for an ALD cycle (Figure 4.8a). As substrate speed is reduced the exposure time of a point on the substrate to the precursors increases, allowing enough time for the substrate to become saturated. Here GPC is equal to one ALD cycle. At slower speeds still, the GPC becomes independent of speed due to saturation of the substrate and deposition occurs in the ALD regime. A second growth mechanism, which follows a decomposition 'CVD-like' process may also occur (Figure 4.8b). In this case, the growth per cycle increases linearly against exposure time (*i.e.* there is no exposure time where the reactions become self-limiting). This may occur when the deposition

temperature is higher than the decomposition temperature of the metal precursor, or when gas intermixing occurs in the space between the substrate and the precursor delivery manifold. Whilst the reaction mechanism is not pure ALD in this case, excellent control of film thickness is still maintained, whilst thin films can often deposit at faster rates than for an ALD process.[218]

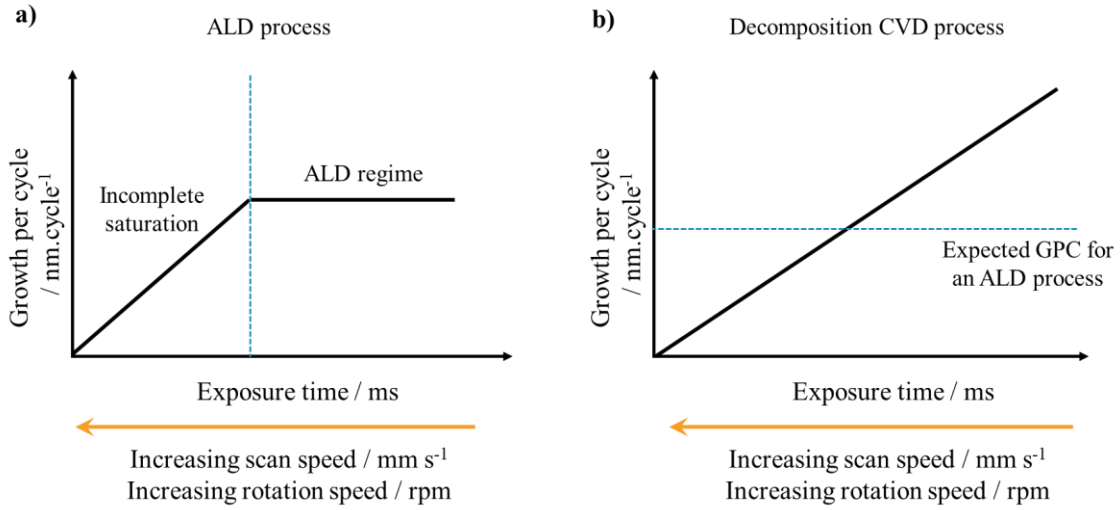

Figure 4.8 The growth per cycle against exposure time for a) a spatial ALD reaction and b) a decomposition 'CVD-like' process.

4.3.2.1 Spatial atomic layer deposition and atmospheric pressure spatial atomic layer deposition reactors

The first spatial ALD reactors were designed to work under vacuum.[217,221] ASTRaL researchers developed a system using a rotating drum to move flexible substrates between gas delivery zones, with the potential to be suitable for roll-to-roll processing.[212] Al_2O_3 was deposited from trimethylaluminium and water at up to 0.12 nm/s; up to two orders of magnitude faster than ALD.[212,222] However, in the GPC *vs.* rotation speed plot, drag effects caused large fluctuations in GPC near the ALD-regime, making deposition rates highly sensitive to the rotation speed.[212] Sharma *et al.* developed a similar reactor, with 31 positions around the drum between which precursor and inert gas channels could be easily switched (Figure 4.9), aiding process optimisation.[223] GPC *vs.* rotation speed curves were more consistent, but the films had poor thickness uniformity, with thickening towards the substrate edges. Additionally, both reactors discussed were developed for vacuum deposition; removing the need for vacuum would reduce costs and be more suitable for upscaling manufacture.

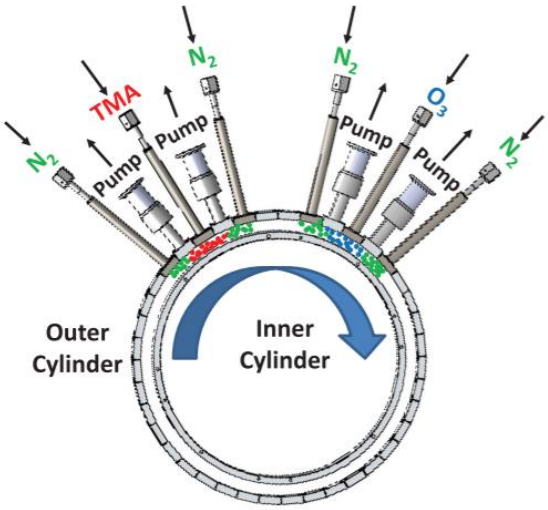

Figure 4.9 Schematic of a spatial ALD reactor suitable for flexible substrates designed by Sharma *et al.* The precursor, purge and pump lines slot into an outer cylinder and can be moved between 31 positions for process optimisation, whilst the substrate rotates around the outside of the inner cylinder. Figure reproduced with permission from reference [223].

Several groups have overcome the need for vacuum conditions, designing reactors which work at atmospheric pressure. These are known as atmospheric pressure spatial atomic layer deposition (AP-SALD) reactors. These reactors have gas delivery manifolds with alternating gas channels (precursor **A** | inert | precursor **B** | inert). The channels are situated close together (typically a few mm apart), meaning the substrate only has a small distance to move between half-reactions.[217,224] The small spacing between channels is facilitated by maintaining a small gap between the substrate and gas delivery manifold (< 100 μm), around 10 times smaller than in the ASTRaL design.[212] Reducing this gap allows the inert gas channels to effectively shield the precursor channels from one another, preventing intermixing of the gaseous precursors before they reach the substrate surface.[220] Examples are shown in Figure 4.10. These reactors are called Close Proximity reactors, and different designs will be discussed below.

Kodak first introduced such Close Proximity reactors. Their design featured isolated rectangular gas channels (gas inlets in Figure 4.10a), separated by exhaust channels.[225] Whilst in the initial design the substrate was held mechanically above the reactor head, they demonstrated that levitating the substrate above the head created pressure gradients which forced waste gas to the exhaust, thus preventing intermixing of gases from separate channels.[225] ZnO produced for TFTs by this method gave mobilities > 15 cm^2/Vs and structural properties similar to vacuum produced films, whilst the growth characteristics of Al_2O_3 matched well with temporal ALD. However, concerns over compatibility with heavier substrates, particularly if the reactor was to be scaled up, remain.[220]

Poodt *et al.* developed a circular rotating reactor (Figure 4.10b), also relying on gas bearings to maintain a small separation (~20 μm) between the substrate and the reactor head, but with the gas manifold suspended above the substrate.[226] Using this system, researchers at TNO have deposited Al_2O_3 at > 1 nm/s,[226] as well as ZnO, $In_xZn_{1-x}O$[227] and $Al_xZn_{1-x}O$.[228] They also demonstrated the possibility of using an atmospheric plasma in place of the oxygen containing precursor, allowing reduced deposition temperatures for sensitive substrates.[229] Additionally, their spin-off company SoLayTec has developed a conveyor type production line for passivating silicon wafers with Al_2O_3.[135,230] However, the reactor head is constrained to circular substrates, a limitation in processes where continuous substrate feeds are required.

In 2011, Fitzpatrick *et al* at the University of Colorado developed a linear system where the substrate sat on a platform which moved back and forth (Figure 4.10c).[224] Unlike the previous examples, the substrate to gas manifold spacing was maintained mechanically using a micrometer. Substrate to gas manifold spacings < 100 μm were required for good film uniformity, due to difficulty in maintaining the same spacing throughout the movement of the substrate precisely. However, the system is less restricted in terms of substrate weight and shape relative to the Kodak and TNO designs.[220,225,226]

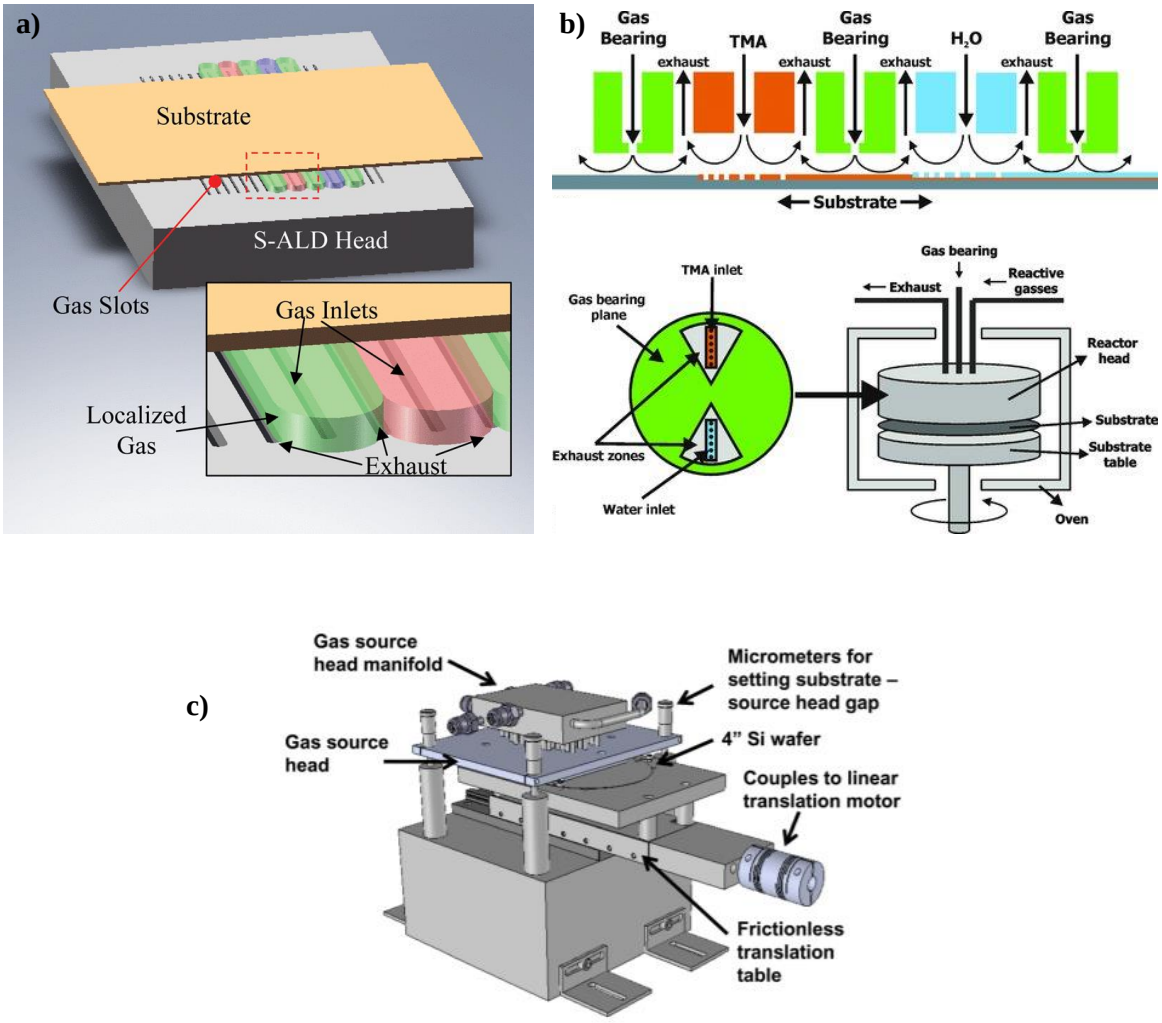

Figure 4.10 Schematic of a) the gas manifold of the spatial ALD reactor developed by Kodak, in which the substrate levitates above the precursor delivery head,[225] b) the circular spatial ALD reactor developed by Poodt *et al* at TNO[226] and c) the spatial ALD reactor developed by Fitzpatrick *et al* at the University of Colorado, where the substrate is translated below the gas manifold on a moving table.[224] Images were reproduced with permission from references [224–226].

4.3.2.2 The Vertical Cambridge University Close Proximity Reactor

The Vertical Cambridge University Close Proximity (VCUCP) reactor was used for work in this thesis (Figure 4.11). This was developed using Kodak's gas manifold but, unlike their design, the substrate sits below the gas manifold. The metal precursor leaves the middle channel in Figure 4.11b. Oxidiser channels sit at either side, separated by inert gas channels. This allows deposition of metal oxide when the substrate moves in either direction (therefore one back and forth translation is equal to two ALD cycles). Exhaust channels located between the gas channels collect waste gases *via* local pressure differences. Gas separation is maintained by flowing equal gas flow rates through the channels and using a gas manifold to substrate spacing of < 50 μm.[135]

Regarding the delivery of precursors, solid or liquid precursors are loaded into glass bubblers in an inert atmosphere. For compounds with a low vapour pressure, the bubbler is heated until a suitable vapour pressure (≃ 13 Pa or above) is reached. Inert carrier gas is bubbled through the bubbler and carries precursor vapour to the gas manifold (Figure 4.11a). For gaseous precursors such as molecular oxygen, gas bottles are connected directly to the gas lines. Like the University of Colorado design, the substrate sits on a metal platform which is moved back and forth by a motor. The substrate speed and scan size are controlled using a homemade LabView program. The substrate to gas manifold distance is controlled with a micrometer. Whilst suffering from difficulties in precisely controlling the substrate to gas manifold spacing, this allows for study of the influence of this spacing on deposition rates, whilst also being compatible with a range of substrate shapes, weights and sizes. To date, films have been deposited on glass substrates, silicon wafers, transparent conducting oxides and flexible plastic substrates.[135,226,231]

As mentioned, mechanically constraining the gas manifold over the substrate using a micrometer makes it difficult to accurately control the size of the gap above the substrate. As a result, gas intermixing can occur such that reactions are no longer self-limiting. In this case, deposition is generalised to a decomposition CVD-like reaction (Figure 4.8b). The GPC *vs* scan speed (or exposure time) becomes linear, and GPC increases with exposure time (*i.e.* at slow substrate speed). Whilst monolayer thickness control is lost, this means growth rates greater than one ALD cycle can be achieved, with good enough thickness control for applications with less stringent thickness constraints such as CTMs in solar cells and charge injection materials in light emitting diodes.[218] Additionally, good coverage of rough substrates is still achieved.[232]

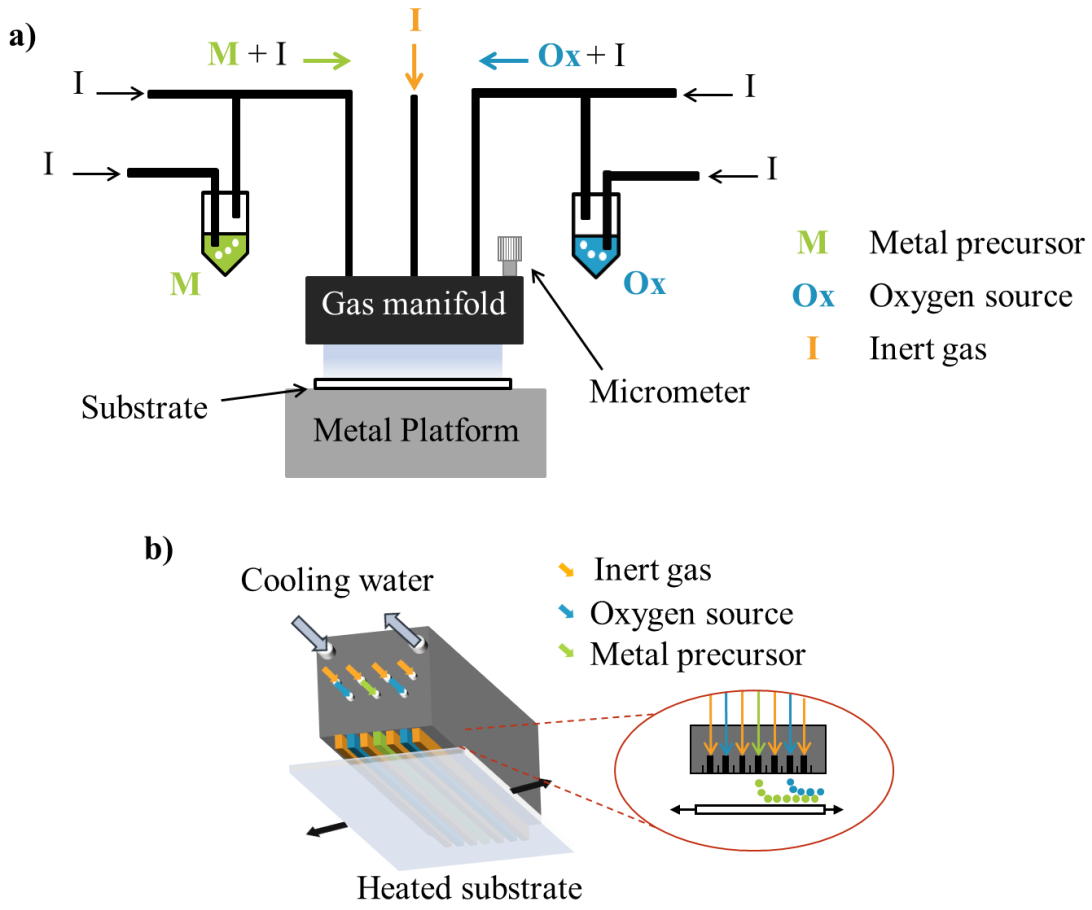

Figure 4.11 Schematic of a) the Vertical Cambridge University Close Proximity AP-SALD reactor, illustrating the transport of reacctive precursors towards the gas manifold using carrier inert gas and b) the Vertical Cambridge University Close Proximity AP-SALD gas manifold, illustrating the movement of precursors through separate channels in the reactor head.

Al_2O_3, ZnO, TiO_2, Ga_2O_3, Nb_2O_5 and Cu_2O have been deposited using the Vertical Cambridge University Close Proximity reactor.[2,218,219,231,233] Muñoz-Rojas *et al.* demonstrated deposition of Cu_2O at ~ 0.17 Å/s; two orders of magnitude faster than ALD.[231] Meanwhile, Hoye *et al.* addressed concerns over the uniformity of films deposited with a mechanically constrained system.[218,224] Over a deposition area of 375 mm^2 they measured only a 3% variation in thickness of ZnO films. By bubbling through two metal precursor bubblers with controlled flow rates at the same time, Hoye also demonstrated that metal oxide doping can be readily achieved with the VCUCP reactor.[218,234] ZnO was controllably doped with Mg to raise the conduction band, resulting in improved electron injection in perovskite light emitting diodes.[234] Otherwise TiO_2, ZnO and Nb_2O_5 have been employed as charge blocking layers in organic,[219] quantum dot and perovskite solar cells,[233,234] with TiO_2 and ZnO films deposited at temperatures $\leq$ 100 °C, allowing deposition on temperature sensitive substrates.

Whilst much progress has been made in the development of AP-SALD systems, the field is dominated by *n*-type metal oxides. As such, NiO_x has not been deposited by AP-SALD to date. However, NiO_x has been deposited by ALD, and ALD precursors are usually compatible with AP-SALD reactors. Therefore, progress in ALD NiO_x deposition will be discussed in the following section.

4.3.3 Deposition of nickel oxide by atomic layer deposition

NiO_x has been deposited from several ALD precursors, which can be separated into two categories. The first set are high-melting solids: $Ni(apo)_2$ (apo = 2-aminopent-2-en-4-onato), $Ni(acac)_2$ (acac = acetylacetonate) and $Ni(thd)_2$ (thd = 2,2,6,6-tetramethylheptane-3,5-dionato), from which polycrystalline NiO_x films have been deposited at 200 – 275 ºC.[235–237] However, their melting points of > 200 ºC makes them incompatible with the VCUCP reactor bubblers, whilst poor reactivity has meant O_3 has often been required as the oxygen source, making scaling up problematic. The second set of precursors are low-melting and reactive and have been used to deposit NiO_x at 90 – 150 ºC. These precursors are $Ni(dmamb)_2$ and $Ni(dmamp)_2$, where dmamb = 1-dimethylamino-2-methyl-2-butanolate and dmamp = 1-dimethylamino-2-methyl-2-propanolate.[238,239] However, in these cases NiO_x was amorphous, making them likely to have poor electrical properties. For example, $MAPbI_3$ solar cells using ALD NiO_x deposited from $Ni(dmamb)_2$ by Seo *et al.* saw a 26 % increase in efficiency when NiO_x was annealed at 300 ºC in air, compared to devices with NiO_x as-deposited at 200 ºC.[112] Additionally, these precursors are not currently commercially available.

Metallocene compounds (MCp_2 where Cp = cyclopentadiene) are commonly used ALD precursors. $NiCp_2$ has been used to deposit ALD NiO_x but is again incompatible with the VCUCP reactor due to its melting point of ~ 170 ºC.[240–242] However, the addition of alkyl chains on the Cp ligand reduces its melting point such that $Ni(CpMe)_2$ (where Me = CH_3) melts at ~ 36 ºC,[240] making it compatible with the CPP system. This is due to the steric effects of the alkyl chains reducing the interactions between molecules. Ishikawa calculated the vapour pressure of $Ni(CpMe)_2$ to follow:

$$log(p) = 9.17 - \frac{3310}{T} \qquad \textbf{(4.17)}$$

Where *p* is pressure in mmHg and T is temperature (K). Considering this, $Ni(CpMe)_2$ has a vapour pressure of 22.7 Pa when heated to ~ 60 ºC, comparable to that of $Mg(CpEt)_2$ (Et = C_2H_5) at 65 ºC which was used to Mg dope ZnO films using the VCUCP reactor previously.[243] Additionally,

$Ni(CpMe)_2$ is stable to decomposition up to ~ 250 ºC, making deposition by AP-SALD possible up to these temperatures.[240]

NiO_x has been prepared from $Ni(CpMe)_2$ in the past using H_2O_2 as the oxygen source.[244] However, films were deposited at 400 ºC, above the decomposition temperature, therefore deposition occurred by CVD. Despite this, NiO_x has been grown by ALD from $Ni(CpEt)_2$ and O_3 at temperatures as low as 150 ºC.[241] $Ni(CpEt)_2$ is assumed to be less reactive than $Ni(CpMe)_2$, due to an increased inductive effect from the longer alkyl chain into the aromatic Cp ring which acts to strengthen the Ni-ligand bond. This offers the possibility that NiO_x can also be deposited by ALD (and thus AP-SALD) from $Ni(CpMe)_2$. Otherwise, deposition by AP-CVD using the VCUCP reactor, with greater deposition rates than AP-SALD whilst maintaining excellent control of film thickness, are a possibility at temperatures > 250 ºC.

The advantages of AP-SALD discussed in section 4.3.2 and the feasibility of several Ni precursors discussed above motivated the investigation of $Ni(CpMe)_2$ as a precursors for AP-SALD NiO_x films. This provides the background into work for the second half of this thesis.

4.3.4 Aims for chapter 10:

1. Deposit NiO_x from $Ni(CpMe)_2$ and an oxygen source using the Vertical Cambridge University Close Proximity AP-SALD reactor
2. Measure growth characteristics to determine whether the deposition occurs by an ALD or CVD mechanism
3. Employ AP-SALD NiO_x films in perovskite solar cells

5 Methods and Materials

5.1 Thin film deposition

5.1.1 Thermal chemical vapour deposition of bismuth oxyiodide

BiOI was grown in a two-zone tube furnace, depicted in Figure 5.1. A mass flow controller was used to independently control the flow rates of oxygen and argon, which were fed into the furnace. BiI_3, which was used to supply the bismuth and iodine, was loaded into a crucible and placed into a quartz furnace tube. Substrates were aligned within the furnace tube 2 – 5 cm from the BiI_3 crucible. The furnace was heated, causing BiI_3 to sublime and react with oxygen gas, forming BiOI thin films on the substrates at temperatures between 325 – 500 ºC.

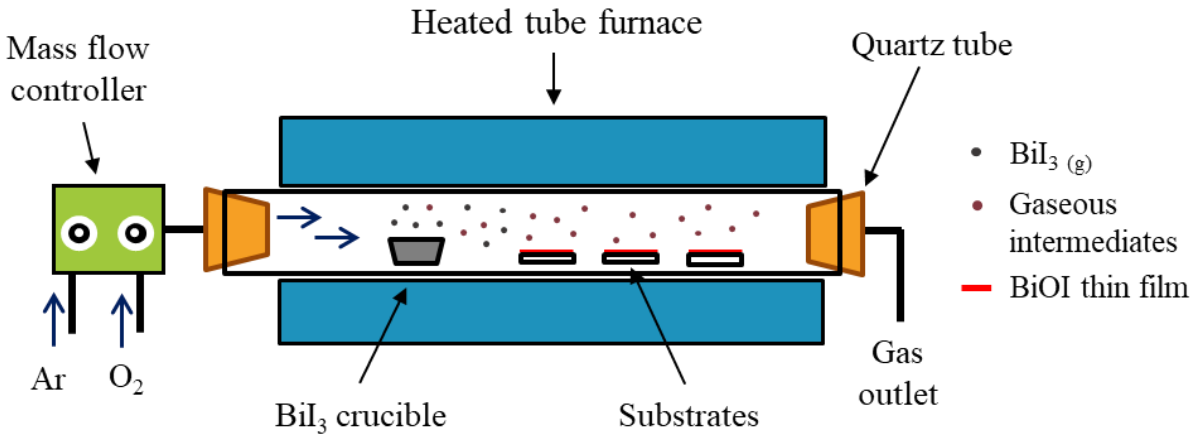

Figure 5.1 Schematic of the thermal chemical vapour deposition set up for fabrication of BiOI films from bismuth iodide and oxygen at 325 – 500 ºC. The oxygen gas is supplied through a gas flow mixer, where it is mixed with argon carrier gas, whilst bismuth iodide powder is loaded into a crucible into a furnace. On heating the bismuth iodide sublimes, depicted by grey circles. The red-brown circles represent the gaseous intermediates from reaction between bismuth iodide and oxygen and the red lines represent bismuth oxyiodide thin films.

For BiOI films grown for chapter 6, the two-zone furnace was heated to 360 °C in the left-hand zone and 350 °C in the right-hand zone. Note that the crucible and substrates were all contained within the left-hand zone of the furnace, where < 3 ºC variation in surface temperature of substrates located up to 10 cm from the crucible was expected based on furnace temperature profiling. Thus, the temperature gradient was used only to aid gas flow. Substrates were cut to roughly 12 x 12 mm using a diamond scribe and were adhered to a microscope slide using silver paint. 500 mg BiI_3 powder (Alfa Aesar, Puratronic, 99.999% metals basis) was loaded into a

ceramic crucible. The substrates and BiI_3 crucible were loaded into the left-hand side of the furnace tube 2 cm apart. Gas flows were set to 20 mL/min argon (BOC) and 5 mL/min oxygen (Air Products) and the furnace tube was sealed (maintaining a 1:4 ratio of oxygen: argon flow rates). Films were deposited for 15, 30, 50, 60, 90 and 120 minutes, after which they were removed from the furnace and quenched in air. Between batches the furnace tube was rinsed with 37% HCl and absolute ethanol respectively, dried with an air gun and baked out at 800 °C for 4 hours to remove residual contaminants on the inner walls of the furnace tube.

For generation of a phase diagram for the CVD reaction between BiI_3 and O_2 in Figure 7.1, the same general procedure as above was followed. However, the ratio of argon:oxygen flowed through the furnace was varied to find the correct fraction of oxygen required to grow phase pure BiOI at each temperature. Additionally, the mass of BiI_3 precursor used and the total flow rate of gas was increased with increasing deposition temperature. This was to account for the higher vapour pressure/faster rate of depletion of BiI_3 with increasing temperature, meaning that the gas flow needed to be increased to achieve good coverage within the substrate zone. The reaction conditions are stated in Table 5.1. The deposition time was the time taken to grow a ~ 700 nm film. 325 ºC was the lowest temperature where BiOI could be grown; beyond this, the temperature was increased in 50 ºC increments between 350 – 500 ºC. Note that the temperature of the left-hand and right-hand zones was equal for this work and all work in chapters 7 and 8, as the 10 ºC temperature gradient used for work in chapter 6 was determined visually to have little effect on vapour flow and subsequent coverage of the furnace tube.

Table 5.1 Deposition parameters used to generate the phase diagram for the CVD reaction between BiI_3 and O_2 (Figure 7.1). The time represents the time taken to grow a ~ 700 nm film.

Temperature LHS / °C	Temperature RHS / °C	Oxygen flow rate / mL/min	Argon flow rate / mL/min	$\frac{[\text{Flow oxygen}]}{[\text{Total gas flow}]}$ / %	Mass BiI_3 / g	Time / min
325	325	0.2	23.1	0.9	0.5	120
325	325	5	18	21.7	0.5	120
350	350	0.3	25	1.2	0.5	60
350	350	5	20	20.0	0.5	60
400	400	0.3	30	1.0	1.0	20
400	400	5	25	16.7	1.0	20
400	400	6	24	20.0	1.0	20
450	450	0.4	40	1.0	1.0	7.33
450	450	5	35	12.5	1.0	7.33
450	450	8	32	20.0	1.0	7.33
500	500	0.5	50	1.0	1.0	2
500	500	10	40	30.0	1.0	2

For all other work in all other sections of chapter 7 BiOI was deposited between 325 – 500 ºC where the ratio of oxygen:argon flow rates through the furnace was roughly 1 %. The deposition conditions used are given in Table 5.2. The conditions at 350 ºC were used to grow films for all work in chapter 8.

Table 5.2 Deposition parameters for BiOI films grown for work in section 7.1.1 onwards. The conditions at 350 ºC were used to grow films for all work in chapter 8.

Temperature LHS / °C	Temperature RHS / °C	Oxygen flow rate / mL/min	Argon flow rate / mL/min	$\frac{\text{[Flow oxygen]}}{\text{[Total gas flow]}}$ / %	Mass BiI_3 / g	Time / min:s
325	325	0.2	23.1	0.9	0.5	120
350	350	0.3	25	1.2	0.5	60
400	400	0.3	30	1.0	1.0	20
450	450	0.4	40	1.0	1.0	7:20
500	500	0.5	50	1.0	1.0	2

5.1.2 Atmospheric pressure spatial atomic layer deposition of nickel oxide

A detailed description and schematic of the Vertical Cambridge University Close Proximity atmospheric pressure spatial atomic layer deposition reactor was given in section 4.3.2.2. Nickel oxide was deposited using bis(methylcyclopentadienyl)nickel(II), $Ni(CpMe)_2$ (97 %, Sigma-Aldrich), and oxygen gas (BIP®, Air Products) as precursors. $Ni(CpMe)_2$ was heated to 60 °C to increase its vapour pressure (from 1.6 Pa at room temperature to 22.7 Pa at 60 ºC) and thus its gas fraction in the carrier gas stream at the gas manifold. Note that at temperatures above 60 ºC the precursor degraded. A spacing of 90 μm between the gas manifold and substrate was used. Argon gas was bubbled through the $Ni(CpMe)_2$ bubbler at 250 mL/min, which was diluted by argon gas flowing at 50 mL/min through the metal dilution line. Oxygen gas flowed directly from a cylinder at a rate of 100 mL/min and diluted by a flow of argon through the oxygen dilution line at 500 mL/min. The argon gas flow rate through the inert gas lines was 1000 mL/min. The substrate was held on the heated platform at a temperature of 350 ºC and was moved back and forth below the gas manifold at a speed of 10 mm/s, unless otherwise stated. The number of movements below the gas manifold was varied to achieve the desired thickness, where the growth per cycle was 0.14 nm/cycle (*i.e.* per backwards or forwards movement) for a substrate speed of 10 mm/s.

5.1.3 Solution processed nickel oxide

Solution processed NiO_x was used as the hole transport material for BiOI solar cells. 1454 mg nickel nitrate hexahydrate (Sigma-Aldrich) was dissolved in 5 mL anhydrous ethylene glycol (Sigma-Aldrich, 99.8 %) and 334 μL ethylenediamine (Sigma-Aldrich) inside a glovebox. The solution was stirred for 1 hour and filtered through a 0.2 μm syringe filter. Substrates were cleaned sequentially in soapy deionised water, deionised water, acetone and iso-propyl alcohol for 10 minutes each in an ultrasonic bath. They were dried with an air gun and further cleaned by oxygen plasma for 10 minutes. The nickel nitrate solution was cast onto the substrates at 5000 rpm for 45 s using a spin coater. The substrates were dried on a hot plate at 125 ºC for 30 minutes then annealed at 300 ºC for 1 hour. They were quenched by removing from the hot plate directly onto aluminium foil.

5.2 Thin film annealing

5.2.1 Vacuum annealing of bismuth oxyiodide

Vacuum annealing of BiOI was carried out in a tube furnace. BiOI was deposited onto solution processed NiO_x on glass/ITO substrates at 350 ºC using the conditions in Table 5.2. Kapton tape was used to attach the substrates to a metal gauze substrate holder. The holder was loaded into a quartz furnace tube fitted with vacuum flanges. The tube was evacuated to a pressure of 25 Pa. The furnace was heated to 100 °C for 5 s and 1, 10, 30, 60, 120, 1380 and 2880 minutes. After this time had elapsed the tube was vented, and the samples were removed.

5.2.2 Vacuum annealing of nickel oxide

150 nm Ni films were sputtered onto 12 x 12 mm silicon substrates by Dr Jack Alexander-Webber, University of Cambridge. 20 nm NiO_x was deposited onto the sputtered Ni using the conditions in subsection 5.1.2 using 70 oscillations. Samples were placed face down onto Ni foil (99.98 %, Sigma Aldrich) on a heat strip inside a vacuum chamber. The chamber was evacuated to a pressure of 0.1 Pa. Samples were heated rapidly to 700 ºC for 3, 10 and 20 minutes. They were cooled under vacuum before removing from the chamber.

5.3 Solar cell fabrication

5.3.1 Bismuth oxyiodide solar cells

Solution processed nickel oxide was prepared on glass/ITO substrates using the method in subsection 5.1.3. Four NiO_x substrates were then stuck to a microscope slide in 2 x 2 formation using silver paint to cover the end 2.5 x 2.5 cm^2 of the microscope slide. The two-zone furnace was pre-heated to left-hand zone 360 ºC and right-hand zone 350 ºC and BiOI was deposited according to the procedure and conditions in subsection 5.1.1. A 40 nm ZnO film was deposited as the electron transport layer using AP-SALD with diethylzinc and oxygen as the precursors. The temperature of the platform was set to 80 ºC and the substrate scan speed was 50 mm/s. Argon gas was bubbled through the diethyl zinc bubbler at 25 mL/min, and 100 mL/min argon was added to the metal dilution line. The oxygen flow was 100 mL/min, which was undiluted. Argon was flowed through the inert gas line 500 mL/min. 60 full movements backwards and forwards were used to grow a 40 nm film. Finally, Cr (20 nm)/Ag (100 nm) electrodes were deposited by thermal evaporation. Devices were patterned using an evaporation mask so that each device had 8 pixels with an active area 4.5 mm^2. The devices were completed by attaching metal legs to each electrode to provide an electrical contact and were stored in a glove box until measurement to prevent degradation of the electrodes in air.

5.3.2 Perovskite solar cells

Perovskite solar cells for section 10.3 were prepared by Dr Baodan Zhao (University of Cambridge). 16 nm nickel oxide thin films were deposited with the AP-SALD reactor using the conditions in subsection 5.1.2. This thickness was achieved with 60 full back and forth movements (or oscillations) under the gas manifold. Methylammonium iodide (127.2 mg), lead iodide (461.0 mg) and formamidinium iodide (34.4 mg) were dissolved in 900 μL of a mixture of 70 vol% γ-butyrolactone (Sigma-Aldrich) and 30 vol% DMSO (dimethyl sulphoxide, Sigma Aldrich) and stirred for 12 hours at 60 ºC. The NiO_x substrates were cleaned for 20 seconds by oxygen plasma before transferring to a glovebox. The solution was dropped onto the substrate which was spin coated at 1000 rpm for 40 s followed by 4000 rpm for 60 s. To aid better crystallisation, 100 μL toluene was dripped onto the film 70 s into the spin procedure. The films were annealed inside the glovebox for 30 minutes at 100 ºC. A solution of $PC_{61}BM$ (25 mg, Solenne BV) in chlorobenzene (1 mL, Sigma-Aldrich) was prepared. This was spin coated on top of the perovskite layer for 60 s at 1500 rpm as the electron transport layer. Using thermal evaporation, 100 nm aluminium electrodes were deposited using an evaporation mask to give 8 pixels of area 4.5 mm^2. Devices were finished by adding metal legs to provide an electrical contact.

Perovskite solar cells for comparison to BiOI solar cells in section 6.3.4 were prepared by Dr Robert Hoye, University of Cambridge. Solution processed NiO_x was prepared on glass/ITO substrates using the method in subsection 5.1.3. A 1:1 molar ratio of methylammonium iodide (Dyesol) and lead iodide (TCI) were added to 30 vol% γ-butyrolactone (Sigma-Aldrich) and 70 vol% DMSO (dimethyl sulphoxide, Sigma Aldrich) to make a 10 M solution. The solution was stirred for 1 hour at 70 ºC. The solution was spin cast onto the NiO_x substrates for 40 s at 1000 rpm then 60 s at 4000 rpm, where after 68 s of spinning 75 μL of toluene (Sigma-Aldrich) was dropped onto the film. Samples were annealed inside the glovebox at 60 ºC for 2 min followed by 30 min at 100 ºC. $PC_{60}BM$ (20 mg, Solenne BV) was dissolved in 1 mL of chlorobenzene (Sigma-Aldrich) for the electron transport layer. It was spin cast onto the perovskite film in a two-step spin process for 40 s at 1600 rpm then 10 s at 3000 rpm. 100 nm aluminium electrodes were deposited, and metal legs were added to provide electrical contact during current-voltage measurements.

5.4 Thin film characterisation

5.4.1 X-Ray diffraction

Theta-2theta scans were measured on a Bruker D8 diffractometer with Cu K_α radiation ($\lambda = 1.5406$ Å), with tube current 40 mA and a generator voltage of 40 kV. Samples were rotated during measurement. For all measurements, 0.5 º divergence and anti-scatter slits and a 0.2 mm receiving slit were used. For BiOI films, a step size of $2\theta = 0.039$ º and a dwell time per step of 1 s was used. For NiO_x films, a step size of $2\theta = 0.049$ º and a dwell time of 2.4 s per step was used. For perovskite films, a step size of $2\theta = 0.015$ º and a dwell time of 0.5 s was used. Line profile fits were applied to the data using HighScore Plus software in order to determine the peak positions and full width at half maximum (FWHM). Instrument line broadening was measured using a LaB_6 standard, and the FWHM of the instrument line broadening was subtracted from the fitted data values. The fitted peak positions were matched to PDFs (Powder Diffraction Files) stored in the ICDD database. The corresponding PDF files are listed in Table 5.3.

Table 5.3 Powder Diffraction Files (PDF) fitted to measured diffraction patterns for work within this thesis.

Phase	PDF number
Cubic NiO	00-047-1049
BiOI	00-010-0445
Monoclinic-Bi_5O_7I	00-038-0669
$Bi(IO_3)_3$	00-058-0583
$Bi_2O_{2.33}$	00-027-0051
β-Bi_2O_3	00-001-0709

For BiOI films a Pawley refinement was used to fit the data. A crystallographic information file (CIF) from reference [183], containing the space group (P4/*nmm*) and lattice parameters for BiOI was used to simulate a theoretical diffraction pattern, which was fitted to the data by a least-squares refinement method.

Lattice parameters were calculated using the *d*-spacing, calculated from the Bragg equation (eqn. **5.18**), and the Miller indices, [*hkl*], of the diffraction peaks. Equation **5.19** was used for NiO_x, which has cubic symmetry, whilst equation **5.20** was used for tetragonal BiOI.

$$n\lambda = 2d\,sin\theta \qquad \textbf{(5.18)}$$

$$\frac{1}{d^2} = \frac{h^2 + k^2 + l^2}{a^2} \qquad \textbf{(5.19)}$$

$$\frac{1}{d^2} = \frac{h^2 + k^2}{a^2} + \frac{l^2}{c^2} \qquad \textbf{(5.20)}$$

The Scherrer equation was used to estimate the crystallite size:

$$D = \frac{K\lambda}{\beta cos\theta} \qquad \textbf{(5.21)}$$

where D is the crystallite size (Å), λ is the X-Ray wavelength (Å), K is a shape factor, β is the full width at half maximum of peak [*hkl*] (radians) and θ is the Bragg angle of peak [*hkl*] (radians).[245]

5.4.2 Atomic force microscopy

Atomic force microscope images were taken with a Veeco AFM Multimode Nanoscale III system operating in tapping mode. In this mode, the cantilever oscillates at a constant amplitude near its resonant frequency. A laser beam is focussed onto the top of the cantilever and deflects into a photodiode. Changes in height of the sample during scanning result in different interactions with the cantilever (*e.g.* an increase in van der Waals interaction when the tip of the cantilever and the sample are closer together) causing a change in amplitude. This is counteracted by the tip moving further away from the sample, which causes the laser beam to deflect at a different angle (or hit the photodiode at a different position). The position of the beam on the photodetector during scanning is converted into an image. A silicon tip was used at a resonant frequency of 325 kHz.

5.4.3 Scanning electron microscopy

Scanning electron microscopy (SEM) images taken by the author used a Camscan MX2600 microscope. Samples were sputter coated with ~ 10 nm Pd and grounded by taping to metal stubs with carbon tape to prevent charging during imaging. A beam voltage of 5 kV was used for measurements. Images for chapter 7 were measured by Tahmida Huq, Device Materials Group, University of Cambridge using a Fei Magellan 400 electron microscope with a beam voltage of 5 – 15 kV. Cross-sectional SEM images in chapter 6 were taken by Dr Robert Hoye (whilst at the Photovoltaics Research Lab, Massachusetts Institute of Technology) using a LEO VP-1530 electron microscope with a beam voltage of 3 kV. Samples were sputtered with ~ 10 nm Pd/Au to prevent charging. Samples were cleaved using a diamond scribe for cross-sectional images.

ImageJ software was used to determine particle size from SEM images. The width of 30 – 40 randomly chosen particles was measured, and the mean and standard deviation values calculated. For the surface particulate size determination in 7 the diameter of randomly chosen particulates was measured in 15 directions, and the mean and standard deviation calculated.

5.4.4 Profilometry

BiOI film thickness was measured using a Dektak profilometer. A step edge was created by scratching away the part of the film using a razor blade. The stylus was lowered until it contacted the film surface and the tip was moved across the step edge at a speed of 100 μm/s with a force of 9.8 μN. The resultant profile was flattened to determine the height of the step edge.

5.4.5 X-Ray reflectivity

Borosilicate glass (cut to 10 x 10 mm, Soham Scientific) was used as the substrate for X-ray reflectivity measurements of NiO_x. Measurements were taken using a Bruker D8 Advance with CuK_α radiation (λ = 1.5406 Å), using a tube current of 40 mA and an acceleration voltage of 40 kV. Divergence and receiving slits of 0.1 º were used. Samples were aligned to ensure that the surface was completely flat to the incoming beam such that an offset in θ would not be measured. θ-2θ scans were measured at an incident angle range θ = 0.15 – 2.5 º, with a step size 0.0005 º and a dwell time of 0.5 s per step. LEPTOS software was used to fit a model to the data, assuming densities of 5.15 g/cm^3 and 3.8 g/cm^3 for NiO and borosilicate glass respectively.

5.4.6 UV-visible spectrophotometry

Transmission and reflectance were measured using a Perkin Elmer Lambda 750 UV/Vis/NIR spectrometer with an integrating sphere, which allows the reflectance of highly scattering samples to be measured. For measurements of BiOI, films were deposited onto solution processed NiO_x on glass due to difficulty achieving good coverage on glass substrates.

5.4.7 Photoluminescence spectroscopy

NiO_x was deposited using the AP-SALD reactor onto crystalline silicon samples for photoluminescence measurements so that no interference from the substrate was measured. An ACCENT RPM 2000 spectrometer was used to measure the photoluminescence, using a 266 nm laser fitted with a 295 nm high pass filter was used to excite the samples at power 1.95 mW. Photoluminescence of BiOI on crystalline silicon or quartz substrates (Spectrosil® 2000, Heraeus) were measured by Dr Robert Hoye, University of Cambridge, using a Horiba LabRam Evolution multiline PL/Raman spectrometer. The excitation wavelength was 532 nm.

5.4.8 Time correlated single photon counting measurements

Time correlated single photon counting (TCSPC, or transient photoluminescence) measurements were measured of 1 μm BiOI on quartz substrates (Spectrosil® 2000, Heraeus) by Dr Alex Polizzotti (Massachusetts Institute of Technology). Samples were excited by a laser at 532 ns, and the photons emitted between wavelengths 640 – 700 nm were counted by at 0.008 ns intervals using a photodiode (Micro Photon Devices $PD-100-C0C). A bi-exponential decay was fitted to the data using Origin software.

5.4.9 X-Ray photoelectron spectroscopy

X-Ray photoelectron spectroscopy measurements were carried out by Dr Weiwei Li, Device Materials Group, University of Cambridge. X-Ray photoelectron spectroscopy was used to measure the core level and valence band spectra of BiOI and NiO_x films. Samples were contacted to a gold reference within the measurement chamber using silver paint, preventing charging during measurement and allowing alignment of the Fermi level with gold (to which the binding energy scale was calibrated). An Al K_α X-ray source ($h\nu$ = 1486.6 eV) was used to excite the samples, causing photoemission of electrons. The kinetic energy of the emitted electrons was measured with a SPECS PHOIBOS 150 electron energy analyser. This converts the electrons kinetic energy into its binding energy (BE), the energy required to remove an electron from an atomic orbital to vacuum, using the relationship:

$$BE = h\nu - KE \qquad \textbf{(5.22)}$$

where KE is kinetic energy (eV) and $h\nu$ is the incident photon energy (eV, 1486.6 eV for Al source).

Elemental composition of BiOI and NiO_x films was calculated from the XPS core level spectra. Relative sensitivity factors, RSFs, for each atomic orbital considering an Al X-ray source were used to scale the area of each spectrum, as will be described in more detail in section 7.2.2. The relative sensitivity factors of the atomic orbitals used are listed in Table 5.4.[246]

Table 5.4 XPS core level spectra fitted and the corresponding relative sensitive factors used to determine the composition of BiOI and NiO_x thin films.[246] The X-Ray excitation source was aluminium.

Element	Core level	RSF
Bi	Bi $4f_{7/2}$	13.90
O	O 1*s*	2.93
I	I $3d_{5/2}$	19.87
Ni	Ni $2p_{3/2}$	14.61

5.4.10 Photothermal deflection spectroscopy

Photothermal defection spectroscopy of BiOI on quartz was measured by Dr Mojtaba Abdi-Jalebi, Optoelectronics Group, University of Cambridge. In this technique, the sample is immersed in an inert liquid (in this case the fluorocarbon FC-72 Fluorinert). Monochromatic light (the pump

beam) irradiates the film surface from the normal direction, whilst a probe beam (a 670 nm laser) runs parallel to the film surface. Absorption of light from the pump beam results in heating of the sample. This in turn heats the Fluorinert, causing a change in its density and subsequently its refractive index. This results in deflection of the probe beam, which is measured by a position sensing detector (PSD). As the absorption of light increases, the deflection of the probe beam increases proportionally. The deflection can be measured as a function of pump beam wavelengths due the use of a monochromator and is used to generate an absorption spectrum to a high sensitivity.

5.4.11 Mott-Schottky measurements

Mott-Schottky measurements of NiO_x were carried out using the method of Thimsen *et al.* and using a Versastat 4 potentiostat.[3,247] Before deposition, an approximately 1 x 2 mm^2 area on the edge of an ITO substrate was masked with silver paint. 20 nm NiO_x was deposited by AP-SALD onto the ITO to form the ohmic contact. The silver paint was scratched away after deposition to reveal an area of bare ITO. A copper wire was adhered to the ITO using silver paint to allow electrical contact to be made. Epoxy resin was used to encapsulate the sample, leaving approximately 5 x 5 mm^2 of the NiO_x film exposed. To provide the Schottky barrier, the sample was submerged in an electrolyte containing 1 M Na_2SO_4 and 0.1 M monobasic sodium phosphate buffer, which was raised to pH 11.9 using a 1 M solution of NaOH. Mott-Schottky measurements were performed using a three-electrode set-up, with the sample acting as the working electrode, the Ag/AgCl couple as the reference electrode and Pt as the counter electrode. A bias sweep from -1 to 0 V with step size 40 mV was applied to the working electrode (*vs* Ag/AgCl) and the impedance when a ± 10 mV AC excitation voltage was applied at 5 – 20 kHz was measured. This was used to generate a plot of $1/C^2$ against V. The applied bias *vs* the Ag/AgCl couple was converted to a potential *vs* RHE (the reference hydrogen electrode) using the equation $E_{RHE} = E_a + E_{ref} + 0.059pH$, E_{RHE} is potential *vs* the RHE, E_{ref} is the potential of the Ag/AgCl couple (0.230 V *vs* RHE) and E_a was the applied bias.[247]

5.5 Solar cell characterisation

5.5.1 Current-voltage (JV) measurements

Current voltage (JV) measurements were used to characterise the solar cell performance. Samples in an electrically connected sample holder were placed under a solar simulator (Newport, Class A – Oriel 92250A) which simulates the AM 1.5 G spectrum at a power density of 100 mW/cm^2,

calibrated to a silicon reference cell. A Keithley source meter (Keithley 2636A) was used to apply voltage and measure the resultant current both under illumination and in the dark. The sourcemeter was controlled by a LabView program. Optical density filters were used for the light intensity dependent measurements. For BiOI devices, a step size of 50 mV and a scan speed of 10 mV/s was used. For perovskite devices, a step size of 20 mV and a scan speed of 10 mV/s was used. Light intensity dependent JV measurements were carried out by Dr Robert Hoye by placing optical density filters between the device and the solar simulator light source.

5.5.2 External quantum efficiency measurements

EQE measurements were used to measure the efficiency of conversion of light into current by measuring the current output of the device under monochromated light. An Oriel Cornerstone 130 monochromator was used with a tungsten halogen lamp (250 W) to illuminate the sample. A silicon diode was used for calibration, and a LabView program was used to convert current into EQE.

Part A

6 Chemical vapour deposition of bismuth oxyiodide

For work in this chapter, the potential of thermal CVD BiOI as a photovoltaic material was explored. Deposition parameters towards phase pure films with sharp XRD peaks and a minority carrier lifetime of 2.75 ns were established. Through the optimisation of device materials and processing conditions, devices with the record PCE (1.8%) and EQE (80%) for BiOI were developed. Additionally, BiOI was shown to be twenty times more stable than $MAPbI_3$ on storage in humid air, addressing stability concerns. Despite these advancement, transport properties were found to limit EQEs at short wavelengths, providing motivation for the rest of the thesis.

6.1 Optimisation of bismuth oxyiodide deposition

Depositions were carried out in the two-zone tube furnace described in section 5.1.1. In separate experiments, the temperature was increased in 25 ºC increments until film formation occurred after 2 hours. This happened when the left-hand side of the furnace was set to 360 ºC and the right-hand side set to 350 ºC (which will be described herein as T = 360|350 ºC). The characterisation of resultant films is presented in the next section. Note that the temperature gradient was used as the reaction was initially thought to occur by chemical vapour transport, in which a temperature gradient is used to drive endothermic or exothermic reactions in the alternate zone to where the precursor is located. However, the temperature gradient was later not found to be necessary for the work in later chapters. Larger temperature gradients, where the zone containing BiI_3 was at 350 ºC and the temperature of the second zone ranged from 250 – 450 ºC were also studied, however BiOI was always found to deposit close to the precursor crucible in the 350 ºC zone.

6.2 Characterisation of bismuth oxyiodide thin films

6.2.1 Structural characterisation of bismuth oxyiodide

Initial optimisation of BiOI growth was carried out on glass substrates. The XRD pattern for a 1 μm BiOI film deposited on glass, a simulated XRD pattern for BiOI and that of the glass substrate are shown in Figure 6.1a. The simulated diffraction pattern was generated using the crystallographic information file from Kandanapitiye *et al.* and using VESTA software.[183] The diffraction peaks for the BiOI film matched with peaks in the simulated diffraction pattern, corresponding to the tetragonal *P4/nmm* space group.[183] This indicates that the BiOI was phase pure, or that any impurity phases were amorphous or not of the correct orientation to diffract. Using the average *d*-spacing from diffraction patterns of four films, lattice parameters $a = b =$ 3.987 Å and $c =$ 9.112 Å were calculated, matching well with reported values for BiOI.[179] A

broad peak extended from $2\theta = 15 – 30$ º due to the amorphous glass substrate. Although all the diffraction peaks matched with the simulated pattern, many of the expected peaks were not present, whilst the [001] reflection dominated. This indicates texturing of the sample with preferential *c*- axis growth, making the other crystal planes of incorrect orientation to diffract the incoming X-ray beam. Using Scherrer analysis and a form factor of 0.9, the average particle size was calculated as 82.2 ± 15.5 nm. However, this value is likely to be inaccurate due to the highly anisotropic shape of BiOI crystals[248] and the limitations of the Scherrer equation when the full width at half-maximum (FWHM) of the diffraction peaks approaches instrument broadening.[245]

SEM was used to assess the morphology of the films. SEM images for a 1 μm BiOI film on glass are presented in Figure 6.1b and c. A 10 nm Pd coating was sputtered onto the samples to prevent charging. From the SEM images, large platelets strongly oriented parallel to the substrate surface were grown. This matches well with the XRD data, where *c*- axis texturing was dominant. Taking the width of 30 random platelets, the average platelet size was 945 ± 408 nm. This is much greater than the particle size estimated using the Scherrer equation, likely due to the breakdown of the Scherrer approximation for highly anisotropic particle shapes (as the crystallite size differs in different directions) and large crystallites.[245,248] Regarding coverage, the films were non-compact, with visible pinholes indicating incomplete surface coverage. This indicates unfavourable interaction between the growing film and the substrate. However, the particle size was much larger than BiOI films in the literature grown by the solvothermal method.[190]

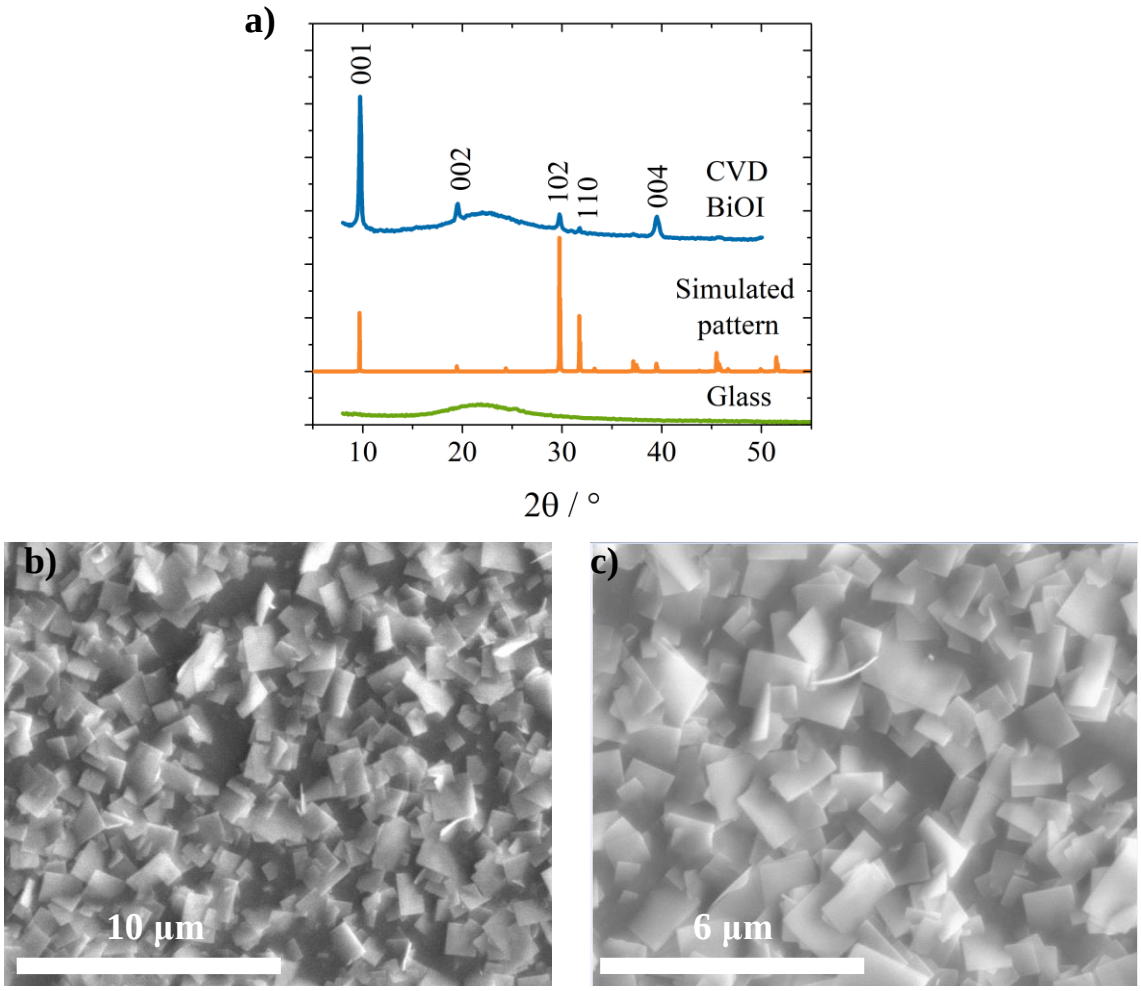

Figure 6.1 a) Measured XRD pattern of thermal CVD BiOI deposited on a glass substrate (blue) and the simulated diffraction pattern (orange) generated using VESTA software and the crystallographic information file made by Kandanapitiye *et al.*[183] The XRD trace of the substrate is shown in green. b) and c) show SEM images of glass|BiOI(1 µm)| Pd(10 nm) samples deposited by thermal CVD on a glass substrate with scale bars of 10 µm and 6 µm respectively.

6.2.2 Optical characterisation of bismuth oxyiodide

The transmittance and reflectance of a 700 nm BiOI film on solution processed NiO_x on glass was measured by UV-visible spectrophotometry (UV-vis), using an integrating sphere to account for scatter due to sample roughness. Note that NiO_x coated glass was used as the substrate due to improved coverage relative to glass substrates, as will be discussed later in the chapter (section 6.3.1). From this, the absorption coefficient was calculated using the following derivative of the Beer-Lambert law.[249]

$$\alpha = -\frac{\ln\left(\frac{T_{BiOI}}{T_{NiO_x}(1 - R_{BiOI})}\right)}{d} \quad \textbf{(6.23)}$$

Where α is the absorption coefficient (cm^{-1}), T_{BiOI} is the transmittance of BiOI, T_{NiOx} is this transmittance of NiO_x on glass and R_{BiOI} is the reflectance of BiOI and *d* is the BiOI thickness (cm), measured by profilometry.

The absorption coefficient as a function of wavelength is shown in Figure 6.2. It has a slow onset at ~1.9 eV and rises to > 1 x 10^5 cm^{-1} beyond 2.6 eV. Band structure simulations have shown that BiOI is an indirect semiconductor;[182] this is responsible for the slow onset of absorption. An absorption coefficient >10^5 cm^{-1} is large for an indirect semiconductor.[2] It should be noted that the absorption coefficient determination by this method is prone to sources of error. For example, there were differences in film thickness/uniformity across the film, whilst an average value for the thickness was used to determine α from equation **6.23**. Additionally, T_{BiOI} and R_{BiOI} were not measured at the exact same point on the film. It would therefore be ideal to repeat the measurement at multiple locations across the film, allowing average and standard deviation values for α to be determined at each wavelength.

It is possible to determine the bandgap of BiOI using α and the Tauc equation:[250,251]

$$(\alpha h\nu)^{\frac{1}{r}} = A(E_g - h\nu) \quad \textbf{(6.24)}$$

where E_g is the bandgap (eV), *hν* is the energy of the incident photon (eV), A is a constant and r is representative of the type of transition, (r =2 for an indirect transition, r = ½ for a direct transition).[186] As BiOI is an indirect semiconductor, $(\alpha h\nu)^{1/2}$ was plotted against energy to give the plot in the inset of Figure 6.2. From equation 6.24, the band-gap energy was determined from the intercept with the *x*-axis (*i.e.* $(\alpha h\nu)^{1/2} = 0$):

$$(\alpha h\nu)^{\frac{1}{2}} = E_g - h\nu = 0 \quad \textbf{(6.25)}$$

Hence,

$$E_g = h\nu \quad \textbf{(6.26)}$$

From Figure 6.2 (inset), the bandgap of BiOI was 1.91 eV. This is in good agreement with literature values for BiOI.[185,186] The bandgap energy is large for a single junction solar cell material; the Shockley-Queisser limit is < 25% at this energy.[31] However, for a two-junction tandem with a silicon bottom cell a bandgap of 1.9 eV is optimum, for which a theoretical maximum efficiency of ~ 45% has been calculated for a four-terminal device.[32]

The absorption depth was obtained from the inverse of the absorption coefficient and is plotted as a function of wavelength in Figure 6.2b. The bandgap is labelled at 1.9 eV (~650 nm). The absorption depth was < 1 μm from 400 – 600 nm, after which it increased to 3 μm at the band-edge (650 nm). The implication for devices is that films of micron-scale thickness are required to absorb all incident light. This necessitates carrier diffusion lengths > 1 μm for good current collection in devices, placing stringent requirements on the defect characteristics of BiOI.[2]

The photoluminescence spectrum of BiOI was also recorded, shown in Figure 6.2c. Here, quartz was used as the substrate to avoid emission peaks from the substrate, as it is non-emissive. BiOI gave weak emission, typical for an indirect semiconductor due to the change in electron momentum required for an indirect transition. Weak PL emission has been reported for many other bismuth-based absorber compounds, which tend to have indirect bandgaps.[1] A broad emission peak centred at ~ 1.9 eV was present, in agreement with the value measured by UV-vis photo-spectroscopy. This means that emission occurred from the band-edge as opposed to a defect state.[2] However, the PL had a long tail towards lower energies, indicating a defect tail at the band edges.

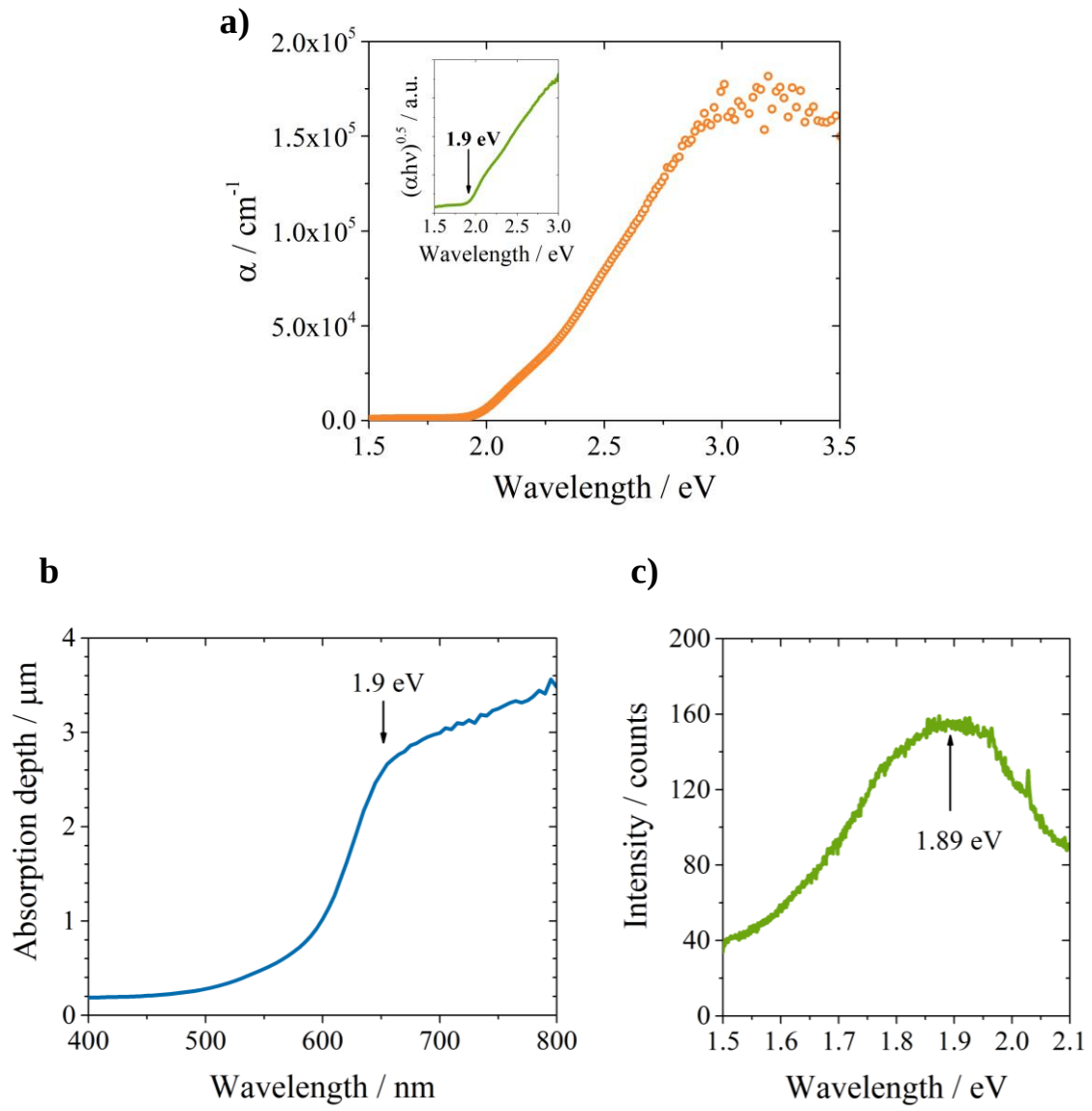

Figure 6.2 a) The absorption coefficient, α, as a function of wavelength for BiOI (orange), calculated from uv-visible spectrophotometry data of a 1 μm BiOI film on a glass|solution processed NiO_x substrate. The inset shows the Tauc plot for BiOI considering an indirect transition (*i.e.* a plot of $(\alpha hv)^{1/2}$ against wavelength), **b)** the absorption depth of BiOI as a function of wavelength, with the band-gap energy labelled at 1.9 eV. **c)** shows the photoluminescence emission spectrum of a 1 μm BiOI film on quartz.

Time correlated single photon counting (TCSPC) was used to measure the lifetime of BiOI. A 1 μm BiOI film was grown onto a quartz substrate, again to avoid emission from the substrate. Samples were excited by a laser of wavelength 532 nm with a fluence 400 nJ cm^{-2}, and the photons emitted between 640 and 700 nm were counted, yielding the data in Figure 6.3. The laser pulse occurred at 0 s.

A bi-exponential decay function:

$$y = y_0 + A_1 e^{-t/\tau_1} + A_2 e^{-t/\tau_2} \quad \textbf{(6.27)}$$

where y is intensity, y_0 is an off-set, A_1 and A_2 are constants of amplitude, t is time and τ_1 and τ_2 are values of the lifetime, was fitted to the data using Origin software. Lifetimes τ_1 = 0.40 ns and τ_2 = 2.75 ns were extracted from the fit. The shorter lifetime, τ_1, is often attributed to surface recombination, whilst the τ_2 refers to the lifetime of the bulk.[2,252] Screening through the lifetime of a series of establish light absorbers, Jaramillo *et al* previously deduced that materials with a lifetime > 1 ns in early stage research are worth exploring for photovoltaics.[50] By this metric, by possessing a bulk lifetime of 2.75 ns, CVD-deposited BiOI is identified as a promising photovoltaic material.[1,2] This motivated the fabrication of devices from BiOI, the development and characterisation of which will make up the rest of this chapter.

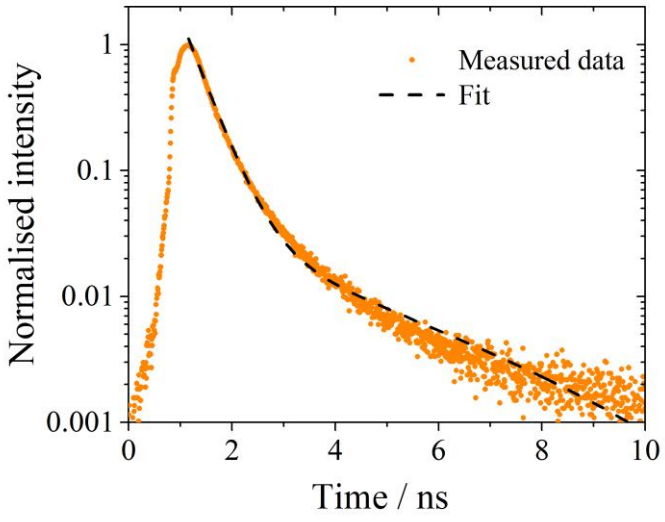

Figure 6.3 TCSPC spectrum of a 1 μm BiOI film on quartz. The sample was excited at 532 nm at a fluence of 400 nJ cm^{-2} and photons were counted between 640 and 700 nm at 0.008 ns intervals. A bi-exponential decay was fit to the data, yielding τ_1 = 0.4 ns and τ_2 = 2.75 ns.

6.3 Development of solid-state bismuth oxyiodide photovoltaic devices

6.3.1 Determination of a suitable substrate for bismuth oxyiodide devices

Good morphology of each component was highlighted in earlier chapters as essential for preventing shunt pathways in devices.[1] Therefore, the morphology of 1 μm BiOI on different charge transport materials was investigated. BiOI was grown onto TiO_2 and ZnO (*n*-type oxides) and NiO_x (*p*-type oxide) before sputter coating with 10 nm Pd to prevent charging during the SEM measurement. SEM and XRD measurements were taken, shown in Figure 6.4.

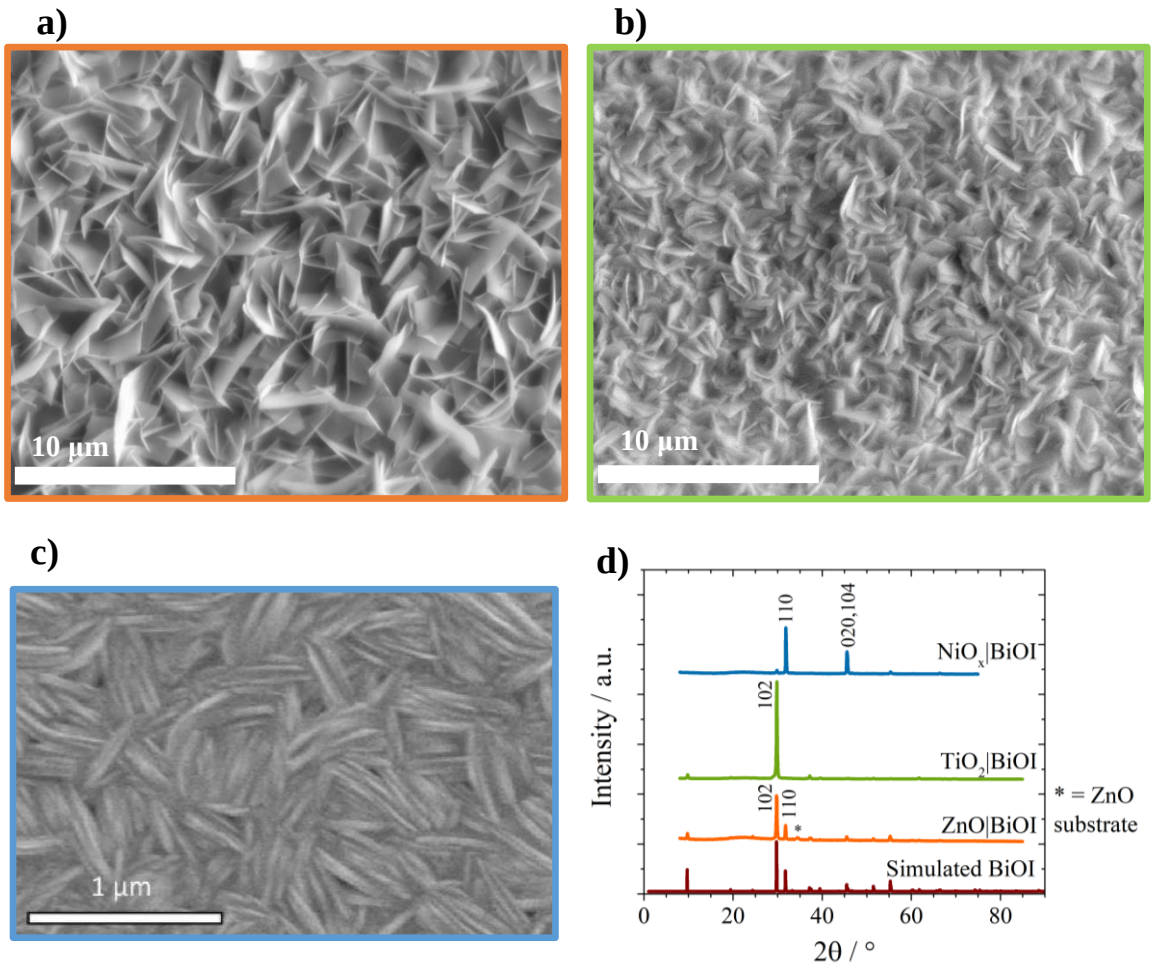

Figure 6.4 SEM images of 1 μm BiOI grown at 360ºC for 2 hours on a) atomspheric pressure CVD ZnO, b) solution process TiO_2 and c) solution processed NiO_x. The scale bars are 10 μm for a) and b) and 1 μm for c). Samples were sputter coated with ~10 nm palladium to prevent charging during measurement. d) shows the simulated BiOI XRD pattern and the measured XRD data for ZnO|BiOI (orange), TiO_2|BiOI (green) and NiO_x|BiOI (blue). The * shows the reflection from the ZnO. Image c) was measured by Tahmida Huq (Device Materials Group, University of Cambridge).

BiOI growth on atmospheric pressure CVD ZnO (Figure 6.4a) gave non-compact coverage, with gaps between platelets. Additionally, platelets appeared to be curved, which may have been due to strain effects. ZnO was deemed a non-suitable substrate for devices due to the non-compact coverage by BiOI. BiOI on TiO_2 (Figure 6.4b) was more compact, with no visible pinholes on the scale of the image. The BiOI was visibly textured, determined to show preferential [102] oriented growth from the XRD data in Figure 6.4d. In section 3.4 it was discussed that *a*- or *b*- axis oriented films would be optimum for transport between the electrodes in a device, as mobility is predicted to be greatest through the covalently bonded backbone of the platelets.[181] Thus, whilst achievement of pinhole-free films was an improvement over deposition on ZnO, the BiOI platelets were still not of optimum orientation for transport in devices. BiOI grown on NiO_x (Figure 6.4c) was compact and textured. Films were determined to be [110] oriented from XRD measurements; the optimum for charge transport through the device.[181] However, it should be noted that this orientation was found to develop with thickness, and thinner films (~ 300 nm) had roughly equal [102] contribution. Figure 6.4 demonstrates that BiOI orientation was substrate dependent. This is likely due differences of the different substrate surfaces, meaning that each interacted differently with the growing BiOI film. This would in turn influence the lowest energy surface for a growing crystal, the pathway *via* which crystal growth is fastest, resulting in different preferred orientations.[193]

Clearly, control of film orientation on any substrate would be ideal as it would allow more device architectures to be accessed. Beyond changing substrate, altering the surface using treatments such as plasma cleaning or chemical treatments, or changing deposition parameters such as pressure may provide routes to control of film orientation. This is beyond the scope of the current work but may be a route to explore in future work.

6.3.2 Bismuth oxyiodide device architecture

A solid-state *p-i-n* device structure inspired by lead halide perovskite devices was chosen to test thermal-CVD grown BiOI in a device; ITO|NiO_x|BiOI|ZnO|Al (Figure 6.5). Regarding ZnO processing, a deposition route which would conformally coat the rough surface of BiOI was needed to inhibit shunting. Therefore, the Vertical Cambridge University Close Proximity AP-SALD reactor, which has previously been used to coat heat-sensitive lead halide perovskites at 60 ºC, was used to coat BiOI.[234] It should be noted that the ZnO deposition occurred by a CVD decomposition-type mechanism under the conditions used.[218] Aluminium was used as the top electrode due to its low work-function, which is well aligned with the conduction band of ZnO for electron extraction.[1,253]

A schematic of the ITO|NiO_x|BiOI|ZnO|Al device and a cross-sectional SEM image of the device stack is shown in Figure 6.5. The cross-sectional SEM shows that the BiOI platelets were continuous through the thickness of the film, with no visible pinholes. This would enable a clear pathway for charge transport throughout the device with minimal shunting pathways. Due to the resolution of the microscope it is difficult to see the ZnO layer (which was 30 – 40 nm), and whether it covered the BiOI conformally.

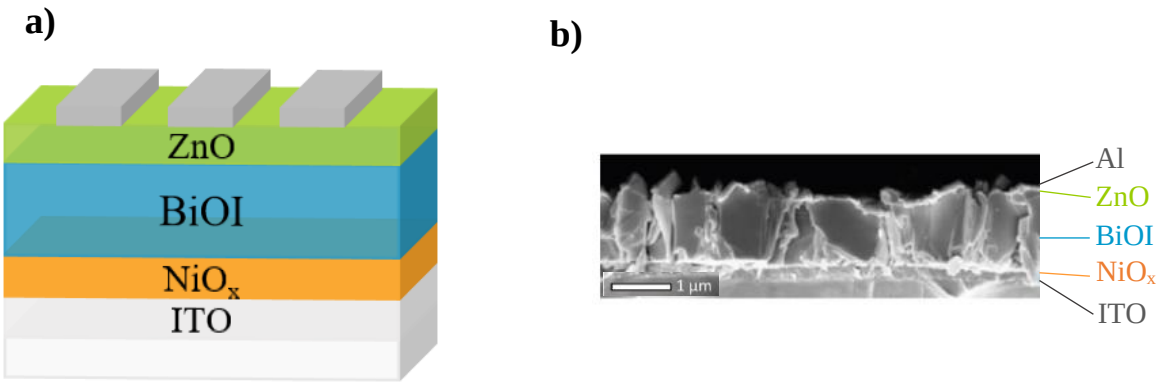

Figure 6.5 a) Schematic and **b)** cross-sectional SEM image of an ITO|NiO_x|BiOI|ZnO|Al device stack, with scale bar 1 µm. The device was measured with illumination from the glass side.

6.3.3 Bismuth oxyiodide device performance

6.3.3.1 Influence of BiOI thickness on device performance

NiO_x was fabricated by a solution processing method optimised for perovskite devices. For the ZnO layer, the optimum thickness was determined to be 40 nm; beyond this a contact barrier existed causing a kink in the *J-V* curve near the V_{OC}. This was deposited at 80 ºC to minimise damage to the BiOI layer.

First, the influence of BiOI film thickness on performance was investigated. BiOI films were deposited for between 15 and 120 minutes onto ITO|NiO_x substrates, as this substrate was to be used for devices. Example cross-sectional SEM images after 30, 60 and 120 minutes are shown in Figure 6.6. The film thickness after each deposition time was measured by taking 12 measurements from the base to the surface of the film from cross-sectional SEM images using imageJ software. The average thickness after each deposition time is shown in Table 6.1.

Table 6.1 Film thickness of BiOI deposited at 360ºC on ITO|NiO_x for different deposition times. Film thickness was determined from cross-sectional SEM images. Values are given as the average ± standard deviation of 12 measurements.

Deposition time / min	BiOI thickness / nm
15	450 ± 30
30	550 ± 60
50	710 ± 70
60	980 ± 70
90	1160 ± 80
120	1630 ± 70

Linear regression analysis of the thickness as a function of deposition time was carried out using R software, to determine whether there was a strong correlation between the two parameters. A linear fit was obtained, which gave the relationship:

$$d = (10.8 \pm 0.7)t + (268.9 \pm 39.1)$$

where *d* was the film thickness (nm) and *t* was the deposition time (min). The R-squared value describes the fraction of the variation in the dependent variable (thickness) which can be explained by the variation in the independent variable (time).[254] An R-squared value of 0.98 was calculated for the data in Table 6.1, meaning that 98 % of the variation in BiOI thickness was due to the deposition time changing; thus the two were strongly related. Note that the regression line

did not pass through the origin. This may have been caused by precursor depletion over time, causing the growth rate to reduce towards longer deposition times, which could be avoided by feeding BiI_3 into the furnace from an external source rather than subliming it within the furnace tube.

From the SEM images in Figure 6.6, as well as an increase in film thickness, the grain structure was seen to develop over time. For a 30-minute deposition time (Figure 6.6a) the grains were small and randomly oriented. After 60 minutes (Figure 6.6b), whilst some random orientation was maintained at the base of the films, the grains became more columnar, consisting of columns throughout the film thickness, whilst also having grown in the lateral direction. After 120 minutes (Figure 6.6c), the surface texturing and individual grains were less clearly defined, possibly due to further merging of grains over time.

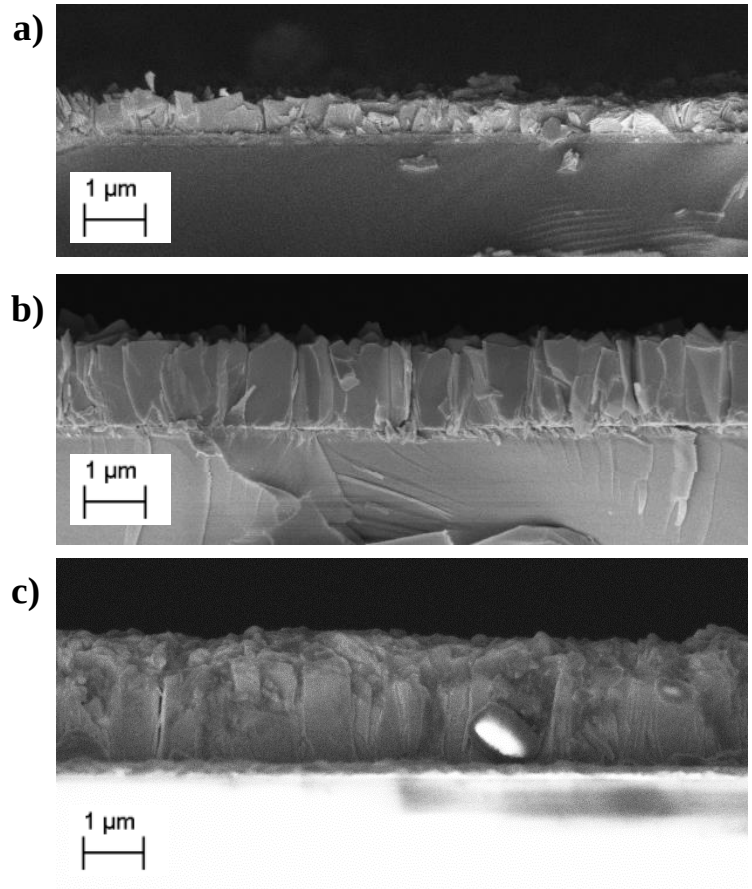

Figure 6.6 Cross sectional SEM images for BiOI grown on ITO|NiO_x for **a)** 30 minutes (550 ± 60 nm), **b)** 60 minutes (980 ± 70 nm) and **c)** 120 minutes (1630 ± 70 nm). The scale bar is 1 µm for all images.

The *J-V* and EQE response of the devices fabricated using BiOI deposition times of 15 to 120 minutes were measured. An example *J-V* curve is shown in Figure 6.7a. This had good matching between the forward and reverse scans, meaning that the devices showed negligible hysteresis.[2] The average device performance metrics for each thickness are listed in Table 6.2.

Table 6.2 The J_{SC}, V_{OC}, FF and PCE of ITO|NiO_x|BiOI|ZnO|Al devices for a range of BiOI film thicknesses. Values show the average ± standard deviation.

Thickness / nm	J_{SC} / mA cm^{-2}	V_{OC} / V	FF / %	PCE / %
450 ± 30	-5.47 ± 0.43	0.67 ± 0.04	34.6 ± 2.2	1.27 ± 0.17
550 ± 60	-5.46 ± 0.29	0.65 ± 0.00	33.7 ± 1.0	1.20 ± 0.10
710 ± 70	-6.04 ± 0.29	0.75 ± 0.00	31.0 ± 2.5	1.41 ± 0.22
980 ± 70	-5.66 ± 1.17	0.64 ± 0.02	35.5 ± 2.3	1.29 ± 0.20
1160 ± 80	-3.94	-	29.3	-
1630 ± 70	-0.42 ± 0.13	0.74 ± 0.05	23.6 ± 1.5	0.07 ± 0.02

The fill factor generally decreased with increasing BiOI thickness, likely due to an increase in resistance through the device. The V_{OC} value remained relatively constant. Note that the very small standard deviation in values was due to the reasonably large step in voltage in the measurements (0.05 V). The J_{SC} increased up to a BiOI thickness of 710 ± 70 nm, before dropping. The best PCE was also achieved at this thickness, with an average efficiency of 1.41 ± 0.22 % and a champion PCE of 1.68 %.

The origin of the trend in J_{SC} could be studied further through external quantum efficiency measurements. For EQE measurements, devices were illuminated from the ITO side of ITO|NiOx|BiOI|ZnO|Al devices. The EQE curves at different BiOI thicknesses are shown in Figure 6.7b. The EQE onset started at ~ 620 nm (2.0 eV) for all devices, matching well with the bandgap of BiOI. The onset of EQE was slow due to the indirect band-gap of BiOI, in agreement with optical data meaning that several microns of material would be required to absorb all incident light just above the band-gap (Figure 6.2b). A peak EQE of 80% was achieved for 450 nm films at λ = 450 nm; this is the maximum recorded for any Bi-based light absorber compound,[1,2] and close to the EQEs achieved for $MAPbI_3$ devices (~ 90%).[99] Such a high EQE may have resulted from the layered crystal structure of BiOI discussed in section 3.4, proposed to enable good charge separation due to the presence of an in-built electric field along the *c*-axis.[180] However, $MAPbI_3$ tends to have squarer EQEs, *i.e.* better charge collection across the whole absorbing region;[99] reasons for the non-square shape for BiOI will be discussed in the following. As the BiOI

thickness increased, the peak EQE (%) decreased and shifted to longer wavelengths. This meant that as the film thickness increased, fewer high energy photons were converted into current effectively. As mentioned, the devices were illuminated from the ITO side of ITO|NiO_x|BiOI|ZnO|Al, thus short wavelength photons would be absorbed within ~100 nm of the NiO_x|BiOI interface (Figure 6.2b). As the BiOI thickness increased, electrons in the conduction band would have further to diffuse to the BiOI|ZnO interface, making them more likely to recombine with holes in the valence band as this distance increased.[2] Thus, the electrons generated by short wavelength photons would be less likely to contribute to the current as the thickness increased, accounting for the reduced EQE at short wavelengths in Figure 6.7b. As the J_{SC} is equal to the EQE integrated over the solar spectrum, the data suggests that J_{SC} is limited by the carrier diffusion length of BiOI.[2] Improvements in device performance can therefore be achieved by increasing this length *via* a reduction in the density of defect states, which act as sites for recombination. Depositing films at a higher homologous temperature may be one route to achieving this and will be discussed in chapter 7.

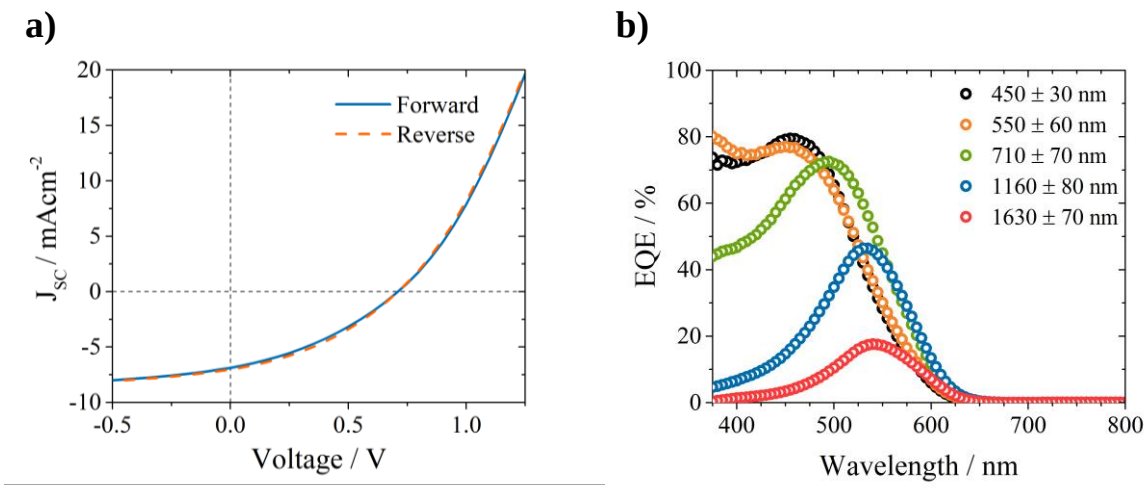

Figure 6.7 a) An example *J-V* curve for an ITO|NiO_x|BiOI|ZnO|Al device and **b)** the external quantum efficiency against wavelength for ITO|NiO_x|BiOI|ZnO|Al devices, where the BiOI thickness was 450 to 1630 nm.

6.3.3.2 *Influence of zinc oxide deposition temperature on device performance*

Further device optimisation was achieved by fabricating devices with ZnO deposited at 80, 100 and 120 ºC.[2] Box plots for the PCE and FF are shown in Figure 6.8. The BiOI thickness was 710 ± 70 nm. From Figure 6.8a there was no obvious trend between performance and ZnO deposition temperature. However, the highest efficiency was achieved for ZnO deposited at 80ºC, at 1.82%. This gave the best efficiency for any BiOI solar cell to date.[1,2] Additionally, there was less spread in data for the devices with 80ºC ZnO, making these devices more reliable. Whilst there was little difference in J_{SC} and V_{OC} of the devices, from Figure 6.8b the fill factor followed a similar trend to the PCE. Thus, the decrease in efficiency when ZnO was deposited above 80ºC may have been due to heat damage of the BiOI, causing an increase in series resistance in devices.

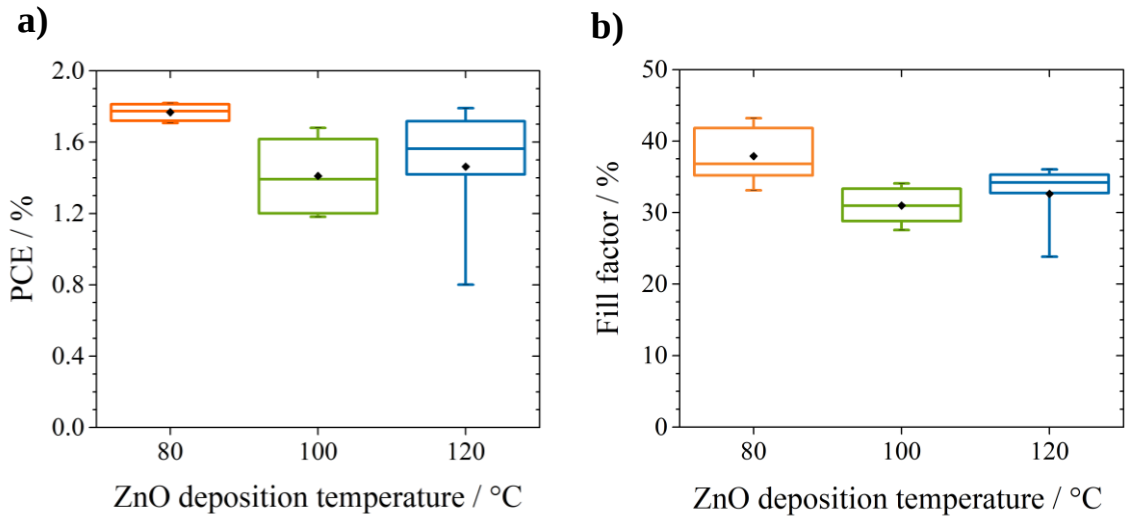

Figure 6.8 Box plots of **a)** the power conversion efficiency and **b)** the fill factor of ITO|NiO_x|BiOI|ZnO|Al devices, where ZnO was deposited by AP-CVD at 80, 100 and 120ºC. The whiskers represent the 5th and 95th percentile and the black diamond represents the mean.

6.3.3.3 *Light intensity dependent JV measurements of bismuth oxyiodide devices*

The current-voltage response of the champion device (BiOI thickness 710 ± 70 nm) was measured under varying light intensity. The J_{SC} and V_{OC} are plotted as a function of light intensity in Figure 6.9. The J_{SC} increased linearly with light intensity. This is as expected; an increase in the number of photons incident on the device means that more electron-hole pairs can be photogenerated and thus converted into current.[2] The V_{OC} also increased linearly with light intensity. A greater number of electrons and holes are expected to be in the conduction and valence bands respectively with under higher light intensity.[13] This would cause higher quasi-Fermi level splitting as the light intensity increases, thus an increased photovoltage.[2,13,255] A plot of V_{OC} against *ln*(light intensity) was used to determine the ideality factor of the device.[46] From the gradient and equation **2.9**, an ideality factor of 1.93 was calculated. As a value close to 2, this implies that SRH recombination was dominant in devices,[45] as would be expected for an indirect semiconductor. Reducing the density of defect states may be a route to reducing this number.

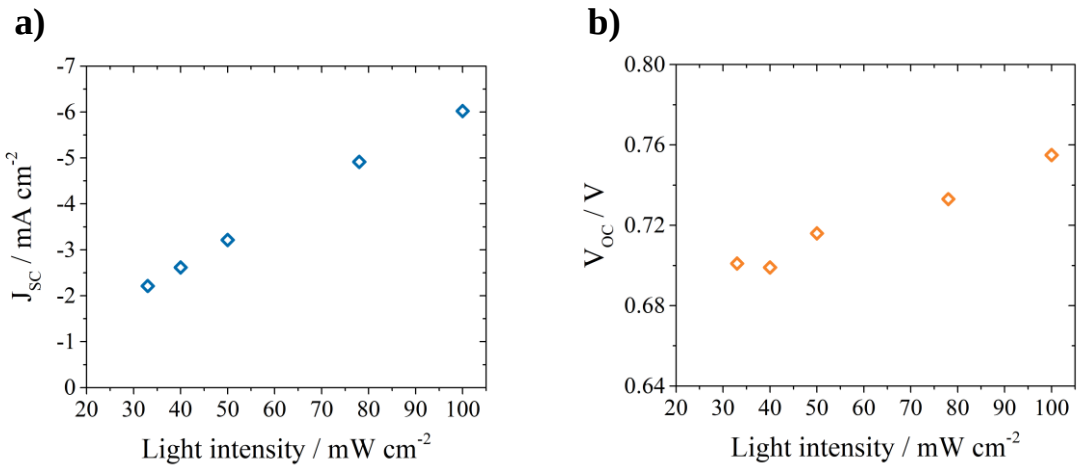

Figure 6.9 a) short-circuit current density and **b)** open-circuit voltage as a function of light intensity for an ITO|NiO_x|BiOI|ZnO|Al device with a BiOI thickness of 710 ± 70 nm.

6.3.4 Investigating the stability of bismuth oxyiodide

A major drawback of the lead halide perovskites is their limited stability, which has raised questions over their suitability for large scale application. Therefore, it was important to determine the stability of BiOI. Due to difficulty fabricating devices from many of the Bi-based compounds recently studied for photovoltaics, researchers often report the phase stability of a thin film or single crystal over time after storage under different conditions as an indicator of stability.[1,52,166,169] Figure 6.10a shows the XRD pattern of 1 μm BiOI grown on solution processed NiO_x on the day of growth (day 1) and after 170 days storage in air in the dark at 1 % relative humidity (RH). In Figure 6.10b, glass|BiOI samples were measured by XRD on the day of growth and after 44- and 197-days storage in air under ambient illumination at 40 – 67 % RH. For the latter, a glass substrate was used as the film was fabricated before substrate optimisation (leading to the use of NiO_x coated substrates) was carried out. Both sets of samples were stored at room temperature.

Samples stored in the dark at 1 % relative humidity retained their phase purity after 170 days. Phase purity was also retained for samples stored under illumination in humid air after 197 days.[2] In a similar experiment performed on $MAPbI_3$ and methylammoniumbismuth iodide films, formation of PbI_2 in $MAPbI_3$ films stored under illumination in humid air was visible after 5 days, whilst BiOI and Bi_2O_3 were present in methylammoniumbismuth iodide films after 25 days.[52] Additionally, after 60 days storage under 30 – 50 % relative humidity under ambient illumination, $Cs_2AgBiBr_6$ single crystals contained the degradation product $CsAgBr_6$.[169] Thus, BiOI showed a 20- fold stability improvement over $MAPbI_3$, and an 8- and 3- fold improvement over the alternative Bi-based solar absorber materials methylammoniumbismuth iodide and $Cs_2AgBiBr_6$.

For a comparison of device stability with $MAPbI_3$, ITO|NiO_x|BiOI|ZnO|Al and ITO|NiO_x|$MAPbI_3$|PCBM|Al devices were fabricated. Figure 6.10c shows the change in efficiency of BiOI and $MAPbI_3$ devices under 1 full sun constant illumination for 30 minutes. The BiOI device showed an initial drop in efficiency in the first 2 minutes of measurement, after which the efficiency stabilised at 85 % of its initial value for the entirety of the measurement. Conversely, the $MAPbI_3$ device initially improved in performance in the first 3 minutes, before gradually decreasing to 62 % of its initial performance after 30 minutes under illumination. Hence BiOI devices were more stable than $MAPbI_3$ within the period measured.[2] The superior stability of BiOI devices under constant illumination is important for in-the-field applications, where solar panels are under constant illumination (particularly in climates with little cloud coverage). The devices also showed superior stability over previously reported BiOI devices. In photoelectrochemical cells with an $NaSO_4$ electrolyte, devices degraded after only 100 s of testing.[180] The improved stability of the solid-state devices was likely due to the absence of a corrosive liquid electrolyte.

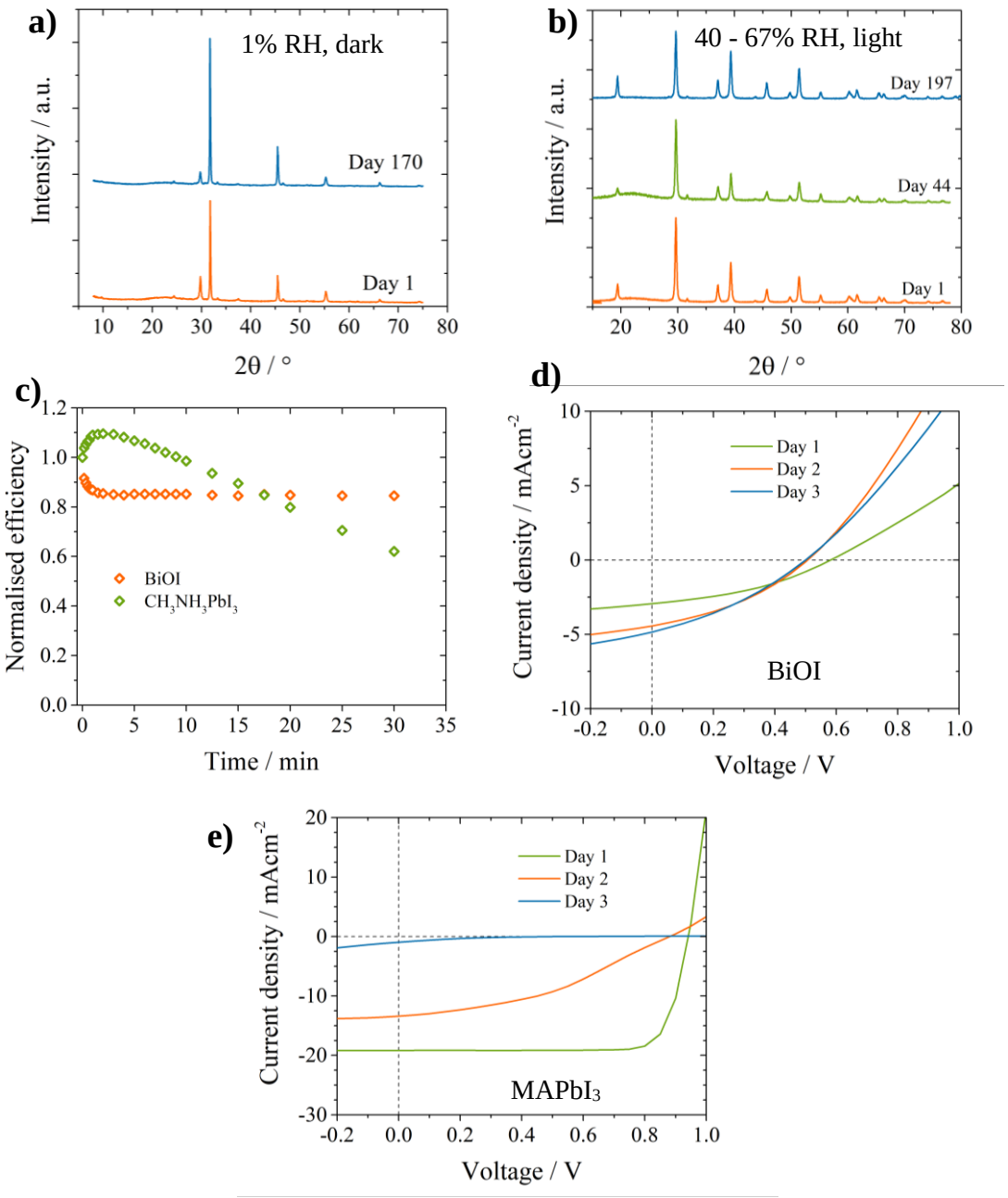

Figure 6.10 XRD patterns of a) NiO_x|BiOI on the day of growth (day 1) and after 170 days storage in the dark at 1% relative humidity and b) glass|BiOI on the day of growth (day 1) and after 44- and 197- days storage under laboratory illumination at 40-67 % relative humidity. Figure c) shows the normalised efficiency of an ITO|NiO_x|BiOI|ZnO|Al device (orange diamonds) and an ITO|NiO_x|$MAPbI_3$|PCBM|Al device (green diamonds) measured under constant illumination (1 full sun) for 30 minutes. The JV curves for d) ITO|NiO_x|BiOI|ZnO|Al and e) ITO|NiO_x|$MAPbI_3$|PCBM|Al devices taken daily after storage in air under laboratory illumination for 3 days. XRD data in part b) was measured by Dr Robert Hoye.

Device performance was also measured after storage in air for 3 days at 60% relative humidity. JV curves were taken at daily intervals for ITO|NiO_x|BiOI|ZnO|Al and ITO|NiO_x|$MAPbI_3$|PCBM|Al, shown in Figure 6.10d and e. The efficiency of the BiOI device initially improved from 0.64% to 0.81% between day 1 and 2, after which the efficiency remained relatively constant at 0.79% on day 3. Conversely, the $MAPbI_3$ device degraded rapidly, dropping from 14.7% to 4.7% by day 2, and having completely degraded by day 3. The rapid degradation of the $MAPbI_3$ device is likely due to the humid conditions, as $MAPbI_3$ is known to readily degrade to PbI_2 in the presence of water.[2,256] This data, along with the XRD data in Figure 6.10a and b, suggests that BiOI shows greater stability to humid conditions than $MAPbI_3$.[2] Additionally, the use of metal oxide charge transport materials is likely to have protected BiOI devices from water ingress.[113]

6.4 Summary of section

In this chapter, the potential of BiOI as a photovoltaic material was investigated. Thermal CVD BiOI deposited at 360 ºC and atmospheric pressure was large grained and had sharp XRD peaks. TCSPC measurements recorded a minority carrier lifetime of 2.75 ns, highlighting it as worth further investigation for PV applications. Despite sub-optimal morphology on ZnO and TiO_2, highly [110]- oriented films were grown on NiO_x, deemed optimal for charge transport in devices. As such, ITO|NiO_x|BiOI|ZnO|Al devices achieved the best efficiency to date (1.8 %) for BiOI and the highest EQE (80 % at λ = 450 nm) for a bismuth-based photovoltaic material. Additionally, devices were up to 20 times more stable than methylammonium lead iodide analogues, with BiOI retaining phase purity after 197 days storage in light, humid conditions. Despite these advances, EQEs were found to be limited at short wavelengths by the carrier transport properties, whilst SRH recombination was found to be significant in device. To address this, the influence of homologous growth temperature on the properties of BiOI will be investigated in the following chapter.

7 Investigating the influence of growth temperature on the properties of bismuth oxyiodide

From structure-zone models, growth or annealing of a thin film at a higher fraction of the material's melting point can cause improvements to the grain structure. In this section, an investigation of the influence of homologous growth temperature on the properties of BiOI is presented. By altering the percentage of oxygen in the CVD furnace, growth of phase pure BiOI was achieved up to 450 ºC in a 1 % oxygen atmosphere. BiOI grown at 400 ºC and higher contained larger crystallites than at 350 ºC, whilst platelet thickening was apparent. Additionally, BiOI retained its phase purity despite up to 30 % iodine loss in the high temperature range, whilst iodine vacancies did not dope the films or introduce defect states at the band edge, supporting theoretical calculations which suggest that BiOI is tolerant to iodine vacancies.

7.1 Optimisation of bismuth oxyiodide growth at a range of homologous temperatures

Improvements in the structural properties of a thin film can be achieved by growing or annealing at a higher fraction of its melting point. Regarding annealing, whilst the melting point, T_m, of BiOI is 827 ºC (1100 K),[257] it starts to decompose at 210 ºC.[258] As a result (from equation **4.16**) annealing experiments are limited to a maximum homologous temperature, T_h, of 0.44. At this T_h, grain mobility is typically low, resulting in V-shaped grains throughout the thickness of the film as described in chapter 4.[193,195,198] Thus, annealing of as grown BiOI to study the influence of T_h on grain structure was deemed unsuitable, and to access a higher range of homologous growth temperatures deposition parameters for growth of BiOI above 350 ºC needed to be established. The deposition temperatures used for work in this chapter and the corresponding homologous temperature are listed in Table 7.1.

Table 7.1 Deposition temperatures investigated in this chapter and the corresponding homologous growth temperature (T/T_m, where T is deposition temperature and T_m is the melting point of BiOI, 1100 K).

Deposition temperature / ºC	Homologous growth temperature (T/T_m)
325	0.54
350	0.57
400	0.61
450	0.66
500	0.70

In their study on the chemical vapour of bismuth oxides under vacuum, Schuisky and Hårsta identified that as well as BiOI, multiple $Bi_xO_yI_z$ phases are stable in the BiI_3-O_2 system, with x, y and z dependent on temperature and oxygen partial pressure.[179] Calculated phase diagrams generated by collaborators at NREL also predict BiOI, BiI_3, $Bi_4I_2O_5$ to be thermodynamically stable where Bi, O and I are considered as reactants.[2] Therefore, it was necessary to find the parameter space for the growth of phase pure BiOI within the BiI_3-O_2 system at atmospheric pressure. Films were grown onto NiO_x coated glass from BiI_3 and O_2 at 325 – 500 ºC. At each deposition temperature, the percentage of oxygen was varied by changing the ratio of O_2 and Ar flow through the furnace, according to the conditions in section 6.1. The percentage of oxygen was given as $F_{O2}/(F_{O2}+F_{Ar})$, where F_x is the flow rate of gas *x* through the furnace. Again, solution processed NiO_x coated substrates were used as these were determined to be the most suitable for good BiOI coverage. The phase(s) of the films grown was determined using XRD, allowing the experimental phase diagram in Figure 7.1 to be generated.

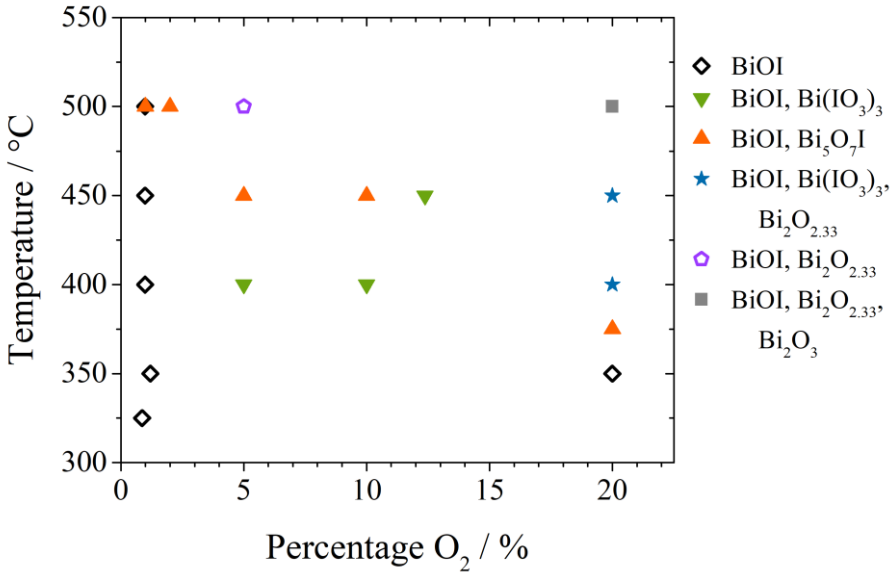

Figure 7.1 The experimental phase diagram for chemical vapour deposition of the BiI_3-O_2 system at atmospheric pressure, generated by depositing films from BiI_3 and O_2 on glass|NiO_x between 300 – 500 ºC with the composition of gas through the furnace tube varying from 0 – 20 % oxygen. The phases were identified by XRD, using Powder Diffraction Files (PDF) for BiOI (00-010-0445), monoclinic Bi_5O_7I (00-038-0669), $Bi(IO_3)_3$ (00-058-0583), $Bi_2O_{2.33}$ (00-027-0051), *β*-Bi_2O_3 (00-001-0709). The percentage of oxygen was determined from $F_{O2}/(F_{O2}+F_{Ar})$, where F_x is the flow rate of gas *x* through the furnace.

As the percentage of oxygen increased, the temperature where phase pure BiOI deposited decreased. Conversely, BiOI could be grown at higher temperatures by reducing the percentage of oxygen through the furnace. Hence, at approximately 1 % O_2, films were phase pure BiOI from 325 – 450 ºC. When oxygen partial pressure was kept constant, increasing the temperature resulted in Bi- and O- rich and I- poor phases. These iodine deficient phases of Bi_5O_7I, BiO_9I_3, $Bi_2O_{2.33}$ and Bi_2O_3 have been previously identified in the BiI_3-O_2 system.[179]

$Bi_4I_2O_5$, predicted to be thermodynamically stable by collaborators at NREL, was not seen experimentally, whilst BiOI was predicted to be stable over only a small range of chemical potentials of Bi, I and O in Figure 3.6.[2] However, in this experiment, BiI_3 partial pressure increased by several orders of magnitude between 325 and 450 °C,[259] yet BiOI remained phase pure with 1 % O_2. University of Uppsala researchers similarly deposited BiOI at temperatures higher than which it was thermodynamically predicted to be stable.[179] The possible reason for this will be discussed in the next section.

The XRD data for films deposited at 1 % oxygen between 325 – 500 ºC on glass|solution processed NiO_x substrates is shown in Figure 7.2. There was a good match between the patterns from 325 – 450 ºC, where films were determined as phase pure BiOI. At 500 ºC, a broad shoulder on the [102] peak appeared at 2θ = 29 º (Figure 7.2b). The broadening may have been due to a small amount of Bi_5O_7I, which has a [113] peak centred at 2θ = 29.5 º, whilst the [102] peak for BiOI is at 29.7 º.[183,260] As BiOI deposited using 1 % O_2 was phase stable up to 450 ºC, these conditions were used for all work in this chapter, whilst those deposited at 500 ºC were also measured to study the effect of phase impurity on properties.

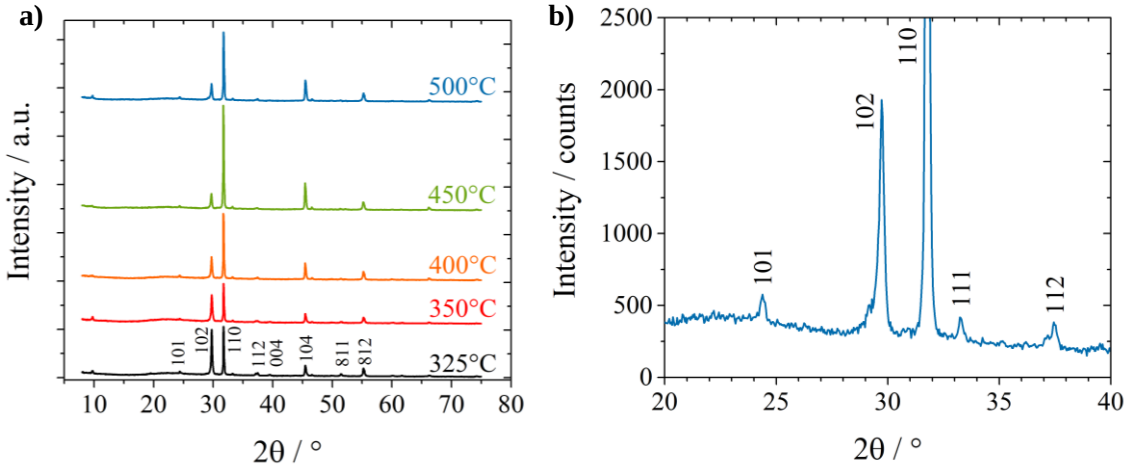

Figure 7.2 a) XRD patterns of ITO|NiO_x|BiOI samples grown by chemical vapour deposition from BiI_3 and O_2 at 325 – 500 ºC and b) the XRD pattern between 2θ = 20 – 40 º for an ITO|NiO_x|BiOI sample grown at 500 ºC. The broadening to the left of the [102] peak has been identified as due to monoclinic-Bi_5O_7I (PDF number 00-038-0669).

7.1.1 Determination of the growth regime for thermal chemical vapour deposition bismuth oxyiodide

The growth rate of BiOI at 325 – 500 ºC was estimated by determining the time required to grow a ~700 nm film on glass|solution processed NiO_x at each temperature. The average of 5 thickness measurements on two films was taken for each sample. A plot of the growth rate against temperature is shown in Figure 7.3. The inset shows the natural logarithm of the growth rate against the inverse of temperature (K).

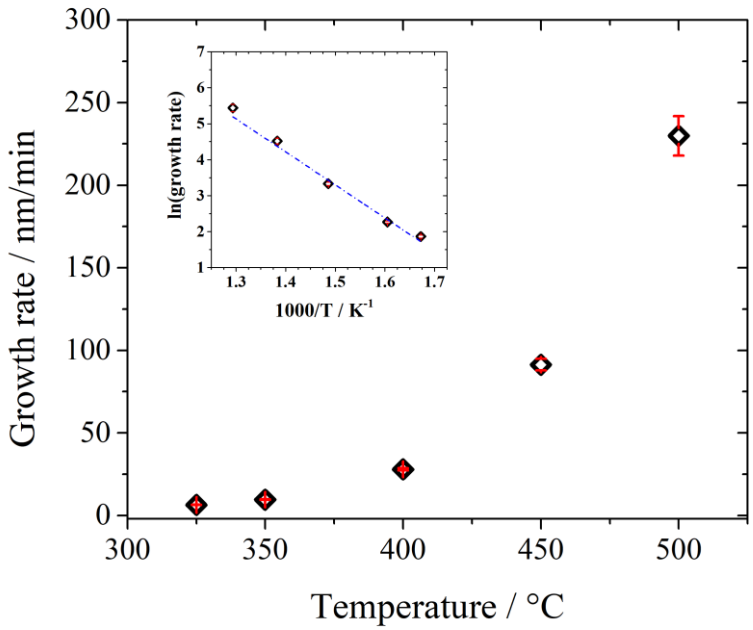

Figure 7.3 Plot of the growth rate against temperature for chemical vapour deposition of BiOI on glass|NiO_x substrates. The error bars represent twice the standard error. The inset Arrhenius plot shows the natural logarithm of the growth rate against the inverse of the temperature in Kelvin.

Figure 7.3 shows a strong exponential dependence of the growth rate on temperature, indicating that growth was limited by reactions kinetics, *i.e.* growth occurred in the kinetic regime.[201] This may explain why BiOI was phase pure over a larger range of temperatures and precursor partial pressures than expected; the simulated phase diagram, Figure 3.6 was calculated based on thermodynamic principles, whilst formation of BiOI may be kinetically favoured. Similarly, $Bi_4I_2O_5$ may not have formed because reaction is too slow, despite being a thermodynamically favoured phase.

From the gradient of *ln*(growth rate) against the inverse of temperature (inset Figure 7.3) an estimated activation energy of -80.0 ± 4.05 kJ/mol for the reaction was determined. This is

typical for a CVD reaction in the kinetic regime. However, it must be noted that this value is only an estimate as the partial pressure of BiI_3 also changes with temperature.[201,259]

7.2 Influence of deposition temperature on the physical properties of bismuth oxyiodide thin films

7.2.1 Influence of deposition temperature on the structural properties of bismuth oxyiodide thin films

For XRD studies, 700 nm BiOI films were grown on glass. θ-2θ scans were measured, and the line profile of the diffraction patterns were fitted to determine the full width at half maximum (FWHM) of each peak. FWHM against temperature was plotted for the prominent peaks ([001], [002], [102] and [013]), Figure 7.4a. The particle size was estimated from each peak using the Scherrer equation and is shown as a function of temperature in Figure 7.4b.

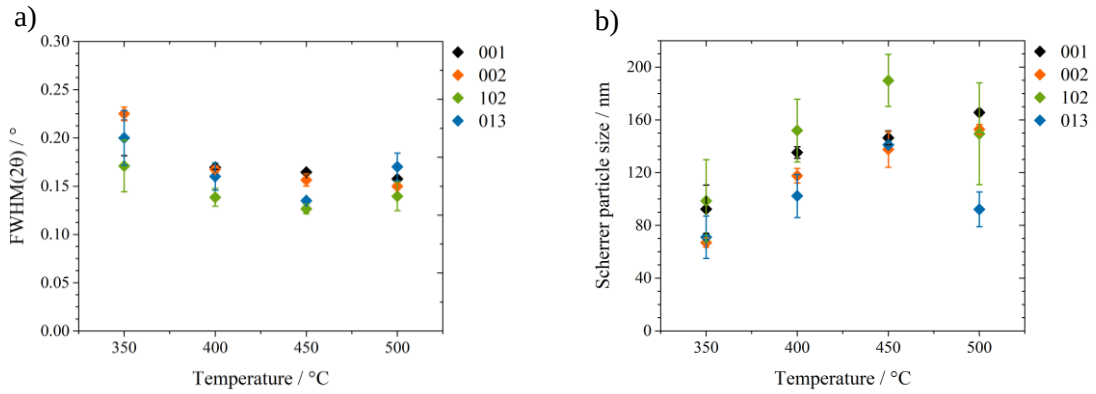

Figure 7.4 a) FWHM and b) the estimated particle size calculated from the Scherrer equation for the [001] (black), [002] (orange), [102] (green) and [013] (blue) X-ray diffraction peaks of BiOI deposited on glass as a function of deposition temperature.

A smaller FWHM for a peak in XRD indicates an increase in grain size or a reduction in the density of structural defects within a film. The FWHM of all peaks was largest for films at 350 ºC. The FWHM decreased beyond 350 ºC, but there was no obvious trend from 400 – 500 ºC. This was reflected in Figure 7.4b; the estimated particle size was smallest for the films deposited at 350 ºC (at 60 – 100 nm) and increased as the temperature increased (100 – 190 nm). Whilst the particle size estimated from the [001] and [002] peaks increased linearly with temperature, those estimated from the [102] and [013] peaks increased until 450 ºC, before decreasing at 500 ºC. The decrease in FWHM and associated increase in Scherrer particle size above 350 ºC indicates better lattice ordering at higher temperatures. This result is in accordance with structure zone theory; at higher temperature, growing species have more surface mobility which results in the growth of larger grains with fewer structural defects.[193,194] Note that for these studies, BiOI was deposited

on glass. In future it would be ideal to repeat the same study using NiO_x coated substrates, for more confidence in the direct comparison with all other analyses in which BiOI was deposited onto NiO_x coated glass. This also provides the advantage of improved surface coverage relative to deposition on glass.

SEM images of 700 nm BiOI films deposited at 350 – 500 ºC on glass|NiO_x substrates are shown in Figure 7.5. At all deposition temperatures, the BiOI platelets were similar in length, at 0.5 – 1 μm, whilst the thickness of the particles appeared to change with deposition temperature. ImageJ software was used to measure the thickness of 20 random particles for each image, for which the average thickness is quoted in Table 7.2.

Table 7.2 The average thickness ± the standard deviation for BiOI platelets deposited between 350 and 500 ºC. Platelet thickness was determined from SEM images using imageJ software to measure the thickness of 20 random particles for each image.

Deposition temperature / ºC	Average platelet thickness / nm
350	52.4 ± 13.4
400	62.8 ± 24.6
450	99.4 ± 32.6
500	78.6 ± 23.6

The average thickness of the platelets increased from 52.4 to 99.4 nm between 350 and 450 ºC, before dropping to 78.6 nm at 500 ºC. As well as having the greatest thickness of the series, the platelets were most densely packed at 450 ºC. Denser platelet packing is desirable for devices, as this enables fewer shunt pathways, whilst a larger platelet thickness (and thus particle volume) results in a relatively lower density of trap states due to species such as dangling bonds on the surface of the particles.

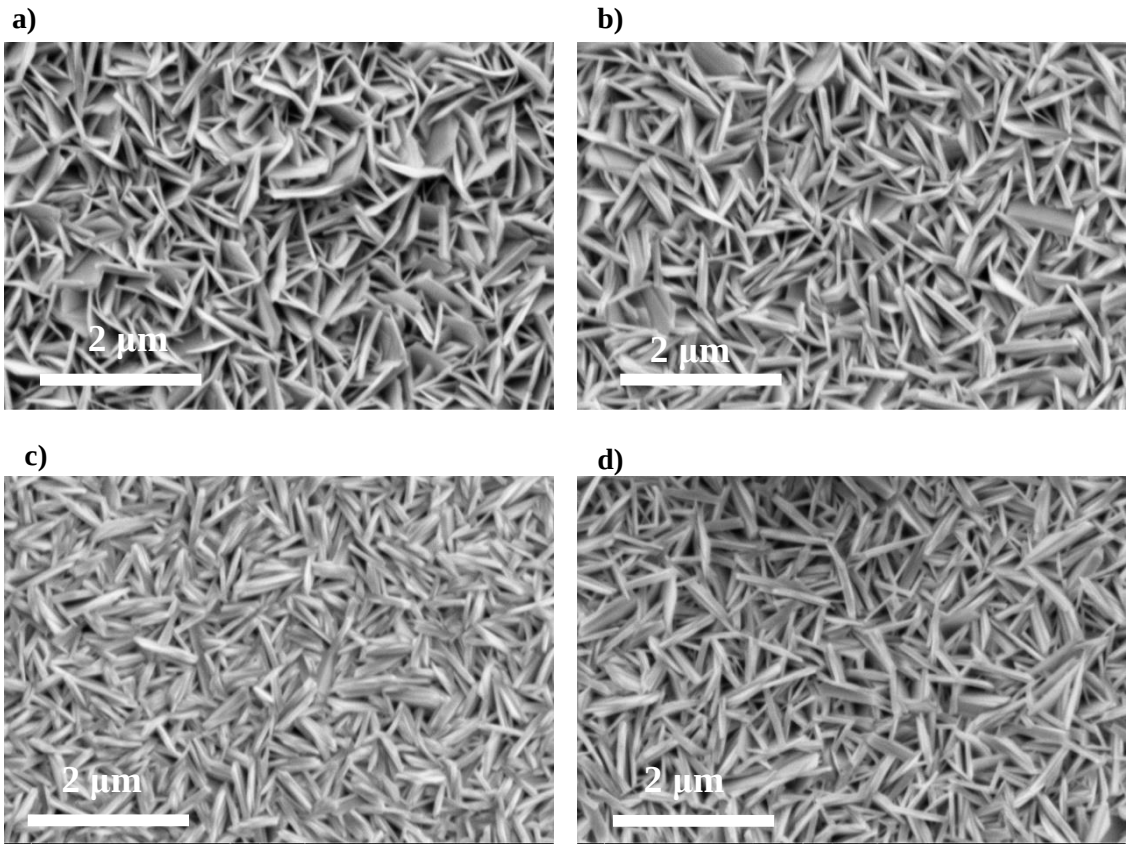

Figure 7.5 SEM images of 700 nm thick BiOI films on glass|ITO|NiO_x substrates, deposited at a) 350°C, b) 400°C, c) 450°C and d) 500°C. The scale bar for all images is 2 µm.

Figure 7.6 shows SEM images of the same samples taken with a lower magnification. Whilst BiOI deposited at 350 ºC had no surface particulates, an onset of particle formation on the film surface at 400 ºC was visible. The surface particle size and density increased with temperature, with the average particle width 1.27 ± 0.16 µm at 400 ºC, 1.95 ± 0.67 µm at 450 ºC and 4.21 ± 1.72 µm at 500 ºC. As discussed in section 4.2, particle formation can occur in thermal CVD due to gas phase reactions at temperatures above the decomposition temperature of reaction intermediates.[200,203] As for CVD BiOI the density and size of the particles increased with temperature, this was likely the cause of the particle formation. The surface particles would likely have negative implications on devices due to difficulty conformally coating them with ZnO, introducing shunt pathways into the device. In future, deposition in a cold wall reactor (where only the substrate rather than the full chamber is heated), or deposition at low pressures such that the precursors are less likely to meet in the gas phase could be used to prevent gas phase reactions.[200,203,204]

Despite the formation of surface particulates, investigation of the bulk properties of the film was still deemed appropriate for the remainder of the chapter.

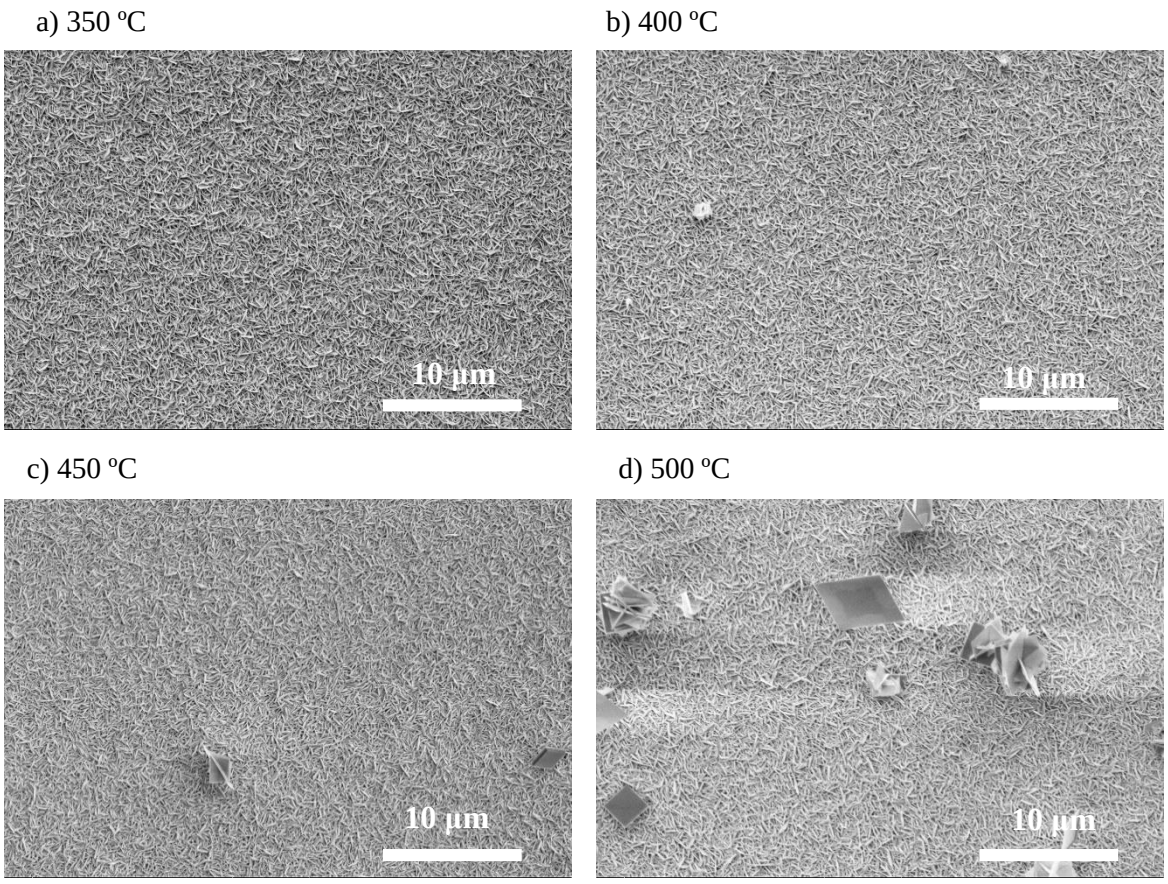

Figure 7.6 SEM images of 700 nm BiOI films deposited on ITO|NiO_x at a) 350 °C, b) 400 °C, c) 450 °C and d) 500 °C. The scale bar for all images is 10 µm.

7.2.2 Influence of deposition temperature on the composition of bismuth oxyiodide thin films

X-ray photoelectron spectroscopy (XPS) was used to determine the composition of 700 nm BiOI deposited on ITO|NiO_x at 325 – 500 ºC. NiO_x coated ITO was used as the substrate to provide a conductive contact to the ground of the XPS chamber, so that charging of the sample did not occur during the measurement. Example Bi 4*f*, O 1*s* and I 3*d* core level spectra are shown in Figure 7.7. Using CasaXPS software, a Shirley background was applied to the peaks to account for the asymmetry of the background. The Bi 4*f*, O 1*s* and I 3*d* spectra were then fitted with mixed Lorentzian/Gaussian functions to yield areas A_x (where *x* is the element which the atomic orbital belongs to). This area was scaled using the relative sensitivity factor, RSF, of the corresponding atomic orbital considering an Al X-ray source (which are listed in the Methods and Materials section):

$$a_x = \frac{A_x}{RSF} \qquad \textbf{(7.28)}$$

Where a_x is the scaled area for the atomic orbital of element *x*. The fraction of each element in the film was then taken as:

$$f_x = \frac{a_x}{a_x + a_{x'} + a_{x''}} \qquad \textbf{(7.29)}$$

where *x, x'* and *x''* are the elements in the film (*i.e.* Bi, O and I).

The fraction of each element in BiOI deposited at 325 – 500 ºC was determined, and is plotted against temperature in Figure 7.8. For stoichiometric BiOI, the expected Bi:O:I content would be 0.33:0.33:0.33. Therefore, films were non-stoichiometric at all temperatures. At 325 ºC and 350 ºC, the composition of the films was relatively constant, at ~30 % oxygen, 32 % iodine and 38 % bismuth. Beyond 350 ºC, the iodine content decreased down to 20 % at 500 ºC, whilst the oxygen and bismuth content increased to 39 and 41 % respectively. The non-stoichiometry of films at 325 ºC and 350 ºC suggests that growth conditions were bismuth rich and iodine poor. The significant loss of iodine as deposition temperature increases was likely due to the volatility of iodine, which readily forms molecular iodine rather than incorporating into the lattice. Despite this significant iodine loss, the films retained their phase purity up to 450 ºC as demonstrated by the XRD data in Figure 7.2. This implies that at temperatures above 350 ºC, BiOI with a high density of iodine vacancies, rather than a different phase, was formed.

To determine whether the formation of iodine vacancies doped the films (*i.e.* caused a shift in the Fermi level), the valence band to Fermi level offset was determined from the XPS valence band spectra. The spectra were fitted using a Matlab script written by Dr Robert Hoye. The model was generated by convolving the calculated DOS of BiOI with a Gaussian, such that instrument broadening could be mimicked. This was then fitted to the band edge of the BiOI valence band spectra, allowing the valence band maximum to be determined from the intercept of the calculated DOS and the fit. As the samples were aligned to a gold reference during the measurement the Fermi level sat at 0 eV, and the valence band to Fermi level offset was deduced as the distance between the fitted band edge and 0 eV.

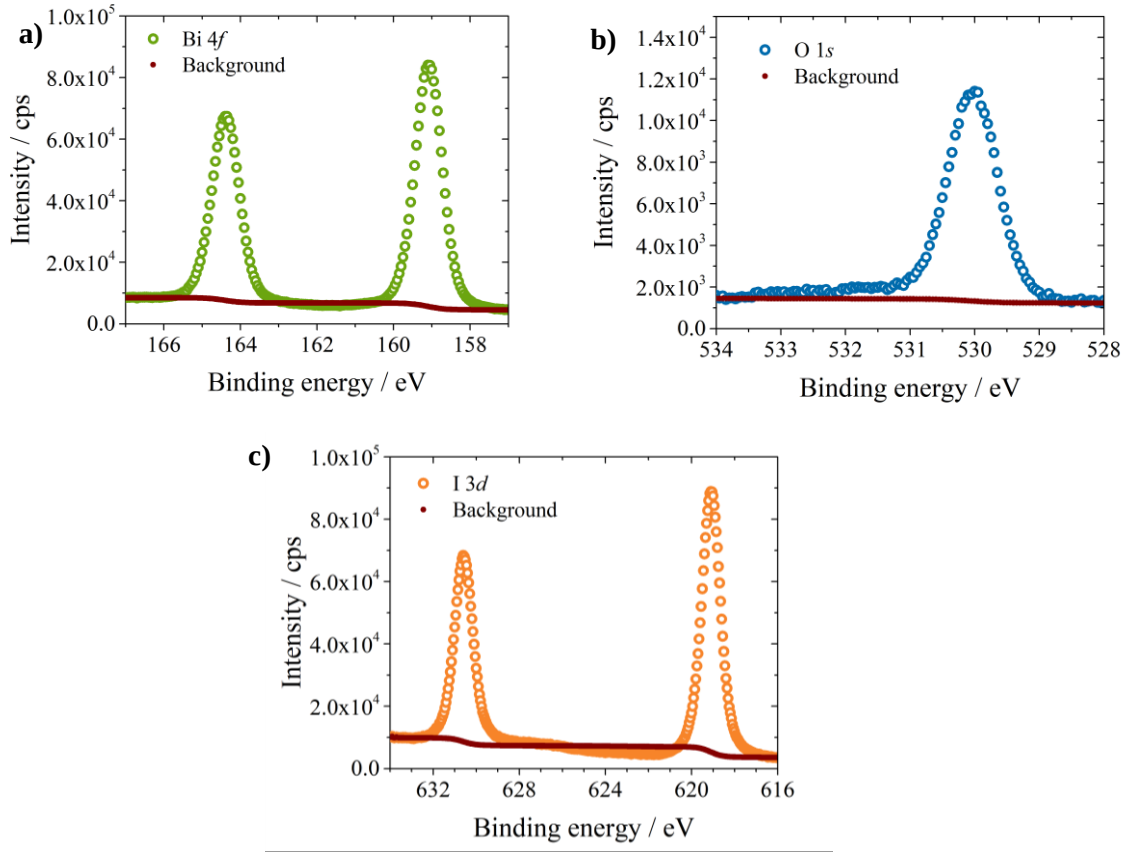

Figure 7.7 Example a) Bi 4*f*, b) O 1*s* and c) I 3*d* core level spectra measured by XPS. The 700 nm thick BiOI films were deposited at 350 ºC on ITO|solution processed NiO_x substrates.

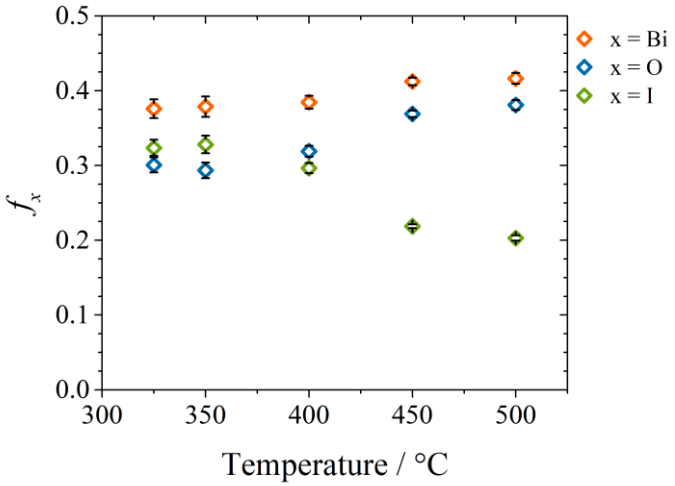

Figure 7.8 Compositional analysis of BiOI films deposited at 325 – 500 ºC. The composition was determined from the area of the core level XPS spectra (Bi 4*f*, O 1*s*, I 3*d*), accounting for the relative sensitivity factor of each orbital. The error bars represent the standard deviation doubled, where the area of each spectrum was fitted five times, such that 96 % of the values sat within this range.

The fitted valence band spectra for BiOI deposited onto ITO|NiO_x are shown in Figure 7.9a – e, whilst the Fermi level position as a function of temperature is plotted in Figure 7.9f. For all deposition temperatures, the valence band to Fermi level offset was ~ 1 eV. Additionally, there was no significant trend in the Fermi level position with temperature. Table 7.3 gives the bandgap of BiOI films deposited from 325 – 500 ºC, which were determined using Tauc plots. The bandgap remained constant at ~ 1.85 eV across all deposition temperatures, and as such the Fermi level sat roughly mid-gap and all samples were intrinsic. From Figure 7.8, it was proposed that a high density of iodine vacancies formed at deposition temperatures > 350 ºC, as the iodine content dropped from 33 % to 20 % between 350 and 500 ºC. The lack of trend in the Fermi level against temperature shows that despite the formation of iodine vacancies, no doping of BiOI occurred. This suggests that the transition level for iodine vacancies does not sit within the bands (otherwise the formation of negative iodine vacancies within the bandgap would cause *n*-type doping of BiOI). This supports the defect calculations which predicted that the defect transition level for iodine vacancies sits within the conduction band of BiOI.[2]

Table 7.3 The band-gap of BiOI determined from Tauc plots for glass|NiO_x|BiOI where BiOI was deposited at 325 – 500 ºC. Samples were measured by UV-vis photospectroscopy and an indirect transition was considered for BiOI to determine the bandgap.

Deposition temperature / ºC	Bandgap / eV
325	1.86 ± 0.02
350	1.86 ± 0.01
400	1.85 ± 0.01
450	1.85 ± 0.01
500	1.84 ± 0.01

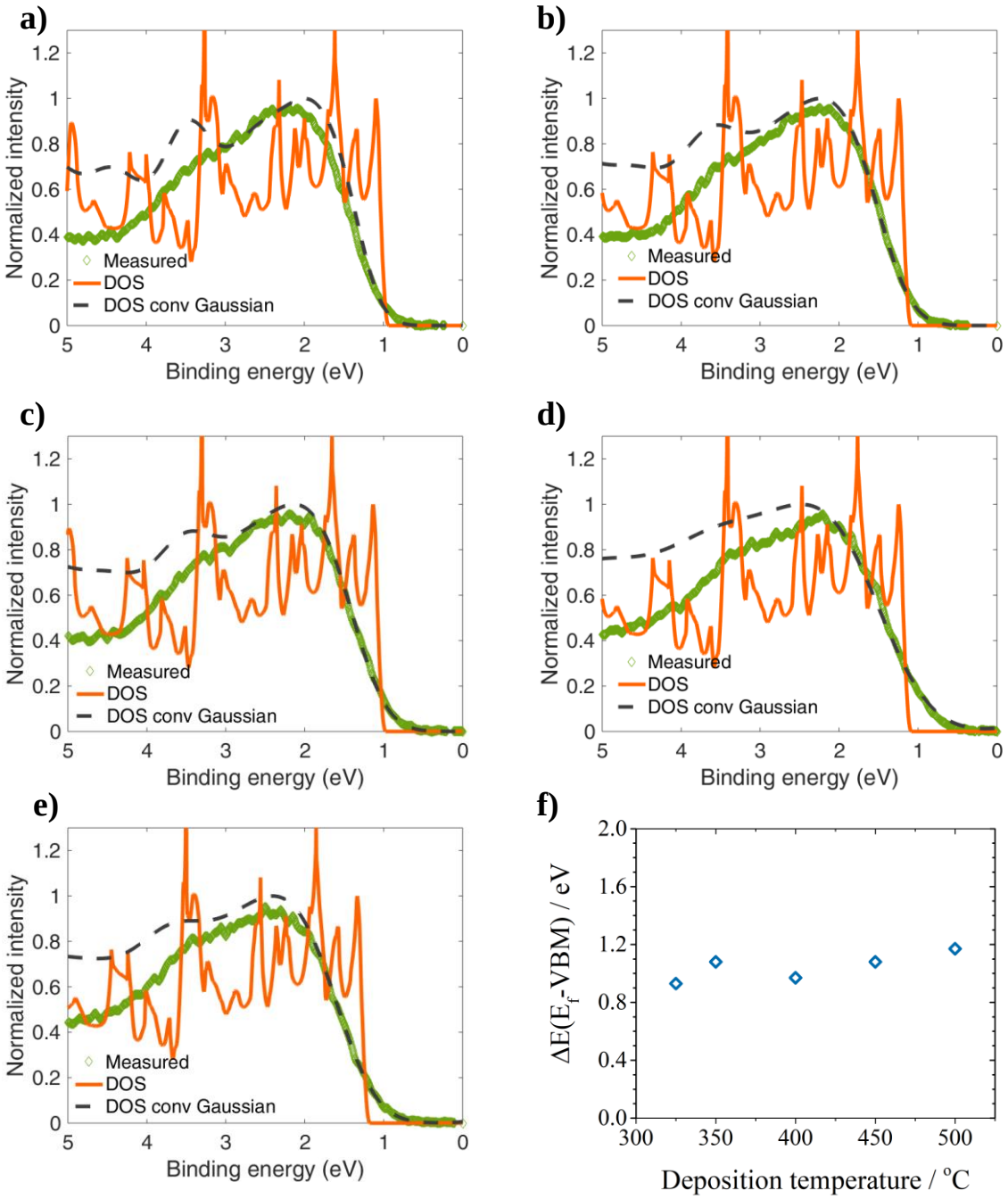

Figure 7.9 The measured valence band spectra (green), density of states (orange) and the fit of the density of states to the measured data (black dashes) fitted using a Matlab script. The samples are ITO|NiO_x|BiOI deposited at a) 325 ºC, b) 350 ºC, c) 400 ºC, d) 450 ºC and e) 500 ºC. Figure f) shows the plot of the valence band to Fermi level offset as a function of deposition temperature.

7.2.2.1 The limitations of XPS for determination of composition

The major limitation of XPS using soft X-ray sources such as Al, where Al K_α radiation has a photon energy 1486.6 eV, is that it is a surface sensitive technique. At such excitation energies, electrons have short mean free paths, meaning that typically only the top few nanometres of film are studied; typically around 5 nm.[261] Thus, the technique is highly sensitive to surface effects which may not occur in the bulk, and the measured composition may not represent the bulk of the material.[262,263] Hard X-ray photoelectron spectroscopy (HAXPES) uses higher energy photons (> 2 keV) to probe samples.[264] Consequently, the kinetic energy of the excited electrons increases, resulting in a longer electron mean free path. This makes excited electrons from deeper within the film more likely to be emitted from the surface before scattering relative to using soft X-ray sources (< 2 keV). As a result, films can be probed further below the surface (at roughly 20 nm), where composition is likely to be more representative of the bulk.[261] Such hard X-ray sources are available at synchrotron facilities.[262] In future, it would be useful to measure the samples by HAXPES to determine whether the same compositional changes measured using a soft X-ray source at the film surface are present within the bulk. Otherwise, energy dispersive X-ray spectroscopy can measure bulk composition, whilst XPS equipment can be fitted with an Ar^+ sputter gun, allowing measurement as the film is destructed thus enabling depth profiling.[265]

7.2.3 Influence of deposition temperature on the Urbach energy of bismuth oxyiodide thin films

Structural disorder such as from dangling bonds at grain boundaries and structural defects create electronic states at the band-edges.[58,266] The density of these states decreases exponentially into the bandgap, forming an exponential band tail.[267] It is possible to compare the density of defects within samples fabricated under different conditions by comparing the width of this band tail, known as the Urbach energy (E_u).[266] The Urbach energy can be determined from the absorption coefficient of the material.[266,268]

$$\alpha(v) = \alpha_0 \, exp\,(hv/E_u) \qquad \textbf{(7.30)}$$

Hence,

$$\ln[\alpha(v)] = \frac{hv}{E_u} - ln[\alpha_0] \qquad \textbf{(7.31)}$$

where E_u is the Urbach energy (eV), $\alpha(v)$ is the absorption coefficient at frequency v (cm^{-1}), and α_0 is a constant (cm^{-1}).

Photothermal deflection spectroscopy (PDS) was used to measure the absorption coefficient of BiOI samples deposited on quartz at 360, 400 and 500 ºC. E_u was determined from the inverse of the gradient in the plot of $ln(\alpha)$ against photon energy, equation **7.31**.[267] Quartz was used as the substrate due to its clean band-gap, preventing any interference from the substrate in the data. Note that due to poor coverage of BiOI on quartz, samples at T < 360 ºC could not be measured. The Urbach energy for BiOI at each deposition temperature is shown in Table 7.4.

Table 7.4 The Urbach energy of BiOI deposited at 360, 400 and 450 ºC on quartz, determined from PDS measurements.

Deposition temperature / ºC	Homologous temperature (T/T_m)	Urbach energy / meV
360	0.58	70
400	0.62	49
500	0.70	40

From Table 7.4, the Urbach energy decreased as the deposition temperature increased. This is as expected from the structure-zone model; depositing at higher temperatures results in fewer structural defects and grain boundaries due to higher mobility of grain boundaries and species arriving at the growing film surface.[193,195,198] This could have a direct implication on devices, for example a reduction in Urbach energy has resulted in an increased V_{OC} in amorphous silicon and CIGS solar cells.[269] This is because states at the band edge can act as recombination sites resulting in a large dark current, whilst thermal de-trapping of carriers from these states also results in energy loss. Thus, reducing the density of defect states at the band edge can cause an improvement in device voltage. Therefore, the data in Table 7.4 suggests that deposition of devices at 500 ºC could improve devices *via* an improved V_{OC}. The decrease in Urbach energy with increasing deposition temperature also provides further evidence that iodine vacancies do not form close to the band-edge. Otherwise, they would contribute towards the band tail, causing an increase in its width.

It should be noted that despite the small amount of Bi_5O_7I impurity in BiOI grown at 500 ºC (Figure 7.2b), the Urbach energy was smallest at this growth temperature. This implies that this phase impurity did not create states at the band edge. It should also be stated that despite the apparent improvement in structural properties of BiOI at higher temperatures, routes to deposit BiOI at these temperatures which avoid the formation of surface particles must be explored so that films can be incorporated into devices.

7.3 Summary of section

In this section, the influence of growth of BiOI at homologous temperatures between 0.54 – 0.70 on the properties of BiOI was explored. XRD was used to determine the parameter space for the growth of phase pure BiOI, which could be grown in a 1 % oxygen atmosphere up to 450 ºC. Growth of BiOI above 350 ºC resulted in an increase in crystallite size from XRD data, whilst platelet thickening was visible in SEM images. These effects would have positive implications for devices, however surface particulate formation at 400 ºC and above occurred, highlighting the need for growth in a cold wall reactor or under reduced pressure. Whilst films grown at 450 and 500 ºC exhibited significant iodine loss, this did not cause doping of the films or introduce defect states at the band edges, implying that BiOI shows tolerance to iodine vacancies. This will be explored further in the next chapter, where the influence of iodine deficiency introduced deliberately into films will be explored in more detail.

8 Investigating the tolerance of bismuth oxyiodide to iodine deficiency

Calculations in section 3.4.1 predicted that BiOI shows tolerance to defects, which either had transition levels within the bands or formation enthalpies > 1.5 eV. For work in this chapter, iodine deficiency was induced by annealing BiOI under low pressure, such that iodine vacancies would form. XPS and XRD data showed that BiOI retained its phase purity after losing up to 40 % of its iodine. Additionally, the Fermi level remained constant, indicating that the iodine deficiency did not cause doping. Further analysis of the O 1*s* core spectra and valence band spectra of as deposited and low pressure- annealed BiOI, as well as mixed phased films, further supported that no phase change occurred on iodine loss. These results support the theoretical predictions that BiOI shows tolerance to iodine vacancies.

8.1 Low pressure annealing of bismuth oxyiodide

Whilst the previous chapter showed that increasing the deposition temperature increased the lifetime and decreased the Urbach energy of BiOI despite significant changes in composition, the effects of temperature and composition on the properties could not be distinguished. To uncouple temperature and composition for work in this chapter, samples were annealed under low pressure to induce iodine deficiency. For all analysis in the following section, 700 nm BiOI samples were deposited onto ITO|solution processed NiO_x substrates and annealed for up to 2 days in 25 Pa residual gas at 100 ºC. The main reason for the use of ITO|NiO_x substrates was to provide an electrically conductive contact to prevent charging during XPS measurements, as well as benefitting from good BiOI coverage. Note that the composition of the residual gas within the furnace was not monitored, however it is likely that it mainly consisted of water, as well as traces of nitrogen, oxygen and carbon dioxide. The influence on the film properties was investigated to further study the tolerance of BiOI to iodine vacancies or deficiency.

8.1.1 Influence of annealing at low pressure on the composition and phase of bismuth oxyiodide

The composition of BiOI samples before and after annealing was determined from XPS data. The areas of the Bi 4*f*, O 1*s* and I 3*d* core spectra were each fitted five times to determine the average area. The fraction of each component measured in the film, f_x where x = Bi, O or I, was determined using equation **7.29**. The composition against anneal time is shown in Figure 8.1. The dashed lines represent the average f_x of 8 pre-annealed samples.

With annealing for only 1 minute, the iodine content dropped from 33 % to 20 %, after which it stayed relatively constant with continued annealing. Conversely, the oxygen content increased after 1 minute from 30 % to 43 % and continued to gradually increase to around 55 % after 48 hours annealing. This was mirrored by a drop in the relative bismuth content, from 40 % to 30 % after 48 hours. The relative ease of iodine loss was likely due to its high volatility. The change in oxygen and bismuth composition was unexpected; it would be anticipated that as iodine was lost (forming iodine vacancies or iodine deficient films), the relative content of bismuth and oxygen would both increase at the same time. The increase in oxygen coupled with the decrease in bismuth content over time may indicate the formation of a protective oxide layer on the surface. The origin of the oxygen may be due to reaction with residual gas in the furnace tube or from the diffusion of oxygen from the bulk of the films towards the surface. In the case of residual gas, reaction would likely occur with water which tends to be the main component of residual gas. The origin of the increased surface oxygen content with annealing will be discussed in more detail later in the chapter.

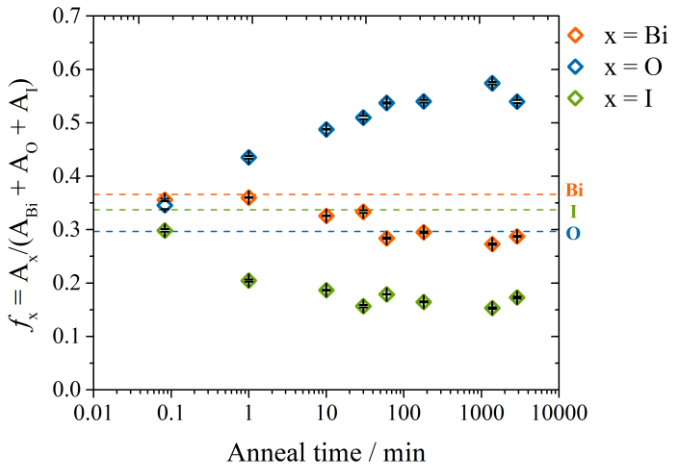

Figure 8.1 The fraction of Bi, O and I (f_x where x = Bi, O, I) in BiOI films annealed at 100 ºC and 25 Pa residual gas for up to 48 hours, determined from XPS core level spectra. The dashed lines represent the average fraction of Bi (orange), O (blue) and I (green) in 8 BiOI films before annealing. For all samples, 700 nm BiOI was grown on ITO|NiO_x substrates.

To study whether phase changes occurred due to the change in BiOI composition, the same samples were measured by XRD before and after annealing. The data is presented in Figure 8.2. It should be noted that any differences in overall intensity and relative intensity of peaks was due to small sample-to-sample thickness variation. From Figure 8.2, there was no phase change in bulk BiOI after annealing for up to two days. This phase stability is important for device processing, allowing for less stringent restrictions for processing subsequent layers. However, it

should be noted that XRD is only able to probe bulk properties, whilst XPS is a surface technique. Thus, the composition changes may have only occurred at the surface, whilst the bulk may have been stoichiometric giving rise to the XRD data in Figure 8.2. Additionally, phase changes may have still occurred at the surface, which could not be detected by XRD. Thus, analysis of the surface would also be required to study any phase changes.

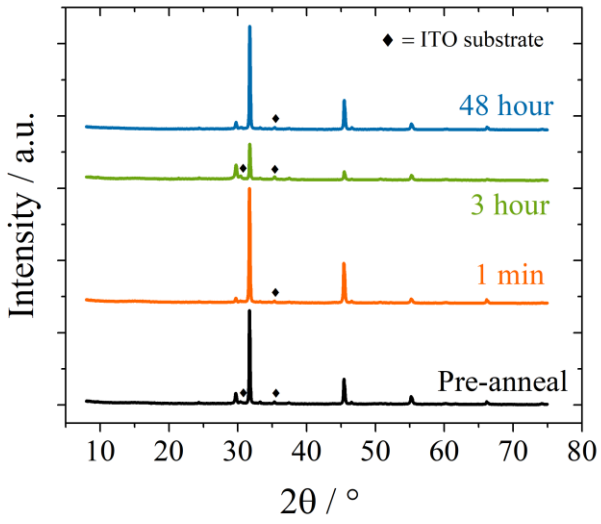

Figure 8.2 Theta-2theta scan of ITO|NiO_x|BiOI(700 nm) samples as grown (pre-anneal, black) and after annealing for 1 minute (orange), 3 hours (green) and 48 hours (blue). The ♦ represents peaks from the ITO substrate.

As a surface sensitive technique, XPS can give further information about phase purity at the sample surface, enabled by differences in Bi 4*f* binding energy in $Bi_xO_yI_z$ of different composition. For example, compared to BiOI, Liu *et al.* reported 0.4 eV and 0.6 eV shifts of the Bi $4f_{7/2}$ peak to higher binding energies for $Bi_4O_5I_2$ and Bi_5O_7I respectively.[270] Additionally, a Bi $4f_{7/2}$ binding energy of 159.1 eV has been reported for Bi_2O_3.[271] Thus, a significant shift in Bi 4*f* binding energy would be expected if different phases were forming at the film surface on annealing. Therefore, the Bi 4*f* core spectra were measured by XPS before and after annealing. A plot of the Bi $4f_{7/2}$ binding energy against annealing time is shown in Figure 8.3. The average Bi $4f_{7/2}$ binding energy taken from 8 samples before annealing is represented by the orange line, whilst the shaded area is twice the standard deviation.

After annealing, the Bi $4f_{7/2}$ binding energy for all samples was randomly spread around the average value for the as grown samples. An R-squared value of 0.08 was calculated, meaning that the variation in Bi $4f_{7/2}$ binding energy was random with respect to changes in annealing

time. This indicates that vacuum annealing did not cause a phase change in BiOI, despite the significant change in composition.

Figure 8.1 to Figure 8.3 indicate that BiOI can retain its phase purity despite significant changes in composition. BiOI also retains its phase after a much greater iodine loss than $MAPbI_3$ does. In a similar experiment in which $MAPbI_3$ was constantly irradiated with X-ray radiation for 2 days, a phase change was detected in XPS data after a 16.7 % iodine loss,[151] whilst no change was detected by XPS in BiOI after 40 % iodine loss. Again, it should be noted that in both cases changes in composition and phase were only measured at the surface;[151] the iodine deficiency may not have been present throughout the whole film. However, the surface measurements are still representative of the response of BiOI to composition changes.

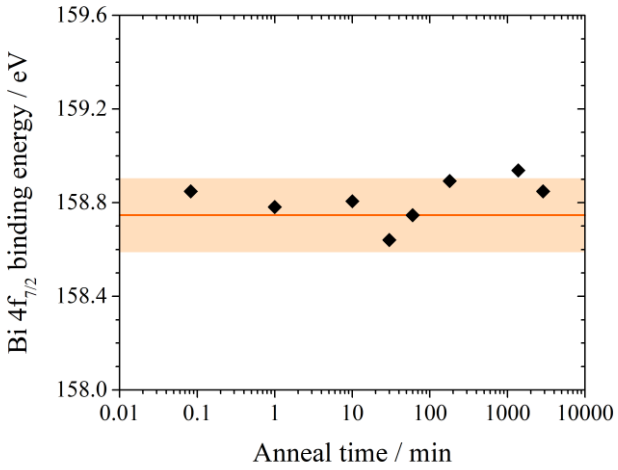

Figure 8.3 Bi $4f_{7/2}$ binding energy for BiOI samples after vacuum annealing for up to 48 hours (100 ºC, 25 Pa). The orange line represents the average of 8 samples measured before annealing, and the orange box represents two times the standard deviation at either side of the mean. For all samples, 700 nm BiOI was grown on ITO|NiO_x substrates.

8.1.2 Influence of iodine deficiency on the electronic and optical properties of bismuth oxyiodide

To experimentally determine whether BiOI is tolerant to the defects formed on vacuum annealing (such as iodine vacancies) it was necessary to probe the position of the Fermi level of the same samples before and after annealing. As well as introducing sites for recombination, defects with transition levels within the bandgap cause doping, causing a shift of the Fermi level upwards (downwards) for a donor (acceptor) defect. Conversely, a defect with a transition level within either of the bands does not cause any change in Fermi level. In the latter case the material is considered defect tolerant.[151]

Considering this, XPS was used to determine the valence band to Fermi level offset of the same samples before and after annealing, by measurement of the valence band spectra. The data was fitted using the method described in section 7.2.2. The valence band to Fermi-level offset against anneal time is presented in Figure 8.4. The dashed green line is the average value of 8 as-grown BiOI samples, and the green box represents twice the standard deviation at either side of the mean. The Fermi level to valence band offset for post annealed samples was randomly scattered around the as-deposited average. Additionally, all values sat within two standard deviations of the as-deposited average, the range within which 96 % of the as-deposited values sat. The lack of significant change in Fermi level with annealing supports the defect calculations for BiOI in the introduction (section 3.4.1).[2] Despite the large loss in iodine shown in Figure 8.1, the Fermi level did not change, indicating that iodine vacancies did not cause doping of the films. This suggests that the transition level for iodine vacancy formation sits within the conduction band as predicted, implying that BiOI is tolerant to iodine vacancies.[2]

This theory was also supported by photoluminescence data, plotted in Figure 8.5a. This data shows the change in maximum photoluminescence intensity against vacuum annealing time for BiOI. Again, the dashed line represents the value for an as-deposited BiOI film. The maximum photoluminescence intensity was scattered randomly about the as deposited sample. This implies that the iodine vacancies did not form charged defects states within the bandgap. If this was the case, the charged defect states would act as recombination centres within the bandgap, introducing a pathway for Shockley-Read-Hall (non-radiative) recombination in the films.[37,39,42] This would be reflected by a loss in photoluminescence intensity, which directly probes radiative recombination, for all annealed samples relative to the as-grown sample. Figure 8.5b shows example PL spectra for as-deposited BiOI and after 3 hours of vacuum annealing. There was no change in shape of the spectra, meaning that the formation of defect states within the bandgap was not detected. However, it should be noted that considering the excitation wavelength of 400 nm, the penetration depth of the laser was 187 nm (Figure 6.2). Thus, the bulk of the film was

measured relative to XPS measurements (which probe the surface ~ 5 nm). Therefore, it is not possible to say whether the iodine deficiency at the film surface was also present in the bulk. Note that time of flight elastic recoil detection analysis (TOF-ERDA) measurements, an elemental analysis which probes composition throughout film depth, were attempted but did not give useful data due to scattering by the rough films. Alternative measurements of bulk composition, such as HAXPES and EDX, were mentioned in section 7.2.2.1 and would be useful in future to determine whether the iodine deficiency was present in the bulk of the film or only at the surface. This would indicate whether the PL data, which probe the bulk, is representative of the behaviour of iodine deficient BiOI.

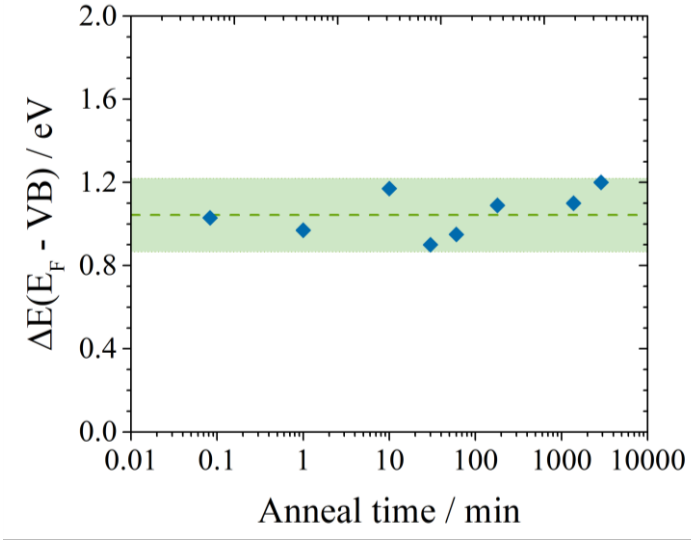

Figure 8.4 The valence band – Fermi level offset of BiOI annealed at 100 ºC under 25 Pa of residual gas for up to 48 hours, determined from the XPS valence band spectra. The green dashed line represents the average value of 8 samples before annealing, and the green box represents two times the standard deviation at either side of the mean. For all samples, 700 nm BiOI was grown on ITO|NiO_x substrates.

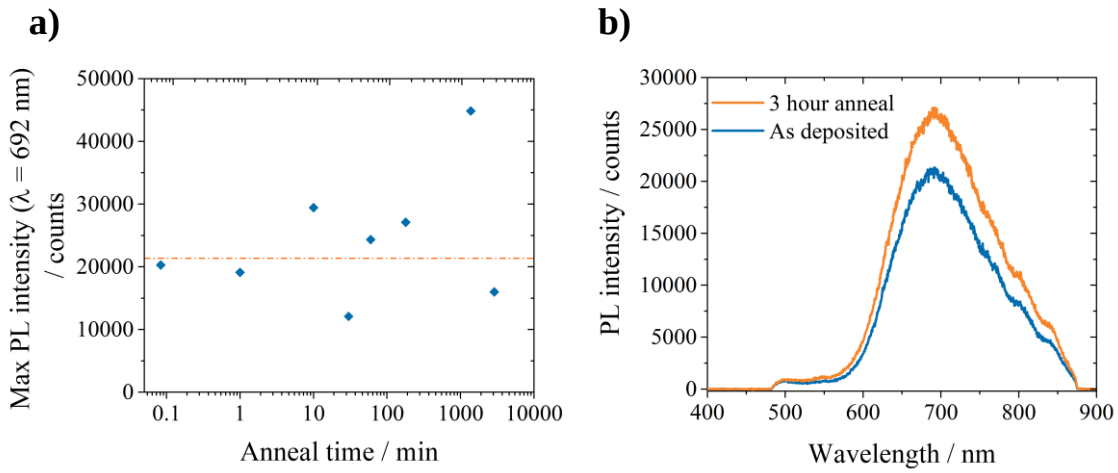

Figure 8.5 a) Maximum photoluminescence intensity (at λ = 692 nm) for BiOI samples annealed at 100 ºC under 25 Pa of residual gas for up to 48 hours. The orange dashed line represents the maximum photoluminescence intensity before annealing and **b)** representative PL spectra of as-deposited BiOI (blue) and after annealing for 3 hours. For all samples, 700 nm BiOI was grown on ITO|NiO_x substrates.

The above XPS, XRD and PL data indicate that despite significant loss of iodine with vacuum annealing, hence the formation of iodine vacancies, the phase, Fermi level position and density of recombination centres within the bandgap did not change in BiOI films. However, it should be noted that whilst XPS is a surface sensitive technique, PL and XRD are bulk measurements. Therefore, the validity of the latter two bulk techniques in this case can only be confirmed if the iodine deficiency is confirmed to be present throughout the whole film. In section 7.2.2.1, the benefit of HAXPES over photoelectron spectroscopy using soft X-ray sources such as Al K_α radiation, in that higher energy photons are able to probe deeper into the bulk of the film, was highlighted. Again, such a bulk composition measurement method would be useful to determine whether the changes in composition with annealing were present through the bulk of the films. Despite this, the conclusions from XPS that no change in phase or Fermi level occurs on compositional changes at the surface may still be a valid representation of the behaviour of iodine deficient BiOI.

Whilst focus so far has been placed on the change in iodine content on annealing, the compositional analysis in Figure 8.1 also showed a significant increase in oxygen content over time, relative to iodine and bismuth. This was speculated to come from either the formation of a protective surface oxide, or from oxygen diffusion from the bulk. The next section studies the origin of the oxygen in more detail, through comparison of the oxygen XPS data with that of mixed phase films containing BiOI and $Bi_xO_yI_z$ where x and y > z. This would also provide further evidence of whether phase changes occurred with vacuum annealing.

8.1.3 The influence of iodine deficiency on the O 1*s* XPS spectrum of bismuth oxyiodide

8.1.3.1 Analysis of the components of the O 1s spectrum

In Figure 8.1, the iodine content of BiOI films annealed at 100 ºC under 25 Pa residual gas for 48 hours was found to decrease from 30 % to 17 %. This was coupled by a reduction in bismuth content and a significant increase in the oxygen content (from 35 % to ~ 60 %) within the region probed by XPS. To further investigate the origin of the increase in oxygen content at the BiOI surface with vacuum annealing, the O 1*s* core level XPS spectra were further analysed. The O 1*s* spectra of as grown BiOI on ITO|NiO_x, and BiOI annealed at low pressure for 1 minute, 10 minutes and 23 hours are shown in Figure 8.6a – d. Additionally, the fractional contribution of each peak to the O1*s* spectra (f_{BE} where BE is the peaks at binding energies 529 eV, 531 eV and 533 eV) against annealing time is shown in Figure 8.6e. This was calculated from:

$$f_{BE} = \frac{A_{BE}}{A_{O1s}} \qquad \textbf{(8.32)}$$

Where A_{BE} is the area of the peak at binding energy BE, and A_{O1s} is the total area of the O1*s* trace ($A_{O1s} = A_{529eV} + A_{531eV} + A_{533eV}$).

For as grown BiOI (Figure 8.6a), the peak at binding energy 529 eV dominated the O 1*s* spectrum, accounting for 82 % of the signal. With annealing, its contribution gradually decreased to ~30 % of the total signal after 48 hours. Meanwhile, the area of the peak at 531 eV initially increased from 11 % to 40 % after 1 minute (Figure 8.6b), before gradually reducing again over time, whilst the area of the signal at 533 eV increased from 7 % to ~60 % of the signal over 48 hours of annealing.

The peak at 529 eV has been previously identified as 'lattice oxygen' in BiOI, which explains why it provides such a large contribution to the O1*s* spectrum of as-grown BiOI.[272] However, the peaks at ~531 and 533 eV are not well documented; whilst some authors label the peak at 531 eV as from the oxygen in absorbed water or organic contaminants,[180,272] this is highly unlikely in this case due to the evolution of the peak with annealing time. Otherwise, the peaks at 531 eV and 533 eV have been present in higher oxides (such as Bi_2O_3, Bi_5O_7I),[273,274] but not in the ratios presented in Figure 8.6e, particularly towards longer annealing times. Therefore, it was necessary to further investigate whether the rise in oxygen content was due to surface oxidation or from other sources.

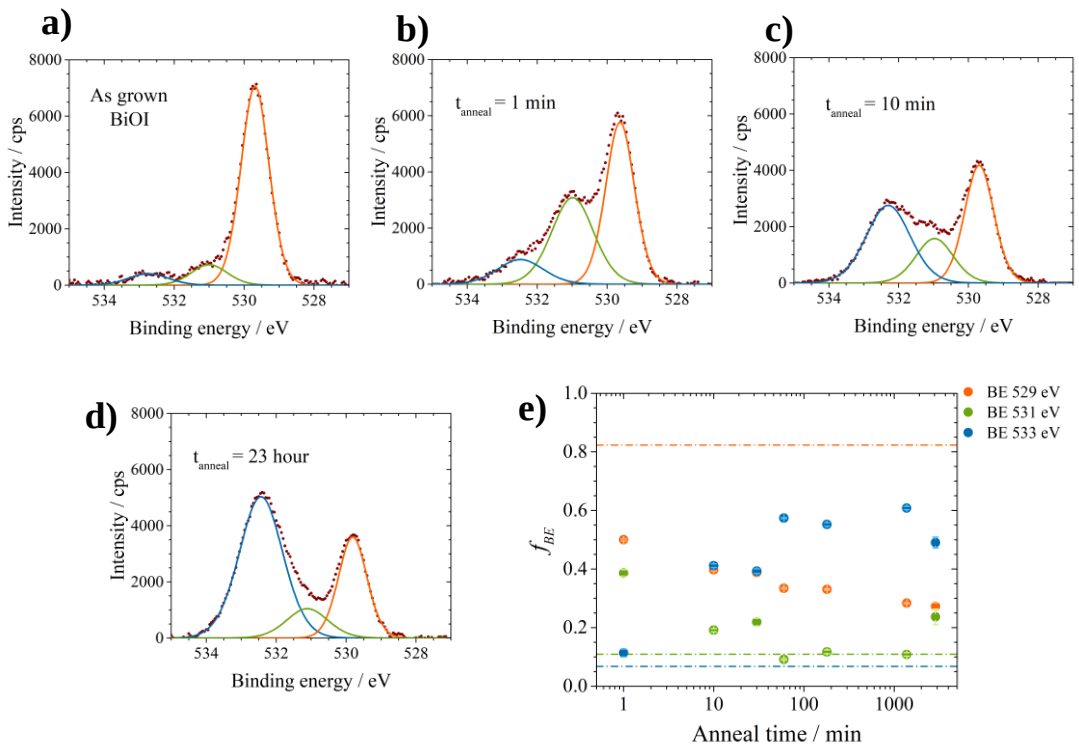

Figure 8.6 O1*s* core spectra of a) as grown BiOI, b) BiOI vacuum annealed for 1 minute, c) BiOI vacuum annealed for 10 minutes and d) BiOI vacuum annealed for 23 hours at 100 ºC, 25 Pa. Figure e) shows the change in fractional contribution (f_{BE}) of the peaks at binding energies 529 eV, 531 eV and 533 eV to the O 1*s* spectra as vacuum annealinng time increased. The dashed lines show the fractional contribution of the peaks at binding energy 529 eV (orange), 531 eV (green) and 533 eV (blue) to the O 1*s* spectrum for an as grown BiOI sample. All samples were 700 nm thick and were grown on ITO|NiO_x substrates.

8.1.3.2 Growth and phase identification of mixed phase bismuth, oxygen and iodine containing thin films

To test whether the change in composition of the BiOI films with vacuum annealing was due to surface oxidation from reaction with residual gases at low pressure, such as water and oxygen, a series of mixed phase films containing BiOI and $Bi_xO_yI_z$, where x and y > z, were grown on ITO|NiO_x substrates, aided by the phase diagram in Figure 7.1. The growth conditions and phases present, identified by XRD, are listed in Table 8.1.

Table 8.1 The conditions used to grow mixed phase samples **A, B** and **C**, the colour of the film and the phases present as determined by XRD. Powder Diffraction Files (PDF) were used to identify BiOI (00-010-0445), Bi_5O_7I (00-038-0669), $Bi(IO_3)_3$ (00-058-0583) and $Bi_2O_{2.33}$ (00-027-0051) and β-Bi_2O_3 (00-001-0709).

Sample ID	Growth conditions		Film colour	Phases present
	Temperature / ºC	O_2 flow / %		
A	450	5	Red	BiOI, Bi_5O_7I
B	450	50	Red	BiOI, Bi_5O_7I, $Bi_2O_{2.33}$
C	400	50	Yellow	BiOI, $Bi(IO_3)_3$, Bi_5O_7I, β-Bi_2O_3

Samples **A**, **B** and **C** were all mixed phases samples. The main phase in **A** and **B** was BiOI, which dominated the XRD spectrum, whilst **C** had a larger contribution from all phases. As a result, **A** and **B** retained the red colour of BiOI. The bandgap of the $Bi_xO_yI_z$ series has been demonstrated to shift from red towards the UV as the bismuth and oxygen content increases.[275,276] This effect is responsible for the yellow colour of **C**; whilst BiO_9I_3 and Bi_5O_7I are both white, the band-gap of β-Bi_2O_3 is ~ 2.4 eV, likely causing the yellow colour.[275]

It may seem counterintuitive that **C** contained phases with higher oxygen content than **B**, as both were grown in 50 % oxygen with sample **C** grown at the lower temperature. However, BiI_3 has a lower partial pressure at 400 ºC than 450 ºC.[259] This means that the ratio of O_2:BiI_3 in the furnace was higher at 400ºC, resulting in the growth of more oxygen rich phases. For ease of reference, samples **A**, **B** and **C** have been named in order of decreasing iodine/increasing oxygen containing phases (as will be verified in the next section).

8.1.3.3 Compositional analysis of mixed phase films

XPS was used to determine the composition of **A**, **B** and **C**, using the core level spectra and equations **7.28** and **7.29**. The results are shown in Figure 8.7.

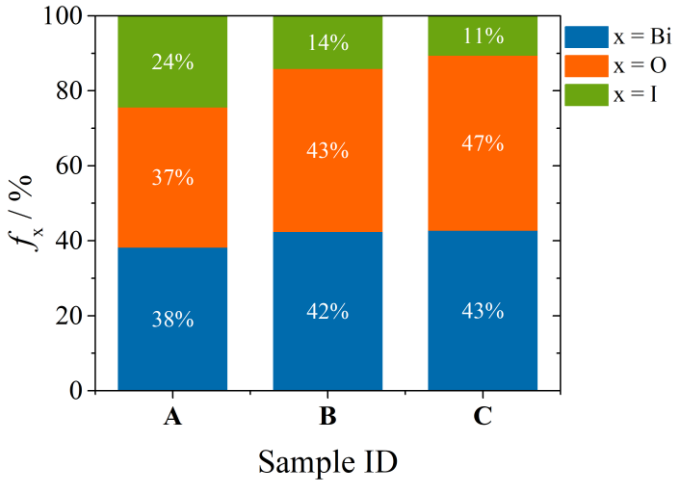

Figure 8.7 The composition of samples **A**, **B** and **C** determined using the areas of the XPS core level spectra, accounting for the relative sensitivity factor for each orbital.

From Figure 8.7, all samples were iodine deficient relative to BiOI (which has 33 % Bi, O and I). The iodine content decreased from **A** to **B** to **C**, whilst the bismuth and oxygen content both increased. This is expected based on the phases present in Table 8.1, where the mixed phase films have increasing bismuth and oxygen content and lower iodine content going through the series. For all samples, the Bi and O content was approximately equal, both rising by a similar amount relative to stoichiometric BiOI to account for the loss in iodine. Note that this trend differs from that for vacuum annealed BiOI, where both iodine and bismuth content decreased whilst the oxygen content increased over time.

8.1.3.4 Study of the valence band spectra of mixed phase films

A change in Fermi level might be expected on formation of a surface oxide, due to differing band structure and doping levels of different phases in the Bi-O-I system.[275] Therefore, the VB-E_f offset of the mixed phase samples was measured to compare the vacuum annealed and mixed phase samples. The plot of the valence band edge for samples **A**, **B** and **C** is shown in Figure 8.8. Due to differences in the density of states of mixed phase samples at the band edges, it was not possible to fit the spectra using the method used in previous sections, which fits the density of states of BiOI to the valence band spectrum. Instead, the VB-E_f offset was estimated by taking the intercept

of the gradient at the band-edge with the background beyond the band-edge. The estimated Fermi level positions are listed in Table 8.2.

Table 8.2 The estimated valence band – Fermi level offset of mixed phase samples **A**, **B**, and **C**, as predicted from the XPS valence band spectra.

Sample	Valence band – E_f offset / eV
A	0.55
B	0.87
C	1.24

From Figure 8.8, the band-edge visibly shifted to a higher binding energy as the iodine content of the samples decreased (*i.e.* moving from **A** to **B** to **C**). This is reflected by the increasing values of the VB – E_f offset in Table 8.2. The data suggests that the different phases (BiOI, BiO_9I_3, Bi_5O_7I, $Bi_2O_{2.33}$ and β-Bi_2O_3) influenced the Fermi level of the mixed phase films. Only the value for sample **B** (0.87 eV) sat within the average ± twice the standard deviation of the BiOI calculated in Figure 8.4 (1.04 ± 0.18 eV). Additionally, the value sat 0.01 eV from the lower bound of this range. This suggests that the change in Fermi level for the mixed phases samples relative to BiOI was significant. Conversely, the Fermi level for the vacuum annealed films (Figure 8.4) all sat within twice the standard deviation for pre-annealed BiOI films. This evidence suggests that the rise in oxygen content of the vacuum annealed films (Figure 8.1) wasn't due to formation of a different phases on the surface (*i.e.* was not a result of surface oxidation from reaction with components of residual gas), otherwise a shift in Fermi level with vacuum annealing would have occurred.

This theory is further supported by analysing the shape of the VB spectra for BiOI, vacuum annealed BiOI and the mixed phase films, which are presented in Figure 8.9.

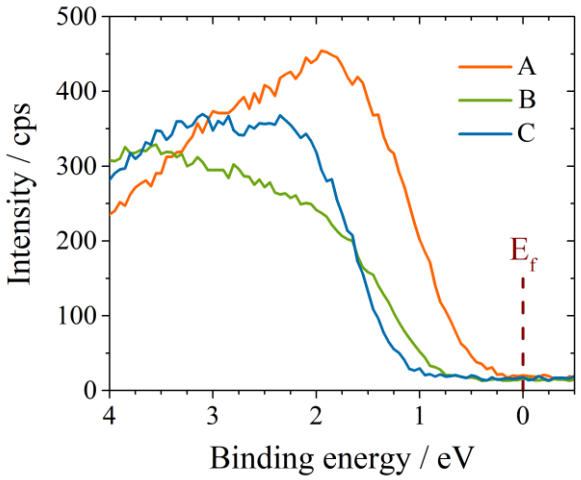

Figure 8.8 The band edge region of the valence band spectra of mixed phase samples **A**, **B** and **C** on ITO|NiO_x as measured by XPS. The Fermi level (E_f) is marked by the dashed line at 0 eV.

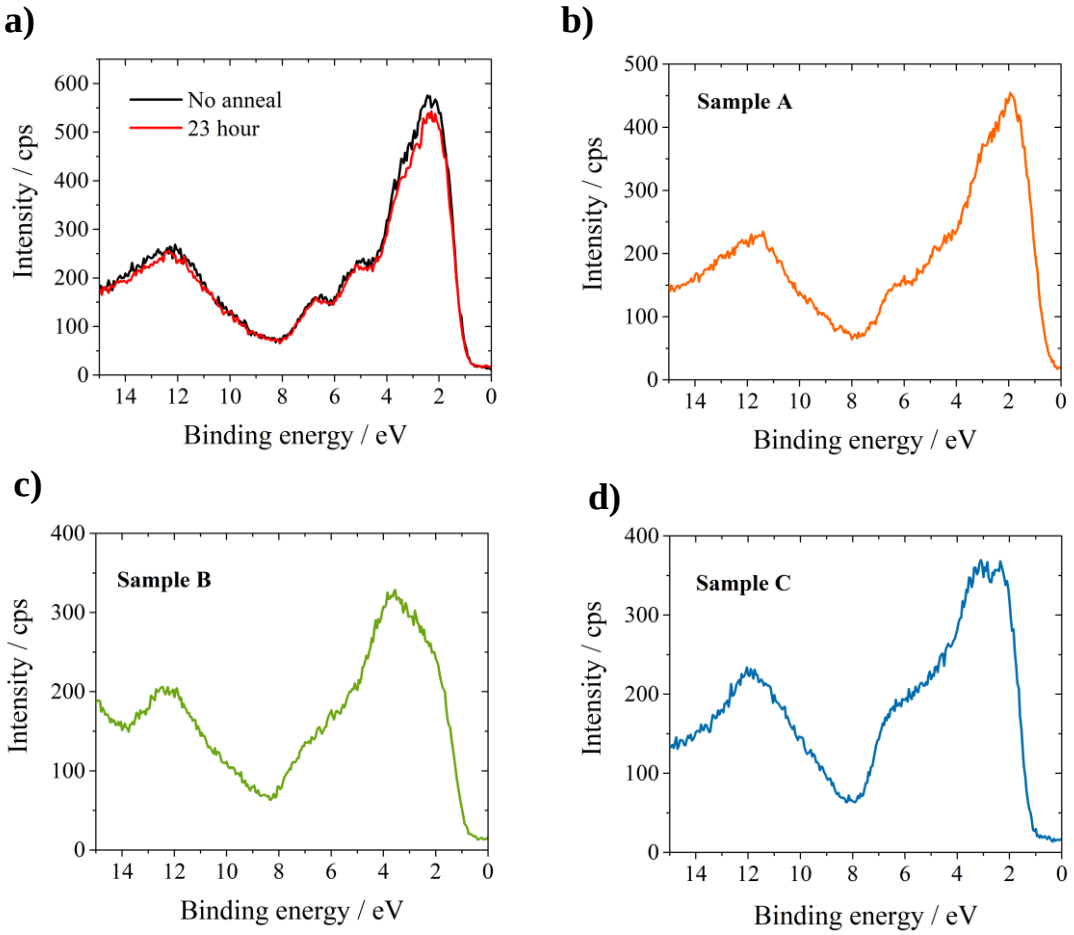

Figure 8.9 The full valence band spectra for a) as-deposited BiOI (black line) and BiOI vacuum annealed for 23 hours at 100ºC, 25 Pa (red line), b) sample **A**, a mixed phase sample containing BiOI and Bi_5O_7I, c) sample **B**, a mixed phase sample containing BiOI, Bi_5O_7I and $Bi_2O_{2.33}$, and **d)** sample **C**, a mixed phase sample containing BiOI, BiO_9I_3, Bi_5O_7I and β-Bi_2O_3. In all cases, ITO|NiO_x was used as substrate.

For the as prepared sample and BiOI vacuum annealed for 23 hours, there was no visible change in shape of the valence band spectrum (Figure 8.9a). However, for the mixed phase samples, moving from sample **A** to **B** to **C** (through Figure 8.9b – d) there was an initial loss in definition in the binding energy region 4 – 7 eV, followed by a complete change in shape in this region. This was due to the changing contributions of the Bi 6*p*, O 2*p* and I 3*d* orbitals to the valence band spectra for the phases with higher bismuth and oxygen and lower iodine contents.[182,275] Again, the lack in change of shape of the valence band spectra for the vacuum anneal films suggests that oxidation to a different phase due to reaction with residual gas was not occurring at the surface with low pressure annealing.

Evidence from the previous sub-sections suggests that the rise in oxygen content with vacuum annealing was not due to surface oxidation. For vacuum annealed films, there was no significant change in Fermi level, whereas for more oxygenated mixed phase films the Fermi level changed position. Additionally, there was no change in the shape of the VB spectra with vacuum annealing.

Another possible cause of the rise in oxygen content on the surface of BiOI with vacuum annealing may have been diffusion of oxygen through the lattice to counteract/balance iodine loss. Iodide has an ionic radius 2.2 Å.[277] Thus, the removal of an iodide ion would leave a large space in the lattice. This would reduce the activation energy for diffusion of oxygen through the lattice (the oxide ion has radius 1.4 Å)[278], where it may sit between atoms (oxygen interstitial) or on the empty iodine site (anti-site defect). The resultant oxygen positions would be in a different environment to the lattice oxygen atoms. As a result, the binding energy of the electrons would be different to the those on the lattice oxygen sites, as they would have a different electronegativity based on their proximity to bismuth. This would explain the trend seen in the O 1*s* spectra with vacuum annealing; the increase in area of peaks at 531 and 533 eV with annealing time (which would therefore correspond to interstitial oxygen and oxygen on an iodine site). Additionally, from the defect diagram, the oxygen anti-site and interstitial defects do not have transition levels within the bandgap of BiOI, therefore would not cause a change in the Fermi level position.[2] However, further experimentation would be required to determine whether oxygen interstitials and anti-site defects are responsible for the change in O 1*s* spectra with vacuum annealing. These may include depth profile compositional analysis, to study the change in oxygen content throughout the film, and deep-level transient spectroscopy (DLTS) for a more in-depth study of the nature of the defects.

8.2 Summary of section

The influence of iodine deficiency, induced by vacuum annealing, on the phase, composition and electronic properties of BiOI was studied. On probing the film surface by XPS, no phase change was seen on iodine loss of up to 40 %, whilst the position of the Fermi level remained constant indicating that no doping occurred. A lack of phase change was confirmed by comparing XPS data of vacuum annealed samples with mixed phase films. These results support theoretical predictions that the iodine vacancy has a defect transition level within the conduction band. XRD and PL data also indicated that no phase change nor formation of defect states within the bandgap occurred with vacuum annealing, however the validity of these bulk measurements was questioned. Alternative measurements of bulk composition, such as HAXPES and EDX, were suggested for future work to probe the composition deeper into the films, to validate whether compositional changes were present throughout the films and therefore whether XRD and PL data was representative. Finally, the evolution of higher binding energy peaks within the O 1*s* core level spectrum with increased vacuum annealing time was investigated. It was speculated that this change was due to an increase in interstitial and anti-site oxygen defects which diffuse from the bulk on iodine loss. However, further experimentation, such as depth profile analysis and DLTS, is needed to confirm this.

9 Bismuth oxyiodide: future work

In chapter 7, the influence of temperature on the properties of BiOI was studied. At growth temperatures ≥ 400 ºC, formation of surface particles which would likely be detrimental to device performance appeared in SEM images. These were thought to be caused by the reaction of intermediates in the gas phase before meeting the substrate surface. Potential routes to overcome this which would be useful to study in future are growth in a vacuum furnace, where the intermediates have a longer mean free path length and are less likely to meet in the gas phase, and cold wall reactors, where only the substrate is heated meaning there is insufficient energy for gas phase reactions.[200] It should be noted that cold-wall reactors tend to be used under vacuum to minimise convection in the chamber, which otherwise causes poor film uniformity.[200,203] Vacuum growth would also enable enhanced control over reaction rates, and variation of pressure would allow a greater range of film morphologies to be explored.[200,201] Through careful design of the reactor, an external BiI_3 source would allow pulsing of precursor into the reaction chamber, giving better control over the amount of BiI_3 delivered. The overall aims of these modifications would be to allow surface particle-free thin films to be grown at ≥ 400 ºC to explore the effect of higher homologous temperature growth on device properties.

Another route for further exploration is the use of BiOI films in tandem devices with silicon. In section 6.2.2 a bandgap of 1.9 eV was measured for BiOI. Whilst the SQ limit for a solar cell with this band-gap energy is below 25 %, a theoretical maximum efficiency of 45 % is predicted for a two-junction tandem device with silicon.[32] The best lab scale silicon devices using single crystal silicon wafers have already achieved > 26 %, whilst modules using polycrystalline silicon can reach up to ~ 20 %. A tandem with BiOI could offer an increase in performance of several percent using relatively low energy input processing steps to improve performance of an already established photovoltaic technology, meaning that their existing infrastructure could be built upon.

Part B

10 Growth of nickel oxide using the Vertical Cambridge University Close Proximity reactor: thin films properties and their application in solar cells

Section 2.5.4 highlighted the need for a high throughput route to NiO_x thin films if *p-i-n* perovskite solar cells are to reach commercialisation. For work in this chapter, the deposition of NiO_x using the Vertical Cambridge University Close Proximity reactor was explored. Deposition occurred by a chemical vapour deposition decomposition mechanism, achieving growth rates 36 times faster than conventional atomic layer deposition. The pin-hole free, phase pure films showed *p*-type conductivity as a result of a high density of nickel vacancies. Application in a mixed cation *p-i-n* perovskite solar cell resulted in a champion device efficiency of 16.6 %, comparable with the best devices in the literature. Additionally, routes to further improve device efficiency through tuning defect density and doping methods are identified, whilst the need for further exploration into methods to determine the carrier concentration of NiO_x is highlighted.

10.1 Growth characterisation of nickel oxide fabricated using the Vertical Cambridge University Close Proximity Reactor

10.1.1 Introduction to X-ray reflectivity

X-ray reflectivity (XRR) was used to generate growth curves for NiO_x grown using the AP-SALD reactor. This allowed direct comparison of growth rates with other methods such as temporal ALD, as well as determination of the growth mechanism of NiO_x. In XRR, a sample is irradiated by an incident X-ray beam at low angles (typically $\theta \sim 0.1 - 3$ º), and the intensity of reflected light is measured as a function of the incident angle.[279,280] On incidence to the sample surface, the X-ray beam reflects off the film surface or is refracted.[281] Refracted X-rays which are subsequently reflected at the film|substrate interface constructively or destructively interfere with those reflected from the film surface (Figure 10.1a).[282] This results in interference fringes known as Kiessig fringes.[283] The distance between the fringes is inversely proportional to the thickness of the film, *i.e.* the fringes move closer together as the film thickness increases.[282] This is evident in Figure 10.1b, where 18, 23 and 38 nm AP-CVD NiO_x films were deposited by changing the number of oscillations. As well as thickness, the shape of the trace is also dependent on the roughness of the film and the density difference between the film and the substrate. Thus, data is fitted using modelling software to extract the film thickness.[283]

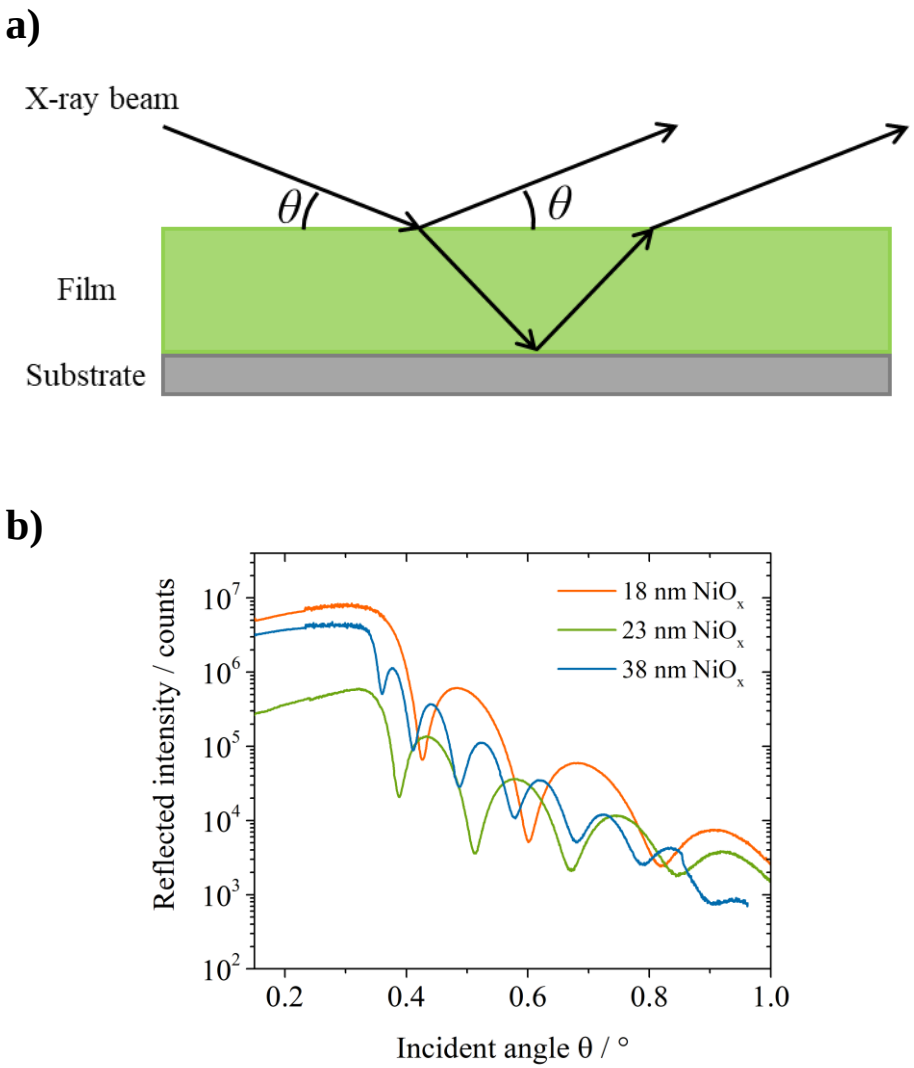

Figure 10.1 a) Reflection and refraction of an X-ray beam of incident angle θ at the surface of a thin film. Reflection of the refracted beam from the film|substrate interface can result in constructive interference, causing interference fringes in the plot of reflected intensity against incident angle. b) Shows example XRR data for NiO_x on borosilicate glass substrates. The NiO_x film thicknesses are 18 nm (orange), 23 nm (green) and 38 nm (blue). Figure a) was adapted from references [281,282].

10.1.2 Characterisation of the growth mechanism of nickel oxide

Bis(methylcyclopentadienyl)nickel ($Ni(CpMe)_2$) (Figure 10.2a) and oxygen were used as the precursor combination to deposit films at 350 ºC onto borosilicate glass. Borosilicate glass was used due to its smooth surface (< 1 nm RMS roughness) which is required for XRR.[284] Borosilicate substrates were used in optimisation and characterisation of NiO_x films in this chapter (aside from device work) unless otherwise stated. Using a scan speed of 10 mm/s, depositions were carried out at intervals between 120 – 480 cycles (6 – 24 min). It should be noted that one full movement of the substrate backwards and forwards under the gas manifold equals two cycles, as each point on substrate exposed to the metal channel twice. Thickness measurements were carried out by X-ray reflectivity (XRR) for calculation of the growth rate and GPC. The sample thickness against number of cycles and time is shown in Figure 10.2.

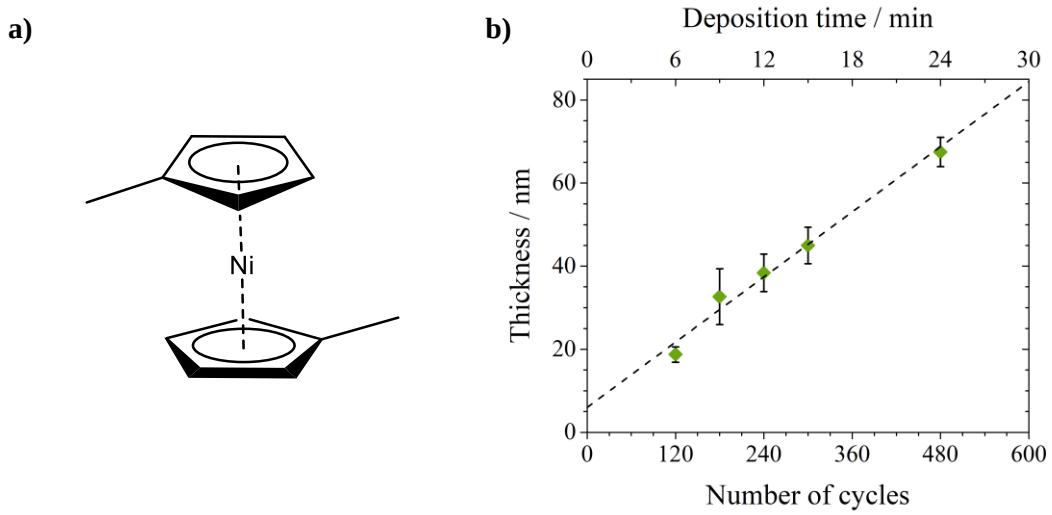

Figure 10.2 a) Bis(methylcyclopentadienyl)nickel precursor ($Ni(CpMe)_2$) and **b)** film thickness against number of cycles for NiO_x thin films deposited at 350 ºC from bis(methylcyclopentadienyl)nickel and oxygen onto borosilicate glass substrates using the Vertical Cambridge University Close Proximity AP-SALD reactor and a scan speed of 10 mm/s.

The film thickness as a function of number of cycles gave a linear relationship, as expected for a deposition using an AP-SALD reactor. A growth per cycle (GPC) of 0.14 nm/cycle was achieved. R- analysis was used to fit the linear equation between the variables:

$$d = (0.13 \pm 0.02)x + 6.01 \pm 2.78$$

Where *d* is the film thickness (nm) and *x* is the number of cycles. From the graph and equation, it is apparent that the linear regression line did not pass through the origin. This may have been due

to precursor depletion skewing the data to lower thickness values at a higher number of cycles. An R-squared value of 0.91 was calculated. This means there was statistically a strong relationship between the number of cycles and the film thickness, as is expected for an AP-SALD deposition.[254] Considering that the time per cycle was 3 s for a scan speed of 10 mm/s, a growth rate of 0.052 nm/s was calculated. This is 36 times faster than conventional vacuum ALD grown NiO_x which has been used in perovskite solar cells,[112] making AP-SALD a more suitable fabrication route to high throughput NiO_x, providing the quality of the films are suitable for devices.

Thickness measurements were also used to determine the GPC as a function of exposure time. The exposure time was varied by scanning the borosilicate substrate under the deposition head at different speeds. GPC against exposure time is plotted in Figure 10.3.

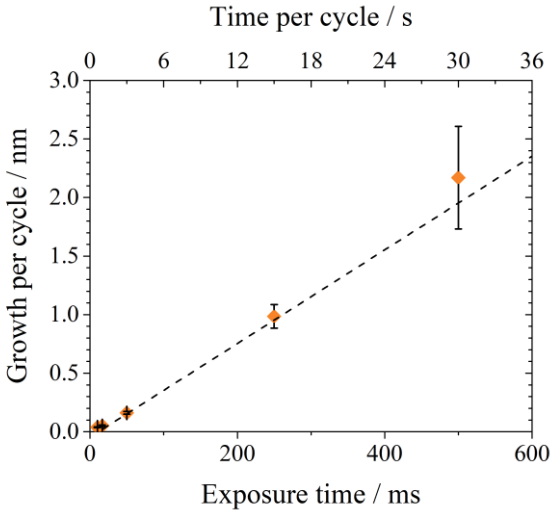

Figure 10.3 The growth per cycle (GPC) of NiO_x against exposure time of a point on the substrate to the metal channel. The exposure time was varied by changing the scan speed of the substrate under the gas manifold. Films were deposited onto borosilicate glass at 350 ºC.

The GPC increased linearly with exposure time, from 0.04 nm/cycle for a 10 ms exposure time to 2.17 nm/cycle for a 500 ms exposure time. Using R- analysis, the following linear relationship was determined:

$$GPC = (4.4 \times 10^{-3} \pm 1.6 \times 10^{-4})t - 4.8 \times 10^{-2} \pm 3.1 \times 10^{-2}$$

where *t* is exposure time. The small error in GPC against exposure time indicates that excellent thickness control can be achieved using this method.

For the data fitted, an R-squared value of 0.96 was calculated, meaning that 96 % of the variation in GPC was due to change in deposition time, such that the two were strongly related.[254] The linear relationship between GPC and exposure time is evidence that the deposition occurred under CVD conditions. Otherwise, for an ALD type reaction, the GPC value would plateau at long exposure times due to saturation of the surface sites (and subsequent self-limiting reactions). This is strongly supported by the GPC of 2.17 nm/cycle at a 500 ms exposure time; this thickness is well in excess of that of a monolayer of NiO_x (< 1 nm).[121]

Whilst many mechanical factors relating to the equipment set-up can cause CVD-type deposition (such as unbalanced flow rates, large spacing between the substrate and gas manifold), the deposition temperature was the cause of the CVD growth in this case. The decomposition temperature of $Ni(CpMe)_2$ is ~ 250 ºC, whilst the deposition temperature was 350 ºC.[240] Thus, reaction occurred at temperatures above the ALD window *via* a decomposition process. It should be noted that deposition was not possible below 290 ºC using this set of precursors and heat, making it impossible to achieve ALD conditions with this set-up. In future, ALD growth may be achievable using a more reactive oxygen source, such as O_3, or plasma- or UV- enhanced deposition. Nevertheless, whilst ALD type growth could not be achieved within the parameter space explored, benefits of sub-nanometre thickness control whilst achieving high deposition rates compared with conventional ALD methods were still achieved.

As the reaction mechanism was found to occur *via* a CVD process, the resultant NiO_x films will be referred to as AP-CVD NiO_x is the rest of the work to follow. Note that the equipment will still be referred to as the AP-SALD reactor or the VCUCP AP-SALD reactor, *i.e.* AP-CVD NiO_x was deposited using an AP-SALD reactor.

10.2 Characterisation of nickel oxide growth using the Vertical Cambridge University Close Proximity Reactor

10.2.1 Characterisation of the materials properties of nickel oxide thin films

XRD was used to determine the phase purity of the samples. The XRD data for a 100 nm film on ITO is presented in Figure 10.4. ITO was used as the substrate as this is a typical substrate used for *p-i-n* perovskite devices and will be used as the substrate for devices later in the chapter.

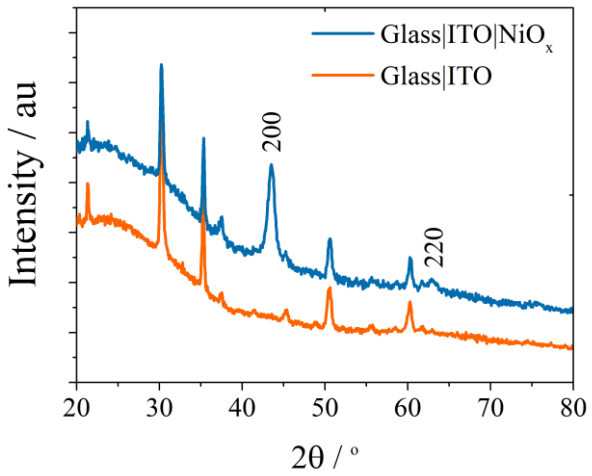

Figure 10.4 XRD pattern of a glass|ITO substrate (orange trace) and a 100 nm AP-CVD NiO_x film deposited on glass|ITO (blue trace). The NiO_x peaks were matched to PDF 00-47-1049 for cubic NiO_x.

Samples were phase pure, with all peaks corresponding to either cubic rock salt NiO (powder diffraction file 00-47-1049, space group *Fm3m*) or the ITO substrate. The samples possessed strong texturing, with the [200] peak dominating the diffraction profile at $2\theta = 43$ °. They also had small grains, as evident from the broadness of the [200] peak. Using the Scherrer equation, the crystallite size was calculated as 19 nm.[3,245] Taking the average *d*-spacing of the [200] peak for four NiO_x films, a lattice parameter of 4.152 Å was calculated, in good agreement with that reported for cubic rock-salt NiO.[121]

The sample morphology was probed using AFM. A 1 μm^2 micrograph of NiO_x on borosilicate glass is shown in Figure 10.5.

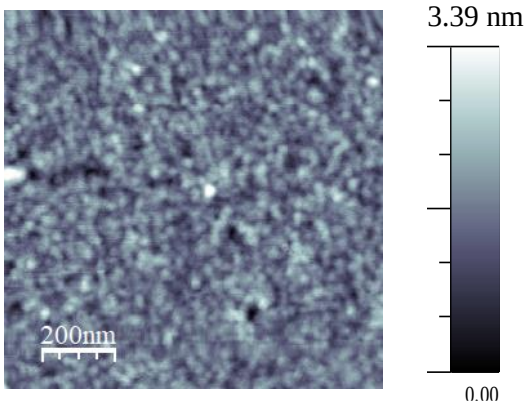

Figure 10.5 The 1 μm^2 AFM micrograph of a 30 nm AP-CVD NiO_x film on a borosilicate glass substrate. The scale bar is 200 nm, whilst the height bar is from 0 to 3.39 nm.

The NiO_x was very smooth, with an RMS roughness of 0.39 nm determined for the 1 μm^2 scan (note that this increased to 0.67 nm for a 5 μm^2 scan size). Additionally, there were no visible pin holes in the film, essential for preventing shunting within devices.[3] The AFM image also confirms that the films were small grained, with particle sizes of ~ 25 nm visible in the image. This correlates well with the estimated particle size from the XRD data of 19 nm.

10.2.2 Characterisation of the optical properties of nickel oxide thin films

Measurement of the optical properties of AP-CVD NiO_x was carried out to determine its suitability for solar cells. The UV-visible transmission spectra of 18 – 70 nm AP-CVD NiO_x films on borosilicate substrates are shown in Figure 10.6a.

Films showed good transmission in the visible region (400 – 1000 nm), where transmission was ~95 % for an 18 nm film and decreased with increasing thickness to ~70 % for 70 nm film. This is as expected from the Beer-Lambert law. Below ~ 325 nm, the transmission dropped significantly due to absorption by NiO_x in the UV region. Using a Tauc plot (inset, Figure 10.6a), where $(\alpha h\nu)^2$ was plotted against wavelength to account for the direct optical transition for NiO_x, the bandgap was determined as 3.75 eV.[3] This agrees well with the range of values reported for NiO_x.[119,285] The typical thickness of NiO_x in PHJ perovskite solar cells is around 20 nm. Thus, the AP-CVD NiO_x films were determined suitable as a window layer, with ~ 95 % of incident light transmitted to the perovskite layer at this thickness and the wide bandgap of 3.75 eV meaning little parasitic absorption from the NiO_x layer.

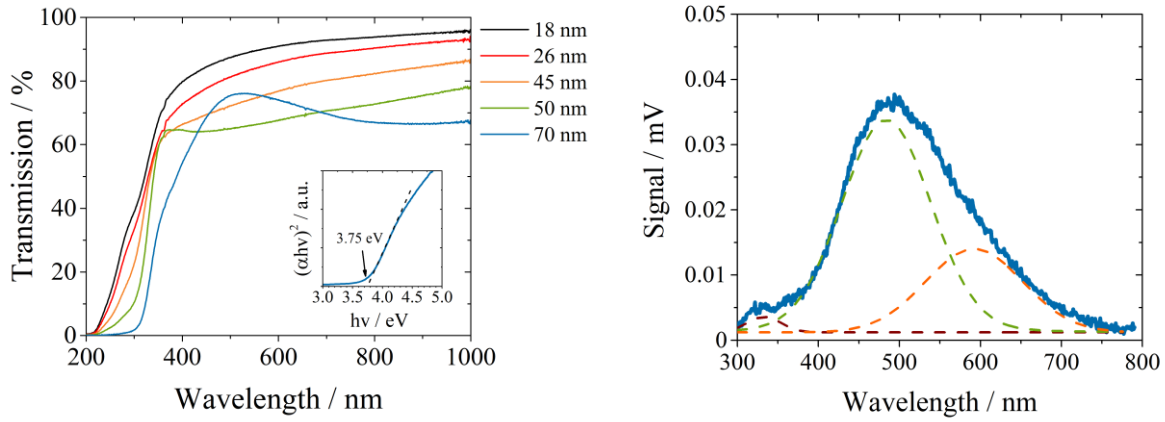

Figure 10.6 a) Transmission spectra of 18 – 70 nm AP-CVD NiO_x on borosilicate glass measured by UV-visible photo-spectroscopy and (inset) Tauc plot for a 50 nm AP-CVD NiO_x film on borosilicate glass. $(\alpha hv)^2$ is plotted against wavelength assuming a direct optical bandgap for NiO_x. b) Steady-state photoluminescence spectrum for a 100 nm AP-CVD NiO_x film on crystalline silicon, using an excitation wavelength of 266 nm.

The photoluminescence spectrum of a 100 nm NiO_x sample on single crystal silicon is shown in Figure 10.6b. Single crystal silicon was used as substrate due to its clean band-gap, such that emission from the substrate would not be measured (after subtraction of the background peak at ~ 1.1 eV). The PL spectrum in Figure 10.6b consists of a low intensity peak centred at 330 nm and a broad, asymmetric peak ~ 8 times more intense centred at 500 nm. The emission at 333 nm (3.72 eV) matched well with the bandgap calculated from the Tauc plot in Figure 10.6a (3.75 eV) and therefore was due to band-to-band recombination. The broad peak centred at ~ 500 nm occurred at a lower energy than the bandgap and was therefore due to emission from defect states, which dominated the PL spectrum. These point defects, such as metal and oxygen vacancies and interstitials, arise from non-stoichiometry and their emission energies have been previously characterised in detail for NiO_x.[285,286]

The signal was deconvolved into two bands centred at 484 and 592 nm (green and orange traces in Figure 10.6b), corresponding to two main defects within the films. The main defect present in NiO_x is the nickel vacancy, which gives rise to its *p*-type conductivity (in nickel deficient NiO_x). Recombination of an electron trapped within a nickel vacancy with a hole in the valence band is commonly assigned to emission between 460 – 500 nm.[285,286] This matches well with the fitted peak at 484 nm, therefore nickel vacancies are the main defect present within the samples. Regarding the band centred at 592 nm, recombination at an oxygen interstitial gives rise to emission at ~ 600 nm.[285] Oxygen interstitials can also be present in nickel deficient/oxygen abundant NiO_x and are likely to be responsible for the tail of the peak towards longer wavelengths.

10.2.3 Characterisation of the electronic and electrical properties of nickel oxide thin films

XPS gives information about the stoichiometry and doping of NiO_x and can be used to determine the presence of defects within samples. The stoichiometry is determined from the core level spectra, as was performed for BiOI in previous chapters, whilst the doping type of the films can be determined from the valence band spectrum. XPS measurements of a 20 nm NiO_x film on a silicon substrate were taken. Silicon was used to provide an electrically conductive contact to prevent the sample from charging throughout the measurement. The Ni $2p_{3/2}$ and O 1*s* core level spectra are shown in Figure 10.7a and b. The area of each spectrum was fitted and scaled using the corresponding relative sensitivity factor. The films contained 47% nickel and 53% oxygen, amounting to a stoichiometry of $NiO_{1.13}$. The nickel deficiency of the samples indicates the presence of nickel vacancies, which is known to result in *p*-type conductivity of NiO_x. The presence of nickel vacancies was further confirmed by studying the Ni $2p_{3/2}$ spectrum. On the formation of nickel vacancies, two holes sit in the vacant site within the lattice so that the overall charge is neutral. These holes are localised on nearby Ni^{2+} ions, creating Ni^{3+}.[123] Due to differences in oxidation state, Ni^{2+} and Ni^{3+} have different binding energies resulting in separate peaks in the Ni $2p_{3/2}$ core level spectrum. Peaks corresponding to both ions are present in Figure 10.7a; the Ni^{3+} peak centred at 855.5 eV and the Ni^{2+} peak at 853.8 eV, meaning that nickel vacancies were present in AP-CVD NiO_x.[123]

Additional evidence of *p*-doping by nickel vacancies was seen by considering the valence band spectrum of NiO_x, shown in Figure 10.7c. The valence band position was determined from the intercept of the gradient of the band edge with the background, to give a valence band to Fermi level offset value of 0.6 eV. The bandgap of NiO_x was previously determined as 3.75 eV. This means that the Fermi level sat around a sixth of the way into the bandgap (at 0.6 eV above the valence band maximum), implying that the samples were *p*- doped.

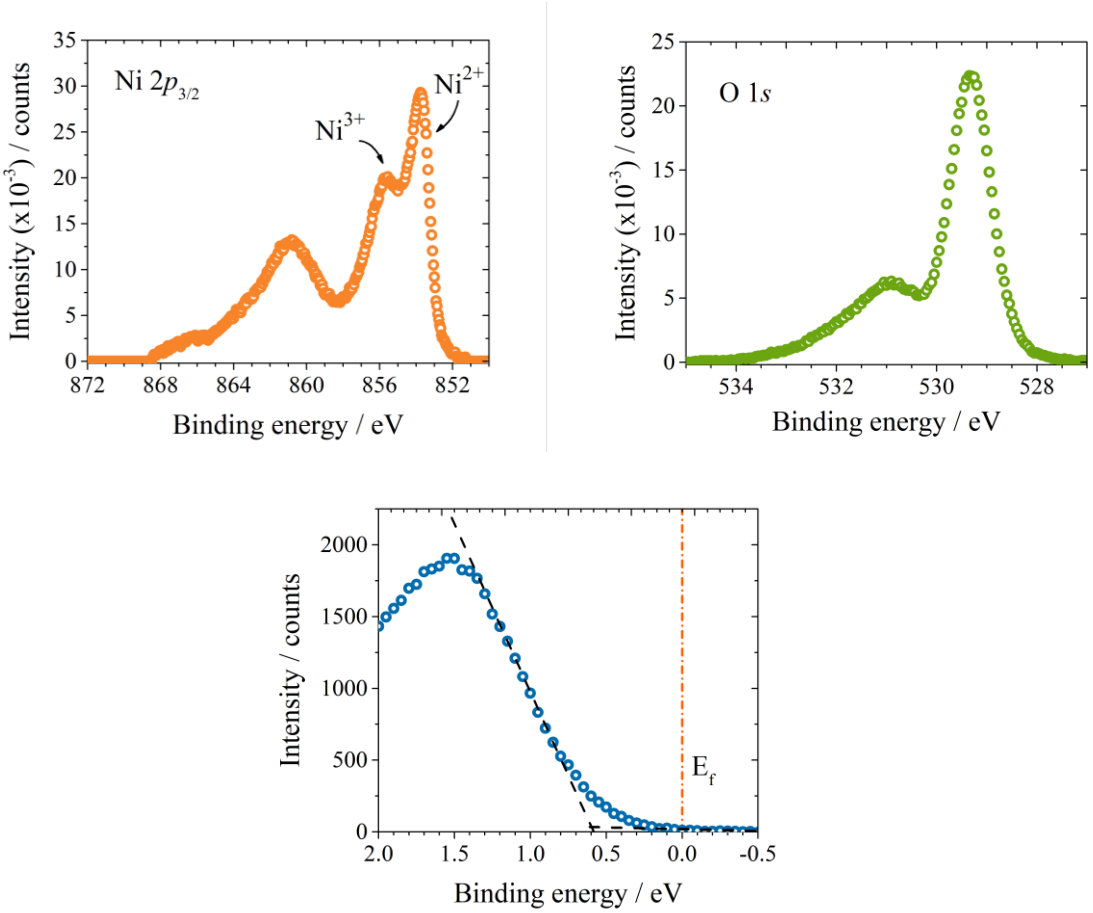

Figure 10.7 a) Ni $2p_{3/2}$ and b) O 1*s* core level spectra and c) the valence band spectrum for AP-CVD NiO_x deposited at 350 ºC onto a crystalline silicon substrate.

10.2.3.1 Introduction to Mott-Schottky measurements

Mott-Schottky plots can be used to determine the carrier concentration of a semiconductor.[287] A metal-semiconductor-electrolyte device is fabricated, where the Fermi-level of the semiconductor is below that of the electrolyte to form a Schottky barrier (for a *p*-type semiconductor) at this interface (Figure 10.8a). An ohmic contact is present at the metal-semiconductor interface.[288] During measurement, a positive bias, V, is applied to the metal contact (Figure 10.8b), lowering the Fermi level of the semiconductor and therefore reducing the height of the Schottky barrier to $V_{bi} - V$. As a result, following equation **10.33**, the depletion width, *w* (m), at the Schottky junction is reduced (Figure 10.8c).[288]

$$w = \left[\frac{2\varepsilon}{qN}(V_{bi} - V)\right]^{1/2} \quad \textbf{(10.33)}$$

Where V is the applied bias (V), V_{bi} is the built-in potential at the Schottky barrier (the difference in energy between the Fermi level of the semiconductor and the electrolyte, V), N is the carrier concentration (cm^{-3}), which is positive for holes and negative for electrons, q is elementary charge (C) and ε is the dielectric constant of the semiconductor ($F\ m^{-1}$).

As capacitance is given by:

$$C = \frac{A\varepsilon}{w} \quad \textbf{(10.34)}$$

where C (F) is capacitance and A (m^2) is the area of the capacitor plates, through substitution of equation **10.33** into **10.34**, carrier concentration can be probed directly by measuring capacitance as a function of applied bias:[247,288]

$$\frac{1}{C^2} = \frac{-2}{qA^2\varepsilon N}(V - V_{bi}) \quad \textbf{(10.35)}$$

In this case, C^{-2} is plotted against V. N is calculated from the gradient (negative for a p-type semiconductor and positive for an *n*-type semiconductor, Figure 10.8e). V_{bi} is deduced from the intercept of the plot with the *x*-axis (*i.e.* at flat band conditions, Figure 10.8d, where V = V_{bi}).[247,288]

The capacitance is measured by electrochemical impedance spectroscopy, where a small AC voltage is applied at a range of frequencies, ω, and the imaginary part of the impedance, Z'', is used to calculate capacitance:[247,287]

$$C = \frac{-1}{\omega Z''} \qquad \textbf{(10.36)}$$

The measurement is repeated at different applied bias values to generate a Mott-Schottky plot.

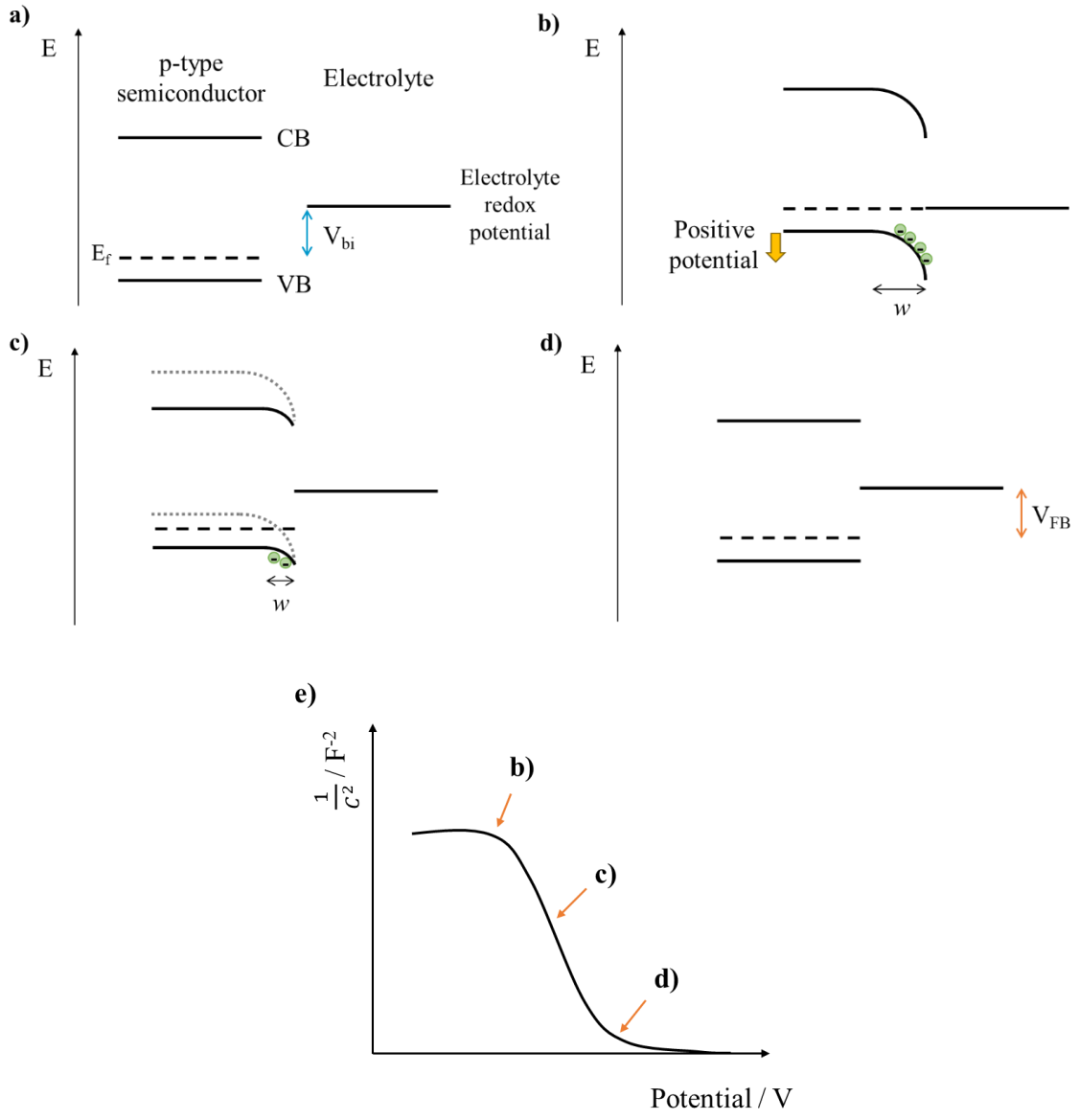

Figure 10.8 a) Energy levels of a *p*-type semiconductor and a redox active electrolyte before contact, b) the formation of a Schottky barrier when the *p*-type semiconductor and redox active electrolyte are brought into contact, where *w* is the depletion width, c) reduction of the depletion width and band-bending at the Schottky barrier when a positive bias is applied to the *p*-type semiconductor, d) flat band conditions on further application of positive bias and e) a typical Mott-Schottky plot for a *p*-type semiconductor, where points b, c and d refer to figures b, c and d.

10.2.3.2 Mott-Schottky measurements of AP-CVD NiO_x

Mott-Schottky plots of AP-CVD NiO_x were measured using the method reported by Thimsen *et al* and described in section 5.4.11.[112,247] Fluorine doped tin oxide (FTO) was used as the substrate to provide an ohmic contact to NiO_x, whilst an electrolyte containing 1 M sodium sulphate and 0.1 M sodium dihydrogen phosphate provided a Schottky junction at the NiO_x|electrolyte interface. The Mott-Schottky plot is shown in Figure 10.9.

From Figure 10.9, the gradient was frequency dependent. This is a common drawback of EIS for polycrystalline samples and is due to the non-uniformity of a polycrystalline surface (both atomically and energetically), leading to non-ideal capacitance behaviour over the electrode area.[289] As a result, the capacitance shows frequency dependence. Additionally, trap de-filling and instrument interference occur at high and low measurement frequencies which also influence the measured capacitance. To account for this, similar to the method of Thimsen, the frequency range where the imaginary component of the impedance was constant was used (between 15 kHz – 20 kHz).[247]

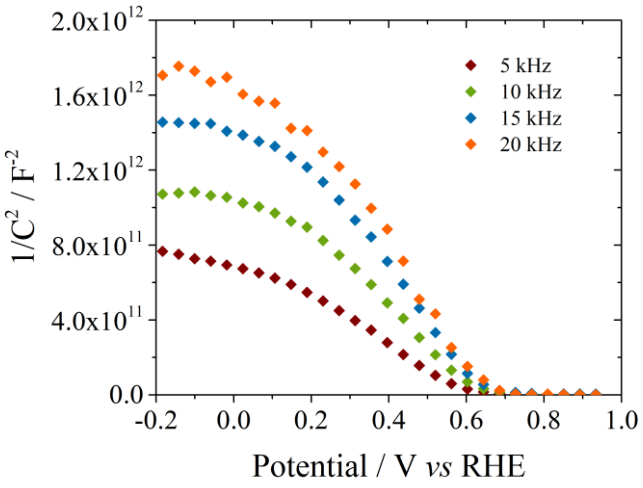

Figure 10.9 Mott-Schottky plots ($1/C^2$ against potential) measured at frequencies 5 – 20 kHz for FTO|NiO_x in a 1 M sodium sulphate and 0.1 M sodium dihydrogen phosphate electrolyte at pH 12.

A negative gradient was obtained. This indicates that the samples were *p*-doped,[288] in good agreement with the XPS valence band data. Over several samples, an average carrier concentration of $5.7\times10^{19} \pm 2.0\times10^{19}$ cm^{-3} and a flat-band potential of 0.68 ± 0.02 V *vs* RHE were calculated. The carrier concentration was relatively high, but in good agreement with the literature value for ALD NiO_x annealed in air at 300 ºC, for which a carrier concentration of 2.7×10^{19} cm^{-3} was calculated.[3,112] Note that sample roughness often results in an overestimate of the carrier

concentration. Similarly, the flat-band potential matches well with the literature value of 0.69 ± 0.01 V *vs* RHE (reversible hydrogen electrode). Thimsen *et al.* estimated the potential difference between the RHE and vacuum as 4.43 eV (RHE *vs* vacuum).[247] Therefore, the work-function of NiO_x (the energy required to remove an electron from the Fermi level to the vacuum level) is deduced as 5.11 ± 0.02 eV. Combining this with the XPS analysis in Figure 10.7, where the valence band was determined to sit 0.6 eV below the Fermi level, the position of the valence band maximum is estimated at ~ 5.7 eV *vs* vacuum. The work-function and valence band position are in good agreement with literature values for vacuum and solution processed NiO_x used in solar cell applications.[112,118,247]

Given that the position of the Fermi level and valence band have been determined using XPS and EIS, the carrier concentration of the films can also be determined by calculating the density of states in the valence band, N_v. This is determined from:[247]

$$N_v = 2\left(\frac{2\pi m_h^* kT}{h^2}\right)^{3/2} \quad \textbf{(10.37)}$$

Where N_v is the density of states in the valence band (cm^{-3}), m_h^* is the hole effective mass (reported as $0.8m_e$ – $1.0m_e$),[124] k is Boltzmann's constant (J K^{-1}) , T is temperature (K) and *h* is Planck's constant (J s). Using the literature values for m_h^*, N_v is calculated as 1.8×10^{19} cm^{-3} – 2.5×10^{19} cm^{-3}. This is smaller than the estimated carrier concentration from the Mott-Schottky plot, implying that EIS gives a large overestimation of the carrier concentration (as is commonly reported).

Using the positions of the Fermi level and valence band maximum previously determined, the carrier concentration (*p*, cm^{-3}) can be calculated from:

$$p = N_v exp\left(\frac{-(E_f - E_v)}{k_b T}\right) \quad \textbf{(10.38)}$$

where E_f is the Fermi energy (eV) and E_v is the energy of the valence band maximum (eV). Using N_v from equation **10.37** and the valence band to Fermi level offset determined from XPS measurements, a carrier concentration of 1×10^9 - 1.4×10^9 cm^{-3} is calculated. Clearly there is a severe discrepancy between the calculated carrier concentration and that determined by EIS (2.7×10^{19} cm^{-3}). A possible reason for this is pinning of the Fermi level at a defect transition level 0.6 eV above the VBM. Osorio-Giullén *et al*. calculate a defect transition level for the nickel vacancy with a low formation energy (0.25 eV) situated 0.7 eV above the VBM.[122] This is in reasonable agreement with the Fermi level position determined from XPS, which may suggest

Fermi level pinning at this defect transition level in AP-CVD NiO_x. Future work to more accurately determine the carrier concentration of NiO_x, for example through methods such as deep level transient spectroscopy, microwave conductivity measurements or by measuring field effect transistors, would be useful. It should be noted that Hall effect measurements were attempted but gave invalid results due to the poor mobility of the NiO_x.

Work so far has shown that it is possible to deposit phase pure, pin-hole free, *p*-type NiO_x by an AP-CVD mechanism using the Vertical Cambridge University Close Proximity AP-SALD reactor. Inspired by work in the literature, the next section explores the performance of AP-CVD NiO_x in perovskite solar cells.

10.3 *p-i-n* perovskite devices using nickel oxide as the *p*-type layer

Perovskite devices were made to the structure ITO|AP-CVD-NiO_x|$FA_{1-y}MA_yPbI_3$|PCBM|Al (Figure 10.10). A mixed cation formamidinium-methylammonium lead iodide perovskite was used, where the molar ratio of formamidinium (FA):methylammonium (MA) was 1:5.6. Thus, in $FA_{1-y}MA_yPbI_3$, $y \simeq 0.85$ based on the molar ratio and assuming 100% incorporation of precursors. $FA_{0.15}MA_{0.85}PbI_3$ will be commonly referred to as 'perovskite' throughout this section.

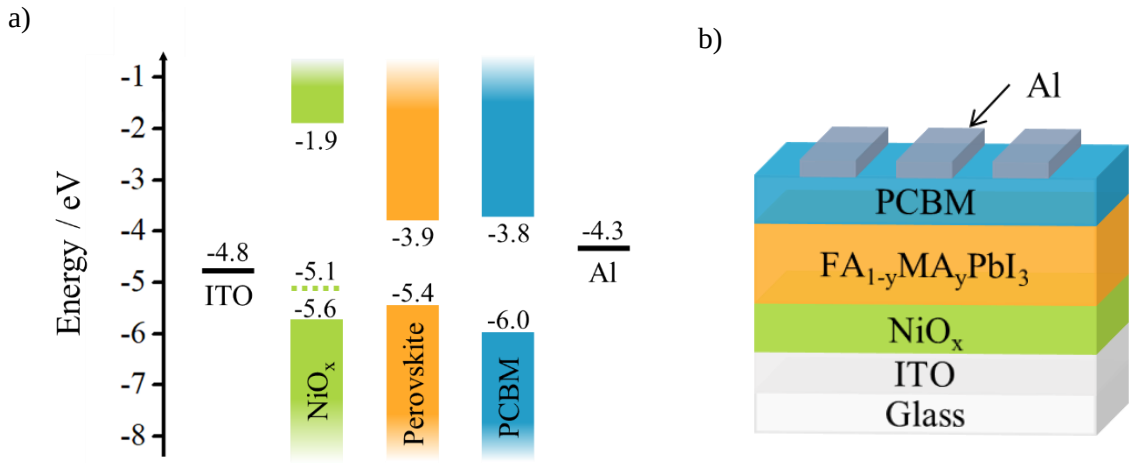

Figure 10.10 a) Energy alignment and b) schematic of the ITO|AP-CVD-NiO_x|$FA_{0.15}MA_{0.85}PbI_3$|PCBM|Al device stack. The band and Fermi level positions are based on the XPS and EIS measurements for AP-CVD NiO_x and are taken from references [290] for ITO, PCBM and [3] for Al, perovskite.

10.3.1 Characterisation of the structure and morphology of the perovskite device components

In Figure 10.5, the morphology of AP-CVD NiO_x was studied on glass using AFM. However, it was also necessary to probe its morphology on ITO, the transparent electrode used in devices. Figure 10.11 shows AFM images of the bare ITO substrate (a) and a 30 nm layer of AP-CVD NiO_x on ITO (b).

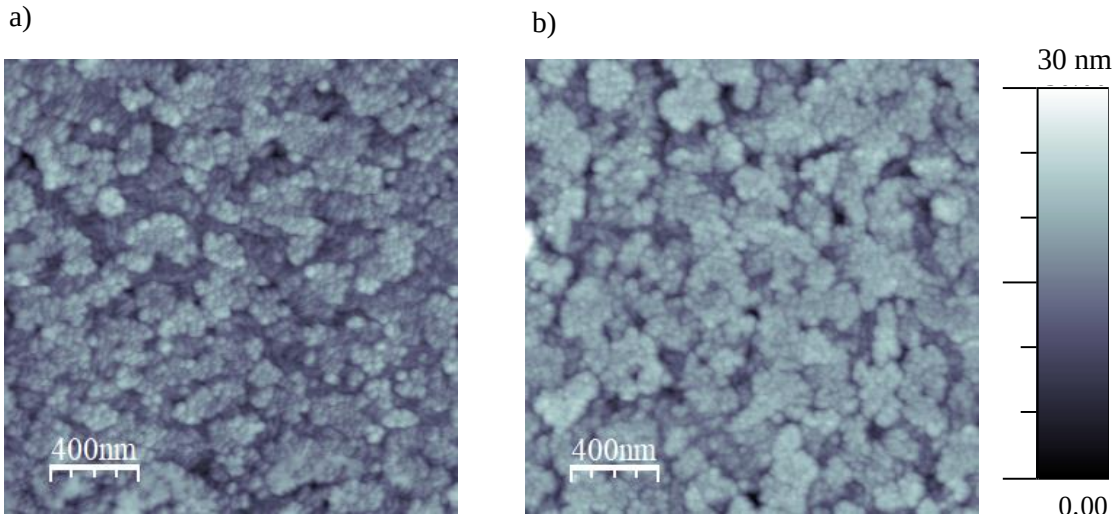

Figure 10.11 2 μm^2 AFM images of a) ITO and b) ITO|AP-CVD NiO_x (30 nm). The scale bar represents 400 nm whilst the height bar is from 0 to 30 nm.

From the images, AP-CVD NiO_x covered the ITO substrate conformally, following the morphology of the surface. This was confirmed by the similarity in RMS roughness for the two samples; 3.22 nm for ITO compared to 3.34 nm for ITO|AP-CVD NiO_x. The NiO_x films also appeared pin-hole free, essential to achieve a high shunt resistance in devices.[1,3]

Devices were fabricated using a one-step spin casting method outlined in the Methods and Materials section. A cross-sectional SEM image of the device stack is shown in Figure 10.12a. No pinholes were visible in the NiO_x layer, effectively shielding the perovskite layer from the ITO electrode. However, it should be noted that the NiO_x thickness was around 75 nm for the sample imaged; the coverage may have been different for thinner NiO_x films. Figure 10.12b shows a top down SEM image of perovskite on AP-CVD NiO_x. The perovskite layer was compact, essential for preventing shunting within devices. Measuring the diameter of 30 random perovskite particles, the average diameter was 134 ± 59 nm. This particle size is typical for perovskite films deposited by the one-step processing route with the solvent combination used.[3,112]

a) b)

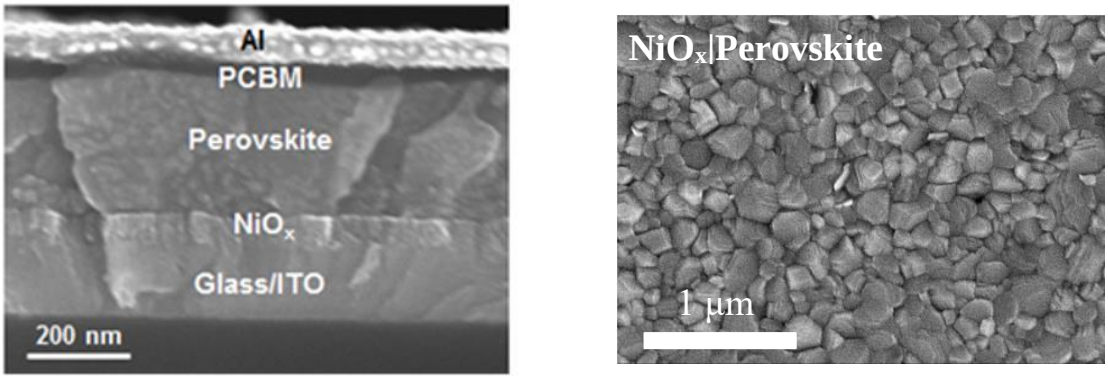

Figure 10.12 a) cross-sectional SEM image of the ITO|AP-CVD $NiO_x|FA_{0.15}MA_{0.85}PbI_3|PCBM|Al$ device stack (scale bar is 200 nm) and b) top down SEM image of AP-CVD $NiO_x|FA_{0.15}MA_{0.85}PbI_3$ (scale bar 1 µm).[3]

X-Ray diffraction was used to study the phase purity and crystallite size of the perovskite layer. A single crystal silicon wafer (c-Si) was used as the substrate to give a flat background, so that any broad, amorphous signals present could be attributed to either the perovskite film or NiO_x. The XRD pattern for c-Si|AP-CVD $NiO_x|FA_{0.15}MA_{0.85}PbI_3$ is shown in Figure 10.13.

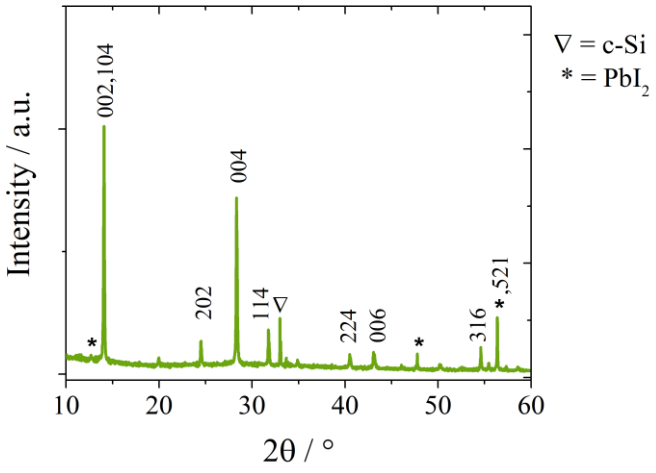

Figure 10.13 The XRD traces for Si|AP-CVD $NiO_x|FA_{1-y}MA_yPbI_3$. The triangle represents peaks from the silicon substrate, whilst the asterisk (*) represents PbI_2 impurity. $FA_{0.15}MA_{0.85}PbI_3$ was fitted to the cystallographic information file from reference [291].

Small peaks corresponding to PbI_2 were present in the XRD data at 2θ = 12.7 º, 47.8 º and 56.4 º, meaning samples contained a small amount of phase impurity.[3,292] This came from unreacted precursor and is commonly reported for perovskite films. The perovskite showed some *c*-axis

texturing, with the [002] and [004] peaks the most dominant. The sample was also highly crystalline, demonstrated by the flat background which indicates the absence of amorphous material. Scherrer analysis was performed on several peaks of the XRD data for two samples. Taking an average of all the values, the estimated crystallite size of $FA_{0.15}MA_{0.85}PbI_3$ was 99 ± 17 nm. This is within the lower error bound of the crystallite size estimated from the SEM image in Figure 10.12, as summarised in Table 10.1.

Table 10.1 The estimated size of formamidinium methylammonium lead iodide crystallites on AP-CVD NiO_x as determined from XRD and SEM data. The Scherrer equation was used to estimate the average crystallite size from XRD data, taking the average from a number of peaks over two samples. From the SEM data the average diameter of 30 random particles was measured using imageJ software.

	XRD	SEM
Estimated perovskite crystallite size / nm	99 ± 17	134 ± 59

10.3.2 Electrical characterisation of perovskite devices using nickel oxide as the hole transport material

The current-voltage characteristics of ITO|AP-CVD NiO_x|$FA_{1-y}MA_yPbI_3$|PCBM|Al devices were measured under solar simulation to evaluate their performance. The JV curves for the best performing device is shown in Figure 10.14.

a)

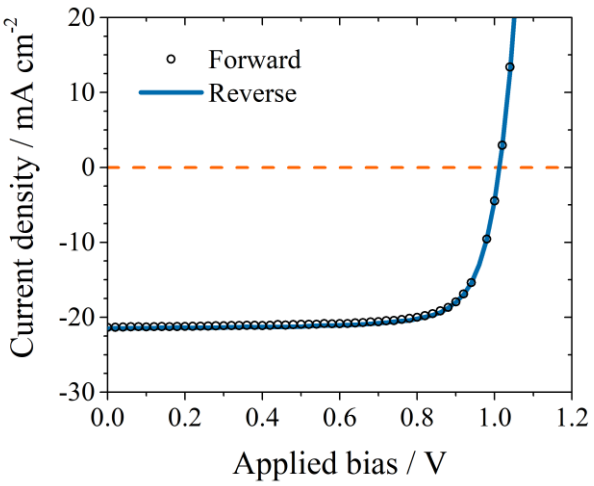

b)

J_{SC}	21 mA cm^{-2}
V_{OC}	1.01 V
FF	76.9 %
PCE	16.6 %

Figure 10.14 **a)** The J-V response of the champion ITO|AP-CVD NiO_x|$FA_{0.15}MA_{0.85}PbI_3$|PCBM|Al device under solar simulation. The black circles show the forward scan (0 to 1.2 V) whilst the solid blue line shows the backwards scan (1.2 to 0 V). **b)** lists the J_{SC}, V_{OC}, FF and PCE for the champion device.

The efficiency of the champion device was 16.6 %. This is comparable to champion efficiencies in the literature; solution and vacuum processing routes to NiO_x have both achieved 16.5 to 17.5 %,[126,130,134] whilst ALD NiO_x has achieved 16.4%.[112] It should be noted that in most of these cases methylammonium lead iodide was used. There was a good match between the forward and reverse scans, thus hysteresis was negligible. To better evaluate the device performance, the average metrics from several identical batches of devices are summarised in Table 10.2. The average PCE was 14.8 ± 0.69 %. The average efficiency for devices using AP-CVD NiO_x was again comparable to the best in the literature, where the best devices incorporating solution or vacuum processed NiO_x achieved 14.9 – 15.3 % PCE.[126,130,134]

Table 10.2 The device metrics for ITO|AP-CVD NiO_x|$FA_{0.15}MA_{0.85}PbI_3$|PCBM|Al devices. Values show the mean ± standard deviation (over ~ 20 devices).

J_{SC} / mA cm^{-2}	V_{OC} / V	FF / %	PCE / %	Champion device PCE / %
19.7 ± 0.24	1.00 ± 0.03	74.6 ± 0.51	14.8 ± 0.69	16.6

External quantum efficiency measurements give information about current losses within a device. The EQE of the best performing device is shown in Figure 10.15.

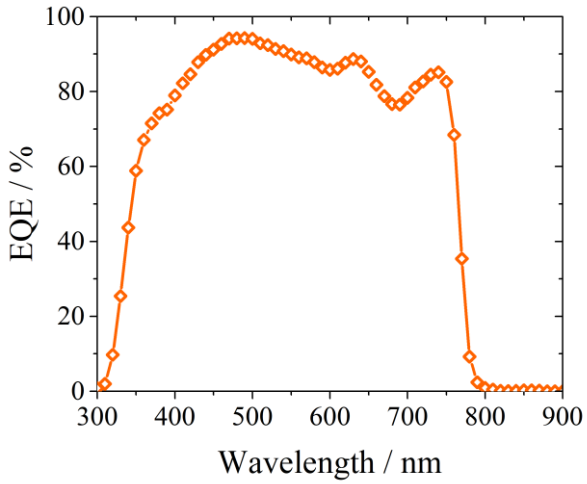

Figure 10.15 The EQE curve of the champion ITO|AP-CVD NiO_x|$FA_{0.15}MA_{0.85}PbI_3$|PCBM|Al device.

The EQE had a steep onset at around 780 nm (1.58 eV). This corresponds well with literature values of the bandgap of the perovskite.[3] The EQE peaked at a wavelength of 490 nm, at which 94 % of incident photons were converted into current. Additionally, between 410 and 750 nm, the EQE was above 80 % for all wavelengths aside from a slight drop at 660 – 710 nm. As well as being due to the excellent absorption, transport properties and low exciton binding energy of perovskite, the high EQE demonstrates excellent charge collection at the perovskite|charge transport material interfaces, meaning that AP-CVD NiO_x extracted holes efficiently.[3] Integration of the EQE over the solar spectrum gives the J_{SC}, as shown in equation **2.8**. Integration of the EQE curve in Figure 10.15 gave a short-circuit current density of 21.45 mA cm^{-2}. This is in good agreement with the value of 21.49 mA cm^{-2} determined by current-voltage measurements under solar simulation (Figure 10.14).

Despite comparable performance of perovskite devices using AP-CVD NiO_x with the best NiO_x based devices in the literature, sources of efficiency loss were still present in devices.

The best V_{OC} recorded was ~ 550 meV smaller than the perovskite bandgap, meaning that over a third of the maximum achievable voltage was lost. Recent works have highlighted the importance of optimising the HTM|perovskite interface to reduce losses at this interface.[130,293] Reducing the density of defects at the NiO_x surface may reduce interfacial non-radiative recombination, thereby reducing voltage losses at this interface. Additionally, reducing the carrier concentration of NiO_x may make it suitable in *p*-type TFT applications to enable switching.

10.4 A strategy towards reducing the density of nickel vacancies in nickel oxide

Nickel vacancies give rise to the *p*-type conductivity of non-stoichiometric NiO_x films, where $x > 1$.[123] Whilst a higher density of nickel vacancies increases the work-function of the films, which may in turn improve the V_{OC} of perovskite devices, this must be balanced with the density of defect states at the NiO_x|perovskite interface which act as non-radiative interfacial recombination centres. Annealing metal oxides in metal rich environments has been demonstrated to fill metal vacancies. For example, Iza *et al.* demonstrated that annealing ZnO in a Zn-rich environment reduced the intensity of the PL peak attributed to zinc vacancies.[294] This inspired experiments annealing NiO_x in a nickel rich environment with the aim to reduce the density of nickel vacancy defects.

20 nm NiO_x was deposited onto sputtered Ni films as the source of nickel. Initially films were annealed in an argon furnace, however residual oxygen within the furnace resulted in complete oxidation of the stack to form transparent NiO_x. To prevent this, films were instead annealed face down onto Ni foil in a vacuum chamber for 3, 10 and 20 minutes at 700 ºC, 1 x 10^{-3} mbar. XPS was used in two ways to determine whether nickel vacancies were filled during the annealing; (i) by analysing the ratio of Ni^{2+}/Ni^{3+} using the O 1*s* core level spectrum and (ii) by studying the position of the Fermi level before and after annealing.

As mentioned previously, charge compensation on the formation of nickel vacancies results in Ni^{3+} formation.[123] Electrons in oxygen bound to Ni^{3+} in the lattice have a different binding energy (531 eV)[295] to those in oxygen bound to Ni^{2+} (529 eV).[123] Thus, the ratio of the two peaks indicates the relative doping of the samples. Figure 10.16 a and b show the O 1*s* spectra for as deposited NiO_x and after annealing for 20 minutes, whilst Figure 10.16c shows the fraction of the O 1*s* signal corresponding to Ni^{2+} and Ni^{3+} against annealing time. The Ni^{3+} content of the films increased relative to Ni^{2+} with annealing, from 41 % before annealing to > 50 % for all annealing times. This means that the density of nickel vacancies increased with annealing. The aim of this experiment was to fill nickel vacancies; therefore, the experiment was unsuccessful.

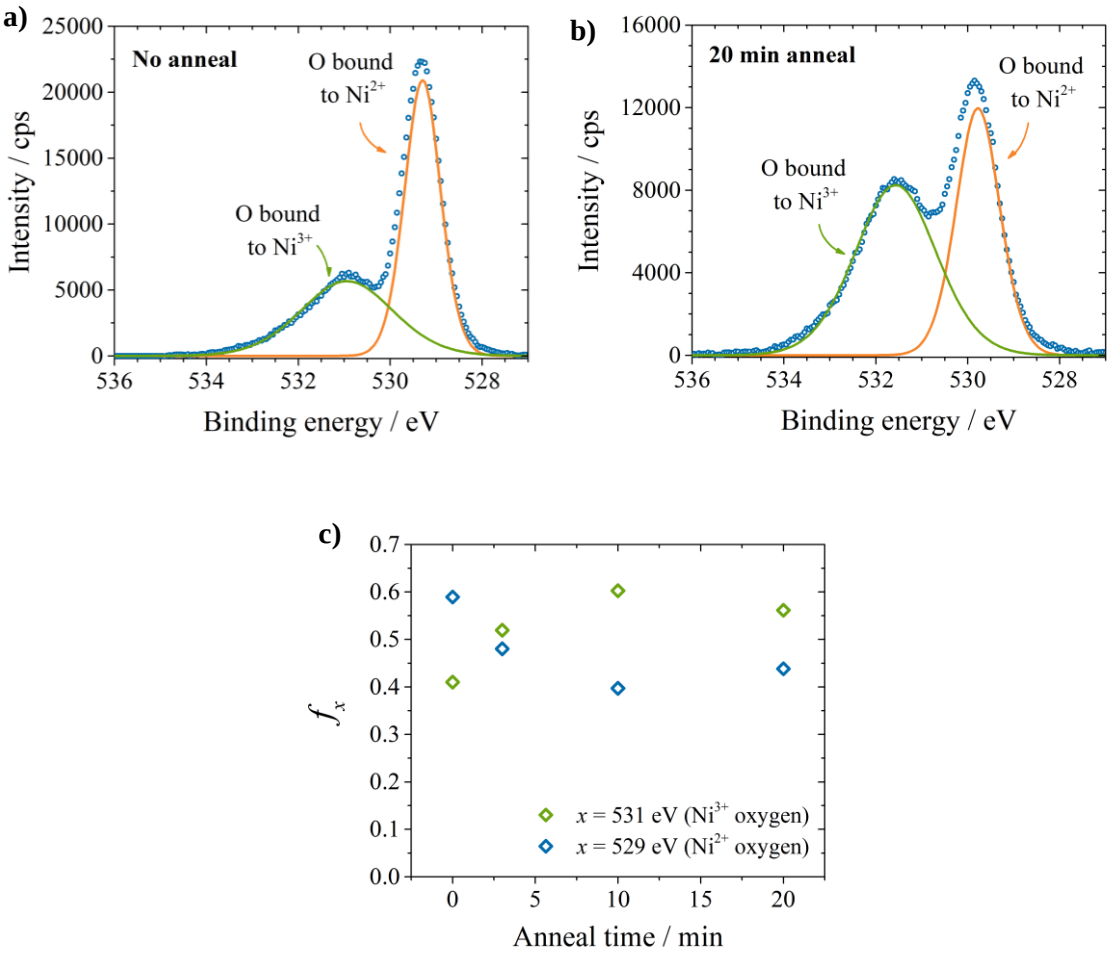

Figure 10.16 a) The XPS O 1*s* core level spectra of Ni|NiO_x samples a) as deposited and b) after annealing face-down on Ni foil under vacuum for 20 minutes. Figure c) shows the fraction contribution of the peaks at 529 eV (blue, corresponding to oxygen bound to Ni^{2+}) and 531 eV (green, corresponding to oxygen bound to Ni^{3+}).

Evaluation of the Fermi level position could also be used to study changes in the density of nickel vacancies in NiO_x; a reduction in the density of nickel vacancies would be expected to cause the Fermi level to move closer to mid-gap corresponding to a lower level of *p*- type doping. The valence band spectra for as deposited and annealed samples were measured, and the valence band-Fermi level offset was approximated from the intercept of the gradient of the leading edge with the background. The values are presented in Table 10.3.

Table 10.3 The valence band to Fermi level offset for Ni|NiO_x samples annealed face down on Ni foil for 0 – 20 minutes, determined from the intercept of the leading edge of the valence band spectra with the background signal.

Anneal time / min	VB – E_f / eV
0	0.59
3	0.94
10	0.97
20	0.92

With annealing, the valence band to Fermi level offset increased by > 300 meV, meaning it moved closer to mid-gap. However, an increase in intensity of sub-gap absorption was present for annealed samples, indicating the formation of defect states. Whilst the increase in Fermi level with annealing in a Ni- rich environment might suggest a reduction in density of nickel vacancies, the similar position of the Fermi level for all annealing times may be evidence of Fermi level pinning. Such pinning would be caused by a defect formed during the annealing process, supported by the increase in sub-gap signal above the band-edge. A similar shift in Fermi level was previously seen in vacuum annealing studies of NiO_x, where the formation of oxygen vacancies gave rise to Ni^0 defects within the films which pinned the Fermi-level and caused an increase in signal above the valence band edge.[296] Meanwhile, defect computations have predicted a low defect formation energy of ~1.2 eV for oxygen vacancies, with the defect level situated ~0.6 eV above the valence band edge.[122] Thus, comparison with the literature indicates that Ni^0 defects formed on annealing may have caused Fermi level pinning in the samples.

This was further supported by analysing the Ni $3p_{3/2}$ core level spectrum. Figure 10.17a shows the Ni $2p_{3/2}$ spectra of the Ni|NiO_x films before (0 min) and after annealing for 3, 10 and 20 minutes. With annealing, broadening at the onset of the signal at ~853 eV occurred. Fitting of the spectra revealed that as well as the Ni^{2+} and Ni^{3+} peaks at binding energies 854 and 856 eV (Figure 10.17b), a third peak centred at 853 eV emerged for annealed samples (Figure 10.17c). This has previously been attributed to metallic Ni^0 in the literature.[296] Note that the Ni^0 signal at 853 eV was present in all annealed samples, and is presented as a percentage of the fitted Ni $3p_{3/2}$ spectrum in Figure 10.17d. The percentage of Ni^0 was non-linear with annealing time, which may have been due to overshooting or fluctuations of the heat tape (which had temperature fluctuations of up to ± 50 ºC). Metallic nickel may have formed due to oxygen loss (the formation of oxygen vacancies) under the annealing conditions.[296] Whilst the samples were annealed face down on Ni foil, the pressure at the sample surface would still be expected to be lower than atmospheric due to the vacuum conditions within the furnace (1 x 10^{-3} mbar). Thus, on oxygen vacancy formation,

reduction of Ni^{2+} to Ni^{0} by the two resultant electrons in the lattice would be expected to maintain charge neutrality.

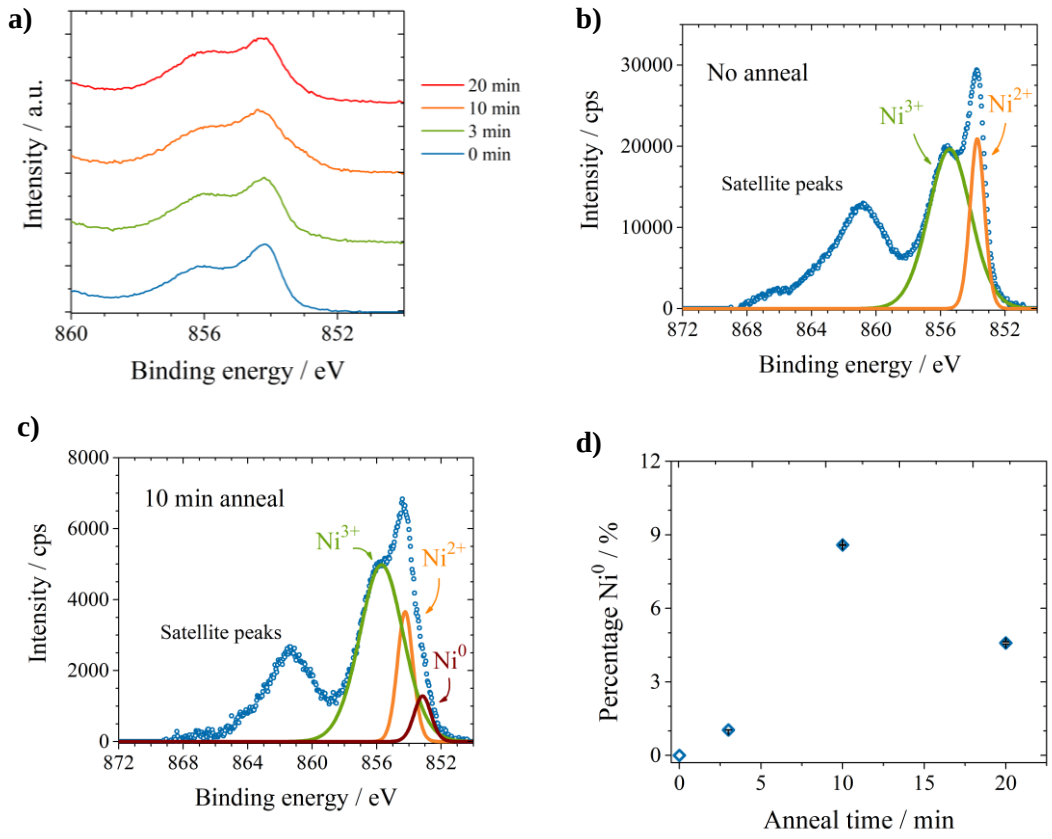

Figure 10.17 a) The XPS Ni $2p_{3/2}$ core level spectra of Ni|NiO_x samples as deposited (blue) and after annealing face-down on Ni foil under vacuum for 3 min (green), 10 min (orange) and 20 min (red), b) the fitted Ni $2p_{3/2}$ spectrum of Ni|NiO_x as-deposited, c) the fitted Ni $2p_{3/2}$ spectrum of Ni|NiO_x after annealing for 10 minutes under vacuum face-down on Ni foil and d) the percentage of Ni^0 contributing towards the Ni $2p_{3/2}$ core level spectra for as-deposited Ni|NiO_x samples and samples annealed under vacuum face-down on Ni foil for up to twenty minutes.

XPS data from these preliminary experiments showed that annealing Ni|NiO_x films face down on Ni foil at 700 ºC and 1 x 10^{-3} mbar for up to 20 minutes resulted in an increase in both Ni^{3+} and Ni^0 species within NiO_x. Whilst the origin of Ni^0 was speculated to come from charge compensation on formation of oxygen vacancies within the lattice, the overall finding was that this set of experiments were unsuccessful (*i.e.* filling of nickel vacancies did not occur). In a successful experiment, filling of nickel vacancies by annealing NiO_x in a nickel rich environment would cause an increase in the Ni^{2+} content of the films. Whilst it would be interesting to further probe the reason behind the increase in both Ni^{3+} and Ni^0 content under these annealing conditions, it would be more useful in future to repeat the experiments (annealing NiO_x in a Ni-rich environment) in an inert atmosphere at 1 atm to eliminate (or reduce) the possibility of

oxygen vacancy formation. This would require a furnace which can be fully evacuated to remove oxygen before filling with an inert gas such as argon; such equipment was not available when these experiments were carried out.

10.5 Conclusion

In this chapter, deposition of NiO_x using the Vertical Cambridge University Close Proximity AP-SALD reactor was reported. Growth rate characterisation using XRR showed that deposition occurred by an atmospheric pressure CVD decomposition type mechanism, and growth rates as high as 0.52 Å/s, over 30 times faster than for conventional ALD, were achieved. This highlights this technique as a potential route to high throughput NiO_x desirable for commercialisation of *p-i-n* thin film solar cells. The resultant phase pure, smooth films were pinhole free and showed good transparency in the visible range, ideal for a window layer for a solar cell. From XPS and EIS, films were determined as *p*-type, however large discrepancies in the estimated carrier concentration by these methods indicated Fermi level pinning at a defect transition level whilst also highlighting the need to explore further methods of carrier density determination in future. On incorporation into $FA_{0.15}MA_{0.85}PbI_3$ solar cells, device efficiencies as high as 16.6 % were achieved, comparable with the best *p-i-n* perovskite devices using a NiO_x HTM in the literature. The large defect density of the NiO_x films, identified by a dominant sub bandgap emission in the PL spectrum was identified as a potential source of voltage loss due to interfacial non-radiative recombination with photogenerated carriers in the perovskite layer. A route to reduce the density of nickel vacancies, by annealing NiO_x in a Ni-rich environment, was investigated. Whilst the Fermi level moved closer to mid-gap with annealing, an indicator of *p*-doping, an increase in both Ni^{3+} and Ni^0 species within the film were identified. The latter was proposed to be responsible for the shift (and pinning of) the Fermi level, whilst the former proved that the experiment was unsuccessful, resulting in an increase in nickel vacancies under the anneal conditions used. Annealing in an oxygen- and vacuum- free, nickel- rich environment has been proposed as an improved experiment for future work.

11 Nickel oxide: future work

11.1 Modified mesoporous super-structured perovskite devices

In the previous chapter planar heterojunction *p-i-n* perovskite solar cells using AP-CVD NiO_x as the HTM achieved comparable performance with the best in the literature. However, further improvements may be possible by exploring alternative device architectures, with the aim to improve current collection. As mentioned in section 2.5.4, early perovskite device designs were inspired by dye-sensitised solar cells, which implement a mesoporous charge transport material to increase the surface area for dye absorption and charge injection. *n-i-p* devices using mesoporous *n*-type oxides have achieved the best efficiencies for the lead halide perovskites, benefitting from enhanced J_{SC}s relative to planar heterojunction devices.[85,297] However, *p-i-n* devices using mesoporous NiO_x as the HTM have only achieved ~ 17 % due to the poor conductivity of NiO_x, compared to > 22 % for *n-i-p* devices.[298] One route to overcome this would be to use a mesoporous transparent conductive oxide (TCO) such as ITO coated with a thin conformal layer of NiO_x, thereby combining the excellent conductivity of the TCO with the electron blocking properties of NiO_x. This would be achievable due to the ability to deposit conformal films using the VCUCP reactor.

Preliminary experiments were carried out for one batch of devices using a planar heterojunction control device (PHJ, ITO|AP-CVD NiO_x|$FA_{0.15}MA_{0.85}PbI_3$|PCBM|Al) and a mesoporous super-structured device (MSSC). Here, mesoporous ITO was coated with 25 – 120 oscillations of AP-CVD NiO_x (planar-ITO|mesoporous-ITO|AP-CVD NiO_x|$FA_{0.15}MA_{0.85}PbI_3$|PCBM|Al). The mesoporous ITO films and devices were fabricated by Dr Bart Roose, University of Cambridge. Device performance characteristics are shown in Figure 11.1. Whilst the V_{OC} and fill factor of all MSSC devices were lower than the PHJ control (figs b and c), the J_{SC} was greater for MSSC devices using 60 – 120 oscillations of NiO_x than the PHJ control (Figure 11.1a). This could be attributed to the larger surface area for current collection for NiO_x coated mesoporous ITO relative to thin film NiO_x. Below 60 oscillations, there was likely incomplete coverage of the mesoporous ITO layer, causing shunt pathways and associated losses in J_{SC}, V_{OC}, fill factor and PCE. The PCE of devices using 120 oscillations of NiO_x on mesoporous ITO gave, within error, the same PCE as the control PHJ devices, approximately 10.5 %. In the case of PHJ devices the device fabrication process was optimised, whilst the process for the mesoporous devices was un-optimised. This suggests that further improvements to performance are possible (*e.g.* by optimising the pore size and processing conditions for mesoporous ITO). These preliminary results highlight this as a promising route to enhancing the performance of *p-*

i-n perovskite solar cells using NiO_x as the HTM and provide an exciting direction for future work.

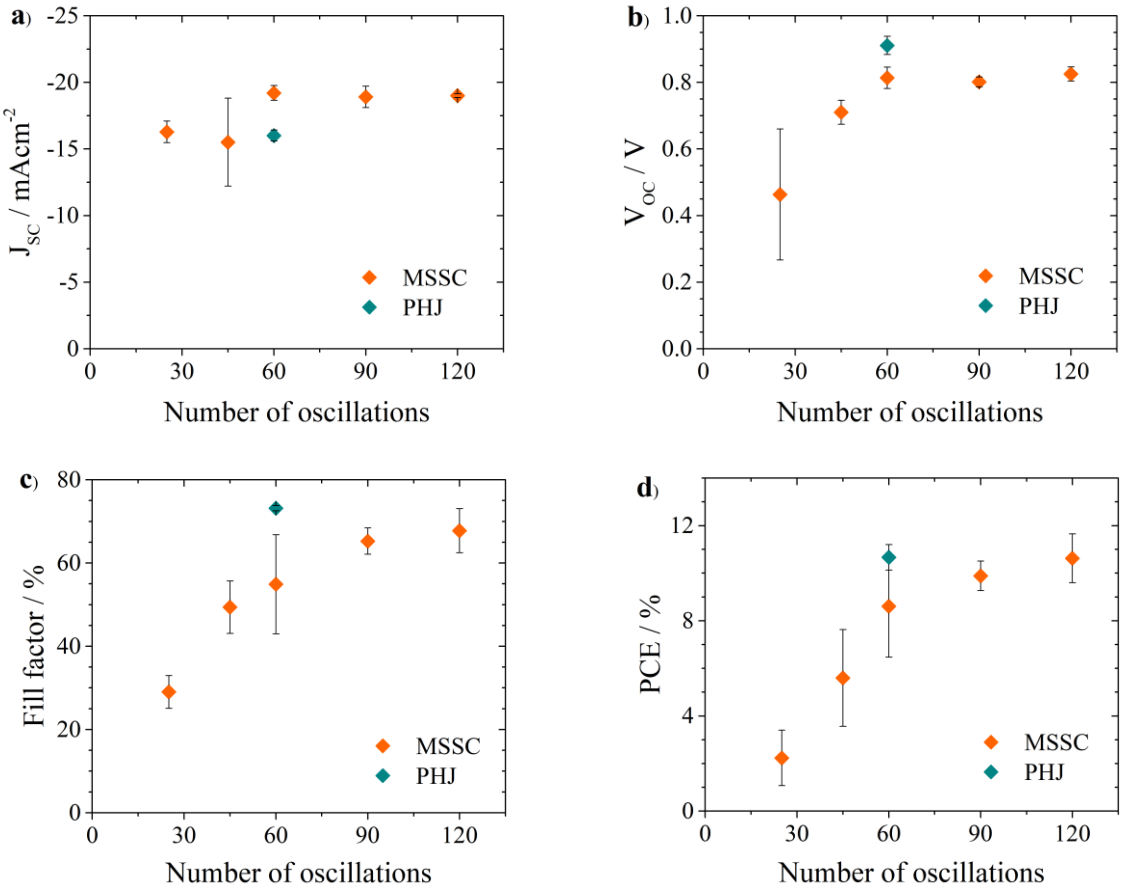

Figure 11.1 The a) short-circuit current density, b) open-circuit voltage, c) fill factor and d) power conversion efficiency of meso-superstructure solar cells (MSSC, planar-ITO|mesoporous-ITO|AP-CVD NiO_x|$FA_{0.15}MA_{0.85}PbI_3$|PCBM|Al, *orange*) and control planar heterojunction solar cells (PHJ, ITO|AP-CVD NiO_x|$FA_{0.15}MA_{0.85}PbI_3$|PCBM|Al, *blue*) as a function of the number of oscillations used to fabricate the AP-CVD NiO_x layer.

11.2 Further ideas for future work

Further potential future work includes deposition of AP-CVD NiO_x on larger area substrates. In the current work, a substrate size of 12 x 12 mm was used, whilst the active electrode area of the devices was 4.5 mm^2. The Cambridge Close Proximity reactor can coat areas of up to ~ 65 x 65 mm^2, at which methods such as spin coating have difficulty producing films of uniform thickness. Thus, it would be interesting to assess device performance on larger area substrates to validate the potential of this deposition technique in scaled up, large area applications. Additionally, the exploration of more reactive Ni precursors for deposition of NiO_x at temperatures suitable for

flexible plastic substrates to further assess to ability of this technique for larger scale applications would be interesting.

12 Conclusions

In this thesis, the vapour phase synthesis of BiOI and NiO_x, was investigated. For work in chapter 6, chemical vapour deposition, using heat as the energy source, was used to deposit large grained, phase pure and compact BiOI thin films, which maintained their phase purity after 197 days storage in ambient conditions. ITO|NiO_x|BiOI|ZnO|Al devices gave a power conversion efficiency of 1.8 %, almost doubling literature records, whilst a maximum EQE of 80 % (at 450 nm) was achieved, indicating excellent charge separation and extraction. Chapter 7 investigated whether growth of BiOI at higher temperatures could improve structural and optoelectronic properties. Growth at 500 ºC resulted in a reduced Urbach energy of 40 meV relative to 70 meV for growth at 360 ºC, offering the potential for reduced voltage loss in devices. However, films grown at ≥ 400 ºC suffered from the formation of micron sized clusters on their surface, which could be detrimental to devices. Iodine deficiency was also present in BiOI deposited at temperatures ≥ 400 ºC. However, despite iodine loss of up to 30 %, the Fermi level position remained constant as probed by XPS. This indicated that BiOI shows tolerance to iodine loss. This was further explored in chapter 8, where iodine vacancies were deliberately introduced into BiOI by annealing under vacuum. Both the Fermi level and the position of the Bi $4f_{7/2}$ in the XPS core level spectra remained constant, indicating that iodine deficiency did not cause doping or a change in phase at the BiOI surface. These results support theoretical predictions that iodine vacancies form within the bands of BiOI and therefore do not cause doping effects. Identified routes for future work involved modifying the CVD reactor to avoid particle formation on the surface of BiOI at 400 ºC and above, as well as exploiting the 1.9 eV bandgap of BiOI in tandem devices with a crystalline silicon bottom cell.

Part B investigated the deposition of NiO_x thin films by a high throughput method using the Vertical Cambridge University Close Proximity reactor. NiO_x was found to deposit *via* a decomposition 'CVD' type mechanism at a rate of 0.52 Å/s; over 30 times faster than temporal ALD. Films were phase pure with small grains ~ 25 nm in size and < 1 nm RMS roughness. ITO|NiO_x|$FAMAPbI_3$|PCBM|Al devices gave a champion power conversion efficiency of 16.6 %, which is comparable with the best devices in the literature using NiO_x as the hole transport material. Avenues for future work were identified, based on reducing the defect concentration of NiO_x by annealing in a nickel rich environment as well using alternative devices architectures to maximise current collection from perovskite devices.

13 References

1 L. C. Lee, T. N. Huq, J. L. MacManus-Driscoll and R. L. Z. Hoye, *APL Mater.*, 2018, **6**, 084502.

2 R. L. Z. Hoye, L. C. Lee, R. C. Kurchin, T. N. Huq, K. H. L. Zhang, M. Sponseller, L. Nienhaus, R. E. Brandt, J. Jean, J. A. Polizzotti, A. Kursumović, M. G. Bawendi, V. Bulović, V. Stevanović, T. Buonassisi and J. L. Macmanus-Driscoll, *Adv. Mater.*, 2017, **29**, 1702176.

3 B. Zhao, L. C. Lee, L. Yang, A. J. Pearson, H. Lu, X. J. She, L. Cui, K. H. L. Zhang, R. L. Z. Hoye, A. Karani, P. Xu, A. Sadhanala, N. C. Greenham, R. H. Friend, J. L. MacManus-Driscoll and D. Di, *ACS Appl. Mater. Interfaces*, 2018, **10**, 41849–41854.

4 R. E. Brandt, J. R. Poindexter, P. Gorai, R. C. Kurchin, R. L. Z. Hoye, L. Nienhaus, M. W. B. Wilson, J. A. Polizzotti, R. Sereika, R. Žaltauskas, L. C. Lee, J. L. Macmanus-Driscoll, M. Bawendi, V. Stevanović and T. Buonassisi, *Chem. Mater.*, 2017, **29**, 4667–4674.

5 International Energy Agency, *Global Energy & CO2 Status Report 2018*, 2018.

6 BP, *BP Energy Outlook 2019 Edition*, 2019.

7 IPCC, *Special Report: Global Warming of 1.5 C*, 2018.

8 J. Nelson and C. J. M. Emmott, *Philos. Trans. R. Soc. A Math. Phys. Eng. Sci.*, 2013, **371**, 20120372.

9 S. Philipps, in *Fraunhofer ISE and Werner Warmuth, PSE Conferences & Consulting GmbH*, 2019.

10 R. Fu, D. Feldman and R. Margolis, *U.S. Solar Photovoltaic System Cost Benchmark: Q1 2018, NREL*, 2018.

11 VDMA, *International Technology Roadmap for Photovoltaics (ITRPV) 2018 Results*, 10th edn., 2019.

12 R. C. Newman, *J. Phys. Condens. Matter*, 2000, **12**, R335.

13 J. Nelson, *The Physics of Solar Cells*, Imperial College Press, 2003.

14 D. M. Chapin, C. S. Fuller and G. L. Pearson, *J. Appl. Phys.*, 1954, **25**, 676.

15 S. G. Kumar and K. S. R. K. Rao, *Energy Environ. Sci.*, 2014, **7**, 45–102.

16 A. T. Marin, D. Muñoz-Rojas, D. C. Iza, T. Gershon, K. P. Musselman and J. L. MacManus-Driscoll, *Adv. Funct. Mater.*, 2013, **23**, 3413–3419.

17 G. Barbarino, R. De Asmundi, G. De Rosa, C. Maximiliano Mollo, S. Russo and D. Vivolo, in *Photodiodes - World Activities in 2011*, InTech, 2011, pp. 183–228.

18 J. R. Durrant, *Philos. Trans. R. Soc. A Math. Phys. Eng. Sci.*, 2013, **371**, 20120195.

19 R. E. Brandt, V. Stevanovic, D. S. Ginley and T. Buonassisi, *MRS Commun.*, 2015, **5**, 265–275.

20 T. Meng, *Electrochem. Soc. Interface*, 2008, 30–35.

21 ASTM, 2012.

22 A. Cuevas, *Energy Procedia*, 2014, **55**, 53–62.

23 G. A. H. Wetzelaer, M. Kuik, M. Lenes and P. W. M. Blom, *Appl. Phys. Lett.*, 2011, **99**, 153506.

24 G. L. Araujo and E. Sánchez, *IEEE Trans. Electron Devices*, 1982, **29**, 1511–1513.

25 K. I. Ishibashi, Y. Kimura and M. Niwano, *J. Appl. Phys.*, 2008, **103**, 094507.

26 V. D'Alessandro, P. Guerriero, S. Daliento and M. Gargiulo, *3rd Int. Conf. Clean Electr. Power Renew. Energy Resour. Impact, ICCEP 2011*, 2011, **2**, 164–168.

27 L. Dou, J. You, J. Yang, C. Chen, Y. He, S. Murase, T. Moriarty, K. Emery, G. Li and Y. Yang, *Nat. Photonics*, 2012, **6**, 180–185.

28 J. J. Krich, B. I. Halperin and A. Aspuru-Guzik, *J. Appl. Phys.*, 2012, **112**, 13707.

29 W. Shockley and H. J. Queisser, *J. Appl. Phys.*, 1961, **32**, 510–519.

30 www.pvlighthouse.com.au, Accessed 16/06/19.

31 S. Rühle, *Sol. Energy*, 2016, **130**, 139–147.

32 T. Todorov, O. Gunawan and S. Guha, *Mol. Syst. Des. Eng.*, 2016, **1**, 370–376.

33 P. Ramasamy, P. Manivasakan and J. Kim, *RSC Adv.*, 2014, **4**, 34873–34895.

34 R. W. Miles, G. Zoppi and I. Forbes, *Mater. Today*, 2007, **10**, 20–27.

35 S. Saeed, E. M. L. D. de Jong, K. Dohnalova and T. Gregorkiewicz, *Nat. Commun.*, 2014, **5**, 4665.

36 M. A. Green, Y. Hishikawa, E. D. Dunlop, D. H. Levi, J. Hohl-Ebinger, M. Yoshita and

A. W. Y. Ho-Baillie, *Prog. Photovoltaics Res. Appl.*, 2019, **27**, 3–12.

37 M. Grundmann, *The Physics of Semiconductors*, Springer International Publishing, 2016.

38 C. Battaglia, A. Cuevas and S. De Wolf, *Energy Environ. Sci.*, 2016, 9, 1552–1576.

39 C. Sah, R. N. Noyce and W. Shockley, *Proc. IRE*, 1956, **1**, 1228–1243.

40 D. S. Meyaard, G.-B. Lin, J. Cho and E. F. Schubert, *Nitride Semicond. Light. Diodes*, 2014, 279–300.

41 D. N. Quang, *Phys. status solidi*, 1990, **158**, 669–683.

42 W. Shockley and W. T. Read, *Phys. Rev.*, 1952, **87**, 835–842.

43 A. Maurano, R. Hamilton, C. G. Shuttle, A. M. Ballantyne, J. Nelson, B. O'Regan, W. Zhang, I. McCulloch, H. Azimi, M. Morana, C. J. Brabec and J. R. Durrant, *Adv. Mater.*, 2010, **22**, 4987–4992.

44 T. Kirchartz, B. E. Pieters, J. Kirkpatrick, U. Rau and J. Nelson, *Phys. Rev. B - Condens. Matter Mater. Phys.*, 2011, **83**, 115209.

45 C. Van Berkel, M. J. Powell, A. R. Franklin and I. D. French, *J. Appl. Phys.*, 1993, **73**, 5264–5268.

46 T. Kirchartz and J. Nelson, *Phys. Rev. B*, 2012, **86**, 165201.

47 R. L. Z. Hoye, L. Eyre, F. Wei, F. Brivio, A. Sadhanala, S. Sun, W. Li, K. H. L. Zhang, J. L. MacManus-Driscoll, P. D. Bristowe, R. H. Friend, A. K. Cheetham and F. Deschler, *Adv. Mater. Interfaces*, 2018, **5**, 1800464.

48 V. C. Lopes, A. J. Syllaios and M. C. Chen, *Semicond. Sci. Technol.*, 1993, **8**, 824–841.

49 T. Kirchartz, L. Krückemeier and E. L. Unger, *APL Mater.*, 2018, **6**, 100702.

50 R. Jaramillo, M.-J. Sher, B. K. Ofori-Okai, V. Steinmann, C. Yang, K. Hartman, K. a. Nelson, A. M. Lindenberg, R. G. Gordon and T. Buonassisi, *J. Appl. Phys.*, 2016, **119**, 035101.

51 R. E. Brandt, R. C. Kurchin, R. L. Z. Hoye, J. R. Poindexter, M. W. B. Wilson, S. Sulekar, F. Lenahan, P. X. T. Yen, V. Stevanovic, J. C. Nino, M. G. Bawendi and T. Buonassisi, *J. Phys. Chem. Lett.*, 2015, **6**, 4297–4302.

52 R. Hoye, R. E. Brandt, A. Osherov, V. Stevanovic, S. D. Stranks, M. W. B. Wilson, H. Kim, A. J. Akey, R. C. Kurchin, J. R. Poindexter, E. N. Wang, M. G. Bawendi, V. Bulovic and T. Buonassisi, *Chem. - A Eur. J.*, 2016, **22**, 2605–2610.

53 L. D. Whalley, J. M. Frost, Y. K. Jung and A. Walsh, *J. Chem. Phys.*, 2017, **146**, 1–13.

54 D. B. Mitzi, O. Gunawan, T. K. Todorov, K. Wang and S. Guha, *Sol. Energy Mater. Sol. Cells*, 2011, **95**, 1421–1436.

55 G. E. Eperon, V. M. Burlakov, P. Docampo, A. Goriely and H. J. Snaith, *Adv. Funct. Mater.*, 2014, **24**, 151–157.

56 E. Dornberger, E. Tomzig, A. Seidl, S. Schmitt, H.-J. Leister and C. Schmitt, *J. Cryst. Growth*, 1997, **180**, 461–467.

57 K. Yoshikawa, H. Kawasaki, W. Yoshida, T. Irie, K. Konishi, K. Nakano, T. Uto, D. Adachi, M. Kanematsu, H. Uzu and K. Yamamoto, *Nat. Energy*, 2017, **2**, 17032.

58 S. De Wolf, J. Holovsky, S. J. Moon, P. Löper, B. Niesen, M. Ledinsky, F. J. Haug, J. H. Yum and C. Ballif, *J. Phys. Chem. Lett.*, 2014, **5**, 1035–1039.

59 H. Sugimoto, *2014 IEEE 40th Photovolt. Spec. Conf. PVSC 2014*, 2014, 2767–2770.

60 www.firstsolar.com/en-EMEA, Accessed 16/06/19.

61 www.webelements.com/tellurium/geology, Accessed 16/06/19.

62 www.webelements.com/indium/geology, Accessed 16/06/19.

63 C. Yan, J. Huang, K. Sun, S. Johnston, Y. Zhang, H. Sun, A. Pu, M. He, F. Liu, K. Eder, L. Yang, J. M. Cairney, N. J. Ekins-Daukes, Z. Hameiri, J. A. Stride, S. Chen, M. A. Green and X. Hao, *Nat. Energy*, 2018, **3**, 764–772.

64 D. M. Berg, M. Arasimowicz, R. Djemour, L. Gütay, S. Siebentritt, S. Schorr, X. Fontané, V. Izquierdo-Roca, A. Pérez-Rodriguez and P. J. Dale, *Thin Solid Films*, 2014, **569**, 113–123.

65 K. Rudisch, Y. Ren, C. Platzer-Björkman and J. Scragg, *Appl. Phys. Lett.*, 2016, **108**, 231902.

66 A. Walsh, S. Chen, S. H. Wei and X. G. Gong, *Adv. Energy Mater.*, 2012, **2**, 400–409.

67 A. M. Ganose, C. N. Savory and D. O. Scanlon, *Chem. Commun.*, 2017, **53**, 20–44.

68 K. Tanabe, *Energies*, 2009, **2**, 504–530.

69 B. Maennig, J. Drechsel, D. Gebeyehu, P. Simon, F. Kozlowski, A. Werner, F. Li, S. Grundmann, S. Sonntag, M. Koch, K. Leo, M. Pfeiffer, H. Hoppe, D. Meissner, N. S. Sariciftci, I. Riedel, V. Dyakonov and J. Parisi, *Appl. Phys. A Mater. Sci. Process.*, 2004, **79**, 1–14.

70 S. Mathew, A. Yella, P. Gao, R. Humphry-Baker, B. F. E. Curchod, N. Ashari-Astani, I. Tavernelli, U. Rothlisberger, M. K. Nazeeruddin and M. Grätzel, *Nat. Chem.*, 2014, **6**, 242–247.

71 C. P. Lee, C. T. Li and K. C. Ho, *Mater. Today*, 2017, 20, 267–283.

72 A. Yella, S. Mathew, S. Aghazada, P. Comte, M. Grätzel and M. K. Nazeeruddin, *J. Mater. Chem. C*, 2017, **5**, 2833–2843.

73 P. Mariani, L. Vesce and A. Di Carlo, *Semicond. Sci. Technol.*, 2015, **30**, 104003.

74 www.greatcellsolar.com, Accessed 16/06/19.

75 F. T. F. O'Mahony, T. Lutz, N. Guijarro, R. Gómez and S. a. Haque, *Energy Environ. Sci.*, 2012, **5**, 9760.

76 M. Bernechea, N. C. Miller, G. Xercavins, D. So, A. Stavrinadis and G. Konstantatos, *Nat. Photonics*, 2016, **10**, 521–525.

77 T. L. Li, Y. L. Lee and H. Teng, *Energy Environ. Sci.*, 2012, **5**, 5315–5324.

78 J. Benick, A. Richter, R. Müller, H. Hauser, F. Feldmann, P. Krenckel, S. Riepe, F. Schindler, M. C. Schubert, M. Hermle, A. W. Bett and S. W. Glunz, *IEEE J. Photovoltaics*, 2017, **7**, 1171–1175.

79 B. M. Kayes, H. Nie, R. Twist, S. G. Spruytte, F. Reinhardt, I. C. Kizilyalli and G. S. Higashi, *Conf. Rec. IEEE Photovolt. Spec. Conf.*, 2011, 4–8.

80 L. S. Mattos, S. R. Scully, M. Syfu, E. Olson, L. Yang, C. Ling, B. M. Kayes and G. He, in *Conference Record of the IEEE Photovoltaic Specialists Conference*, IEEE, 2012, pp. 3187–3190.

81 www.energy.gov/eere/solar/cadmium-telluride, Accessed 13/06/19.

82 S. I. Swati, R. Matin, S. Bashar and Z. H. Mahmood, in *Journal of Physics: Conference Series*, 2018, vol. 1086, p. 012010.

83 S. Mori, H. Oh-Oka, H. Nakao, T. Gotanda, Y. Nakano, H. Jung, A. Iida, R. Hayase, N. Shida, M. Saito, K. Todori, T. Asakura, A. Matsui and M. Hosoya, in *Materials Research Society Symposium Proceedings*, Cambridge University Press, 2015, vol. 1737, pp. 26–31.

84 J. Gong, K. Sumathy, Q. Qiao and Z. Zhou, *Renew. Sustain. Energy Rev.*, 2017, **68**, 234–246.

85 N. J. Jeon, H. Na, E. H. Jung, T. Y. Yang, Y. G. Lee, G. Kim, H. W. Shin, S. Il Seok, J. Lee and J. Seo, *Nat. Energy*, 2018, **3**, 682–689.

86 H. J. Snaith, *J. Phys. Chem. Lett.*, 2013, **4**, 3623–3620.

87 M. Hosoya, H. Oooka and H. Nakao, *Proc. 93rd Annu. Meet. Chem. Soc. Japan*, 2013, 21–37.

88 U. Zhokhavets, T. Erb, G. Gobsch, M. Al-Ibrahim and O. Ambacher, *Chem. Phys. Lett.*, 2006, **418**, 347–350.

89 www.nrel.gov/pv/cell-efficiency, Accessed 16/06/19.

90 A. Kojima, K. Teshima, Y. Shirai and T. Miyasaka, *J. Am. Chem. Soc.*, 2009, **131**, 6050–6051.

91 X. Zhao and N.-G. Park, *Photonics*, 2015, **2**, 1139–1151.

92 P. S. Whitfield, N. Herron, W. E. Guise, K. Page, Y. Q. Cheng, I. Milas and M. K. Crawford, *Sci. Rep.*, 2016, **6**, 35685.

93 N. G. Park, *Mater. Today*, 2015, **18**, 65–72.

94 J.-Y. Jeng, K.-C. Chen, T.-Y. Chiang, P.-Y. Lin, T.-D. Tsai, Y.-C. Chang, T.-F. Guo, P. Chen, T.-C. Wen and Y.-J. Hsu, *Adv. Mater.*, 2014, **26**, 4107–13.

95 A. Miyata, A. Mitioglu, P. Plochocka, O. Portugall, J. T. W. Wang, S. D. Stranks, H. J. Snaith and R. J. Nicholas, *Nat. Phys.*, 2015, **11**, 582–587.

96 S. D. Stranks, G. E. Eperon, G. Grancini, C. Menelaou, M. J. P. Alcocer, T. Leijtens, L. M. Herz, A. Petrozza and H. J. Snaith, *Science*, 2013, **342**, 341–344.

97 G. Xing, N. Mathews, S. Sun, S. S. Lim, Y. M. Lam, M. Graïzel, S. Mhaisalkar and T. C. Sum, *Science*, 2013, **342**, 344–347.

98 J. M. Frost and A. Walsh, *Acc. Chem. Res.*, 2016, 49, 528–535.

99 H. Zhou, Q. Chen, G. Li, S. Luo, T. B. Song, H. S. Duan, Z. Hong, J. You, Y. Liu and Y. Yang, *Science*, 2014, **345**, 542–546.

100 H. Huang, M. I. Bodnarchuk, S. V. Kershaw, M. V. Kovalenko and A. L. Rogach, *ACS Energy Lett.*, 2017, **2**, 2071–2083.

101 J. H. Noh, S. H. Im, J. H. Heo, T. N. Mandal and S. Il Seok, *Nano Lett.*, 2013, **13**, 1764–1769.

102 S. A. Kulkarni, T. Baikie, P. P. Boix, N. Yantara, N. Mathews and S. Mhaisalkar, *J. Mater. Chem. A*, 2014, **2**, 9221–9225.

103 www.materialsproject.org, Accessed 16/06/19.

104 J.-H. Im, C.-R. Lee, J.-W. Lee, S.-W. Park and N.-G. Park, *Nanoscale*, 2011, **3**, 4088.

105 M. M. Lee, J. Teuscher, T. Miyasaka, T. N. Murakami and H. J. Snaith, *Science*, 2012, **338**, 643–647.

106 H. S. Kim, C. R. Lee, J. H. Im, K. B. Lee, T. Moehl, A. Marchioro, S. J. Moon, R. Humphry-Baker, J. H. Yum, J. E. Moser, M. Grätzel and N. G. Park, *Sci. Rep.*, 2012, **2**, 1–7.

107 M. Liu, M. B. Johnston and H. J. Snaith, *Nature*, 2013, **501**, 395–8.

108 S. N. Habisreutinger, T. Leijtens, G. E. Eperon, S. D. Stranks, R. J. Nicholas and H. J. Snaith, *Nano Lett.*, 2014, **14**, 5561–5568.

109 Z. Li, M. Yang, J. S. Park, S. H. Wei, J. J. Berry and K. Zhu, *Chem. Mater.*, 2016, **28**, 284–292.

110 K. A. Bush, A. F. Palmstrom, Z. J. Yu, M. Boccard, R. Cheacharoen, J. P. Mailoa, D. P. McMeekin, R. L. Z. Hoye, C. D. Bailie, T. Leijtens, I. M. Peters, M. C. Minichetti, N. Rolston, R. Prasanna, S. Sofia, D. Harwood, W. Ma, F. Moghadam, H. J. Snaith, T. Buonassisi, Z. C. Holman, S. F. Bent and M. D. McGehee, *Nat. Energy*, 2017, **2**, 17009.

111 C. Kim, S. Ryu, J. Seo, S. I. Il Seok, W. S. Yang, J. H. Noh, N. J. Jeon, Y. C. Kim, S. Ryu, J. Seo and S. I. Il Seok, *Science*, 2015, **348**, 1–12.

112 S. Seo, I. J. Park, M. Kim, S. Lee, C. Bae, H. S. Jung, N. G. Park, J. Y. Kim and H. Shin, *Nanoscale*, 2016, **8**, 11403–11412.

113 J. You, L. Meng, T. Bin Song, T. F. Guo, W. H. Chang, Z. Hong, H. Chen, H. Zhou, Q. Chen, Y. Liu, N. De Marco and Y. Yang, *Nat. Nanotechnol.*, 2016, **11**, 75–81.

114 J. A. Christians, R. C. M. Fung and P. V Kamat, *J. Am. Chem. Soc.*, 2014, **136**, 758–764.

115 N. Arora, M. I. Dar, A. Hinderhofer, N. Pellet, F. Schreiber, S. M. Zakeeruddin and M. Grätzel, *Science*, 2017, **358**, 768–771.

116 P. Qin, S. Tanaka, S. Ito, N. Tetreault, K. Manabe, H. Nishino, M. K. Nazeeruddin and M. Grätzel, *Nat. Commun.*, 2014, **5**, 1–6.

117 Y. Han, S. Meyer, Y. Dkhissi, K. Weber, J. M. Pringle, U. Bach, L. Spiccia and Y.-B.

Cheng, *J. Mater. Chem. A*, 2015, **3**, 8139–8147.

118 S. Chen, J. R. Manders, S. W. Tsang and F. So, *J. Mater. Chem.*, 2012, **22**, 24202–24212.

119 Z. Wang, P. K. Nayak, J. A. Caraveo-Frescas and H. N. Alshareef, *Adv. Mater.*, 2016, 28, 3831–3892.

120 Z. Zhu, Y. Bai, T. Zhang, Z. Liu, X. Long, Z. Wei, Z. Wang, L. Zhang, J. Wang, F. Yan and S. Yang, *Angew. Chemie*, 2014, **126**, 12779–12783.

121 A. M. Balagurov, I. A. Bobrikov, J. Grabis, D. Jakovlevs, A. Kuzmin, M. Maiorov and N. Mironova-Ulmane, *IOP Conf. Ser. Mater. Sci. Eng.*, 2013, **49**, 1–5.

122 J. Osorio-Guillén, S. Lany and A. Zunger, *AIP Conf. Proc.*, 2009, **1199**, 128–129.

123 J. R. Manders, S.-W. Tsang, M. J. Hartel, T.-H. Lai, S. Chen, C. M. Amb, J. R. Reynolds and F. So, *Adv. Funct. Mater.*, 2013, **23**, 2993–3001.

124 S. C. Choi, K. Koumoto and H. Yanagida, *J. Mater. Sci.*, 1986, **21**, 1947–1950.

125 M. D. Irwin, J. D. Servaites, D. B. Buchholz, B. J. Leever, J. Liu, J. D. Emery, M. Zhang, J. H. Song, M. F. Durstock, A. J. Freeman, M. J. Bedzyk, M. C. Hersam, R. P. H. Chang, M. A. Ratner and T. J. Marks, *Chem. Mater.*, 2011, **23**, 2218–2226.

126 X. Yin, P. Chen, M. Que, Y. Xing, W. Que, C. Niu and J. Shao, *ACS Nano*, 2016, **10**, 3630–6.

127 Z. Liu, A. Zhu, F. Cai, L. M. Tao, Y. Zhou, Z. Zhao, Q. Chen, Y. B. Cheng and H. Zhou, *J. Mater. Chem. A*, 2017, **5**, 6597–6605.

128 www.materialsproject.org/materials/mp-19009, Accessed 16/06/19.

129 X. Yin, Z. Yao, Q. Luo, X. Dai, Y. Zhou, Y. Zhang, Y. Zhou, S. Luo, J. Li, N. Wang and H. Lin, *ACS Appl. Mater. Interfaces*, 2017, **9**, 2439–2448.

130 Y. Hou, W. Chen, D. Baran, T. Stubhan, N. A. Luechinger, B. Hartmeier, M. Richter, J. Min, S. Chen, C. O. R. Quiroz, N. Li, H. Zhang, T. Heumueller, G. J. Matt, A. Osvet, K. Forberich, Z.-G. Zhang, Y. Li, B. Winter, P. Schweizer, E. Spiecker and C. J. Brabec, *Adv. Mater.*, 2016, **28**, 5112–20.

131 N. Sahu, B. Parija and S. Panigrahi, *Indian J. Phys.*, 2009, **83**, 493–502.

132 M. D. Tyona, *Adv. Mater. Res.*, 2013, **2**, 195–208.

133 M. S. Bayerl, T. Braig, O. Nuyken, D. C. Müller, M. Groß and K. Meerholz, *Macromol. Rapid Commun.*, 2005, **20**, 224–228.

134 J. H. Park, J. Seo, S. Park, S. S. Shin, Y. C. Kim, N. J. Jeon, H.-W. Shin, T. K. Ahn, J. H. Noh, S. C. Yoon, C. S. Hwang and S. Il Seok, *Adv. Mater.*, 2015, **27**, 4013–4019.

135 R. L. Z. Hoye, D. Muñoz-Rojas, S. F. Nelson, A. Illiberi, P. Poodt, F. Roozeboom and J. L. MacManus-Driscoll, *APL Mater.*, 2015, **3**, 040701.

136 F. De Rossi, J. A. Baker, D. Beynon, K. E. A. Hooper, S. M. P. Meroni, D. Williams, Z. Wei, A. Yasin, C. Charbonneau, E. H. Jewell and T. M. Watson, *Adv. Mater. Technol.*, 2018, **3**, 1800156.

137 J. Baker, K. Hooper, S. Meroni, A. Pockett, J. McGettrick, Z. Wei, R. Escalante, G. Oskam, M. Carnie and T. Watson, *J. Mater. Chem. A*, 2017, **5**, 18643–18650.

138 ec.europa.eu/environment/waste/rohs_eee, Accessed 16/06/19.

139 Z. Shi, J. Guo, Y. Chen, Q. Li, Y. Pan, H. Zhang, Y. Xia and W. Huang, *Adv. Mater.*, 2017, **29**, 1605005.

140 R. Mohan, *Nat. Chem.*, 2010, 2, 336.

141 M. Blaskovich, *The periodic table: from its classic design to use in popular culture*, 2019.

142 A. Janotti and C. G. Van De Walle, *Appl. Phys. Lett.*, 2005, **87**, 1–3.

143 A. Janotti and C. G. Van De Walle, *Phys. Rev. B - Condens. Matter Mater. Phys.*, 2007, **76**, 1–22.

144 N. D. M. Hine, K. Frensch, W. M. C. Foulkes and M. W. Finnis, *Phys. Rev. B - Condens. Matter Mater. Phys.*, 2009, **79**, 1–13.

145 W.-J. Yin, T. Shi and Y. Yan, *Appl. Phys. Lett.*, 2014, **104**, 063903.

146 C. W. M. Castleton, A. Höglund and S. Mirbt, *Model. Simul. Mater. Sci. Eng.*, 2009, **17**, 084003.

147 T. R. Durrant, S. T. Murphy, M. B. Watkins and A. L. Shluger, *J. Chem. Phys.*, 2018, **149**, 024103.

148 H. Peng, D. O. Scanlon, V. Stevanovic, J. Vidal, G. W. Watson and S. Lany, *Phys. Rev. B*, 2013, **115201**, 1–7.

149 C. Freysoldt, B. Grabowski, T. Hickel, J. Neugebauer, G. Kresse, A. Janotti and C. G. Van De Walle, *Rev. Mod. Phys.*, 2014, **86**, 253–305.

150 C. G. Van de Walle and J. Neugebauer, *J. Appl. Phys.*, 2004, **95**, 3851–3879.

151 K. X. Steirer, P. Schulz, G. Teeter, V. Stevanovic, M. Yang, K. Zhu and J. J. Berry, *ACS Energy Lett.*, 2016, **1**, 360–366.

152 A. Jain, K. A. Persson and G. Ceder, *APL Mater.*, 2016, **4**, 053102.

153 Q. Jiang, Z. Chu, P. Wang, X. Yang, H. Liu, Y. Wang, Z. Yin, J. Wu, X. Zhang and J. You, *Adv. Mater.*, 2017, **29**, 1703852.

154 K. Eckhardt, V. Bon, J. Getzschmann, J. Grothe, F. M. Wisser and S. Kaskel, *Chem. Commun.*, 2016, **52**, 3058–3060.

155 R. Jakubas, J. Zaleski and L. Sobczyk, *Ferroelectrics*, 1990, **108**, 109–114.

156 C. Ran, Z. Wu, J. Xi, F. Yuan, H. Dong, T. Lei, X. He and X. Hou, *J. Phys. Chem. Lett.*, 2017, 2–8.

157 Z. Zhang, X. Li, X. Xia, Z. Wang, Z. Huang, B. Lei and Y. Gao, *J. Phys. Chem. Lett.*, 2017, **8**, 4300–4307.

158 S. S. Shin, J.-P. Correa-Baena, R. C. Kurchin, A. Polizzotti, J. J. Yoo, S. Wieghold, M. G. Bawendi and T. Buonassisi, *Chem. Mater.*, 2018, **30**, 336–343.

159 S. Öz, J.-C. Hebig, E. Jung, T. Singh, A. Lepcha, S. Olthof, F. Jan, Y. Gao, R. German, P. H. M. van Loosdrecht, K. Meerholz, T. Kirchartz and S. Mathur, *Sol. Energy Mater. Sol. Cells*, 2016, **158**, 195–201.

160 B. W. Park, B. Philippe, X. Zhang, H. Rensmo, G. Boschloo and E. M. J. Johansson, *Adv. Mater.*, 2015, **27**, 6806–6813.

161 F. Wei, Z. Deng, S. Sun, F. Xie, G. Kieslich, D. M. Evans, M. A. Carpenter, P. D. Bristowe and A. K. Cheetham, *Mater. Horizons*, 2016, **3**, 328–332.

162 E. T. McClure, M. R. Ball, W. Windl and P. M. Woodward, *Chem. Mater.*, 2016, **28**, 1348–1354.

163 Z. Xiao, W. Meng, J. Wang, D. B. Mitzi and Y. Yan, *Mater. Horiz.*, 2017, **4**, 206–216.

164 P. Umari, E. Mosconi and F. De Angelis, *Sci. Rep.*, 2014, **4**, 4467.

165 F. Wei, Z. Deng, S. Sun, F. Zhang, D. M. Evans, G. Kieslich, S. Tominaka, M. A. Carpenter, J. Zhang, P. D. Bristowe and A. K. Cheetham, *Chem. Mater.*, 2017, **29**, 1089–1094.

166 A. H. Slavney, T. Hu, A. M. Lindenberg and H. I. Karunadasa, *J. Am. Chem. Soc.*, 2016, **138**, 2138–2141.

167 D. W. de Quilettes, S. M. Vorpahl, S. D. Stranks, H. Nagaoka, G. E. Eperon, M. E. Ziffer, H. J. Snaith and D. S. Ginger, *Science*, 2015, **348**, 683–686.

168 E. Greul, M. L. Petrus, A. Binek, P. Docampo and T. Bein, *J. Mater. Chem. A*, 2017, **5**, 19972–19981.

169 K. Z. Du, W. Meng, X. Wang, Y. Yan and D. B. Mitzi, *Angew. Chemie - Int. Ed.*, 2017, **56**, 8158–8162.

170 A. H. Slavney, L. Leppert, D. Bartesaghi, A. Gold-Parker, M. F. Toney, T. J. Savenije, J. B. Neaton and H. I. Karunadasa, *J. Am. Chem. Soc.*, 2017, **139**, 5015–5018.

171 U. H. Hamdeh, R. D. Nelson, B. J. Ryan, U. Bhattacharjee, J. W. Petrich and M. G. Panthani, *Chem. Mater.*, 2016, **28**, 6567–6574.

172 A. J. Lehner, H. Wang, D. H. Fabini, C. D. Liman, C.-A. Hébert, E. E. Perry, M. Wang, G. C. Bazan, M. L. Chabinyc and R. Seshadri, *Appl. Phys. Lett.*, 2015, **107**, 131109.

173 B. A. Rosales, M. A. White and J. Vela, *J. Am. Chem. Soc.*, 2018, **140**, 3736–3742.

174 A. M. Ganose, K. T. Butler, A. Walsh and D. O. Scanlon, *J. Mater. Chem. A*, 2016, **4**, 2060–2068.

175 Y. Zhou, L. Wang, S. Chen, S. Qin, X. Liu, J. Chen, D.-J. Xue, M. Luo, Y. Cao, Y. Cheng, E. H. Sargent and J. Tang, *Nat. Photonics*, 2015, **9**, 409–415.

176 N. T. Hahn, A. J. E. Rettie, S. K. Beal, R. R. Fullon and C. B. Mullins, *J. Phys. Chem. C*, 2012, **116**, 24878–24886.

177 H. Kunioku, M. Higashi and R. Abe, *Sci. Rep.*, 2016, **6**, 32664.

178 S. Sfaelou, D. Raptis, V. Dracopoulos and P. Lianos, *RSC Adv.*, 2015, **5**, 95813–95816.

179 M. Schuisky and A. Harsta, *J. Electrochem. Soc.*, 1998, **145**, 4234.

180 D. S. Bhachu, S. J. A. Moniz, S. Sathasivam, D. O. Scanlon, A. Walsh, S. M. Bawaked, M. Mokhtar, A. Y. Obaid, I. P. Parkin, J. Tang and C. J. Carmalt, *Chem. Sci.*, 2016, **7**, 4832–4841.

181 Z. Ran, X. Wang, Y. Li, D. Yang, X.-G. Zhao, K. Biswas, D. J. Singh and L. Zhang, *npj Comput. Mater.*, 2018, **4**, 14.

182 A. M. Ganose, M. Cuff, K. T. Butler, A. Walsh and D. O. Scanlon, *Chem. Mater.*, 2016, **28**, 1980–1984.

183 M. S. Kandanapitiye, M. Gao, J. Molter, C. A. Flask and S. D. Huang, *Inorg. Chem.*, 2014,

53, 10189–94.

184 L. Ye, Y. Su, X. Jin, H. Xie and C. Zhang, *Environ. Sci. Nano*, 2014, **1**, 90.

185 H. Cheng, B. Huang and Y. Dai, *Nanoscale*, 2014, **6**, 2009–2026.

186 D. Kandi, S. Martha, A. Thirumurugan and K. M. Parida, *J. Phys. Chem. C*, 2017, **121**, 4834–4849.

187 W. C. Dunlap and R. L. Watters, *Phys. Rev.*, 1953, **92**, 1396–1397.

188 A. J. Strauss, *Rev. Phys. Appliquée*, 1977, **12**, 167–184.

189 I. Strzalkowski, S. Joshi and C. R. Crowell, *Appl. Phys. Lett.*, 1976, **28**, 350–352.

190 K. Zhao, X. Zhang and L. Zhang, *Electrochem. commun.*, 2009, **11**, 612–615.

191 B. Ahmmad, J. Kurawaki and T. Ohkubo, *J. Energy Eng.*, 2013, **139**, 338–342.

192 A. Anders, *Thin Solid Films*, 2010, **518**, 4087–4090.

193 C. V Thompson, *Annu. Rev. Mater. Sci.*, 2000, **30**, 159–190.

194 A. D. Rollett, G. Gottstein, L. S. Shvindlerman and D. A. Molodov, *Zeitschrift für Met.*, 2013, **95**, 226–229.

195 J. A. Thornton, *J. Vac. Sci. Technol.*, 2002, **11**, 666–670.

196 S. Mukherjee and D. Gall, *Thin Solid Films*, 2013, **527**, 158–163.

197 K. H. Müller, *J. Appl. Phys.*, 1985, **58**, 2573–2576.

198 P. . Barna and M. Adamik, *Thin Solid Films*, 1998, **317**, 27–33.

199 A. Cuña, I. Aguiar, A. Gancharov, M. Pérez and L. Fornaro, *Cryst. Res. Technol.*, 2004, **39**, 899–905.

200 K. L. Choy, *Prog. Mater. Sci.*, 2003, **48**, 57–170.

201 A. C. Jones and M. L. Hitchman, *Chemical Vapour Deposition: Precursors, Processes and Applications*, Royal Society of Chemistry, Cambridge, 2008.

202 T. Kääriäinen, D. Cameron, M.-L. Kääriäinen and A. Sherman, *Atomic Layer Deposition: Principles, Characteristics and Nanotechnology Applications, 2nd Edition*, Wiley, 2013.

203 K.-L. Choy, *Chemical Vapour Deposition (CVD): Advances, Technology and Applications*, CRC Press, 2010.

204 H. O. Pierson, *Handbook of Chemical Vapor Deposition: Principles, Technology and*

Applications, Noyes Publications, 2nd edn.

205 www.iue.tuwien.ac.at/phd/holzer/node41, Accessed 16/06/19.

206 L. Qian, C. Wang, A. Chen and H. Yang, *Chinese J. Chem.*, 2017, **35**, 30–34.

207 R. W. Johnson, A. Hultqvist and S. F. Bent, *Mater. Today*, 2014, **17**, 236–246.

208 S. M. George, *Chem. Rev.*, 2010, **110**, 111–131.

209 K. L. Pickrahn, A. Garg and S. F. Bent, *ACS Catal.*, 2015, **5**, 1609–1616.

210 H. C. M. Knoops, A. J. M. Mackus, M. E. Donders, M. C. M. van de Sanden, P. H. L. Notten and W. M. M. Kessels, *Electrochem. Solid-State Lett.*, 2009, **12**, G34.

211 F. J. van den Bruele, M. Smets, A. Illiberi, Y. Creyghton, P. Buskens, F. Roozeboom and P. Poodt, *J. Vac. Sci. Technol. A Vacuum, Surfaces, Film.*, 2015, **33**, 01A131.

212 P. S. Maydannik, T. O. Kääriäinen and D. C. Cameron, *Chem. Eng. J.*, 2011, **171**, 345–349.

213 S. Zaitsu, T. Jitsuno, M. Nakatsuka, T. Yamanaka and S. Motokoshi, *Appl. Phys. Lett.*, 2002, **80**, 2442–2444.

214 O. Sneh, R. B. Clark-Phelps, A. R. Londergan, J. Winkler and T. E. Seidel, *Thin Solid Films*, 2002, **402**, 248–261.

215 D. R. Stull, *Ind. Eng. Chem.*, 1947, **39**, 517–540.

216 M. Leskelä and M. Ritala, *Angew. Chemie - Int. Ed.*, 2003, **42**, 5548–5554.

217 P. Poodt, D. C. Cameron, E. Dickey, S. M. George, V. Kuznetsov, G. N. Parsons, F. Roozeboom, G. Sundaram and A. Vermeer, *J. Vac. Sci. Technol. A Vacuum, Surfaces, Film.*, 2012, **30**, 010802.

218 R. L. Z. Hoye, D. Muñoz-Rojas, K. P. Musselman, Y. Vaynzof and J. L. MacManus-Driscoll, *ACS Appl. Mater. Interfaces*, 2015, **7**, 10684–10694.

219 D. Muñoz-Rojas, H. Sun, D. C. Iza, J. Weickert, L. Chen, H. Wang, L. Schmidt-Mende and J. L. MacManus-Driscoll, *Prog. Photovoltaics Res. Appl.*, 2013, **21**, 393–400.

220 D. Muñoz-Rojas and J. MacManus-Driscoll, *Mater. Horizons*, 2014, **1**, 314–320.

221 J. A. van Delft, D. Garcia-Alonso and W. M. M. Kessels, *Semicond. Sci. Technol.*, 2012, **27**, 074002.

222 M. D. Groner, F. H. Fabreguette, J. W. Elam and S. M. George, *Chem. Mater.*, 2004, **16**,

639–645.

223 K. Sharma, R. A. Hall and S. M. George, *J. Vac. Sci. Technol. A Vacuum, Surfaces, Film.*, 2015, **33**, 01A132.

224 P. Ryan Fitzpatrick, Z. M. Gibbs and S. M. George, *J. Vac. Sci. Technol. A Vacuum, Surfaces, Film.*, 2011, **30**, 01A136.

225 D. H. Levy, S. F. Nelson and D. Freeman, *J. Disp. Technol.*, 2009, **5**, 484–494.

226 P. Poodt, A. Lankhorst, F. Roozeboom, K. Spee, D. Maas and A. Vermeer, *Adv. Mater.*, 2010, **22**, 3564–7.

227 A. Illiberi, R. Scherpenborg, F. Roozeboom and P. Poodt, *ECS J. Solid State Sci. Technol.*, 2014, **3**, P111–P114.

228 A. Illiberi, R. Scherpenborg, Y. Wu, F. Roozeboom and P. Poodt, *ACS Appl. Mater. Interfaces*, 2013, **5**, 13124–13128.

229 M. A. Mione, I. Katsouras, Y. Creyghton, W. van Boekel, J. Maas, G. Gelinck, F. Roozeboom and A. Illiberi, *ECS J. Solid State Sci. Technol.*, 2017, **6**, N243–N249.

230 www.solaytec.com, Accessed 16/06/19.

231 D. Muñoz-Rojas, M. Jordan, C. Yeoh, A. T. Marin, A. Kursumovic, L. A. Dunlop, D. C. Iza, A. Chen, H. Wang and J. L. MacManus Driscoll, *AIP Adv.*, 2012, **2**, 042179.

232 D. C. Iza, D. Muñoz-Rojas, K. P. Musselman, J. Weickert, A. C. Jakowetz, H. Sun, X. Ren, R. L. Z. Hoye, J. H. Lee, H. Wang, L. Schmidt-Mende and J. L. Macmanus-Driscoll, *Nanoscale Res. Lett.*, 2013, **8**, 359.

233 C. L. Armstrong, M. B. Price, D. Muñoz-Rojas, N. J. K. L. Davis, M. Abdi-Jalebi, R. H. Friend, N. C. Greenham, J. L. MacManus-Driscoll, M. L. Böhm and K. P. Musselman, *ACS Nano*, 2015, **9**, 11863–11871.

234 R. L. Z. Hoye, M. R. Chua, K. P. Musselman, G. Li, M. Lai, Z. Tan, N. C. Greenham, J. L. MacManus-Driscoll, R. H. Friend and D. Credgington, *Adv. Mater.*, 2015, **27**, 1414–1419.

235 E. Lindahl, M. Ottosson and J.-O. Carlsson, *Chem. Vap. Depos.*, 2009, **15**, 186–191.

236 M. Utriainen, M. Kröger-Laukkanen and L. Niinistö, *Mater. Sci. Eng. B*, 1998, **54**, 98–103.

237 M. Utriainen, M. Kröger-Laukkanen, L. S. Johansson and L. Niinistö, *Appl. Surf. Sci.*,

2000, **157**, 151–158.

238 T. M. Chung, S. S. Lee, W. Cho, M. Kim, Y. K. Lee, J. H. Hwang, K. S. An and C. G. Kim, *Bull. Korean Chem. Soc.*, 2011, **32**, 783–784.

239 T. S. Yang, W. Cho, M. Kim, K.-S. An, T.-M. Chung, C. G. Kim and Y. Kim, *J. Vac. Sci. Technol. A Vacuum, Surfaces, Film.*, 2005, **23**, 1238.

240 M. Ishikawa, T. Kada, H. Machida, Y. Ohshita and A. Ogura, *Japanese J. Appl. Physics, Part 1 Regul. Pap. Short Notes Rev. Pap.*, 2004, **43**, 1833–1836.

241 H. L. Lu, G. Scarel, C. Wiemer, M. Perego, S. Spiga, M. Fanciulli and G. Pavia, *J. Electrochem. Soc.*, 2008, **155**, H807.

242 J. Chae, H.-S. Park and S. Kang, *Electrochem. Solid-State Lett.*, 2002, **5**, C64–C66.

243 A. Nakamura, K. Yamamoto, J. Ishihara, T. Aoki and J. Temmyo, *Jpn. J. Appl. Phys.*, 2010, 49, 7267.

244 H. Kumagai, M. Matsumoto, K. Toyoda and M. Obara, *J. Mater. Sci. Lett.*, 1996, **15**, 1081–1083.

245 U. Holzwarth and N. Gibson, *Nat. Nanotechnol.*, 2011, **6**, 534–534.

246 CasaXPS software, 2019.

247 E. Thimsen, A. B. F. Martinson, J. W. Elam and M. J. Pellin, *J. Phys. Chem. C*, 2012, **116**, 16830–16840.

248 J. S. J. Hargreaves, *Catal. Struct. React.*, 2016, **2**, 33–37.

249 D. F. Swinehart, *J. Chem. Educ.*, 1962, **39**, 333.

250 E. A. Davis and N. F. Mott, *Philos. Mag.*, 1970, **22**, 0903–0922.

251 J. Tauc, *Mater. Res. Bull.*, 1968, **3**, 37–46.

252 T. P. Weiss, B. Bissig, T. Feurer, R. Carron, S. Buecheler and A. N. Tiwari, *Sci. Rep.*, 2019, **9**, 1–13.

253 E. W. J. Mitchell and J. W. Mitchell, *Proc. R. Soc. London. Ser. A. Math. Phys. Sci.*, 1951, **210**, 70–84.

254 J. A. Cornell and R. D. Berger, *Phytopathology*, 1987, **77**, 63.

255 Y. Shao, Y. Yuan and J. Huang, *Nat. Energy*, 2016, **1**, 1–6.

256 A. M. A. Leguy, Y. Hu, M. Campoy-Quiles, M. I. Alonso, O. J. Weber, P. Azarhoosh, M.

Van Schilfgaarde, M. T. Weller, T. Bein, J. Nelson, P. Docampo and P. R. F. Barnes, *Chem. Mater.*, 2015, **27**, 3397–3407.

257 www.shodhganga.inflibnet.ac.in/bitstream/10603/77169/11/11_chapter%203.pdf, Accessed 16/06/19.

258 Y. Guan, S. Wang, X. Wang, C. Sun, Y. Wang and Z. Ling, *RSC Adv.*, 2016, **6**, 2641–2650.

259 J. H. Kim and S. Blairs, *J. Chem. Thermodyn.*, 1990, **22**, 803–814.

260 Y. Chen, G. Zhu, M. Hojamberdiev, J. Gao, R. Zhu, C. Wang, X. Wei and P. Liu, *J. Hazard. Mater.*, 2018, **344**, 42–54.

261 W. Fredriksson, S. Malmgren, T. Gustafsson, M. Gorgoi and K. Edström, *Appl. Surf. Sci.*, 2012, **258**, 5790–5797.

262 A. X. Gray, C. Papp, S. Ueda, B. Balke, Y. Yamashita, L. Plucinski, J. Minár, J. Braun, E. R. Ylvisaker, C. M. Schneider, W. E. Pickett, H. Ebert, K. Kobayashi and C. S. Fadley, *Nat. Mater.*, 2011, **10**, 759–764.

263 P. Ghods, O. B. Isgor, J. R. Brown, F. Bensebaa and D. Kingston, *Appl. Surf. Sci.*, 2011, **257**, 4669–4677.

264 M. Fondell, M. Gorgoi, M. Boman and A. Lindblad, *J. Electron Spectros. Relat. Phenomena*, 2014, **195**, 195–199.

265 A. Holländer, M. Haupt and C. Oehr, *Plasma Process. Polym.*, 2007, **4**, 773–776.

266 G. D. Cody, T. Tiedje, B. Abeles, T. D. Moustakas, B. Brooks and Y. Goldstein, *Le J. Phys. Colloq.*, 1981, **42**, C4-301-C4-304.

267 Y. Natsume, H. Sakata and T. Hirayama, *Phys. status solidi*, 1995, **148**, 485–495.

268 J. D. Dow and D. Redfield, *Phys. Rev. B*, 1972, **5**, 594–610.

269 M. Nishiwaki, K. Nagaya, M. Kato, S. Fujimoto, H. Tampo, T. Miyadera, M. Chikamatsu, H. Shibata and H. Fujiwara, *Phys. Rev. Mater.*, 2018, **2**, 1–28.

270 C. Liu and X. J. Wang, *Dalt. Trans.*, 2016, **45**, 7720–7727.

271 M. Liu, L. Zhang, K. Wang and Z. Zheng, *CrystEngComm*, 2011, **13**, 5460–5466.

272 N. T. Hahn, S. Hoang, J. L. Self and C. B. Mullins, *ACS Nano*, 2012, **6**, 7712–7722.

273 X. Jiang, Y. Ma, C. Zhao, Y. Chen, M. Cui, J. Yu, Y. Wu and Y. He, *J. Mater. Res.*, 2018,

33, 2385–2395.

274 A. Walsh, G. W. Watson, D. J. Payne, R. G. Edgell, J. Guo, P. A. Glans, T. Learmonth and K. E. Smith, *Phys. Rev. B - Condens. Matter Mater. Phys.*, 2006, **73**, 1–13.

275 X. Xiao, C. Liu, R. Hu, X. Zuo, J. Nan, L. Li and L. Wang, *J. Mater. Chem.*, 2012, **22**, 22840–22843.

276 J. Wang, X. Yang, K. Zhao, P. Xu, L. Zong, R. Yu, D. Wang, J. Deng, J. Chen and X. Xing, *J. Mater. Chem. A*, 2013, **1**, 9069–9074.

277 R. D. Shannon, *Acta Crystallogr. Sect. A*, 1976, **32**, 751–767.

278 chem.libretexts.org, Accessed 16/06/19.

279 M. Yasaka, *Rigaku J.*, 2010, **26**, 1–9.

280 M. Lütt, M. R. Fitzsimmons and D. Li, *J. Phys. Chem. B*, 2002, **102**, 400–405.

281 L. G. Parratt, *Phys. Rev.*, 1954, **95**, 359–369.

282 H. Steinrück, *X-Ray Surface Diffraction & Reflectivity: Stanford Synchrotron Radiation Lightsource, SLAC National Accelerator Laboratory*, 2016.

283 P. Lenormand, A. Lecomte, D. Babonneau and A. Dauger, *Thin Solid Films*, 2006, **495**, 224–231.

284 W. H. Briscoe, F. Speranza, P. Li, O. Konovalov, L. Bouchenoire, J. van Stam, J. Klein, R. M. J. Jacobs and R. K. Thomas, *Soft Matter*, 2012, **8**, 5055.

285 A. Gandhi and S. Wu, *Nanomaterials*, 2017, **7**, 231.

286 D. Y. Jiang, J. M. Qin, X. Wang, S. Gao, Q. C. Liang and J. X. Zhao, *Vacuum*, 2012, **86**, 1083–1086.

287 K. Ingraham, J. McCutchen and T. D. Sparks, *JoVE, Cambridge, MA*.

288 K. Gelderman, L. Lee and S. W. Donne, *J. Chem. Educ.*, 2007, **84**, 685.

289 Z. Kerner and T. Pajkossy, *Electrochim. Acta*, 2000, **46**, 207–211.

290 Y. Xie, K. Lu, J. Duan, Y. Jiang, L. Hu, T. Liu, Y. Zhou and B. Hu, *ACS Appl. Mater. Interfaces*, 2018, **10**, 14153–14159.

291 M. Szafrański and A. Katrusiak, *J. Phys. Chem. Lett.*, 2016, **7**, 3458–3466.

292 T. Du, C. H. Burgess, J. Kim, J. Zhang, J. R. Durrant and M. A. McLachlan, *Sustain. Energy Fuels*, 2017, **1**, 119–126.

293 S. Chen, Y. Hou, H. Chen, M. Richter, F. Guo, S. Kahmann, X. Tang, T. Stubhan, H. Zhang, N. Li, N. Gasparini, C. O. R. Quiroz, L. S. Khanzada, G. J. Matt, A. Osvet and C. J. Brabec, *Adv. Energy Mater.*, 2016, **6**, 1–9.

294 D. C. Iza, D. Muñoz-Rojas, Q. Jia, B. Swartzentruber and J. L. Macmanus-Driscoll, *Nanoscale Res. Lett.*, 2012, **7**, 655.

295 K. S. Kim and N. Winograd, *Surf. Sci.*, 1974, **43**, 625–643.

296 F. Reinert, P. Steiner, S. Hüfner, H. Schmitt, J. Fink, M. Knupfer, P. Sandl and E. Bertel, *Phys. B Condens. Matter*, 1995, **97**, 83–93.

297 D. Ramirez, K. Schutt, J. F. Montoya, S. Mesa, J. Lim, H. J. Snaith and F. Jaramillo, *J. Phys. Chem. C*, 2018, **122**, 21239–21247.

298 T. Wang, D. Ding, X. Wang, R. Zeng, H. Liu and W. Shen, *ACS Omega*, 2018, **3**, 18434–18443.